

THE TECTONIC, THERMAL, AND MAGNETIC EVOLUTION
OF ICY SATELLITES

by

Michael Thomas Bland

A Dissertation Submitted to the Faculty of the
DEPARTMENT OF PLANETARY SCIENCES

In Partial Fulfillment of the Requirements
For the Degree of

DOCTOR OF PHILOSOPHY

In the Graduate College

THE UNIVERSITY OF ARIZONA

2 0 0 8

THE UNIVERSITY OF ARIZONA
GRADUATE COLLEGE

As members of the Final Examination Committee, we certify that we have read the dissertation prepared by Michael Thomas Bland entitled *The Tectonic, Thermal, and Magnetic Evolution of Icy Satellites* and recommend that it be accepted as fulfilling the dissertation requirement for the Degree of Doctor of Philosophy.

Adam Showman

Date: 7 April 2008

William Hubbard

Date: 7 April 2008

Jay Melosh

Date: 7 April 2008

Clem Chase

Date: 7 April 2008

Elizabeth Turtle

Date: 7 April 2008

Final approval and acceptance of this dissertation is contingent upon the candidate's submission of the final copies of the dissertation to the Graduate College.

I hereby certify that I have read this dissertation prepared under my direction and recommend that it be accepted as fulfilling the dissertation requirement.

Dissertation Director: Adam Showman

Date: 7 April 2008

STATEMENT BY AUTHOR

This dissertation has been submitted in partial fulfillment of requirements for an advanced degree at The University of Arizona and is deposited in the University Library to be made available to borrowers under rules of the Library.

Brief quotations from this dissertation are allowable without special permission, provided that accurate acknowledgment of source is made. Requests for permission for extended quotation from or reproduction of this manuscript in whole or in part may be granted by the head of the major department or the Dean of the Graduate College when in his or her judgment the proposed use of the material is in the interests of scholarship. In all other instances, however, permission must be obtained from the author.

SIGNED: _____

Michael Thomas Bland

ACKNOWLEDGMENTS

The journey to a PhD is not made alone and I would like to recognize the people who have assisted and accompanied me along my way. Special thanks go to my advisor Adam Showman, who managed to give me both room to work independently and enough guidance to keep me on the right path. Thanks also go to Ross Beyer and Gabriel Tobie who not only contributed to the work presented in this dissertation, but also taught me about productive collaborative research. Renu Malhotra provided the orbital dynamics code used for half my dissertation work, and I thank her in spite of the headaches she gave me during my oral exam. Finally, I'd like to thank Glinda Davidson and Gina Bailey for making my life easier in enumerable little ways.

I would like to recognize all the people who have made the last six years here in Arizona enjoyable and productive (though I'm sure I will leave someone out). To Jay Melosh, Zibi Turtle, Jason Barnes, and Dave O'Brien for leading great field trips over the years. Thanks to my office mates Curtis Cooper, Matt Chamberlain, Eve Berger, and Kat Gardner-Vandy for their many conversations, both scientific and otherwise. Thanks also to my year-mates Mandy Proctor, Matt Pasek, John Weirich, and Brandon Preblich, who helped me slog through both my major and minor classes. Finally I thank all the grads with whom I've overlapped: the ones who went before me for their scientific and career advise, and the ones who came after me for waiting patiently for my prime office space.

Finally, I would like to thank the people that have affected me personally and contributed to my successes in academia and life in general. Thanks to both of my parents, Tom and Tara, for instilling in me both a strong work ethic and a curiosity about the world around me. Thanks to my sister Kirsten, in whose footsteps I have tread since I can remember. Thanks especially to my wife and best friend Jennifer, without whom I never could have survived the ups and downs of the graduate school experience. Last but certainly not least, thanks to baby Bland for holding on just a few days more.

DEDICATION

To Jennifer:

*For her love, for her support, and most of all
for her patients*

TABLE OF CONTENTS

LIST OF FIGURES	9
LIST OF TABLES	11
ABSTRACT	12
CHAPTER 1 INTRODUCTION	14
1.1 A Historical Perspective	14
1.2 Characteristics of Icy Satellites	16
1.3 Dissertation Outline	20
CHAPTER 2 THE THERMAL EVOLUTION AND GLOBAL EXPANSION OF GANYMEDE	23
2.1 Background	23
2.2 Methods	25
2.2.1 The Orbital Model	26
2.2.2 The Thermal Model	27
2.2.3 The Tidal Dissipation Model	34
2.3 Evolution of the Ice Shell	35
2.3.1 Thermal evolution	35
2.3.2 Influence of Ganymede's Orbital History	38
2.3.3 Variations in Q_J	43
2.3.4 Effect of Ice Grain Size	44
2.4 Global Expansion	48
2.5 Consequences for Ganymede's Geologic History	54
2.5.1 Tectonics and Cratering	54
2.5.2 Cryovolcanism	56
2.5.3 Tidal Deformation	57
2.6 Conclusions	59
CHAPTER 3 THE PRODUCTION OF GANYMEDE'S MAGNETIC FIELD	62
3.1 Background	62
3.2 Methods	68
3.2.1 Energy Balance in the Ice Shell and Silicate Mantle	68
3.2.2 The Core Model	69

TABLE OF CONTENTS – *Continued*

3.2.3	Initial Thermal Conditions	71
3.3	Producing Ganymede’s Magnetic Field	72
3.4	The Influence of Ganymede’s Orbital Evolution	78
3.4.1	Variation in the Silicate Rheology	83
3.4.2	Variations in Q_J	84
3.4.3	The Influence of the Ice Shell	85
3.4.4	Partial Melt	89
3.5	The Timing of Core Formation	93
3.6	Conclusions	94
CHAPTER 4 THE FORMATION OF GANYMEDE’S GROOVED TERRAIN		
	97
4.1	Introduction	97
4.2	The Finite-Element Model	103
4.3	Results	110
4.3.1	Form of the Instability	110
4.3.2	Infinitesimal Strain	117
4.3.3	Finite Strain	123
4.3.4	Effect of Heat Conduction	127
4.3.5	Effect of the Initial Perturbation	129
4.3.6	Non-periodic Initial Perturbations	131
4.4	Sensitivity Analysis	139
4.5	Implications and Conclusion	144
CHAPTER 5 UNSTABLE EXTENSION OF ENCELADUS’ LITHOSPHERE		
	148
5.1	Background	148
5.2	Photoclinometry	153
5.2.1	Method	153
5.2.2	Topography	156
5.3	Numerical Modeling of Unstable Extension	167
5.4	Modeling Results	170
5.5	The Heat Flux and Elastic Thickness	177
5.6	Conclusions	180
CHAPTER 6 CONCLUSIONS AND FUTURE DIRECTIONS		183
6.1	The Resurfacing of Ganymede	183
6.2	Ganymede’s Magnetic Field	184
6.3	Ganymede’s Grooved Terrain	186
6.4	The Tectonic and Thermal Evolution of Enceladus	188

TABLE OF CONTENTS – *Continued*

APPENDIX A SYMBOLS AND PARAMETER VALUES FOR CHAPTERS 2 AND 3	190
APPENDIX B INCLUSION OF MULTIPLE RHEOLOGIES IN TEKTON .	195
B.1 Introduction	195
B.2 The Inclusion of Viscous Deformation in TEKTON	195
B.3 The Inclusion of Multiple Flow Laws	197
B.4 Additional Modifications to TEKTON Files	199
B.5 Testing and Validation	200
REFERENCES	203

LIST OF FIGURES

2.1	Physical and thermal structure of Ganymede	26
2.2	The thermal evolution of Ganymede in the absence of tidal dissipation	37
2.3	Plausible orbital evolution of Ganymede	39
2.4	The thermal evolution of Ganymede including tidal dissipation	41
2.5	Dependence of tidal heat flux and ice shell thickness on Q_J	45
2.6	Influence of ice grain size on ocean formation	47
2.7	Ice phase diagram and ocean adiabats	52
2.8	The global expansion of Ganymede due to melting	53
3.1	Thermal evolution of Ganymede's mantle and core (dry rheology)	73
3.2	Thermal evolution of Ganymede's mantle and core (wet rheology)	76
3.3	Plausible orbital evolution of Ganymede	80
3.4	Thermal evolution including resonance passage	81
3.5	Influence of Q_J on dissipation in the silicate mantle	86
3.6	Influence of the ice shell	88
3.7	The effect of partial melting	92
4.1	Ganymede's grooved terrain	98
4.2	Lithospheric extensional necking	101
4.3	Finite-element model of extensional deformation	111
4.4	Enlargement of near-surface deformation	112
4.5	Simulated topographic profiles	113
4.6	Stress resulting from necking	115
4.7	2nd invariant of the total strain resulting from necking	116
4.8	Exponential growth rate as a function of wavelength	118
4.9	Instability growth at infinitesimal and finite strain	120
4.10	Deformation amplitude at finite strain	125
4.11	Effect of initial perturbation on instability growth	130
4.12	Effect of initial perturbation on instability wavelength	132
4.13	Modification of preexisting terrain	134
4.14	Sensitivity of amplification to physical parameters	141
5.1	Enceladus' equatorial region	150
5.2	Sarandib Planitia	159
5.3	Topography of Sarandib Planitia	160
5.4	Diyar Planitia	162

LIST OF FIGURES – *Continued*

5.5	Topography of Diyar Planitia	163
5.6	The Cufa-Láhej region	165
5.7	Topography of Cufa-Láhej region	166
5.8	Strength envelopes for Enceladus' lithosphere	169
5.9	Finite-element model of Enceladus' extension	171
5.10	Simulated topographic profiles	172
5.11	Total amplification produced by extensional necking	173
5.12	Tectonic resurfacing on Enceladus	175
B.1	Dominant rheology with a composite flow law	201
B.2	Analytically derived expected dominant flow mechanism	202

LIST OF TABLES

2.1	Rheological parameters	32
2.2	Convective scaling parameters	33
4.1	Rheological parameters	106
A.1	Symbols and Parameter Values	190

ABSTRACT

Focusing on Ganymede and Enceladus, this work addresses a number of issues regarding icy satellite evolution, including the ultimate cause of Ganymede’s tectonic and cryovolcanic resurfacing, the production of Ganymede’s magnetic field, the formation of Ganymede’s grooved terrain, and the tectonic and thermal evolution of Enceladus.

Both Ganymede’s resurfacing and the production of its magnetic field may be attributable to the Galilean satellites’ passage through a Laplace-like resonance that excited Ganymede’s orbital eccentricity. I examine how resonance passage effects Ganymede’s thermal evolution using a coupled orbital-thermal model. Dissipation of tidal energy in Ganymede’s ice shell permits high heat fluxes in its past, consistent with the formation of the grooved terrain; however, it also leads to the formation of a thin ice shell, which would have significant consequences for Ganymede’s geologic history. In contrast, negligible tidal dissipation occurs in Ganymede’s silicate mantle. Thus, passage through a Laplace-like resonance cannot reinvigorate Ganymede’s metallic core or enable present-day magnetic field generation.

Ganymede’s thermal evolution has driven tectonic deformation on its surface, producing numerous swaths of ridges and troughs termed “grooved terrain.” Grooved terrain likely formed via unstable extension of Ganymede’s lithosphere, but questions regarding instability growth at large strains remain unanswered. To address these questions, I use the finite-element model TEKTON to simulate the extension of an icy lithosphere to examine instability growth at finite strains. My results indicate that large-amplitude deformation requires lower thermal gradients than have been suggested by analytical models; however, the maximum deforma-

tion amplitudes produced by our numerical models are lower than typical observed groove amplitudes.

Finally, I apply our finite-element modeling to the formation of ridges and troughs on Enceladus. Comparison between our models and photogrammetry profiles of Enceladus' topography indicate that the heat flux was high at the time of ridge and trough formation. Thus, the tectonic resurfacing and high heat fluxes currently observed at Enceladus' south pole may be only the latest episode in a long history of localized resurfacing and global reorientation.

CHAPTER 1

INTRODUCTION

1.1 A Historical Perspective

On January 7th of 1610, Galileo Galilei pointed his newly refined telescope at Jupiter and became the first person to observe its satellites. In a letter written that night Galileo declared, “this evening I have seen Jupiter accompanied by three fixed stars, totally invisible by their smallness. . . . The planets are seen very rotund, like little full moons, and of a roundness bounded and without rays. But the fixed stars do not appear so. . . .” (Drake, 1978). By the time Galileo’s discoveries were printed in *Sidereus Nuncius* on March 12 of that year, he had convinced himself that these “stars” were in fact orbiting Jupiter: “no one can doubt that they complete their revolutions about [Jupiter]. . . . Our vision offers us four stars wandering around Jupiter like the Moon around the Earth . . .” (Galilei, 1989). Galileo had initiated the study of satellites of the outer Solar System.

Within half a century, satellites were discovered beyond Jupiter. In 1655 Christiaan Huygens discovered Saturn’s largest satellite, Titan, and by the end of the century Giovanni Domenico Cassini had observed Saturn’s next four largest satellites: Iapetus, Rhea, Dione, and Tethys. In the three centuries that followed Galileo’s dramatic discovery, approximately 33 satellites with diameters greater than 100 km (including Galileo’s) were discovered.

Prior to the advent of robotic space exploration, study of the satellites of the outer Solar System was limited to their dynamics and what could be observed from the ground. Despite these limitations, a picture of satellites as unique worlds began to emerge. In the 18th and 19th century, Pierre-Simon Laplace and his successors

determined the masses of the Galilean satellites from their orbital motion. At the turn of the 20th century, Edward Barnard measured their radii for the first time, enabling a calculation of the satellites' densities. Gerard Kuiper later coupled these density measurements with a model of equilibrium nebular condensation to suggest that the satellites of Saturn, as well as Ganymede and Callisto, have an icy composition (Kuiper, 1952). Kuiper then provided the first tentative empirical evidence for their icy compositions using near-infrared photometry (Kuiper, 1957; Morrison, 1982). Definite spectroscopic evidence for icy surfaces on Europa and Ganymede was provided fifteen years later by Pilcher et al. (1972) and Fink et al. (1973).

In addition to observational studies, theoretical advances were made in understanding icy satellites. Even before the presence of water ice on their surfaces was confirmed, the structural and thermal models of Lewis (1971) indicated that large icy satellites might contain melted layers within their interiors. These models were later extended to include the thermal evolution of icy satellites over the age of the Solar System (Consolmagno and Lewis, 1977) and were applied both to the Galilean satellites specifically (Consolmagno and Lewis, 1976) and to mid-sized icy satellites in general (Consolmagno and Lewis, 1978). Opposing these models, Reynolds and Cassen (1979) argued that large ice mantles would be unstable to convection, which could prevent internal melting. The question of whether liquid layers are present in icy satellite interiors has not yet been conclusively resolved. In addition to the interior, consideration of the geophysical processes that might affect the lithospheres of large icy satellites led to the correct prediction that tectonic features of extensional origin, rather than compressional origin, would dominate their surfaces (Parmentier and Head, 1979).

Direct exploration of the outer Solar System and its satellites began with the launches of Pioneers 10 and 11 in 1972 and 1973, respectively. Though few measurements of icy satellites were made, the missions refined the masses of all four Galilean satellites and improved the diameter measurements of Callisto and Europa. It was

not until Voyager I and II reached Jupiter in 1979, however, that our knowledge of icy satellites truly blossomed. The exploration of the outer Solar System continued with three additional missions: Galileo to Jupiter in 1989, Cassini-Huygens to Saturn in 1997, and New Horizons to Pluto in 2006. Through the data collected by these missions, a coherent, if complex, picture of icy satellites is now beginning to emerge.

1.2 Characteristics of Icy Satellites

The current conception of icy satellites is a complex one. The following discussion applies to bodies larger than 100 km in radius that orbit a larger non-solar primary body and whose surfaces primarily consist of cosmochemically “icy” material. I exclude smaller bodies (i.e. radius < 100 km) simply because many of the processes discussed in this dissertation do not apply to them. In our Solar System, icy satellites range from small bodies less than 100 km in radius to bodies the size of Mercury. They therefore fill a size niche between large asteroids and planets. The compositions of icy satellites vary widely. Gravity data indicates that the thickness of Europa’s outer water layer (ice or liquid) accounts for only 7% of the satellite’s radius, with the remainder consisting of rock or iron (Anderson et al., 1997a, 1998). In contrast, Tethys’ bulk density of 974 kg m^{-3} (Jacobson et al., 2006) suggests that its composition includes very little rocky material. In addition, bodies in the outer solar system may contain ices more volatile than water ice, some of which can have a profound impact on the thermal histories of the bodies (e.g. Spohn and Schubert, 2003).

The variability in satellite size and composition leads to substantial variability in internal structure. The largest satellites, Ganymede, Callisto, and Titan, have thick ice mantles consisting of both ice I and high-pressure phases of ice (e.g. Fletcher, 1970, see also Fig. 2.7). Bodies with less ice (e.g. Europa) or lower gravity (e.g. Enceladus) primarily have ice I shells overlying rocky cores. Understanding the

internal structure of icy satellites is complicated by the question of how mass is distributed within the satellite. Gravity data suggest that at least a few icy satellites are completely differentiated such that the ice and rock (and in some cases a metallic core) have completely separated into distinct layers. The type example of such a satellite is Ganymede, which has the lowest moment of inertia ($C/MR^2 = 0.3115$) of any solid body in the Solar System (Anderson et al., 1996; Schubert et al., 2004). Many other satellites, however, appear to be undifferentiated or only partially differentiated. Ganymede's neighbor Callisto, which despite its size appears to be only partially differentiated, is the most infamous example (Anderson et al., 1997b). Because detailed gravity data of icy satellites is often limited, determining whether a satellite is differentiated generally relies on somewhat poorly constrained thermal modeling (e.g. Schubert et al., 1981; Ellsworth and Schubert, 1983; Tobie et al., 2005a; Multhaup and Spohn, 2007; Schubert et al., 2007).

The features of icy satellites that perhaps garner the most attention are possible internal liquid layers. The minimum melting temperature for water ice occurs at the ice I/III phase boundary at a temperature of 251 K and a pressure of 209 MPa (Petrenko and Whitworth, 1999). Liquid water can therefore exist in the interiors of icy satellites provided a source of heating exists that can maintain the ice temperature above 251 K. This temperature condition is relaxed further if ammonia or salts that lower the melting point of ice are present (e.g. Spohn and Schubert, 2003). Internal oceans are strongly suspected on Europa, Ganymede, and Callisto based on Galileo magnetometer data, which measured an induced dipole field near each satellite (Khurana et al., 1998; Kivelson et al., 2000, 2002). In the case of Europa, geologic data supports the claim of an ocean (e.g. Pappalardo et al., 1999; Greeley et al., 2004). Furthermore, recent Cassini data indicates that Saturn's satellite Titan is rotating non-synchronously, suggesting an internal liquid layer must be present (Lorenz et al., 2008). Based on thermal modeling, internal oceans have also been suggested on Saturn's moons Enceladus (Schubert et al., 2007), and Rhea (Huss-

mann et al., 2006), as well as the satellites Titania, Oberon, and Triton (Husmann et al., 2006), although uncertainty remains as to the validity of these claims. Despite being well outside the canonical “habitable zone,” these internal oceans have significant astrobiological potential (Greenberg et al., 2000; Chyba and Phillips, 2002).

When a thin ice lithosphere is decoupled from the satellite’s interior by the presence of an ocean, the magnitude of the tidal distortion of the ice shell due to the tidal potential of the satellite’s primary will be large. If the satellite is in an eccentric orbit, the tidal potential varies in time, causing the shell to flex on diurnal timescales. Additionally, because a satellite in synchronous rotation keeps one face locked to the empty focus of its orbital ellipse, the position of the satellite’s tidal bulge librates across the satellite’s surface. These time varying radial and librational tides generate stress within the satellite’s lithosphere (Melosh, 1980; Leith and McKinnon, 1996). While these stresses are often small, they have been suggested to cause cycloidal fracturing and ridge formation on Europa (e.g. Hoppa et al., 1999; Greenberg et al., 1998; Nimmo and Gaidos, 2002) and fracturing and cryovolcanism on Enceladus (Nimmo et al., 2007; Hurford et al., 2007; Smith-Konter and Pappalardo, 2007). Non-synchronous rotation of a floating ice shell can generate even larger stresses within a satellite’s lithosphere (Ojakangas and Stevenson, 1989; Leith and McKinnon, 1996) and may be associated with Europa’s complex fracture patterns (e.g. Helfenstein and Parmentier, 1985; McEwen, 1986; Leith and McKinnon, 1996; Geissler et al., 1998; Greenberg et al., 1998; Figueredo and Greeley, 2000).

In addition to the stress generated by tides, a satellite in an eccentric orbit feels a torque due to its primary that acts to circularize the satellite’s orbit. As the orbit is circularized, orbital energy is converted to thermal energy within the satellite, providing an additional source of heating (Peale and Cassen, 1978). If the satellite’s orbit is allowed to evolve unperturbed, the timescale for circularization is generally short (~ 100 Ma) relative to the age of the Solar System (Peale et al.,

1980). However, if the satellite is in an orbital resonance with other satellites, its eccentricity and the associated dissipation of tidal energy can be maintained for extended periods of time (i.e. the lifetime of the resonance) (Peale et al., 1979). The addition of tidal dissipation as a heat source can have a profound influence on the thermal evolution of a satellite, permitting, for example, oceans to currently be maintained on Europa (e.g. Ojakangas and Stevenson, 1989; McKinnon, 1999; Hussmann et al., 2002; Tobie et al., 2003; Moore, 2006, and many others), and geological activity to presently occur on Enceladus (Porco et al., 2006).

The wide variety in size, composition, degree of differentiation, and heating mechanisms leads to a broad range of surface processes that can operate on icy satellites. Impact cratering is the dominate surface modification process on many satellites and an extensive variety of crater morphologies, including morphologies not seen on the terrestrial planets, exists (see Schenk et al., 2004, for a review). However, extensive modification has occurred by processes other than cratering, including (but not limited to) tectonism and cryovolcanism. In general, extensional tectonics dominates the surface deformation of icy satellites. Thus many icy satellites are marked by complex sets of fractures, graben, and extensional ridges and troughs (Squyres and Croft, 1986). Compressional features have been identified on some icy satellites, such as the Sulci on Enceladus (Kargel and Pozio, 1996; Porco et al., 2006). However, compressional deformation is often more subdued, as in Europa's Astyplaea Linea (Dombard and McKinnon, 2006b), or is seemingly absent altogether, as on Ganymede (e.g. Pappalardo et al., 1998).

In addition to tectonism, there is evidence that cryovolcanism has occurred on Ganymede (Schenk et al., 2001) and Europa (e.g. Greeley et al., 1998; Pappalardo et al., 1999; Greeley et al., 2000; Figueredo and Greeley, 2004) and active cryovolcanism has been observed on Enceladus (Hansen et al., 2006; Porco et al., 2006). Evidence for cryovolcanism on Titan has also been claimed (Lopes et al., 2007; Sotin et al., 2005), although the low resolution of Titan radar and VIMS observa-

tions makes interpretation difficult. While strong evidence supports the notion that cryovolcanism can occur on icy satellites, the mechanisms by which water, with its higher density, can be erupted through lower density ice are only partially understood (e.g. Crawford and Stevenson, 1988; Showman et al., 2004; Manga and Wang, 2007).

1.3 Dissertation Outline

Despite the wealth of information gathered in the past 35 years of spacecraft exploration, many features of icy satellites remain unexplained. This dissertation attempts to add to our understanding of such features. Broadly speaking, it addresses two topics: the thermal evolution of Ganymede, and tectonism on Ganymede and Enceladus.

Jupiter’s satellite Ganymede is one of the Solar System’s great enigmas. Gravity data indicate that it is the most centrally condensed solid object in the Solar System, suggesting a high degree of differentiation (Anderson et al., 1996). Additionally, the satellite is one of only three solid bodies in the Solar System that produces an internally driven magnetic field. Finally, its surface bears the scars of vigorous tectonic activity that were likely created in the middle of the satellite’s geologic history. Furthermore, all these features occur on a satellite that currently receives no tidal heat and whose “twin” (in size and bulk composition) Callisto is only partially differentiated (Anderson et al., 1997b) and dominated by impact cratering. Scenarios for Ganymede’s thermal evolution that assume secular cooling of the satellite over the age of the Solar System have difficulty explaining the observations described above (e.g. Freeman, 2006). However, Malhotra (1991) and Showman and Malhotra (1997) showed that the Galilean satellites may have passed through one or more Laplace-like resonances that excited Ganymede’s eccentricity before they evolved into the current Laplace resonance. The pulse of tidal heating associated with resonance passage might therefore account for Ganymede’s unique features. In Chapter

2 I describe an investigation of the thermal evolution of Ganymede's ice shell including the effects of tidal dissipation during resonance passage. The investigation reexamines the degree of volume expansion expected during melting of Ganymede's ice mantle and considers the geologic consequences of the existence of a thin ice shell in Ganymede's past. The material in this chapter will shortly be submitted for publication in the journal *Icarus*. Chapter 3 focuses on the thermal history of Ganymede's silicate mantle and metallic core both with and without resonance passage and emphasizes mechanisms for producing Ganymede's magnetic field. The material in this chapter has been submitted for publication in the journal *Icarus*. The investigations in Chapters 2 and 3 utilize a model for the dynamical evolution of the Galilean satellites provided by Renu Malhotra and a model for the tidal dissipation in a large satellite provided by Gabriel Tobie.

Ganymede's internal activity is ultimately responsible for driving the tectonic deformation observed on its surface. Understanding how these tectonic features formed therefore provides an alternate window into the satellite's geologic history. Chapter 4 describes a detailed study of the formation of Ganymede's most iconic feature: the grooved terrain. The investigation uses the finite-element model TEKTON (Melosh and Raefsky, 1980) to simulate the extension of an icy lithosphere under conditions relevant to Ganymede at the time of groove formation. As part of the investigation, I constructed a new finite element library that permits the definition of multiple rheological flow laws. The new library is described in Appendix B. The material in this chapter has been published in: Bland, M. T. and A. P. Showman (2007). The formation of Ganymede's grooved terrain: Numerical modeling of extensional necking instabilities. *Icarus*, 189, 439-456.

While Ganymede's grooved terrain is the archetypical icy satellite ridge and trough terrain, similar tectonic features occur on other satellites as well, including the small Saturnian satellite Enceladus. Enceladus is one of the few currently geologically active bodies in the Solar System, with heat fluxes as high as $\sim 250 \text{ mW m}^{-2}$

and an active cryovolcanic plume (Spencer et al., 2006; Hansen et al., 2006; Porco et al., 2006). While current activity is focused at the south pole, Enceladus' highly tectonically deformed surface attests to a long geologic history, with activity occurring across the satellite. Studying this older deformation provides geologic context for the activity observed at the south pole today. In Chapter 5 I apply the model described in Chapter 4 to Enceladus' ridge and trough terrain. I then compare our modeling results to photoclinometry profiles of Enceladus' surface to constrain the heat flux required at the time of ridge and trough formation. The material in this chapter has been published in: Bland, M. T., R. A. Beyer, and A. P. Showman (2007). Unstable extension of Enceladus' lithosphere. *Icarus*, 192, 92-105. The photoclinometry work described was performed by Ross Beyer, and he provided a small portion of the text in Chapter 5.

CHAPTER 2

THE THERMAL EVOLUTION AND GLOBAL EXPANSION OF GANYMEDE

2.1 Background

The surface of Ganymede, the Solar System's largest satellite, displays the tectonic scars of a tumultuous geologic history. Two-thirds of the satellite consists of bright, young terrain that has been modified by tectonic and/or cryovolcanic processes (e.g. Smith et al., 1979a; Pappalardo et al., 1998). The majority of this deformation, termed "grooved terrain," appears to be extensional in origin and consists of periodically spaced ridges and troughs (Smith et al., 1979a; Pappalardo et al., 1998). The formation of the grooved terrain likely occurred via unstable extension of Ganymede's lithosphere, and may have required heat flows up to 100 mW m^{-2} (Dombard and McKinnon, 2001; Bland and Showman, 2007, Chapter 4). Independent of their immediate formation mechanism, Ganymede's period of groove formation must have been marked by vigorous activity in Ganymede's interior that produced high surface heat fluxes, large surface stresses, and possibly satellite expansion.

The ultimate cause of Ganymede's tectonic and cryovolcanic resurfacing is difficult to discern. While the satellite participates in the Laplace resonance with Io and Europa, no forcing of its eccentricity occurs, and thus no tidal energy is currently dissipated in its interior. Early workers suggested that the grooved terrain may have formed during differentiation of the satellite (Squyres, 1980; Mueller and McKinnon, 1988). Differentiation would permit both the high heat flows and global satellite expansion necessary to produce the grooved terrain. However, the mechanism is inconsistent with the apparent youth of the grooved terrain, which has an age of $\sim 2 \text{ Ga}$ (Zahnle et al., 2003). Furthermore, any tectonic structures that resulted

from early differentiation would likely be destroyed by subsequent impact cratering (McKinnon and Parmentier, 1986). Only if differentiation was delayed (requiring slow satellite accretion (Schubert et al., 1981; Canup and Ward, 2002)), or occurred in stages (e.g. Mueller and McKinnon, 1988) is this mechanism consistent with the young age of the grooved terrain.

The formation of grooved terrain therefore appears to require prolonged or renewed geologic activity during Ganymede’s middle history. Such activity is difficult to reconcile with thermal modeling of large icy satellites, which have generally predicted that Ganymede’s period of geologic activity should have ended by ~ 4 Ga (e.g. Reynolds and Cassen, 1979; Schubert et al., 1981; Friedson and Stevenson, 1983; Kirk and Stevenson, 1987). The inclusion of stagnant-lid convection (not included in early thermal models), might prolong the existence of an internal ocean but does not allow high heat flows late in Ganymede’s history (see Section 2.3).

Renewed geologic activity may be possible, however, if the Laplace resonance is not primordial. Malhotra (1991) and Showman and Malhotra (1997) showed that the Galilean satellites may have passed through one or more Laplace-like resonances before evolving into the current Laplace resonance. Like the Laplace resonance, these Laplace-like resonances involve 2:1 mean motion resonances between the satellite pairs Io-Europa and Europa-Ganymede. However, the typical 1:1 commensurability in the conjunction drift rates (ω) of the two satellite pairs ($\omega_1/\omega_2 = 1$, where $\omega_1 = 2n_2 - n_1$ and $\omega_2 = 2n_3 - n_2$ and n_1 , n_2 , and n_3 are the mean motions of Io, Europa, and Ganymede respectively) is replaced by a ratio of 2:1, 1:2, 3:2, etc. Malhotra (1991) and Showman and Malhotra (1997) showed that some of the Laplace-like resonance can excite Ganymede’s eccentricity, leading to the dissipation of tidal energy within the satellite.

The effects of resonance passage on Ganymede’s thermal evolution were explored by Showman et al. (1997) who found that, if the satellite entered the resonance in a warm initial state, extensive melting of the interior would occur. Additionally, if

the satellite entered the resonance in a not-too-hot but not-too-cold initial state a thermal runaway, in which a positive feedback between the rate of tidal heating and the ice temperature leads to rapid temperature increases and melting, could occur (Showman et al., 1997). Furthermore, the internal melting that occurs during tidal heating causes a small amount of satellite expansion, which can lead to significant surface stress and may have initiated groove formation (Showman et al., 1997).

While the modeling of Showman et al. (1997) provides an important first look at the possible influence of tidal dissipation on Ganymede’s thermal history, advances in our understanding of Ganymede’s internal structure, stagnant-lid convection, and radially varying tidal dissipation warrant a reevaluation of the tidal heating scenario. In this chapter we utilize a coupled orbital-thermal model to investigate the thermal evolution of Ganymede’s ice shell and to reassess the effects of the Galilean satellites’ passage through a Laplace-like resonance. We evaluate both the present and past potential for the existence of large internal oceans within Ganymede’s interior and we reexamine the extent to which melting can generate satellite expansion over a range of assumptions regarding the physical and chemical nature of Ganymede’s ice shell and liquid ocean. Finally, we describe the implications of resonance passage for Ganymede’s geologic history and consider whether these implications are consistent with the geologic evidence.

2.2 Methods

To investigate the effects of resonance passage on the thermo-physical evolution of Ganymede’s ice shell we utilize a coupled orbital-thermal model of Ganymede. The model couples the orbital model of Malhotra (1991) (Section 2.2.1) to a one-dimensional, three-layer thermal model of Ganymede’s ice shell, silicate mantle, and metallic core (Section 2.2.2 and Fig. 2.1). The thermal and orbital models are coupled through the tidal dissipation, which depends upon both the thermal structure and orbital evolution of the satellite. We use the model of Tobie et al.

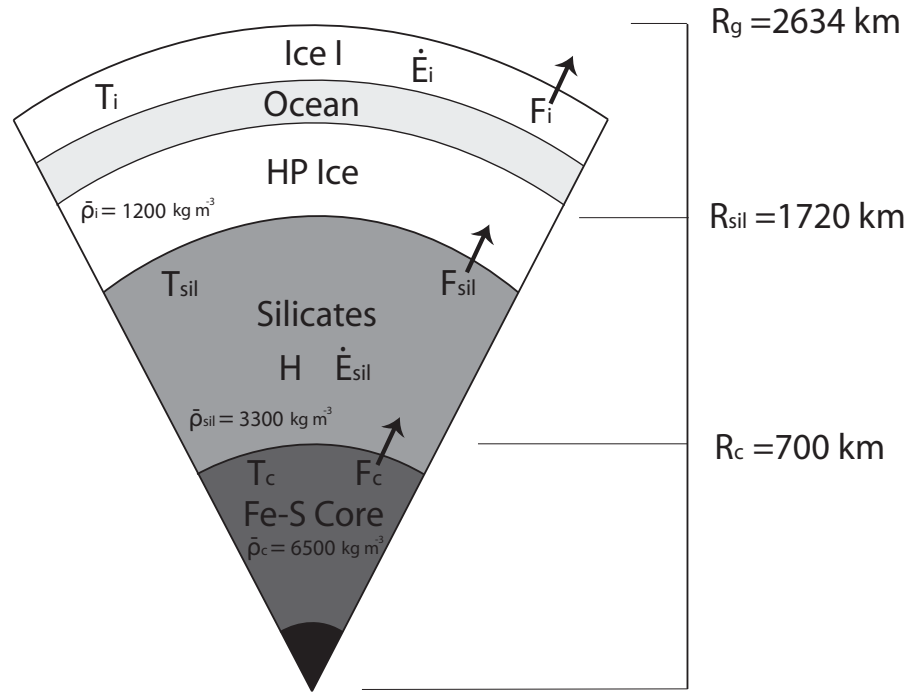


Figure 2.1: Assumed physical and thermal structure for Ganymede. The model allows both inner core formation and ocean formation as illustrated, though these layers are not included in the initial conditions. Symbols correspond to those used in the text and average densities are shown. Other relevant parameters are provided in Appendix A.

(2005b) to calculate the radially varying tidal dissipation within the satellite (Section 2.2.3).

2.2.1 The Orbital Model

We simulate the tidally driven evolution of the Galilean satellites into the Laplace resonance using the orbital model of Malhotra (1991). The model generalizes the evolutionary scenario described by Yoder and Peale (1981) allowing a more complete dynamical investigation of the orbital history of the satellites, including capture into

one or more Laplace-like resonances. These resonances cannot easily be explored by analytical representations of the satellites' tidal evolution, and no analytical formulation for tidal evolution in a Laplace-like resonance comparable to those used for the Laplace resonance (e.g. Ojakangas and Stevenson, 1986; Fischer and Spohn, 1990; Hussman and Spohn, 2004) currently exists. The model includes perturbations due to Jupiter's gravity field, mutual perturbations between the satellites Io, Europa, and Ganymede, and secular perturbations due to Callisto. The effects of orbital inclinations are neglected. Forward integration permits determination of the eccentricity, semi-major axis, mean longitude, and longitude of periapse of each satellite.

2.2.2 The Thermal Model

The thermal evolution of Ganymede is controlled by how energy is transferred between the three layers of the model. We solve for the energy balance in each layer as a function of time using a 4th order Runge-Kutta algorithm. The energy balance in the ice shell, silicate mantle, and metallic core are respectively given by

$$4\pi R_{sil}^2 F_{sil} + \dot{E}_I = 4\pi R_g^2 F_I + \frac{4}{3}(R_g^3 - R_{sil}^3)\rho_I c_{p,I} \frac{dT_I}{dt}, \quad (2.1)$$

$$\frac{4}{3}\pi(R_{sil}^3 - R_c^3)\rho_{sil}H + 4\pi R_c^2 F_c + \dot{E}_{sil} = 4\pi R_{sil}^2 F_{sil} + \frac{4}{3}\pi(R_{sil}^3 - R_c^3)\rho_{sil}c_{p,sil} \frac{dT_{sil}}{dt}, \quad (2.2)$$

$$(E_G + L_{Fe})\frac{dm_{ic}}{dt} = 4\pi R_c^2 F_c + \frac{4}{3}\pi R_c^3 \rho_c c_{p,c} \frac{dT_c}{dt}, \quad (2.3)$$

where R_g , R_{sil} , and R_c are the radius of Ganymede, the silicate mantle, and the metallic core respectively; F_I , F_{sil} , and F_c are the heat flux out of the ice shell, silicate mantle, and metallic core respectively; \dot{E}_I , \dot{E}_{sil} , are the tidal heating rates in the ice shell and silicate mantle respectively; ρ_I , ρ_{sil} , ρ_c , $c_{p,I}$, $c_{p,sil}$, $c_{p,c}$, T_I , T_{sil} , and T_c are the average densities, specific heats, and mean temperatures of the ice shell (I), silicate mantle (sil), and core (c) respectively; t is time; H is the radiogenic heating rate per unit mass calculated after Kirk and Stevenson (1987),

which includes contributions from the decay of K^{40} , Th^{232} , U^{235} , and U^{238} ; L_{Fe} is the latent heat released by condensation of iron; E_G is the gravitational energy release associated with iron condensation after Schubert et al. (1988); and m_{ic} is the mass of the inner core. Equation 2.3 is after Stevenson et al. (1983) and is described further in Chapter 3. For simplicity, we do not treat the thermal balance of Ganymede's high-pressure ice layers separately from the ice I layer, implicitly assuming that ice phase transitions are not a barrier to heat transfer. The inclusion of such phase transitions may ultimately prove important in understanding convective processes in large icy satellites (McKinnon, 1998) but a thorough investigation of their effects is beyond the scope of the present work. All parameter values used in the model are provided in Appendix A.

If the temperature of the ice shell exceeds 251 K (the minimum melting temperature for ice) melting and ocean formation occurs and we modify the energy balance of the ice shell (Eq. 2.1) to account for both the latent heat removed by melting and the larger specific heat of liquid water. These two effects act to buffer changes in the ice shell temperature. The energy balance of the ice shell with an ocean is given by

$$\pi R_{sil}^2 F_{sil} + \dot{E}_I = 4\pi R_g^2 F_I + (M_w c_{p,w} + M_i c_{p,I}) \frac{dT_I}{dt} + L_w \frac{dM_w}{dt}, \quad (2.4)$$

where $c_{p,w}$ is the specific heat of water, L_w is the latent heat of melting, and M_w is the mass of the water given by $\frac{4}{3}\pi\rho_w[r_t^3 - r_b^3]$ where ρ_w is the average density of water, r_t is the radius to the top of the ocean, and r_b is the radius to the bottom of the ocean. M_i , the mass of the ice is simply $\frac{4}{3}\pi[R_g^3 - R_{sil}^3]\rho_I - M_w$. Following Showman et al. (1997), the change in the mass of ocean water can be written as

$$\frac{dM_w}{dt} = \frac{4\pi}{g} \left[r_t^2 \left(\frac{dP_t}{dT_m} \right)_I - r_b^2 \left(\frac{dP_b}{dT_m} \right)_{HP} \right] \frac{dT_I}{dt}, \quad (2.5)$$

where $(dP/dT_m)_I$ and $(dP/dT_m)_{HP}$ are the slope of the ice I and high-pressure-ice melting curves, respectively. The radius of the top of the ocean can be found

from the temperature at the base of the ice shell, the melting curve for ice I, and hydrostatic equilibrium. We determine the radius of the bottom of the ocean by equating an ocean adiabat to the melting curves for high-pressure ice and solving for the depth of intersection assuming hydrostatic equilibrium. We account for the changes in the melting curve as melting proceeds through high-pressure-ice layers (III, V, and VI), as well as the increase in water's coefficient of thermal expansion with depth. Further details of the ocean adiabat are discussed in Section 2.4.

Heat is transferred through the ice shell and silicate mantle either by conduction or convection. We assume a constant thermal conductivity for the silicate layer. The conducted heat flux thus has the form

$$F_{cond} = k_{sil} \frac{\Delta T}{\mathcal{L}}, \quad (2.6)$$

where ΔT is the temperature drop across the silicate layer, k_{sil} is the thermal conductivity, and \mathcal{L} is the thickness of the layer. In the ice shell, we assume a temperature-dependent thermal conductivity so the conducted flux has the form

$$F_{cond} = \frac{\mathcal{C}}{\mathcal{L}} \ln(T_I/T_s), \quad (2.7)$$

where T_s is the surface temperature, and $\mathcal{C} = 651 \text{ W m}^{-1}$ is a constant defined by the temperature-dependent thermal conductivity $k_I = \mathcal{C}/T_I$ (Petrenko and Whitworth, 1999).

We parameterize stagnant-lid convection using the scaling relations of Solomatov and Moresi (2000). The convective heat flux is given by

$$F_{conv} = Nu \frac{k \Delta T}{\mathcal{L}}, \quad (2.8)$$

where ΔT is the temperature drop across the layer, k is the thermal conductivity of the i th layer, and Nu is the Nusselt number with the form

$$Nu = a Ra^\beta \Theta^{-\gamma}, \quad (2.9)$$

where a , β , and γ are experimentally and theoretically derived constants (Solomatov and Moresi, 2000), Ra is the Rayleigh number (defined below) and Θ is the logarithm of the viscosity contrast across the convecting layer. Ignoring the small dependence on pressure, Θ is given by

$$\Theta = \frac{\Delta T Q}{RT}, \quad (2.10)$$

where Q is the rheological activation energy, R is the gas constant, and T is the temperature.

We utilize a power-law rheology in the silicate mantle and ice shell. The stress strain-rate relation in the silicates is given by (Karato and Wu, 1993)

$$\dot{\epsilon} = A_{sil} \left(\frac{\tau}{\mu_{sil}} \right)^n \left(\frac{b}{d} \right)^p \exp[-Q_{sil}/(RT)], \quad (2.11)$$

where $\dot{\epsilon}$ is the strain rate, τ is the shear stress, μ_{sil} is the shear modulus (~ 80 GPa (Karato and Wu, 1993)), n is the power-law exponent, b is the length of the burgers vector (~ 0.5 nm (Karato and Wu, 1993)), d is the grain size, p is the grain size exponent, and A_{sil} is a rheological constant. We have ignored the small dependence of $\dot{\epsilon}$ on pressure since it is poorly constrained (Karato and Wu, 1993) and within the uncertainty imposed by our lack of knowledge of grain size and silicate composition. Rheologically, Ganymede's mantle most likely consists of dry olivine, consistent with a highly differentiated body (Kuskov and Kronrod, 2001; Sohl et al., 2002), but for completeness we investigate both dry and wet rheologies (see Chapter 3). In the temperature and stress regimes examined here, either dislocation creep or diffusion creep can dominate the silicate flow depending on the choice of grain size. To determine which mechanism dominates, we calculate the strain rate associated with each flow mechanism at every thermal timestep. The mechanism with the highest strain rate will dominate the convection.

For the ice shell we assume a power-law rheology with the form

$$\dot{\epsilon} = A_{ice} \tau^n (1/d)^p \exp[-Q_{ice}/(RT)], \quad (2.12)$$

where the variables are defined as above. As with the silicate rheology, one of two viable rheological mechanisms, diffusion creep or grain-boundary-sliding (GBS), dominates depending on the grain size. As the temperature in the ice shell changes we again allow transitions to occur between the two rheological regimes by comparing the strain rates produced by the two flow mechanisms at each timestep. All rheological parameters are shown in Table 2.1.

Calculation of Nu (Eq. 2.9) depends upon the Rayleigh number, which for a power-law fluid is given by

$$Ra = \frac{\alpha g \rho \Delta T d^{(n+2)/n}}{c^{1/n} \kappa^{1/n} \exp[Q/(nRT)]}, \quad (2.13)$$

where $\kappa = k/\rho c_p$ is the thermal diffusivity, and c is a function of rheological parameters and is given by $c = \mu_{sil}^n (d/b)^p / A_{sil}$ for a silicate rheology, and $c = d^p / A_{ice}$ for an ice rheology. The parameters a , β , and γ , used in the scaling of the convective Nusselt number (Eq. 2.9) depend on the power-law exponent of the rheology that dominates each layer (Solomatov and Moresi, 2000). We self-consistently modify these values when (or if) the dominant rheology changes during a simulation. For simplicity we assume only scaling laws derived for time-dependent (vigorous) convection. The convective scaling parameters are shown in Table 2.2.

Using the the rheological laws described, we define effective viscosities for the ice and silicates with the form

$$\eta_e = \frac{c}{\tau^{n-1}} \exp[Q/(RT)], \quad (2.14)$$

where all parameters are defined above. The effective viscosity depends upon the convective stress in each layer, which we calculate from the convective scaling laws as (Solomatov and Moresi, 2000)

$$\tau = 0.027 \alpha \rho g \Delta T_{rh} \delta_{rh}, \quad (2.15)$$

where the value 0.027 is a numerically derived constant, $\Delta T_{rh} = 1.2(n+1)\theta^{-1}\Delta T$ (Solomatov and Moresi, 2000) is the temperature drop across the convective sub-

Table 2.1:

Rheological Parameters					
Creep Regime	A	n	p	Q	Reference
<i>Silicates</i>					
Dislocation creep (dry)	$3.5 \times 10^{22} \text{ s}^{-1}$	3.5	0	540 kJ mol^{-1}	Karato & Wu (1993)
Diffusion creep (dry)	$8.7 \times 10^{15} \text{ s}^{-1}$	1.0	2.5	300 kJ mol^{-1}	Karato & Wu (1993)
Dislocation creep (wet)	$2.0 \times 10^{18} \text{ s}^{-1}$	3.0	0	430 kJ mol^{-1}	Karato & Wu (1993)
Diffusion creep (wet)	$5.3 \times 10^{15} \text{ s}^{-1}$	1.0	2.5	240 kJ mol^{-1}	Karato & Wu (1993)
<i>Ice I</i>					
Diffusion Creep	$1.2 \times 10^{-10} \text{ Pa}^{-n} \text{ m}^p \text{ s}^{-1}$	1.0	2.0	59.4 kJ mol^{-1}	Goldsbey & Kohlstedt (2001)
GBS	$6.2 \times 10^{-14} \text{ Pa}^{-n} \text{ m}^p \text{ s}^{-1}$	1.8	1.4	49.0 kJ mol^{-1}	Goldsbey & Kohlstedt (2001)

Rheological constant 'A' must be multiplied by a factor of $3^{(n+1)/2}$ (Ranalli, 1995).

Table 2.2:
Convective Scaling $Nu = aRa^\beta\Theta^{-\gamma}$

Power-law	a	β	γ
3	0.97	0.6	1.6
2	0.76	0.5	1.5
1	0.53	0.333	1.333

from Solomatov & Moresi (2000)

layer, and $\delta_{rh} \approx \mathcal{L}/Nu$ is the thickness of the convective sublayer beneath the stagnant lid (Solomatov, 1995).

To determine whether each layer is conducting or convecting we calculate the critical Rayleigh number (Ra_{crit}) for convection in a power-law fluid at each timestep. Ra_{crit} is given by (Solomatov, 1995; Solomatov and Barr, 2006)

$$Ra_{crit} = Ra_n \Theta^{\frac{2(n+1)}{n}} \left[\frac{e}{4(n+1)} \right]^{\frac{2(n+1)}{n}}, \quad (2.16)$$

where

$$Ra_n = 1568^{1/n} 20^{(n-1)/n}. \quad (2.17)$$

Convection occurs if Ra is greater than Ra_{crit} . In reality, for a power-law fluid the critical Rayleigh number is also sensitive to the wavelength and amplitude of the temperature perturbation that initiates convection (Solomatov and Barr, 2007). However, for simplicity we assume that once convection is possible (i.e. $Ra \geq Ra_{crit}$) convection will occur.

The heat flux out of the core is controlled by how rapidly heat can be conducted across the core-mantle boundary and is approximated by (Buffett, 2002)

$$F_c = k_{sil} \frac{T_{cmb} - T_{sil}}{\delta_{BL}}, \quad (2.18)$$

where $\delta_{BL} = \mathcal{L}(Ra_{crit}/Ra)^\beta$ is the thickness of the thermal boundary layer in the silicate mantle, where \mathcal{L} is the thickness of the silicate layer, Ra is the Rayleigh number, and Ra_{crit} is the critical Rayleigh number for convection. While Eq. 2.18

neglects a number of complex core-mantle interactions that may alter the core’s heat flux, it is a reasonable approximation given other uncertainties in the model. Further details of the core model are provided in Chapter 3

The model described above implicitly assumes that Ganymede fully differentiated into an ice shell, silicate mantle, and metallic core early in its history (i.e. before the simulations begin). The effects of differentiation are not included here. Our assumption of complete differentiation early in the satellite’s history was made for simplicity. In reality, differentiation, including iron core formation, may have taken a few billion years to complete (Grasset et al., 2000; Schubert et al., 2004). If Ganymede accreted rapidly however, separation of rock and ice would have occurred early (Schubert et al., 1981), and later metallic core formation is unlikely to significantly modify the history of the ice shell. Our use of a fully differentiated model to study the evolution of the ice shell is therefore justified.

2.2.3 The Tidal Dissipation Model

The tidal heating rates \dot{E}_{sil} and \dot{E}_I are determined by the model of Tobie et al. (2005b) which calculates the radial distribution of tidal heating per unit volume within a three-layer Ganymede as

$$h_{tide} = -\frac{21}{10} \frac{n_3^5 R_g^4 e^2}{r^2} H_\mu \text{Im}\{\mu\}, \quad (2.19)$$

where n_3 is Ganymede’s mean motion, e is the eccentricity, r is the radius from the center of the satellite, and H_μ and $\text{Im}\{\mu\}$ are the radial sensitivity to the shear modulus and imaginary part of the complex shear modulus, respectively. The last two parameters are calculated assuming a Maxwell rheology, and they depend upon the viscosity and bulk and shear modulus of each layer. For the purposes of the tidal heating calculation we further subdivide Ganymede’s structure into a core, convecting silicate mantle, silicate stagnant lid, high pressure ice, ocean (if present), ice I, and ice stagnant lid. Furthermore, because Eq. 2.19 calculates the volumetric tidal

dissipation as a function of depth, each layer is subdivided into multiple sublayers. The total dissipation for a given layer (e.g. ice or silicate) is the vertically averaged dissipation that occurs in the actively convective regions of these layers (i.e. tidal dissipation in the stagnant lids is neglected). In addition to the tidal dissipation, the model calculates the global value of k_2/Q_3 , where k_2 is the 2nd degree tidal love number, and Q_3 is Ganymede’s tidal dissipation factor, at each timestep for use in the orbital dynamics calculations.

2.3 Evolution of the Ice Shell

2.3.1 Thermal evolution

We first establish Ganymede’s thermal history in the absence of tidal dissipation. These simulations are consistent with a primordial origin for the Laplace resonance or an evolutionary scenario in which the Galilean satellites do not pass through any Laplace-like resonances that excite Ganymede’s eccentricity. The thermal and physical evolution of Ganymede’s ice shell is shown in Fig. 2.2 for three grain sizes ranging from $100\ \mu\text{m}$ to $1\ \text{cm}$. For each grain size we assume an initial ice shell temperature of $200\ \text{K}$. For grain sizes of $1\ \text{mm}$ or larger, the high heat flux out of the silicates increases the ice shell temperatures until the minimum ice melting point is reached after $\sim 100\ \text{Ma}$ and ocean formation begins (Figs. 2.2a and 2.2b). Ocean formation decreases the rate of temperature increase in the ice shell, which reaches a maximum of $270\ \text{K}$. As energy is supplied to the ice shell, each increase in temperature contributes to additional melting of both ice I and high-pressure ice. At $270\ \text{K}$, the ice shell attains a minimum thickness of $22\ \text{km}$ (Fig. 2.2b). Temperatures then begin to decrease due to the fall-off in radiogenic heat flux (Fig. 2.2a). As radiogenic heating declines, the presence of the ocean buffers the cooling of the ice shell and ice shell temperatures remain higher than would be expected from simply maintaining quasiequilibrium with radiogenic heating. For a grain size

of 1 mm, cooling occurs relatively rapidly (Figs. 2.2a and 2.2c) and the ocean closes completely at 4.3 Ga (Fig. 2.2b). However, the ability of the ocean to close completely in our simulations may be due to our neglect of ocean chemistry. As the ice refreezes, contaminants (e.g. salts or ammonia) will be concentrated in the ocean, decreasing its freezing temperature and hampering ocean closure. Inclusion of such effects are beyond the scope of the present investigation. For larger grain sizes (1 cm and greater), the decreased efficiency of convection (relative to smaller grain sizes) permits relatively high ice shell temperatures throughout the simulation and a large ocean exists into the present epoch.

At grain sizes smaller than 1 mm, diffusion creep dominates the ice rheology and cooling of the ice shell occurs rapidly. In this simulation, ice shell temperatures never exceed the minimum melting point of ice and ocean formation never occurs. While magnetometer data from the Galileo spacecraft suggest that an ocean may currently exist within Ganymede (Kivelson et al., 2002), the present-day lack of an ocean in our small-grain-size simulations is consistent with the models of Spohn and Schubert (2003).

The evolution of Ganymede's heat flux is relatively independent of grain size. In each simulation, the heat flux out of the ice shell (Fig. 2.2c) is initially low due to the cold initial state of the ice (see Eq. 2.8). The flux increases rapidly as the ice shell warms. Ganymede's heat flux generally peaks near 25 mW m^{-2} and radiogenic heating alone is capable of maintaining Ganymede's heat flux above 10 mW m^{-2} for the first 3.25 Ga of the satellite's history. Such a heat flux is consistent with modification of craters on Ganymede's surface (Dombard and McKinnon, 2006a), but is inconsistent with both the formation of furrows (McKinnon and Parmentier, 1986) and grooved terrain (Dombard and McKinnon, 2001; Bland and Showman, 2007, Chapter 4). It is notable, however, that for moderate grain sizes radiogenic heating alone can lead to the formation of a large ocean early in Ganymede's history. These results contrast strongly with those of Freeman (2006) who, using a relatively

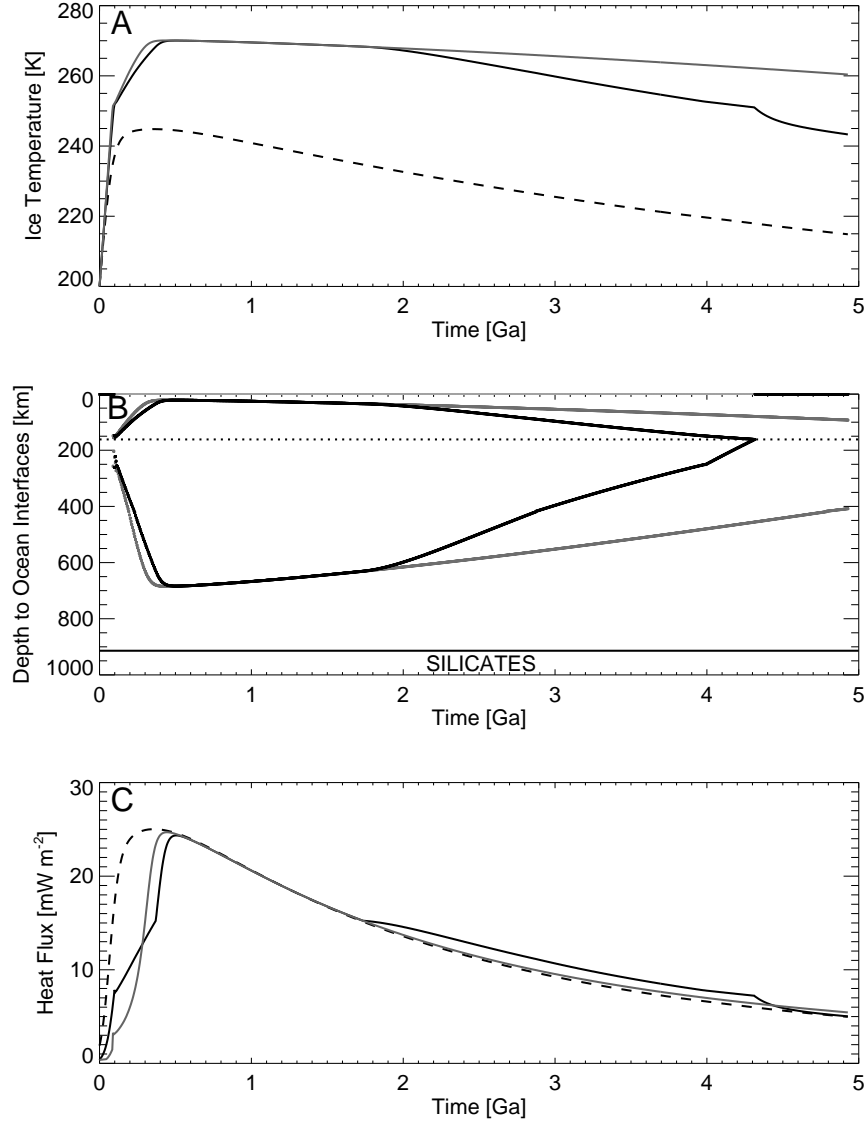


Figure 2.2: The thermal evolution of Ganymede in the absence of tidal dissipation **A.** The temperature of the ice shell as a function of time for three simulations with different grain size (d): $d = 1$ mm (solid black line), $d = 1$ cm (solid grey line), and $d = 100$ μ m (dashed line). **B.** Depth to the top and bottom ice/ocean interfaces as a function of time for two of the simulations described in (A): $d = 1$ mm (solid black line), and $d = 1$ cm (solid grey line). No ocean formation occurs if $d = 100$ μ m. The curves can be interpreted as lenses of ocean in Ganymede’s ice shell as a function of time. For reference, the ice/silicate interface is indicated by a solid black line, and the position of the ice-I/high-pressure-ice phase transition is indicated with a dotted line. **C.** Ganymede’s heat flux as a function of time for the three simulations shown in (A). Use of grain sizes larger than 1 cm yields results essentially identical to the 1 cm simulations.

low ice viscosity, calculated significantly lower temperatures and heat fluxes for Ganymede and did not predict ocean formation.

2.3.2 Influence of Ganymede’s Orbital History

The simulations described above can be compared to simulations in which the Galilean satellites pass through one or more Laplace-like resonances that pump Ganymede’s eccentricity. To investigate the effects of resonance passage on Ganymede’s thermal history we initialize the semi-major axes of the Galilean satellites such that they evolve through the Laplace-like resonance that excites Ganymede’s eccentricity the strongest (the $\omega_1/\omega_2 = 2$ resonance). Assuming a tidal dissipation factor for Jupiter (Q_J) of 10^5 , and Q_s/k_2 ratios, where Q_s is the satellite’s tidal dissipation factor and k_2 is the second degree tidal love number, of 100 and 3261 for Io and Europa respectively (these values yield reasonable values of Q for the expected k of each satellite) (Showman and Malhotra, 1997), the satellites enter the $\omega_1/\omega_2 = 2$ resonance after 180 Ma of simulation time (Fig. 2.3a). Upon entering the resonance, Ganymede’s eccentricity (e_3) quickly increases from near zero to 0.015 (Fig. 2.3b), leading to the dissipation of 10^{12} W of tidal energy in Ganymede’s ice shell (Fig. 2.3c). Tidal dissipation remains relatively constant while the Galilean satellites are in the Laplace-like resonance. At 3.75 Ga, we force the satellites out of resonance by temporarily increasing the tidal dissipation factor of Io (Q_1). Such changes in Q_1 are consistent with thermal-orbital models of Io (Ojakangas and Stevenson, 1986). The satellites then evolve naturally into the Laplace resonance and Ganymede’s eccentricity decreases to its current value, for which tidal dissipation is negligible.

Because of its much higher viscosity, significantly less dissipation of tidal energy occurs within Ganymede’s silicate mantle (10^{10} W). The magnitude of the dissipation in the silicate mantle is less than the radiogenic heat production and it has a negligible influence on the thermal history of the satellite (see Chapter 3). We

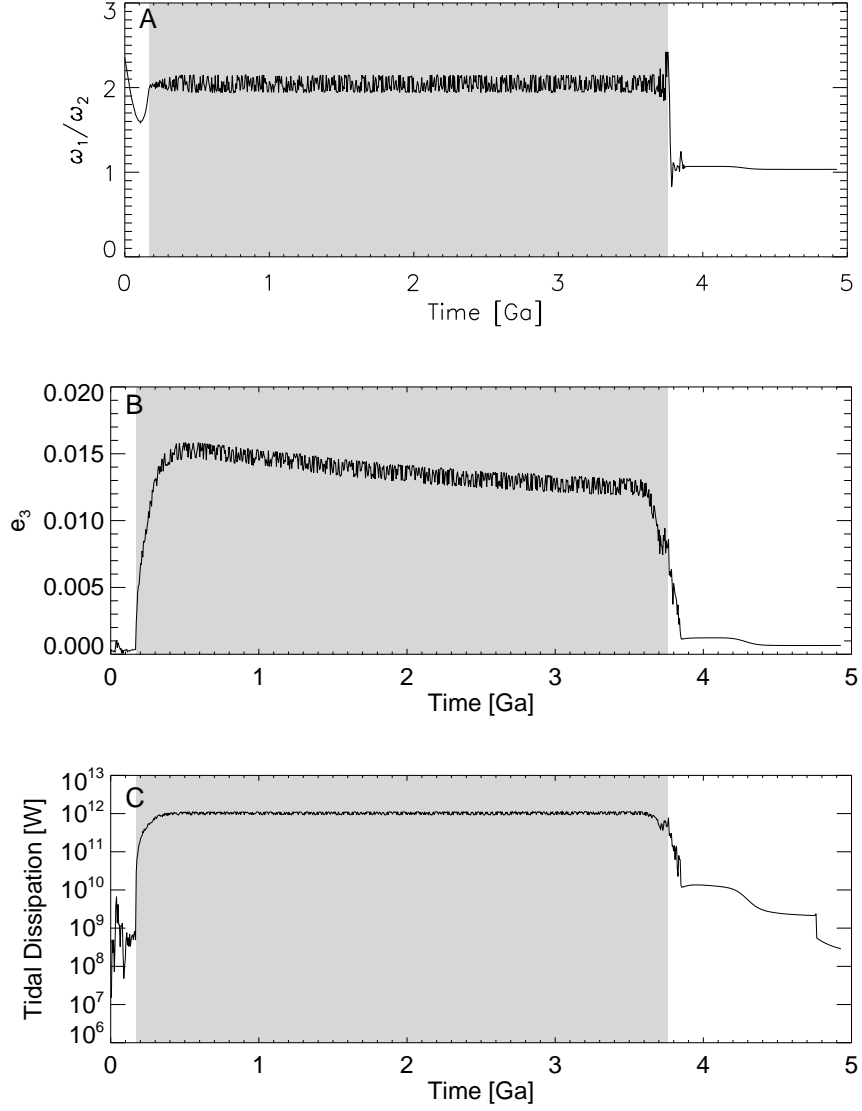


Figure 2.3: **A.** The orbital evolution of the Galilean satellites parameterized as the ratio of $\omega_1 = 2n_2 - n_1$ to $\omega_2 = 2n_3 - n_2$, as a function of time for a simulation in which the Galilean satellites pass through the $\omega_1/\omega_2 = 2$ Laplace-like resonance. Q_J is 10^5 . **B.** Ganymede's eccentricity as a function of time for the simulation described in (A). **C.** The tidal dissipation (W) in Ganymede's ice shell as a function of time for the simulation described in (A). The grey region in each panel corresponds to the period of resonance passage.

therefore focus on the evolution of Ganymede’s ice shell.

The effects of resonance passage on Ganymede’s ice shell are shown in Fig. 2.4. Like the simulation described in Section 2.3.1, temperatures in Ganymede’s ice shell increase rapidly from their cold initial state due to the high radiogenic heat flux emanating from the silicate mantle. After entering the Laplace-like resonance the additional tidal heating drives the temperature to a maximum of 271 K, a temperature that decreases little while the satellites are in resonance (Fig. 2.4a). As temperatures increase, the ice I shell thins until convection shuts down and the supplied tidal heating is balanced by rapid conductive heat transport. The minimum ice shell thickness is ~ 15 km. The relatively thin ice shell exists throughout the Laplace-like resonance passage (Fig. 2.4b). Upon exiting the resonance, the ice shell cools rapidly leading to closure of the ocean at 4.75 Ga. For similar initial conditions, ice shell temperatures in our simulations are generally higher than those of Showman et al. (1997). This difference is due to our inclusion of radiogenic heating and stagnant-lid convection, two processes not included in the Showman et al. (1997) model.

Ganymede’s heat flux peaks at 36 mW m^{-2} shortly after the satellites enter the Laplace-like resonance (Fig. 2.4c). Heat fluxes steadily decline by $\sim 40\%$ while the satellites are in the Laplace-like resonance, predominantly due to the decrease in radiogenic heating with time. Once the satellites exit the resonance, the heat flux drops to values in quasi-equilibrium with radiogenic heat production ($\sim 5 \text{ mW m}^{-2}$ at 4.5 Ga). The heat flux produced by this simulation is lower than, but comparable to, estimates of Ganymede’s ancient heat flux. Using flexural models of Ganymede’s lithosphere, Nimmo et al. (2002) and Nimmo and Pappalardo (2004) inferred that fluxes of 60 to 100 mW m^{-2} were present during the period of groove formation. These fluxes are broadly consistent with models of groove terrain formation, which require heat fluxes from 30 to 120 mW m^{-2} (Dombard and McKinnon, 2001; Bland and Showman, 2007, Chapter 4). Consistent with these values are ancient heat

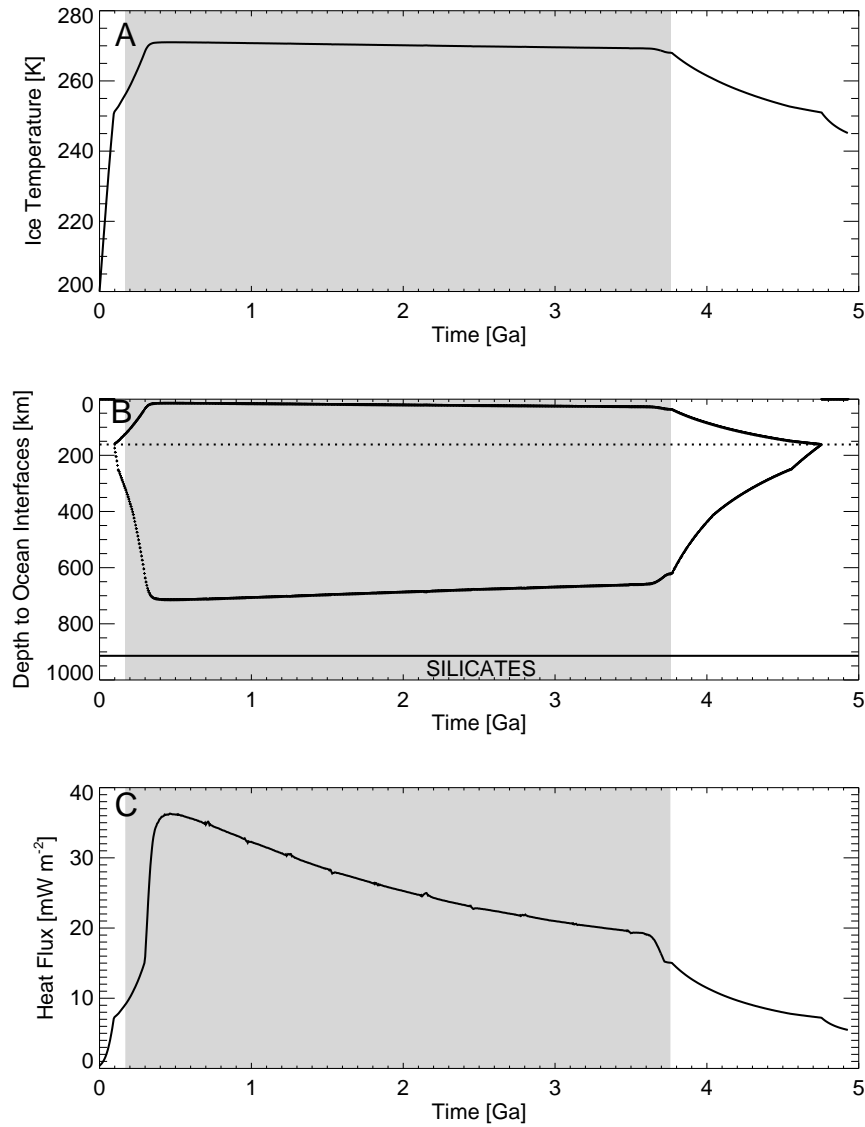


Figure 2.4: The thermal evolution of Ganymede including passage through the $\omega_1/\omega_2 = 2$ Laplace-like resonance. The grain size was 1 mm and $Q_J = 10^5$. **A.** The temperature of the ice shell as a function of time. **B.** Depth to the top and bottom ice/ocean interfaces as a function of time. For reference, the ice/silicate interface is indicated by a solid black line, and the position of the ice-I/high-pressure-ice phase transition is indicated with a dotted line. **C.** Ganymede's heat flux as a function of time. The grey shaded regions correspond to the period of resonance passage shown in Fig. 2.3.

fluxes derived from models of crater relaxation, which require at least 10 mW m^{-2} (Dombard and McKinnon, 2006a). The heat flux of our simulations depends strongly on the value of Q_J assumed in the model, with lower Q_J resulting in significantly larger heat fluxes; thus, fluxes as high as 100 mW m^{-2} are achievable (see Section 2.3.3).

The simulation described above models the Galilean satellites' evolution through the Laplace-like resonance that excites Ganymede's eccentricity the strongest ($\omega_1/\omega_2 = 2$). However, Malhotra (1991) and Showman and Malhotra (1997) showed that there are a number of eccentricity-pumping Laplace-like resonances that may have been encountered before evolution into the Laplace resonance occurs, the primary being $\omega_1/\omega_2 = 1/2$ and $\omega_1/\omega_2 = 3/2$ (in addition to the $\omega_1/\omega_2 = 2$ already described). The probability of capture into these resonances depends on the initial values of ω_1 , ω_2 , and the Q/k of Io and Europa, with capture into at least one of the Laplace-like resonance being likely for a relatively large fraction of the parameter space (Showman and Malhotra, 1997). Furthermore, multiple Laplace-like resonances may have been encountered during the Galilean satellites' orbital evolution. Because of the large range of possible orbital histories, investigating the coupled orbital-thermal evolution for every scenario is not feasible; however, several generalizations can be made. Each simulation described below assumes $Q_J = 10^5$.

Capture into $\omega_1/\omega_2 = 1/2$ resonance commonly occurs when, initially, ω_1 is less than ω_2 . While the lifetime of the resonance depends strongly on the initial values of ω_1 and ω_2 , the resonance can be short lived and escape occurs naturally. In this resonance, Ganymede's eccentricity reaches a maximum value of 0.0116, the lowest of the three resonances considered here, resulting in $6.3 \times 10^{11} \text{ W}$ of tidal dissipation in the ice shell. The combination of its potentially short duration and lower eccentricity forcing renders the $\omega_1/\omega_2 = 1/2$ resonance the least effective of the major Laplace-like resonances at modifying Ganymede's thermal history.

Capture into the $\omega_1/\omega_2 = 3/2$ resonance occurs for a broad range of initial

ω_1/ω_2 values and is commonly encountered after escape from the $\omega_1/\omega_2 = 1/2$ resonance. Like the $\omega_1/\omega_2 = 2$ resonance, the Galilean satellites cannot escape the resonance unless Io's Q value varies in time. The eccentricity that occurs during the $\omega_1/\omega_2 = 3/2$ resonance (0.0117) is similar to that of $\omega_1/\omega_2 = 1/2$ but it is large enough to result in significant tidal dissipation within Ganymede's ice shell (a maximum of 8.6×10^{11} W). The resulting thermal history is essentially identical to that of the $\omega_1/\omega_2 = 2$ resonance (Fig. 2.4). This result is significant because capture into the $\omega_1/\omega_2 = 3/2$ resonance occurs over a broader range of initial ω_1/ω_2 values than for the $\omega_1/\omega_2 = 2$ resonance, increasing the likelihood that tidal dissipation has modified Ganymede's thermal evolution (Showman et al., 1997).

2.3.3 Variations in Q_J

Both the orbital and thermal history of Ganymede are strongly dependent on Jupiter's tidal dissipation factor (Q_J). High values of Q_J result in slow orbital evolution of the satellites and low tidal dissipation rates, while low values of Q_J result in rapid orbital evolution and strong tidal dissipation. Jupiter's actual value of Q_J is poorly constrained (see Peale (1999) for a review). The current semi-major axis of Io places a time averaged lower limit of 4×10^4 on the value (Goldreich and Soter, 1966; Yoder and Peale, 1981); however, theoretical mechanisms for achieving the low values necessary for tidal evolution allow Q_J to periodically drop to lower values (10^3 or 10^4) for short spans of time (Stevenson, 1983; Ioannou and Lindzen, 1993). Furthermore, Q_J is likely a strong function of the tidal frequency (Ogilvie and Lin, 2004), but this frequency dependence is difficult to fold into coupled thermal-orbital models such as the one described here.

The variability in Q_J allows the possibility that significantly more tidal dissipation has occurred in Ganymede's past than suggested by the simulation described in Section 2.3.2. Figure 2.5 shows the maximum heat flux (asterisks) and minimum ice shell thickness (diamonds) as a function of assumed Q_J for the $\omega_1/\omega_2 = 2$ resonance.

The maximum heat flux due to the combination of radiogenic heating and tidal dissipation increases non-linearly with decreasing Q_J (to first order, \dot{E}_I scales as Q_J^{-1} (Ojakangas and Stevenson, 1986)), producing a flux four times greater at $Q_J = 10^4$ (112 mW m^{-2}) than at $Q_J = 3 \times 10^5$ (25 mW m^{-2}). For values of $Q_J \geq 3 \times 10^5$, the magnitude of the tidal dissipation is small enough that radiogenic heating dominates the flux. The increase in heat flux with decreasing Q_J is inversely correlated the ice shell thickness, with a shell thinner than 5 km possible at the lowest values of Q_J considered. The prolonged existence of a thin ice shell on Ganymede may have consequences for the geologic history of the satellite. Whether such a thin ice shell is consistent with geologic observations is discussed in Section 2.5.

The uncertainty and time variability of Q_J also translates into uncertainty in Ganymede's orbital evolution. A Q_J larger than that used in Fig. 2.3 causes the satellites to enter the resonance at a later time (additionally, the timing of resonance capture depends on how close the satellites formed to the Laplace resonance as well as the physical state (Q/k) of Io and Europa). Thus, while the simulation shown in Fig. 2.3 appears inconsistent with the timing of groove terrain formation (i.e. the Galilean satellites enter the Laplace-like resonance early in Ganymede's history), the timing of Laplace-like resonance capture is poorly constrained by the model. Furthermore, the time variability of Q_J permits both late capture into the Laplace-like resonance (which suggests high Q_J) and strong tidal dissipation (which requires low Q_J). Such temporal changes in Q_J are still consistent with a time averaged minimum value of Q_J of 4×10^4 .

2.3.4 Effect of Ice Grain Size

The dominant grain size of Ganymede's ice shell is poorly constrained, with plausible values ranging from $100 \mu\text{m}$ to 10 cm. As discussed in Section 2.3.1, our lack of constraints on the ice grain size leads to major uncertainties in the thermal, structural, and orbital evolution of the satellite. Figure 2.6 shows the effects of

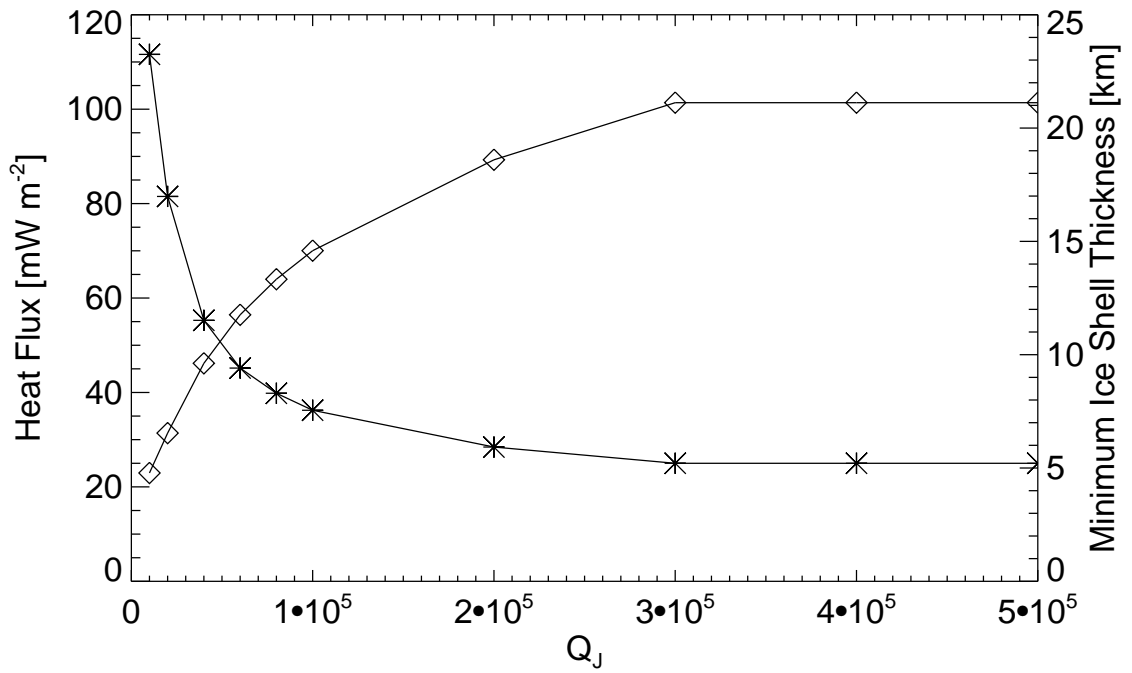


Figure 2.5: The variation in Ganymede's maximum heat flux (asterisks) and minimum ice I shell thickness (diamonds) as a function of Q_J . At high Q_J ($\geq 3 \times 10^5$) the heat flux is dominated by radiogenic heat production rather than tidal dissipation. Minimum ice shell thickness ranges from 5 to 21 km.

grain size on the temporal and spatial extent of Ganymede’s ocean under conditions otherwise identical to the simulation shown in Figs. 2.3 and 2.4, including capture into the $\omega_1/\omega_2 = 2$ Laplace-like resonance. For typical convective stresses, small grain sizes ($d < 1$ mm) cause diffusion creep to dominate the ice rheology. The lower effective viscosities (relative to GBS) associated with diffusion creep allow the ice shell to cool rapidly, limiting ocean formation to a brief period when both radiogenic heating and tidal dissipation are high (Fig. 2.6). If the Galilean satellites entered the Laplace-like resonance late (after radiogenic heating declined), melting becomes more difficult. In the case of low or no tidal dissipation (e.g. $Q_J > 3 \times 10^5$ or the satellites evolve directly into the Laplace resonance) a small grain size prevents melting and ocean formation altogether (see Fig. 2.2). In the absence of significant melting global expansion would be severely limited (discussed below). However, the observation that at least a portion of Ganymede’s magnetic field is due to induction in a conductive layer at depth argues for the existence of an ocean (Kivelson et al., 2002) and against small grain sizes dominating Ganymede’s ice shell.

For larger grain sizes ($d \geq 1$ mm) grain boundary sliding (GBS) dominates the ice rheology. The higher effective viscosities associated with GBS prevent rapid cooling of the satellite and permit large oceans (~ 700 km deep) to form (Fig. 2.6). As grain size increases from 1 mm to 10 cm cooling becomes more difficult and, once formed, a large ocean is maintained for a longer period of time. Convective cooling may be inhibited altogether if ice grain sizes exceed 2 cm (Barr and Pappalardo, 2005), consistent with the increased longevity of the ocean at large grain sizes. Additionally, because large-grained ice is less dissipative, the magnitude of the tidal dissipation occurring in the ice shell decreases as grain size increases (see Chapter 3). This leads to slightly smaller oceans at large grain sizes than at moderate grain sizes.

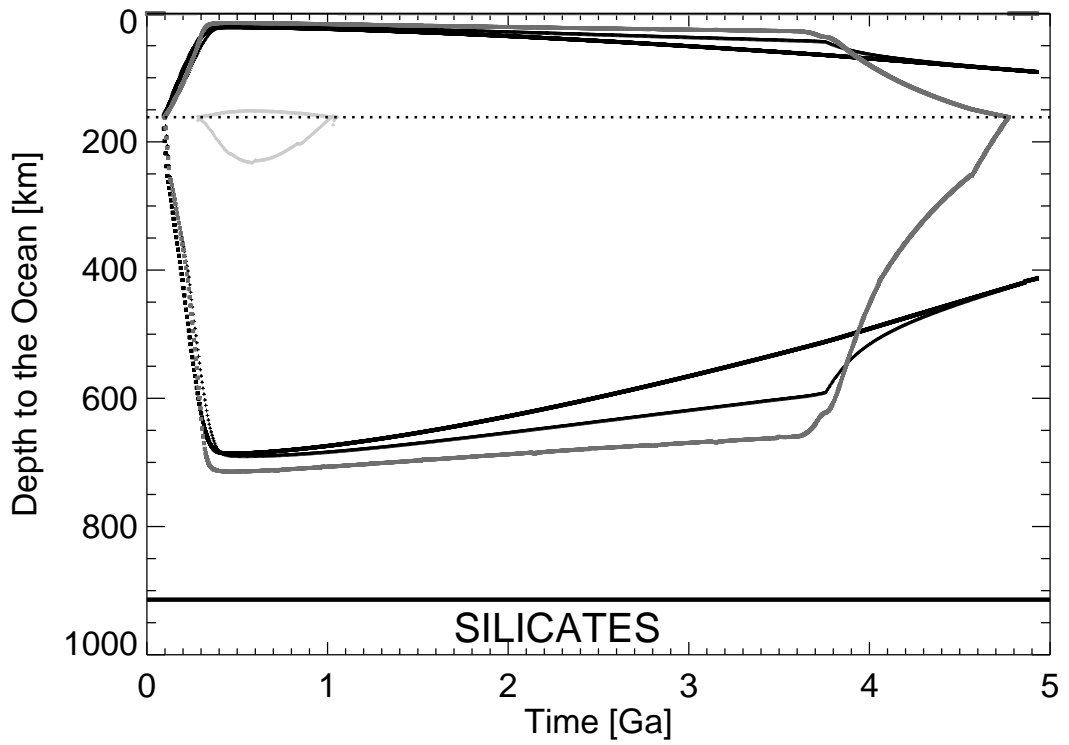


Figure 2.6: The depth to the ocean interfaces over solar system history for four ice grain sizes 10 cm (heavy black), 1 cm (thin black), 1 mm (heavy dark grey), 100 μm (light grey). For reference, the ice/silicate interface is indicated by a heavy black line, and the position of the ice-I/high-pressure-ice phase transition is indicated with a dotted line. In each simulation $Q_J = 10^5$.

2.4 Global Expansion

Not only do Ganymede's surface features require high heat flows, but the predominance of extensional features suggests that much of this deformation formed during a period of global satellite expansion. Based on the survival of Galileo Regio's relatively intact lithosphere, McKinnon (1981) placed an upper limit of 2% by area on this expansion. The same upper limit was reached independently by Golombek (1982) who used fault displacements in the grooved terrain to estimate the expansion of the satellite as a whole. With the acquisition of higher-resolution imaging from the Galileo spacecraft, it was recognized that much of the deformation in the grooved terrain consists of small-scale tilt-block faulting (Pappalardo et al., 1998), suggesting larger surface strains (Collins et al., 1998b). Extrapolating these strains to the whole satellite, Collins (2007) estimated that the increase in surface area was at least 4%, and possibly as large as 7%.

Despite the clear evidence for ubiquitous surface extension, the mechanism by which global expansion has occurred remains unclear. A number of authors have suggested that satellite differentiation could cause a global expansion of up to 6.5% by area (e.g. Squyres, 1980; Pappalardo et al., 2004; Mueller and McKinnon, 1988); however, expansion during early differentiation is inconsistent with the relative youth of the grooved terrain, and is only feasible if differentiation occurred in multiple stages (e.g. Mueller and McKinnon, 1988) or was delayed until late in the satellite's history. Beyond differentiation, an increase in satellite temperature due to radiogenic heating would result in a volume increase of 1% due to simple thermal expansion (Zuber and Parmentier, 1984). Such expansion is consistent with the upper limits of McKinnon (1981) and Golombek (1982). Furthermore, for a differentiated satellite, the expansion and accumulation of surface stress due to radiogenic heating occurs over a period of several billion years, possibly avoiding the timing problems of early differentiation. Unfortunately, this mechanism produces less sur-

face extension than was estimated by Collins (2007), and it remains unclear whether slow expansion of the satellite would result in significant tectonic deformation (Kirk and Stevenson, 1987).

Taking the calculations of Zuber and Parmentier (1984) a step farther, Showman et al. (1997) investigated the global expansion that can be produced by remelting a differentiated satellite during resonance passage. Because ice I is less dense than liquid water, melting of Ganymede’s ice I layer results in contraction. However, high-pressure ice phases have densities greater than liquid water at comparable pressures; thus, melting of Ganymede’s high-pressure ice leads to satellite expansion. For an isothermal ocean, constant gravity and density with depth, constant entropies of transition from ice I, III, V, and VI to liquid water, and a “plane parallel” Ganymede, the volume decrease due to melting ice I offsets the volume increase due to melting high-pressure ice and the net volume change is zero (Showman et al., 1997). However, these assumptions are generally not valid, and relaxing them permits volume expansion to occur. In particular, using a realistic adiabat in Ganymede’s ocean (described below) results in more melting of high-pressure ice than of ice I (note the shape of the oceans in Figs. 2.2, 2.4 and 2.6). Showman et al. (1997) found that a maximum areal expansion of $\sim 1\%$ is possible upon remelting Ganymede’s ice shell. Here we re-evaluate the magnitude of global expansion that can result from melting a large differentiated satellite.

We calculate Ganymede’s volume change (ΔV) upon melting by summing the individual volume changes per unit mass for each ice layer.

$$\Delta V = v_I m_I + v_{III} m_{III} + v_V m_V + v_{VI} m_{VI}, \quad (2.20)$$

where v_i is the local change in volume per unit mass between the i th ice phase and liquid water, and m_i is the mass of the i th ice phase that melts. For a given ice phase, the volume change per unit mass (v_i) is a function of pressure. For simplicity, we extrapolate v_i linearly between triple points to determine the local volume

change per unit mass. We use the volume change values of Fletcher (1970). With the radius and average density of Ganymede as constraints, we calculate the acceleration of gravity and pressure as a function of depth within Ganymede assuming incompressible layers and hydrostatic equilibrium. Using this model, m_i is determined directly from the depth to which melting occurs, which depends strongly on the assumed ocean adiabat.

In its simplest form, the ocean adiabat is given by

$$T_{oc} = T_I \exp \left\{ \frac{\alpha_w(P - P_t)}{\rho_w c_{p,w}} \right\}, \quad (2.21)$$

where T_{oc} is the ocean temperature at pressure P , P_t is the pressure at the ice I/ocean interface, and α_w , ρ_w , and $c_{p,w}$ are the thermal expansivity, density, and specific heat of water. In reality, α_w , ρ_w , and $c_{p,w}$ are also functions of pressure. Over the plausible temperature and pressure range of Ganymede's ocean, the density and specific heat of water change by less than 20%; however, the thermal expansivity can change by nearly an order of magnitude (Dorsey, 1940). At low pressures α_w increases rapidly with increasing pressure, while at high pressures α_w increases more slowly. We assume the increase in thermal expansivity with pressure is piecewise-linear with the two pieces defined by $\alpha_w = a_1 P + a_2$ and $\alpha_w = \acute{a}_1 P + \acute{a}_2$ where a_1 , a_2 , \acute{a}_1 , and \acute{a}_2 are constants. The ocean temperature is then given by

$$T_{oc} = T_{trans} \exp \left\{ \frac{1}{\rho_w c_{p,w}} \left[\frac{\acute{a}_1}{2} (P^2 - P_{trans}^2) + \acute{a}_2 (P - P_{trans}) \right] \right\}, \quad (2.22)$$

where

$$T_{trans} = T_I \exp \left\{ \frac{1}{\rho_w c_{p,w}} \left[\frac{a_1}{2} (P_{trans}^2 - P_t^2) + a_2 (P_{trans} - P_t) \right] \right\}, \quad (2.23)$$

and P_{trans} is the pressure at which the thermal expansivity transitions from rapidly increasing to slowly increasing with pressure. The temperature profiles defined by Eqs. 2.22 and 2.23 are shown in Fig. 2.7 for a basal ice shell temperature of 271 K. The inclusion of the change in thermal expansivity with depth greatly increases

the depth to which melting can occur and hence, increases the maximum volume expansion achievable during melting. Because of the importance of the thermal expansivity on the depth to which melting can occur, and because the increase in thermal expansivity is somewhat poorly constrained over the pressure range of interest (Dorsey, 1940), we calculate Ganymede's volume expansion for two sets of a_1 , a_2 , \acute{a}_1 , \acute{a}_2 . The parameter values used are provided in the caption to Fig. 2.7.

The volume change produced by melting as a percent of Ganymede's total volume is shown in Fig. 2.8 for the two adiabats shown in Fig. 2.7. The maximum relative volume expansion that can be produced by melting is 2.0% to 2.5%. These values are slightly greater than, but consistent with, those of Showman et al. (1997) and correspond to an increase in surface area of no more than 1.8%. While the volume change produced by melting is consistent with early estimates of the magnitude of Ganymede's global expansion, it appears inconsistent with the post-Galileo estimates of Ganymede's surface strain (Collins, 2007). Thus, a different or additional mechanism must be responsible for the satellite's global expansion.

In the above calculations we have assumed that Ganymede's ocean consists of pure liquid water. In reality, Ganymede's ocean is likely to contain a significant concentration of contaminants. Radiogenic heat production is likely sufficient to cause melting of Ganymede's silicate mantle (see Chapter 3). The eruption of melt at the ice-silicate interface would cause localized melting of ice, resulting in percolation of water and dissolved salts upward into the ocean. Even in the absence of such melting, a salty ocean seems likely to result from ice-rock differentiation of a homogeneously accreted satellite. Furthermore, the induced component of Ganymede's magnetic field attests to a conducting layer at depth (i.e. a salty ocean). Does the presence of salts in Ganymede's ocean affect our calculation of Ganymede's volume expansion? The specific heat of sea water (here used as an analog to Ganymede's salty ocean) is less than that for pure water by up to 7.5% (Dorsey, 1940). This would suggest a steeper adiabat and increased melting at depth. However, the den-

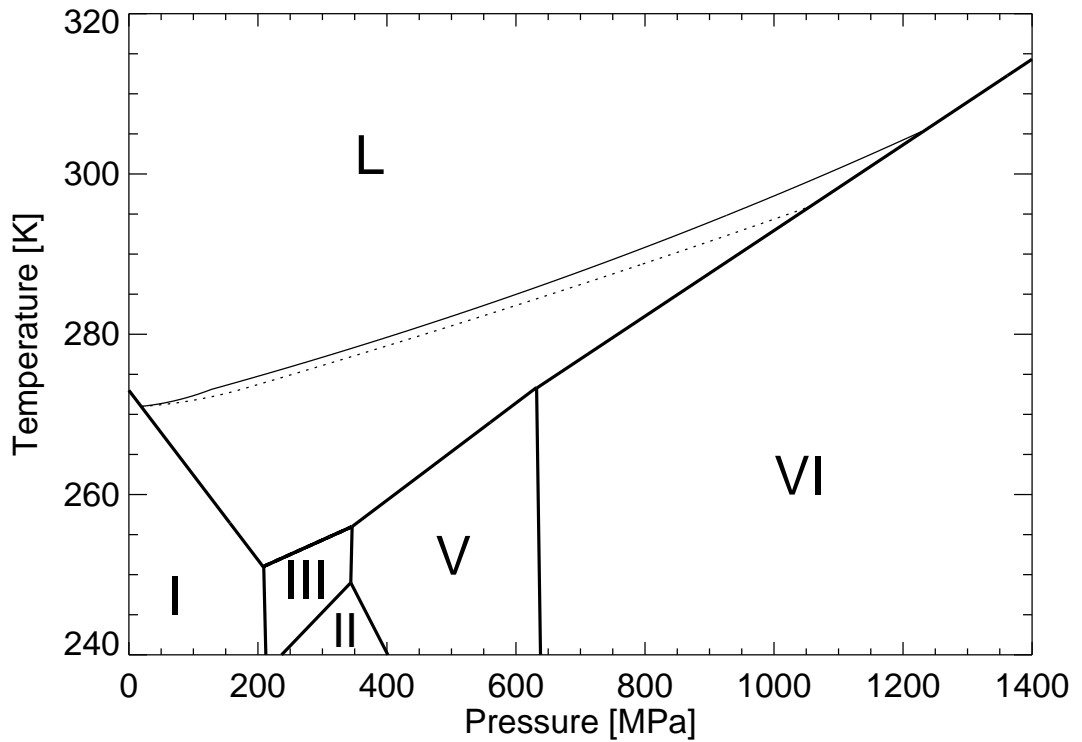


Figure 2.7: Phase diagram of ice over the pressure range relevant to Ganymede's ice shell showing the stability regions of Ice I, II, III, V, VI, and liquid water. Phase boundaries are determined by linear interpolation between the triple points of Hobbs (1974). Two ocean temperature profiles are shown assuming a 271 K ice shell: an adiabat with constant ρ_w and $c_{p,w}$, and a thermal expansivity varying as $\alpha_w = 3.2 \times 10^{-12}P + 6.67 \times 10^{-5}$ at $P < 1.28 \times 10^8$ Pa and $\alpha_w = 1.5 \times 10^{-13}P + 3.25 \times 10^{-4}$ at $P > 1.28 \times 10^8$ Pa (solid line); an adiabat with constant ρ_w and $c_{p,w}$, and a thermal expansivity varying as $\alpha_w = 1.74 \times 10^{-12}P + 4.30 \times 10^{-5}$ at $P < 1.78 \times 10^8$ Pa and $\alpha_w = 4.83 \times 10^{-14}P + 3.54 \times 10^{-4}$ at $P > 1.78 \times 10^8$ Pa (dotted line).

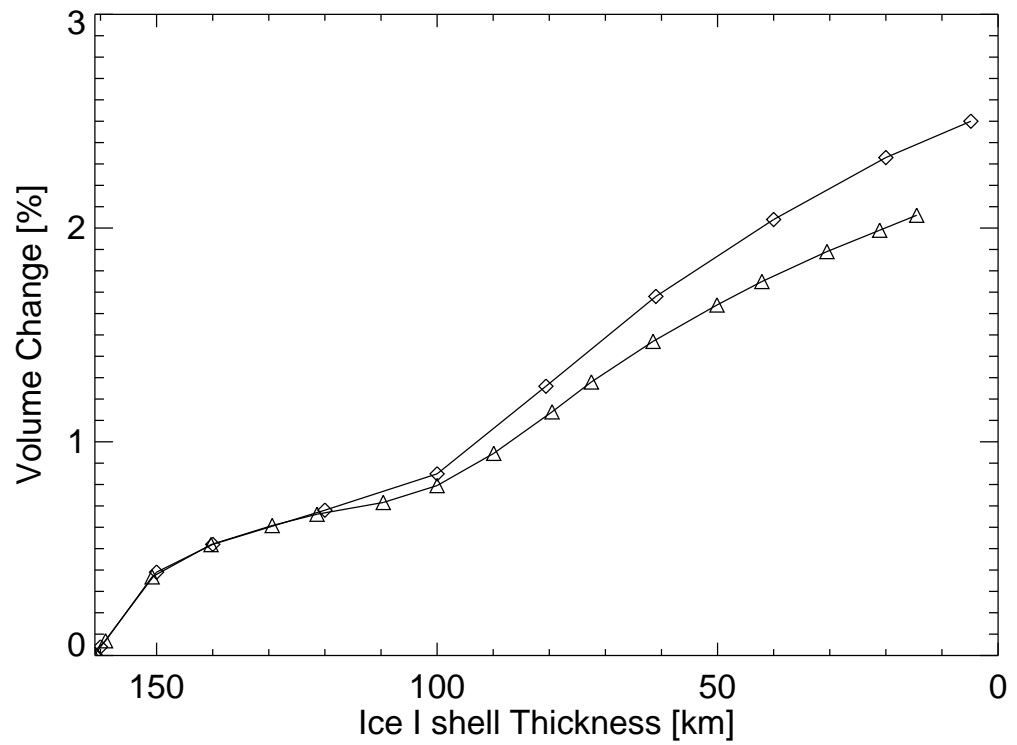


Figure 2.8: The relative volumetric expansion of Ganymede ($\Delta V/V$) as a function of the minimum ice I shell thickness for the two adiabats shown in Fig. 2.7. The curve corresponding to the dotted line of Fig. 2.7 is indicated by triangles, and the curve corresponding to the solid line of Fig. 2.7 is indicated with diamonds. The maximum possible volume increase due to melting an already differentiated Ganymede is $\sim 2.5\%$, equivalent to a surface area change of $\sim 1.8\%$.

sity of sea water is larger than that of pure water by roughly 3% (Dorsey, 1940) and this increase at least partially offsets the decrease in specific heat. Furthermore, available data on the thermal expansivity of sea water suggests it is similar to that for pure water (Sverdrup et al., 1946). We therefore conclude that the presence of salts in Ganymede’s ocean has a negligible effect on the volume expansion that can be produced by melting.

2.5 Consequences for Ganymede’s Geologic History

The high heat flow required to form Ganymede’s furrows and grooved terrain is inconsistent with radiogenic heating alone, suggesting that one or more episodes of tidal heating is required to explain their existence (Nimmo et al., 2002; Nimmo and Pappalardo, 2004; Dombard and McKinnon, 2001; Bland and Showman, 2007, Chapter 4). However, the simulations described above suggest that, if the Galilean satellites passed through the $\omega_1/\omega_2 = 2$ or $\omega_1/\omega_2 = 3/2$ Laplace-like resonances, tidal dissipation would maintain Ganymede’s ice shell at a thickness of only 5-20 km for the lifetime of the resonance. We must therefore consider the consequences a thin ice shell might have on Ganymede’s surface geology

2.5.1 Tectonics and Cratering

Ganymede’s most iconic feature is its grooved terrain, which likely formed by ductile necking of the lithosphere, accompanied by small-scale tilt-block faulting (Pappalardo et al., 1998; Dombard and McKinnon, 2001; Bland and Showman, 2007, Chapter 4). Analytic models of extensional necking posit a ductile half space beneath a stronger lithosphere (Fletcher and Hallet, 1983; Dombard and McKinnon, 2001). If necking occurs in a thin ice shell, the thickness of this half space is reduced. To date, extensional necking in a thin ice shell has not been investigated; however, as long as ductile flow can occur in the low-viscosity region, necking should not

be inhibited. Furthermore, examination of the force balance in an extending ice shell suggests that wide rifts, such as Ganymede's groove terrain, are favored at low ice shell thickness (Nimmo, 2004). Thus, the presence of a thin shell may actually enable the formation of Ganymede's distinctive terrain. Interestingly, the dominant wavelength of the deformation produced by necking may be sensitive to the ice shell thickness. Zuber et al. (1986) showed that the presence of a strong layer at depth (beneath the ductile region) can create additional topographic wavelengths in the surface deformation. The presence of an inviscid layer (i.e. a near surface ocean) may have a similar effect. However, any wavelength signature due to the total ice shell thickness would be largely masked by regional variations in strain rates and lithospheric thermal gradients, which exert a stronger influence over deformation wavelengths (Dombard and McKinnon, 2001; Bland and Showman, 2007, Chapter 4).

The existence of a thin shell on Ganymede may have left evidence in the satellite's cratering record. Crater morphologies vary widely on Ganymede suggesting that the thermal state of Ganymede's lithosphere has changed with time. This trend is generally interpreted to be from a large thermal gradient in Ganymede's past to a smaller thermal gradient at present (Passey and Shoemaker, 1982; Pappalardo et al., 2004). However, the basic trend of decreasing thermal gradients with time does not exclude the possibility that Ganymede experienced an epoch of high heating with a thin ice shell in the middle of its geologic history. Unfortunately, evidence for such a period may be difficult to extract from Ganymede's complex cratering record (see Schenk et al., 2004, for a review). Furthermore, depth to diameter ratios indicate that Ganymede's ice shell was never less than 60 km thick (Schenk, 2002). Additionally, the morphology of large impact basins, which are thought to be ancient, indicates that they formed subsequent to the existence of a thin ice shell. Ganymede's impact cratering record therefore poses a challenge to the existence of a thin ice shell.

2.5.2 Cryovolcanism

While tectonism has played an important role in shaping Ganymede’s surface, evidence suggests that at least some of Ganymede’s resurfacing was accomplished by cryovolcanism (e.g. Schenk et al., 2001). However, the mechanism by which water or slush is erupted onto Ganymede’s surface remains unclear. Showman et al. (2004) showed that, if water is present within ~ 5 to 10 km of the surface, it can be pumped to Ganymede’s surface by topographically induced pressure gradients. The self-regulating nature of this mechanism accounts for the apparent eruption of melt only in topographic lows (such as graben): once a graben fills with cryovolcanic material the pressure gradients driving the cryovolcanism are removed and eruptions cease. However, if Ganymede’s ice shell is thick, the existence of near-surface liquid within the ice shell is difficult to explain. In contrast, if the ice shell is thin the presence of melt is more likely.

The production of partial melt in the ice shell cannot be directly assessed by our simulations, which implicitly assume that the temperature of the ice shell is in equilibrium with the thickness of the ice shell. Any increase in ice shell temperature results in an instantaneous decrease in the ice-I shell thickness. In contrast, the production of partial melt in an ice shell is a non-equilibrium process, and occurs when the temperature of the ice increases more rapidly than melting can occur at the base of the ice shell. The timescale for melting a mass of ice is approximately given by $\tau_m \sim L_w m_I / \dot{E}_{tot}$, where L_w is the latent heat of ice, m_I is the mass of the melting ice, and \dot{E}_{tot} is the rate at which energy is supplied to the ice. Assuming tidal dissipation supplies 10^{12} W of power to the base of the ice shell, the timescale to melt 1 km of ice at the base of a 10-km-thick Ganymedian ice shell is $\tau_m \sim 10^7$ yrs. This rate of melting can be compared to the rate at which the temperature changes in ice shell. During the early period of rapid heating (Fig. 2.4a) the timescale associated with warming Ganymede’s ice shell is $\sim 10^5$ to 10^6 yrs K^{-1} . Under the equilibrium assumptions of our model, decreasing the ice

shell thickness from 10 km to 9 km requires less than a 1 K increase in temperature. Thus, the temperature of the ice shell increases more rapidly than melting can actually occur. This results in melting not just at the base of the ice shell, but throughout the entirety of the shell. Once melt is present in the shell it can be entrained in convective upwellings and brought nearer to the surface (Tobie et al., 2003). Notably, the presence of partial melt in the ice shell is a transient event, limited in duration even if the period of resonance passage lasts billions of years. Once temperatures stabilize, melting catches up with the increased temperatures and the ice shell reaches its equilibrium thickness. Although melt production occurs only briefly, its timing would coincide with the period of satellite expansion, surface extension, and fracturing. The near coincidence of these processes may enable the formation of Ganymede's bright terrains via simultaneous tectonic and cryovolcanic resurfacing of dark terrain.

2.5.3 Tidal Deformation

Tidal stress has played an important role in the geological history of Europa (e.g. Helfenstein and Parmentier, 1985; Schenk and McKinnon, 1989; Leith and McKinnon, 1996; Greenberg et al., 1998; Hoppa et al., 1999). In contrast, Ganymede's surface bears little (if any) evidence of tidally driven tectonic features. The magnitude of diurnal tidal stress on Ganymede is currently low, due to the satellite's low present-day orbital eccentricity. If Ganymede had a larger eccentricity in the past, however, tidal stresses would have been larger. The elastic stresses in a thin shell experiencing a diurnal variation in its tidal potential are given by (Melosh, 1977; Leith and McKinnon, 1996)

$$\sigma_{\theta\theta} = \frac{1}{3}\Delta f\mu_I \left(\frac{1+\nu}{5+\nu}\right) (5 + 3 \cos 2\theta) \quad (2.24)$$

$$\sigma_{\phi\phi} = -\frac{1}{3}\Delta f\mu_I \left(\frac{1+\nu}{5+\nu}\right) (1 - 9 \cos 2\theta), \quad (2.25)$$

where $\sigma_{\theta\theta}$ and $\sigma_{\phi\phi}$ are the meridional and azimuthal stress respectively, Δf is the change in flattening of the satellite, μ_I is the shear modulus (3.52 GPa (Gammon et al., 1983)), ν is Poisson ratio (0.325 (Gammon et al., 1983)), and θ is the colatitude with respect to the tidal axis. The change in flattening can be written as $\Delta f = 3ef_t$ (Greeley et al., 2004), where e is the satellite eccentricity, and f_t is the tidal flattening given by $-3q(3\Lambda + 1)/2$, where Λ is the response coefficient (assumed to be 0.4) and $q = M_J R_g^3 / m_g a_g^3$ where M_J is the mass of Jupiter, m_g is the mass of Ganymede, and a_g is Ganymede's semi-major axis (Leith and McKinnon, 1996). Using values appropriate for Ganymede (Appendix A) and assuming an eccentricity of 0.015, the maximum diurnal tidal stress is ~ 65 kPa. The satellite experiences an additional diurnal stress of 96 kPa due to the libration of its tidal bulge across its surface as it travels in an eccentric orbit. The stresses generated are equivalent to non-synchronous rotation of Ganymede's ice shell by an angle of $2e$ (Greenberg et al., 1998) and is given by (Leith and McKinnon, 1996)

$$\sigma_{NSR} = 6f_t \left(\frac{1 + \nu}{5 + \nu} \right) \sin \Omega, \quad (2.26)$$

where Ω is the non-synchronous rotation angle. Therefore, diurnal elastic stress in Ganymede's ice shell are no more than 100 kPa, an order of magnitude less than the tensile strength of ice. Despite this apparent discrepancy, diurnal stresses of similar magnitude have been invoked to explain a number of Europa's unique features (note that diurnal stresses on Europa are a factor of two higher and ice may be relatively weak at geologic scales) (see Greeley et al., 2004, for a review). The lack of such features on Ganymede may indicate that the ice shell was never thin enough to permit significant deformation, that stresses were not large enough to permit fracturing, or that tectonic features of tidal origin have been obscured by later modification.

Perhaps of greater significance to Ganymede's tectonic history are stresses due to non-synchronous rotation of the ice shell. Modeling of impactor populations in

the Jovian system indicates that crater densities on Ganymede's leading and trailing hemispheres should be asymmetric (Zahnle et al., 2001). While some asymmetry is observed, it is significantly less than the prediction. The most likely explanation for the lack of asymmetry is non-synchronous rotation of the ice shell in Ganymede's past (Zahnle et al., 2001). The satellite's ability to rotate non-synchronously is independent of the thickness of the ice shell, depending instead on whether non-hydrostatic mass anomalies within the interior can stabilize its rotation (Greenberg and Weidenschilling, 1984). However, the timescale for non-synchronous rotation varies as the square root of the thickness of the ice shell (Ojakangas and Stevenson, 1989), thus a thin ice shell allows more rapid non-synchronous rotation than a thick one. Given the limited time span over which Ganymede may have had a large eccentricity, faster rotation corresponds to a greater degree of non-synchronous rotation and larger stresses (Eq. 2.26). The maximum stress due to non-synchronous rotation of Ganymede's ice shell during a period of high eccentricity (90° rotation, Eq. 2.26) is 3.2 MPa, sufficient to permit fracturing to a depth of ~ 2.5 km. The discovery of non-hydrostatic mass anomalies on Ganymede, however, casts doubt as to whether non-synchronous rotation of Ganymede's ice shell can actually occur (Anderson et al., 2004; Palguta et al., 2006).

2.6 Conclusions

The resurfacing of Ganymede is intimately linked to the thermal history of the ice shell and the global expansion of the satellite. Using a coupled orbital-thermal model, we investigated Ganymede's thermal history both with and without the effects of tidal dissipation during a previous period of resonance passage. In the absence of tidal heating (e.g. if the Laplace resonance is primordial) radiogenic heating alone is capable of melting a large ocean if the ice grain size is at least 1 mm. Larger grain sizes (1 cm or more) prevent the ocean from closing by the present epoch, contrasting with the models of Spohn and Schubert (2003) and Freeman

(2006). We find that, with radiogenic heating alone, Ganymede’s maximum heat flux was 24 mW m^{-2} , significantly lower than the inferred flux required to form either Ganymede’s furrows or grooved terrain (McKinnon and Parmentier, 1986; Nimmo et al., 2002; Nimmo and Pappalardo, 2004; Dombard and McKinnon, 2001; Bland and Showman, 2007, Chapter 4). Our results contrast with those of Freeman (2006) who predicted low temperatures in Ganymede’s ice shell and even lower heat fluxes.

If the Galilean satellites passed through one of the Laplace-like resonances that strongly force Ganymede’s eccentricity (especially the $\omega_1/\omega_2 = 2$ or $\omega_1/\omega_2 = 3/2$ resonances), then tidal dissipation in Ganymede’s ice shell has strongly modified its thermal history. For a grain size of $\sim 1 \text{ mm}$, a large ocean and thin ice shell (5 to 20 km) can be maintained for the lifetime of the resonance. For larger grain sizes a near-surface ocean would exist into the present. Smaller grain sizes ($\sim 100 \mu\text{m}$) allow rapid cooling that prevents significant ocean formation; however, such small grain sizes might be ruled out by the existence of an induced dipole component to Ganymede’s magnetic field, which argues for the present-day existence of a salty ocean.

Ganymede’s heat flux during resonance passage may have ranged from 40 mW m^{-2} to 110 mW m^{-2} , depending on the value of Jupiter’s tidal dissipation factor (Q_J). The increased heat flux during resonance passage is consistent with the inferred heat fluxes required to produce Ganymede’s furrows and grooved terrain (McKinnon and Parmentier, 1986; Nimmo et al., 2002; Nimmo and Pappalardo, 2004; Dombard and McKinnon, 2001; Bland and Showman, 2007, Chapter 4). Furthermore, the melting of Ganymede’s ice shell can produce up to a 2.5% volume increase in the satellite, corresponding to a 1.8% increase in surface area. The extent of volume expansion is somewhat greater than, but generally consistent with, previous calculations by Showman et al. (1997). While the value is consistent with early estimates of Ganymede’s global expansion, it falls well short of the minimum surface expansion of 4% estimated by Collins (2007).

The existence of a thin ice shell in Ganymede's past may have enabled the tectonic and cryovolcanic resurfacing of the satellite. Groove formation may be favored in a thin ice shell (Nimmo, 2004) and the rapid heating that occurs upon entering the Laplace-like resonance can enable the formation of near surface partial melt. Partial melting within the ice shell would be a short-lived event; however, it would coincide with the period of satellite global expansion and extensional surface stress. The commensurability between these events may explain Ganymede's complex history of tectonic and cryovolcanic resurfacing. Tidal stresses in Ganymede's thin ice shell could have also contributed to the formation of Ganymede's unique features.

While the simulations described above produce conditions favorable to resurfacing Ganymede, the surface-area expansion that results from remelting a differentiated satellite is several times less than the strains measured on the surface. We therefore may require an alternative mechanism capable of explaining both the timing and magnitude of Ganymede's global expansion. A potential scenario for such expansion stems from the possibility that both Ganymede and Callisto formed undifferentiated (Canup and Ward, 2002) (though see the model of Mosqueira and Estrada (2003), which simultaneously forms an undifferentiated Callisto and a differentiated Ganymede). Like the mechanism of Mueller and McKinnon (1988), complete differentiation of Ganymede (which is inferred from Ganymede's low value of $C/MR^2 = 0.3115$ (Anderson et al., 1996; Schubert et al., 2004)) would occur later in Ganymede's history, possibly during passage through one of the Laplace-like resonances described above. While the scenario contains a number of uncertainties, such delayed differentiation is likely consistent with both the timing and magnitude of Ganymede's global expansion.

CHAPTER 3

THE PRODUCTION OF GANYMEDE'S MAGNETIC FIELD

The material presented in this chapter has been submitted to Icarus and is currently in revision. Some material has been excised to avoid repetition with Chapter 2

3.1 Background

Ganymede is unique among the satellites of the solar system in that it has an intrinsic magnetic field (Kivelson et al., 1996; Gurnett et al., 1996; Williams et al., 1997) while other large satellites do not. Analysis of magnetometer data taken during the Galileo spacecraft's four close Ganymede flybys suggest that the field consists of a Ganymede-centered dipole tilted 10° with respect to the rotation axis (Kivelson et al., 1996). With an equatorial surface-field strength of 750 nT, the field creates a mini-magnetosphere ~ 2 Ganymede radii in extent within Jupiter's larger magnetosphere (Kivelson et al., 1996, 1997, 1998).

The strength of the observed field and Ganymede's high degree of central condensation ($C/MR^2 = 0.3115$ where C is the axial moment of inertia, and M and R are the satellite mass and radius respectively (Anderson et al., 1996; Schubert et al., 2004)) suggest that dynamo action within a metallic core generates the magnetic field (Schubert et al., 1996; Sarson et al., 1997). Other field-producing mechanisms are largely inconsistent with observations. The strength of the field, which is significantly greater than Jupiter's field at Ganymede's location, makes production by induction (the mechanism that produces the fields of Europa and Callisto (Khurana et al., 1998; Kivelson et al., 1999, 2000; Zimmer et al., 2000)) unlikely (Schubert

et al., 1996). Ganymede’s observed field may, in fact, include an induced field component generated in a conducting layer (likely an ocean) at ~ 150 km depth; however, modeling indicates that this component is small (Kivelson et al., 2002). Additionally, the unrealistically high fluid velocities (1 m s^{-1}) required to produce a dynamo in a thick, electrically conducting ocean make such a mechanism unfeasible (Schubert et al., 1996). Furthermore, producing the observed field via remnant magnetization of Ganymede’s rocky mantle requires making rather favorable assumptions regarding the magnetic properties of the rocky materials and requires that a strong dynamo-generated field existed earlier in Ganymede’s history (Crary and Bagenal, 1998). While we cannot eliminate the mechanism entirely, it seems less plausible than a dynamo generated magnetic field (Schubert et al., 1996).

The dynamo mechanism for magnetic field production requires that fluid motions occur within an electrically conducting medium such as a fluid metallic core. In a planetary dynamo, buoyancy driven convection provides this motion (Malkus (1963) and Vanyo et al. (1995) have also suggested that precession can drive motion within a fluid core, however its relevance to dynamo generation is debatable (e.g. Rochester et al., 1975; Loper, 1975)). In the absence of an inner solid core, thermal buoyancy alone must drive convection. The requirement for convection in this case is simply that the heat flux out of the core (F_{total}) is greater than the maximum heat flux that can be carried conductively ($F_{cond,ad}$) (i.e. the heat flux conducted along the core adiabat). Thus, for convection (Stevenson, 2003)

$$F_{total} > F_{cond,ad} \equiv k_c \frac{\alpha_c g_c T_{cmb}}{c_{p,c}}, \quad (3.1)$$

where k_c is the thermal conductivity, α_c is the thermal expansivity, $g_c \approx 1.3 \text{ m s}^{-2}$ is the local gravitational acceleration (c.f. Sohl et al., 2002), T_{cmb} is the temperature at the core-mantle boundary, and $c_{p,c}$ is the specific heat at constant pressure. Equating the minimum required heat flux (Eq. 3.1) to the cooling rate of the core yields a

minimum cooling rate required to maintain thermal convection

$$\left(\frac{dT}{dt}\right)_{min} = \frac{3k_c\alpha_c g_c T_{cmb}}{R_c \rho_c c_{p,c}^2}, \quad (3.2)$$

where R_c and ρ_c are the radius and density of the core respectively. For parameters appropriate to Ganymede (Appendix A) and $T_{cmb} = 2000$ K, the minimum required cooling rate is ~ 250 K Ga⁻¹. If we assume secular cooling of Ganymede's core associated with the decline in radiogenic heating over the age of the solar system, the present cooling rate falls well short of the minimum requirement (see section 3.3) and a dynamo driven by present-day thermal convection appears unlikely.

To maintain a planetary dynamo, it is necessary but not sufficient that fluid motion occurs in a planetary core. In addition, a self-sustained planetary dynamo requires that convection can supply sufficient power to overcome losses due to ohmic dissipation of the field (e.g. Stevenson et al., 1983; Buffett, 2002). The ohmic dissipation Φ can be approximated by (Buffett, 2002)

$$\Phi = \left(\frac{\eta \bar{B}^2}{\mu_o L^2}\right) \frac{4}{3} \pi R_c^3, \quad (3.3)$$

where $\eta \sim 2$ m² s⁻¹ is the magnetic diffusivity, \bar{B} is the average strength of the field at the core-mantle boundary, $\mu_o = 4\pi \times 10^{-7}$ N A⁻¹ is the magnetic permeability, and L is the length scale for convection (a free parameter). Assuming a core radius of 700 km, and a convective length-scale equal to $\sim 10\%$ of the core radius we find $\Phi = 10^8$ W, consistent with the strength of Ganymede's magnetic field extrapolated to the core-mantle boundary. The power requirement (W) for sustaining a dynamo is then (Stevenson et al., 1983)

$$P_B = 4\pi R_c^2 \frac{k_c \alpha_c g_c T_{cmb}}{c_{p,c}} + \frac{\Phi}{\epsilon} - \left(\frac{E_G}{\epsilon} + L_{Fe}\right) \frac{dm_{ic}}{dt}, \quad (3.4)$$

where ϵ is a Carnot-like efficiency factor (~ 0.05 (Buffett et al., 1996)), E_G is the gravitational energy released by inner core formation, L_{Fe} is the latent heat of iron, and dm_{ic}/dt , is the rate at which the mass of the inner core increases. The first

term on the right hand side of Eq. 3.4 is simply the power lost from the core by conduction as given in Eq. 3.1; the second term is the additional power required to overcome ohmic dissipation; the third term is the power provided by compositional convection (see below) and is zero in the absence of an inner core.

Whether thermal convection can occur or not, cooling of the core can lead to the formation of a solid inner core. Inner core growth provides an additional source of energy and buoyancy in the core as heavy elements (e.g. Fe/Ni) freeze out, releasing latent heat, and light elements (e.g. sulfur) are expelled upward, releasing gravitational energy. Earth's magnetic dynamo appears to require such compositionally driven convection (e.g. Verhoogen, 1961; Braginsky, 1963; Gubbins, 1977; Loper, 1978a,b; Lister and Buffett, 1995; Buffett et al., 1996; Gubbins et al., 2004), and it may play a similar role in driving Ganymede's core dynamo (Kuang and Stevenson, 1996; McKinnon, 1996; Hauck et al., 2006).

Equation 3.4 indicates that inner core formation relaxes the power requirements on the dynamo. However, whether compositional convection can account for Ganymede's dynamo remains unclear. In a detailed investigation of compositional convection's impact on the evolution of Ganymede's core, Hauck et al. (2006) used scaling arguments to calculate the magnetic Reynolds number ($Re_m = u\mathcal{L}/\eta$ where u is the flow velocity and \mathcal{L} is the thickness of the convecting layer) associated with compositional convection. When one accounts for the fact that the inner core is $\sim 50\%$ of the total core radius after 4.6 Ga (see Hauck et al., 2006), then Re_m due to compositionally driven convection in Ganymede is ≈ 35 . However, numerical investigations indicate that convectively-driven, self-sustained dynamos require a magnetic Reynolds number of 40 to 50 (Olson and Christensen, 2006; Christensen and Aubert, 2006). Compositional convection's ability to maintain Ganymede's dynamo over geologic time therefore appears marginal.

Furthermore, inner core formation on Ganymede may occur in a novel way relative to the Earth. In contrast to melting relations in the Fe-FeS system at high

pressures (e.g. Boehler, 1996; Usselman, 1975), experimental work at low pressures (< 14 GPa) indicate that, for sulfur concentrations greater than $\sim 3\%$, the melting curve is less steep than Ganymede’s expected core adiabat (i.e. $(dT_{m,Fe}/dP) < (dT/dP)_{ad}$), and for even larger sulfur concentrations the melting temperature can decrease with increasing pressure (i.e. $(dT_{m,Fe}/dP) < 0.0$) (Fei et al., 1997). These observations imply that, for sulfur concentrations greater than 3% , Fe will first condense at Ganymede’s core-mantle boundary (i.e. at the top of the liquid core), rather than at the inner-core/outer-core boundary as occurs on Earth (Kuang and Stevenson, 1996; McKinnon, 1996; Hauck et al., 2006). The relatively dense Fe condensed at the top of the liquid core is buoyantly unstable and will sink downward to form an inner core, releasing gravitational energy (Hauck et al., 2006). Hauck et al. (2006) have argued that such compositional convection is sufficient to drive Ganymede’s dynamo. However, because condensation of Fe occurs at the core-mantle boundary rather than deep in the core, the latent heat released by Fe condensation might not contribute to the convection that drives the dynamo because this heat is immediately removed from the core to the cooler mantle above. The removal of the latent heating term from Eq. 3.4 severely limits the ability of compositional convection to power the dynamo. This is especially true in Ganymede’s small core where the gravitational energy release is relatively small (see section 3.2.2). Furthermore, while the gravitational energy released through iron precipitation is identical to that of Earth-like “bottom-up” core formation, it is unclear whether the simple settling of iron grains can induce sufficient turbulence to generate a dynamo.

Due to the difficulties in maintaining Ganymede’s magnetic field by long-lived-thermal or compositional convection associated only with the decline in radiogenic heating, Stevenson (1996) and Showman et al. (1997) suggested that a period of tidal heating in Ganymede’s past may have enabled generation of the present-day field. The Galilean satellites Io, Europa, and Ganymede currently reside in the Laplace resonance (see Chapter 2 for a description). This system of resonances excites the

eccentricity of both Io and Europa, and the resulting tidal heat strongly influences their thermal histories (e.g. Yoder, 1979; Ojakangas and Stevenson, 1986; Fischer and Spohn, 1990; Hussman and Spohn, 2004). The Laplace resonance does not, however, force Ganymede's eccentricity, and thus negligible tidal heating currently occurs there.

Despite the present lack of tidal forcing of Ganymede's orbit, excitation of the satellite's eccentricity sufficient to drive thermal activity may have occurred in the past (Greenberg, 1987; Tittlemore, 1990; Malhotra, 1991; Showman and Malhotra, 1997; Peale and Lee, 2002). Malhotra (1991) and Showman and Malhotra (1997) investigated one of the more plausible scenarios, which identified additional evolutionary pathways into the Laplace resonance to that described by Yoder and Peale (1981). As described in Chapter 2, unlike the Laplace resonance, several of these resonances can strongly force Ganymede's eccentricity with the resulting tidal heating modifying the satellite's thermal history (Showman et al., 1997). Showman et al. (1997) investigated the potential for thermal runaway in Ganymede's ice shell during such resonance passage, but they did not explore the effect of resonance passage on Ganymede's silicate mantle and metallic core in detail.

In this chapter, we first establish the conditions required to produce Ganymede's present-day core dynamo during its secular thermal evolution. We show that magnetic field production requires a very restrictive set of initial conditions to be met, some of which may be incompatible with realistic models of the satellite. We then test the hypothesis that resonance passage may have broadened the range of conditions under which magnetic field generation is possible by reinvigorating the core dynamo: dissipation of tidal energy within Ganymede's silicate mantle drives a thermal runaway that prevents the metallic core from cooling. Such thermal runaways result from the complex feedback between temperature, viscosity, and tidal dissipation (Showman et al., 1997). Once the system escapes the resonance, tidal dissipation ends and the silicate mantle and metallic core cool rapidly until reaching a new

quasiequilibrium with radiogenic heat production in the mantle. Dynamo action occurs during this period of rapid cooling and high core power output. Wienbruch and Spohn (1995) explored a similar scenario for Io (without the resonance escape) and suggested that tidal heating may prevent dynamo action there. The apparent absence of a strong magnetic field at Io (Kivelson et al., 2001) lends some credence to this scenario. However, even the strongest Laplace-like resonance produces orders of magnitude less tidal dissipation in Ganymede than is currently observed at Io (Showman and Malhotra, 1997; Veeder et al., 1994). Thus, elucidating the conditions (if any) under which tidal heating in Ganymede’s silicates might assist present-day dynamo action in Ganymede’s core is essential to understanding why the satellite has a magnetic field.

3.2 Methods

We investigate the thermal history of Ganymede in an effort to understand the conditions required to produce Ganymede’s magnetic field. In addition, we assess the role that resonance passage may have played in enabling a magnetic dynamo. To do this we utilize the model described in Chapter 2, consisting of a three-layer one-dimensional thermal model of Ganymede’s ice shell, silicate mantle, and metallic core coupled to the orbital model of Malhotra (1991). Coupling between the orbital and thermal models occurs via tidal dissipation, which depends upon both the thermal structure and orbital evolution of the satellite. We calculate tidal heating with the dissipation model of Tobie et al. (2005b), which permits determination of the tidal dissipation in each model layer.

3.2.1 Energy Balance in the Ice Shell and Silicate Mantle

The thermal evolution of Ganymede is controlled by how energy is transferred between the three layers of the model. The model is described in detail in Chapter

2 and I do not repeat that description here. However, a more detailed description of both the core model and the initial conditions used in our simulations is provided below. All symbols and parameters are defined in Appendix A.

3.2.2 The Core Model

Cooling, offset by the energy released by inner core formation, dominates the thermodynamics of Ganymede's core. The core's energy balance can be described as

$$(E_G + L_{Fe}) \frac{dm_{ic}}{dt} = 4\pi R_c^2 F_c + \frac{4}{3}\pi R_c^3 \rho_c c_{p,c} \frac{dT_c}{dt}, \quad (3.5)$$

where L_{Fe} is the latent heat released by condensation of iron, E_G is the gravitational energy release associated with iron condensation (see below), m_{ic} is the mass of the inner core, ρ_c is the density of the core, $c_{p,c}$ is the specific heat of the core, and F_c is heat flux out of the core. In the absence of inner core formation dm_{ic}/dt is zero. The heat flux out of the core F_c is controlled by energy transfer across the core mantle boundary (CMB), which must occur conductively. The heat flux is

$$F_c = k_{sil} \frac{T_{cmb} - T_{sil}}{\delta_{BL}}, \quad (3.6)$$

where $\delta_{BL} = \mathcal{L}(Ra_{crit}/Ra)^\beta$ is the thickness of the thermal boundary layer in the silicate mantle, and \mathcal{L} is the thickness of the silicate mantle. Equation 3.6 is an approximation that must be used with caution. If the silicate mantle is cool, δ_{BL} is large and the flux out of the core will be negligible in spite of large potential differences in T_{sil} and T_{cmb} . Furthermore, radiogenic heating within the silicate layer will modify the thickness of the bottom boundary layer compared to that determined from boundary stability analysis (used above). Finally, we note that a rigorous formulation of the heat flux out of the core must correct for the sphericity of the layer (c.f. Reese et al., 2005). For simplicity we have neglected the effects of curvature as we expect these effects to be less important than other model uncertainties.

When the core temperature drops below the melting point of the Fe-FeS system, condensation of Fe will occur and an inner core will form. We model inner core formation following the approach of Stevenson et al. (1983) and we refer readers there for a more detailed description of the model. We assume an adiabatic temperature profile for the core with the form

$$T_c = T_{cmb} \exp \left[\frac{\alpha_c (P(r) - P_{cmb})}{\rho_c c_{p,c}} \right], \quad (3.7)$$

where T_{cmb} and P_{cmb} are the temperature and pressure (~ 7 GPa (Sohl et al., 2002)) at the core-mantle boundary respectively, α_c is the coefficient of thermal expansion, and $P(r)$ is the pressure at depth r . The melting curve in the Fe-S system is given by

$$T_{m,Fe} = T_o [1 + T_{m1} P(r) + T_{m2} P(r)^2] [1 - \varsigma \chi], \quad (3.8)$$

where T_o , T_{m1} , and T_{m2} are experimentally derived constants, and χ is the mass fraction of light elements. ς is the dimensionless slope of the Fe/FeS liquidus as a function of composition (Fei et al., 1997; Hauck et al., 2006). For simplicity we neglect the small pressure dependence of ς . We calculate the radius of the inner core R_{inner} at each timestep by equating Eqs. 3.7 and 3.8 and solving for $P(r)$, the pressure of the top of the inner core. An inner core radius can be determined from $P(r)$ by assuming hydrostatic equilibrium.

The gravitational energy released by condensation of iron (E_G) is given by (Schubert et al., 1988)

$$E_G = \frac{2\pi G R_c^2 \chi_o \Delta\rho}{(1 - \xi^3)^2} \left(\frac{\rho_{ic}}{\rho_s} \right) \left[\frac{1}{5} (1 - \xi^5) - \frac{\xi^2}{3} (1 - \xi^3) \right], \quad (3.9)$$

where G is the gravitational constant, χ_o is the initial sulfur concentration, $\Delta\rho$ is the density difference between the light element and iron, ρ_{ic} is the density of the inner core, ρ_s is the density of sulfur, and $\xi = R_{inner}/R_c$. For $R_c \sim 700$ km, and an initial sulfur concentration of 10%, typical values of E_G are 10^4 J kg $^{-1}$, an order of magnitude less than the latent heat released by iron condensation. For

an initial sulfur concentration of 1% the gravitational energy is an additional order of magnitude lower. Thus, during inner core growth the release of latent heat dominates the core energy balance.

3.2.3 Initial Thermal Conditions

The model described above implicitly assumes that the satellite differentiated shortly after accretion (i.e. before our simulated tidal evolution begins), and the effects of such differentiation are not included in the model. Thus $t = 0$ should be considered the time after differentiation occurred. We assume that differentiation occurred quickly enough that long-lived radiogenic isotopes did not undergo significant decay (i.e. the timescale for accretion of $\sim 10^3$ yrs (Canup and Ward, 2002) is much shorter than typical radiogenic half life of $\sim 10^9$ yrs). We therefore assume that Ganymede possess its full complement of radiogenic isotopes when the simulations begin.

We assume that the silicate mantle and metallic core begin hot. Starting the simulations with cooler temperatures leads to an initial period of rapid warming as the silicate temperatures come into quasi-equilibrium with radiogenic heating. This initial period of heating does not influence the later temperature evolution of the satellite and it appears more realistic to simply initialize the simulations with high temperatures. Additionally, we initialize our simulations with core temperatures that are slightly overheated relative to the silicate mantle. In reality, the temperature of Ganymede's core shortly after its formation likely depends on the details of how core formation occurs in icy satellites, a topic beyond the scope of the present investigation. Thus, we simply assume reasonable values and assess the sensitivity of our results to those assumptions (discussed below).

3.3 Producing Ganymede’s Magnetic Field

The thermal history of Ganymede was assessed to determine conditions under which a present-day magnetic field can be produced by a thermally or compositionally driven dynamo operating in Ganymede’s core. These simulations do not include tidal dissipation and are consistent with a primordial origin for the Laplace resonance, passage through Laplace-like resonances that do not pump Ganymede’s eccentricity, or tidal evolution directly into the Laplace resonance (i.e. avoiding the Laplace-like resonances). Each simulation was initialized with a hot core (2400 K), hot mantle (2200 K), and cold ice shell (200 K). The grain size of the silicates and ice was 1 mm, and we evaluated the effects of both a wet and dry olivine rheology for the mantle (Table 2.1). Additionally, we investigated two end member core compositions: a sulfur mass fraction of 1%, placing it in the “Earth-like” bottom-up regime for inner core formation, and a sulfur mass fraction of 10%, placing it in the “iron snow” top-down regime of inner core formation.

Figure 3.1 shows the thermal evolution of Ganymede assuming a dry olivine mantle rheology for the two end member core compositions. Silicate and core temperatures (Figs. 3.1a and 3.1b) are controlled by the quasiequilibrium between radiogenic heat production and convective cooling and are maintained between 2200 and 1700 K throughout the simulation. These high temperatures suggest melting should occur within Ganymede’s mantle. The effects of partial melting are described in section 3.4.4. Our calculated temperatures are roughly consistent with previous modeling by Hauck et al. (2006) whose somewhat lower temperatures can be attributed to the use of a wet olivine rheology (see below). The significantly lower silicate temperatures calculated by the thermal models of Freeman (2006) are likely due to the two models’ different assumptions regarding both the rheology and convective scaling of the silicate layer.

For both core compositions, the power output of the core (solid black line in Figs.

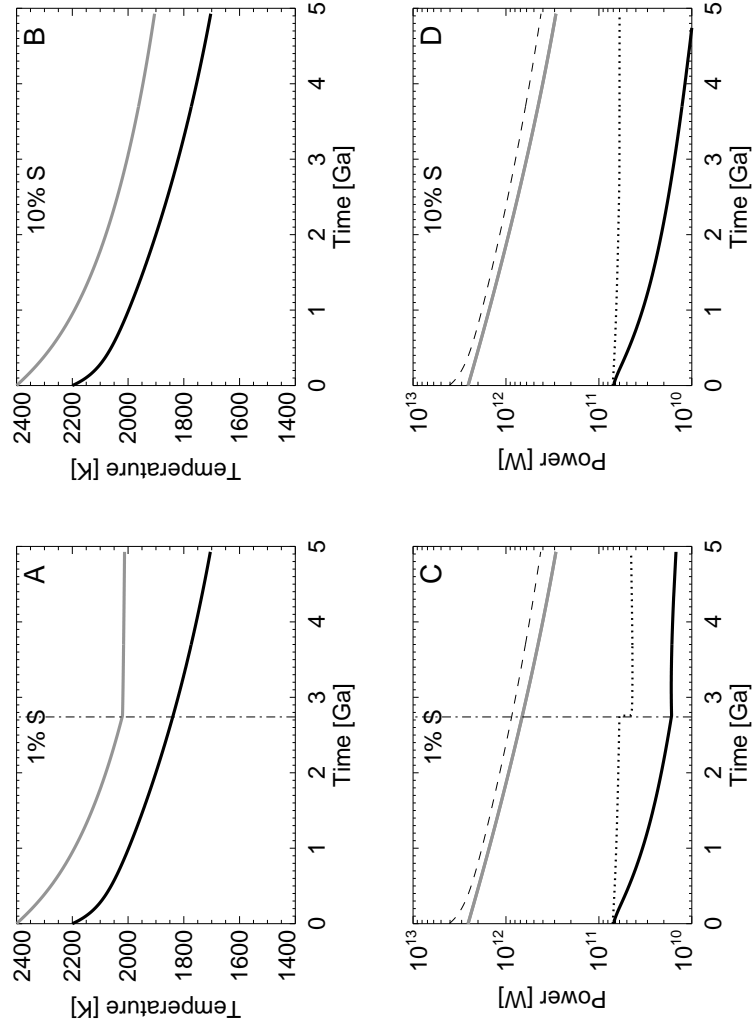


Figure 3.1: Thermal history of Ganymede’s core and silicate mantle assuming a dry silicate rheology with a 1 mm grain size. **A.** Temperature of the silicate mantle (black line) and metallic core (grey line) as a function of time for a simulation with a core sulfur mass fraction of 1%. **B.** As in (A) but for a simulation with a core sulfur mass fraction of 10%. **C.** Power output from the silicate mantle (dashed line) and metallic core (black line) for a simulation with a core sulfur mass fraction of 1%. The power required to drive Ganymede’s core dynamo is indicated by a dotted line. For reference, the radiogenic power is shown as a grey line. **D.** Same as in (C) but for a simulation with a core sulfur mass fraction of 10%. In each panel the onset of inner core formation is indicated by a vertical dot-dash line.

3.1c and 3.1d) is initially equal to the power required to drive the dynamo (Eq. 3.4, dotted line in Figs. 3.1c and 3.1d) but immediately drops below the requirement. A dry mantle rheology therefore does not permit a magnetic field early (or late, see below) in Ganymede's history. In the simulation with a sulfur mass fraction of 1% in the core (Figs. 3.1a and 3.1c), inner core formation (indicated by the vertical dot-dash line) begins after 2.75 Ga, significantly reducing the cooling rate of the core. The onset of chemical convection reduces the power requirement on the dynamo but, because of slow inner core growth, the magnitude of the reduction is insufficient to permit the core power output to exceed the dynamo requirement (Fig. 3.1c). In the simulation with a core sulfur mass fraction of 10% (Figs. 3.1b and 3.1d), temperatures never drop below the core melting temperature (which is reduced by the increased sulfur concentration) and compositional convection never occurs. We therefore conclude that present-day magnetic field production is not possible if Ganymede's mantle cools slowly (i.e. has a rheology similar to dry olivine).

Ganymede's thermal history is substantially different if we assume the silicate mantle behaves like wet olivine (Fig. 3.2). Temperatures decrease rapidly relative to the simulations with a dry olivine rheology and are generally consistent with those of Hauck et al. (2006). In the simulation with a core sulfur mass fraction of 1% (Figs. 3.2a and 3.2c), the power output of the rapidly cooling core initially greatly exceeds the power requirement for the dynamo, suggesting that a magnetic field driven solely by thermal convection may have existed early in Ganymede's history. Inner core formation begins at 0.7 Ga, at which point further cooling of the metallic core is strongly reduced by the release of latent heat and gravitational energy. The chemical energy released during inner core formation is sufficient to significantly reduce the power requirements on the dynamo, which initially drops to near zero. As the rate of core cooling decreases with time, the rate of inner core formation slows and the additional power needed for the dynamo begins to increase. Despite this, the power output of the core exceeds the power required to drive the dynamo

throughout the simulation, suggesting that production of a present-day magnetic field is feasible under these simulated conditions.

A different story emerges in the simulation with a core sulfur mass fraction of 10% (Figs. 3.2b and 3.2d). Like the simulation with a 1% sulfur core composition, the core power output initially exceeds the dynamo power requirement, suggesting a thermally driven dynamo existed early in Ganymede’s history. The greater sulfur concentration in the core lowers the core melting temperature and delays inner core formation until 4.1 Ga (note that the timing of inner core formation, which depends on the assumed initial core temperature, does not affect the results described here). Unlike the simulation described above however, the onset of chemical convection does not substantially decrease the dynamo power requirement. In the “iron snow” regime the latent heat released by iron condensation at the top of the core is immediately removed to the mantle above and is not available to power the dynamo. We therefore neglect the latent heating term in Eq. 3.4 when evaluating the power required to drive the dynamo. Because of Ganymede’s small core, the gravitational energy release is small relative to the latent heat, and the power produced by chemical convection is insufficient to drive the magnetic dynamo. Therefore, this simulation does not predict magnetic field production during the current epoch.

These simulations illustrate that the production of Ganymede’s current magnetic field during secular cooling of the satellite is feasible, but only for a select set of circumstances. Ganymede’s core must contain less than $\sim 3\%$ sulfur by mass. Core formation will then occur in an Earth-like regime in which latent heat is released deep in the core. With greater amounts of sulfur, Fe condensation occurs at the top of the core and the released latent heat is not available to drive the core dynamo. Gravitational energy alone cannot maintain Ganymede’s dynamo and magnetic field production does not occur. This result contrasts with that of Hauck et al. (2006) who find that chemical convection can drive Ganymede’s magnetic dynamo for a broad range of core compositions. The findings of Hauck et al. (2006) are based

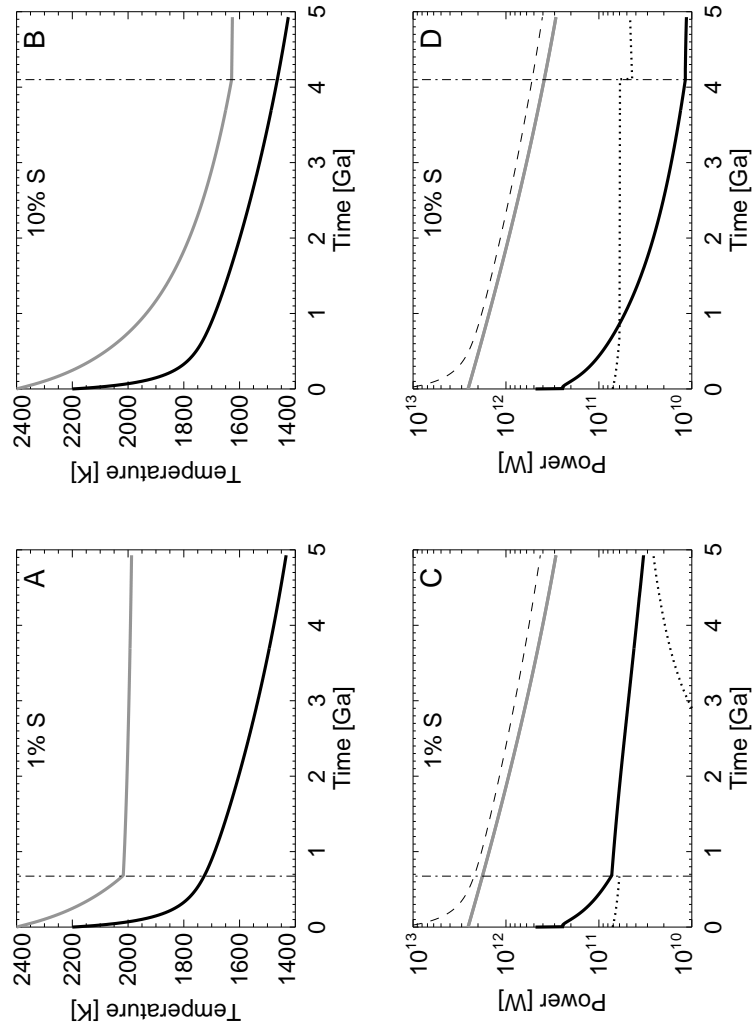


Figure 3.2: As in Fig. 3.1 but for a wet silicate rheology with a 1 mm grain size.

on the result that the core fluid velocities resulting from Fe condensation at the top of the core are consistent with Ganymede’s magnetic field (i.e. they result in a large Re_m). In contrast, our results indicate that the power budget of the core cannot support a magnetic field during top-down inner core formation. We note that sulfur concentrations greater than the FeS eutectic ($\sim 21\%$) may also permit condensation of FeS deep within Ganymede’s core (McKinnon, 1996; Hauck et al., 2006). Such high sulfur concentrations are not investigated here, but they remain a viable possibility for driving a dynamo by compositional convection.

In addition to the requirement on the core composition, chemical convection is a sufficient source of energy only if the core can cool rapidly, requiring that Ganymede’s mantle behaves rheologically like wet olivine. Alternatively, a dry rheology is feasible if the grain size of the silicates is very small ($\sim 100\mu\text{m}$). Finally, the low sulfur concentration in the core requires that Ganymede’s core formed hot ($> 2000\text{K}$).

Unfortunately the conditions described above are not easily met. While some cosmochemical evidence favors an Fe-rich core (Kuskov and Kronrod, 2001) the true core composition is unknown. Additionally, the fact that Ganymede possesses a metallic core argues for a dehydrated mantle composition and a dry silicate rheology (Kuskov and Kronrod, 2001; Sohl et al., 2002). Furthermore, differentiation of a sulfur poor core may require temperatures higher than can be achieved in Ganymede’s mantle (Grasset et al., 2000). Given these difficulties, an investigation of alternative mechanisms for the production of Ganymede’s magnetic field is warranted. We now consider whether a period of tidal dissipation in Ganymede’s silicate mantle can extend the range of conditions needed for the generation of a core dynamo beyond those described above.

3.4 The Influence of Ganymede’s Orbital Evolution

To evaluate the magnitude of the tidal dissipation required to modify the thermal history of Ganymede’s silicate mantle and metallic core and enable magnetic field production we simulated the Galilean satellites’ evolution through the Laplace-like resonance that produces the strongest excitation of Ganymede’s eccentricity ($\omega_1/\omega_2 = 2$) (Showman and Malhotra, 1997). The relevance of other evolutionary pathways is discussed in section 3.6. In the simulations described here we assume a constant value for Jupiter’s tidal dissipation factor (Q_J) of 3×10^5 , consistent with observational and theoretical constraints (see review by Peale, 1999). The effect of variations in Q_J are discussed in section 3.4.2. We assume initial ratios of tidal dissipation factor (Q) to second degree tidal love number (k) for Europa and Io of 3260.9 and 300, respectively. These ratios yield reasonable Q values for the expected k of the satellites. The low Q/k ratio of Io is required for capture into the $\omega_1/\omega_2 = 2$ resonance. The range of Io’s Q/K that permits capture into the $\omega_1/\omega_2 = 2$ resonance depends upon the initial values of ω_1 and ω_2 and we refer the reader to Showman and Malhotra (1997) for more detail. With these parameters, the satellites enter the $\omega_1/\omega_2 = 2$ resonance at 0.5 Ga and remain locked in resonance until ~ 3.8 Ga (Fig. 3.3a), at which point we force the system out of resonance by temporarily increasing Io’s Q/k value. Such changes in Io’s Q/k are predicted by coupled orbital-thermal models of the satellite (Ojakangas and Stevenson, 1986). Once the system has escape the $\omega_1/\omega_2 = 2$ resonance, it evolves naturally into the Laplace resonance (Fig. 3.3a). The eccentricity of Ganymede (e_3) increases significantly while in the Laplace-like resonance (Fig. 3.3b), reaching values as high as 0.011, ~ 10 times greater than the satellite’s current eccentricity. The timing of capture into the $\omega_1/\omega_2 = 2$ resonance and the maximum eccentricity reached by Ganymede depend on the assumed value of Q_J , with lower values causing rapid orbital evolution and larger satellite eccentricities. The increase in Ganymede’s eccentricity

during resonance passage leads to the dissipation of tidal energy in Ganymede's ice shell and silicate mantle (Fig. 3.3c). Negligible dissipation occurs in either layer before the satellites enter the Laplace-like resonance. Once capture occurs however, tidal dissipation increases sharply leading to nearly 10^{12} W of dissipation in the ice shell (grey line), and 10^9 W of dissipation in the silicates (black line).

Figure 3.4 shows the effect of tidal dissipation on the temperature structure of the satellite. Initial temperatures are identical to those used in section 3.3. We use a dry olivine rheology in the silicates, and a grain size of 1 mm in both the ice and silicate layers. As described in Chapter 2, the temperatures in the ice shell rise steadily due to the combination of radiogenic heat from below and tidal dissipation in the ice shell itself (Fig. 3.4a). Once the ice reaches a temperature of 251 K, ocean formation begins and the temperature increase is buffered by melting. As melting proceeds the ice shell transitions to a thin conductive layer, ultimately limiting the temperature of the ice, which then remains constant throughout the resonance passage. The thickness of the remnant ice I shell is generally a few tens of kilometers. After the satellites escape the Laplace-like resonance, ice temperatures decrease slowly, again buffered by the release of latent heat during refreezing of the ocean. See Chapter 2 for further details.

Figure 3.4b shows the temperature of the silicate mantle and core and Fig. 3.4c shows the cooling rate of the core over solar system history. Core temperatures decline monotonically at a rate determined by the cooling silicate layer above. The high initial cooling rates permit early thermal convection in the core (note that thermal convection does not necessarily imply magnetic field production, see below); however, cooling rates decrease rapidly in the first 0.5 Ga. In the late stages of the simulations, the slow cooling of the silicates (Fig. 3.4b) prevents the core from cooling more rapidly than $30\text{-}50$ K Ga⁻¹. Like the previously described simulations with a dry olivine rheology, the high silicate temperatures prevent formation of an inner core, eliminating compositional convection as a potential driver for the

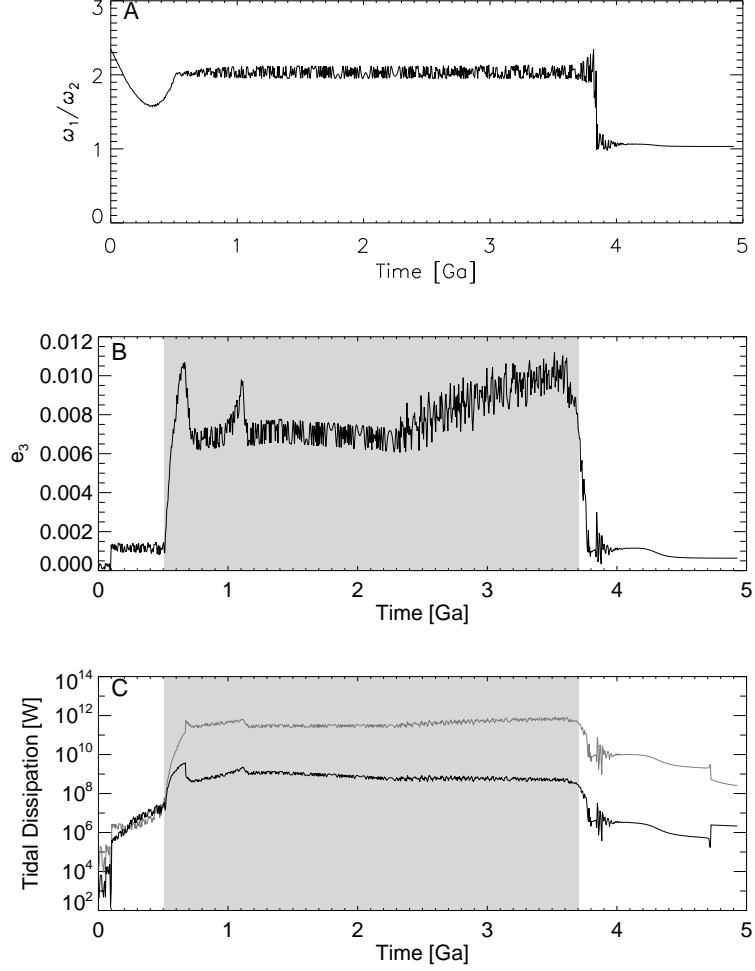


Figure 3.3: A plausible orbital history for Ganymede. **A.** Ratio between ω_1 and ω_2 ($\omega_1 = 2n_2 - n_1$ and $\omega_2 = 2n_3 - n_2$ where n_1 , n_2 , and n_3 are the mean motions of Io, Europa, and Ganymede respectively) as a function of time. The satellites enter the $\omega_1/\omega_2 = 2$ Laplace-like resonance after ~ 0.5 Ga and escape resonance at ~ 3.8 Ga. The system then evolves into the Laplace resonance in which $\omega_1/\omega_2 = 1$. **B.** Ganymede's eccentricity (e_3) as a function of time. During the Laplace-like resonance passage e_3 reaches values of ~ 0.011 , an order of magnitude larger than its current eccentricity. **C.** Tidal dissipation in the ice shell (grey line) and silicate mantle (black line) as a function of time. Maximum tidal dissipation occurs during resonance passage and negligible dissipation occurs outside the resonance. The tidal dissipation in the ice shell is more than two orders of magnitude greater than that in the silicate mantle. Q_J is 3×10^5 . The shaded region in (B) and (C) indicates the period of Laplace-like resonance passage shown in (A).

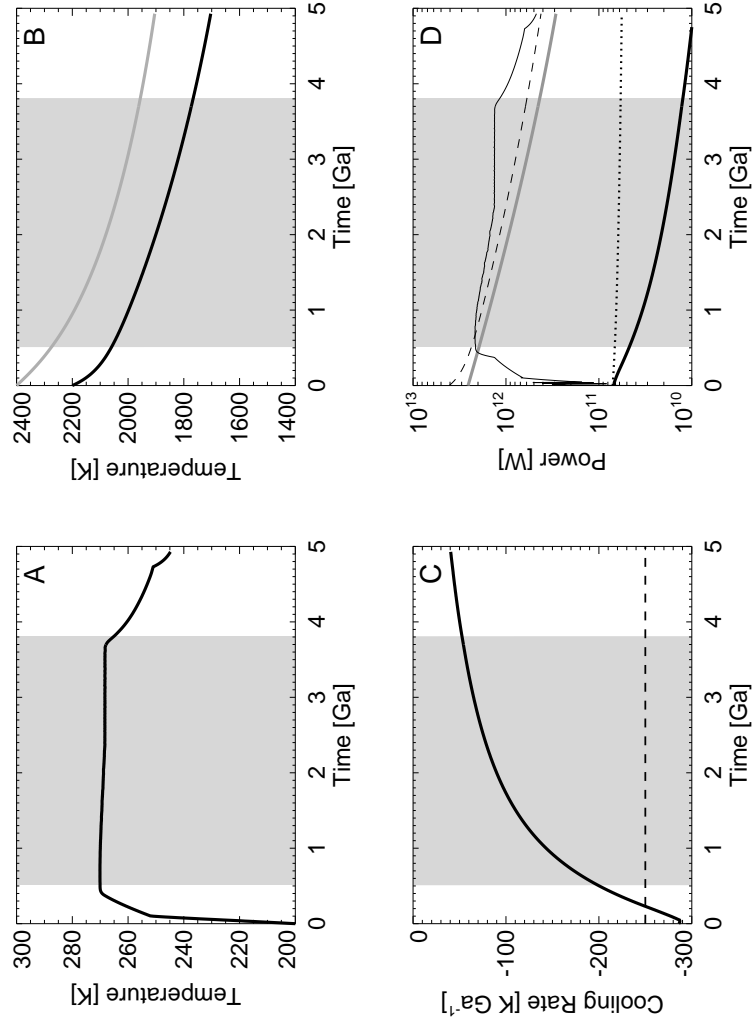


Figure 3.4: The thermal history of Ganymede including Laplace-like resonance passage with $Q_J = 3 \times 10^5$ and assuming a dry silicate rheology with a 1 mm grain size. Initial temperatures are as in Fig. 3.1 and 3.2. **A.** Temperatures in the ice shell. **B.** Temperatures in the core (grey line) and silicate mantle (black line). **C.** The core cooling rate. The thin dashed line indicates the cooling rate required for thermal convection to occur. **D.** Power out of the core (heavy black line), silicate mantle (thin dashed line), and ice shell (thin black line). The radiogenic heat production is shown as the heavy grey line and the power required to drive a core dynamo (Eq. 3.4) is indicated with a dotted line. In each panel, the grey shaded region indicates the period of Laplace-like resonance passage.

dynamo.

Figure 3.4d shows the power transported out of the ice shell (thin, solid line), silicate mantle (thin, dashed line), and metallic core (thick, black line) respectively as a function of time. The power out of the silicates closely follows the radiogenic heat production, illustrating the insignificance of tidal dissipation in the silicates. The power out of the ice shell initially follows the radiogenic heat production but is eventually dominated by tidal dissipation in the ice shell, which exceeds radiogenic heat production after ~ 2.2 Ga. The core power is initially near the required dynamo power (again shown as a dotted line), but it decreases rapidly as the simulation progresses. While thermal convection in the core can occur early in the simulation (Fig. 3.4c), at no point during the simulation does the core power exceed the requirement for driving a dynamo. This result is independent of our assumptions about the ohmic dissipation. Therefore, the simulation described here does not predict a present-day magnetic field to be present at Ganymede.

Clearly, tidal dissipation does not affect the thermal history of Ganymede's mantle or core (Fig. 3.4 is nearly identical to Fig. 3.1), and thus cannot expand the range of conditions under which magnetic field production is achievable. This result is not surprising considering the tidal dissipation in the silicates (Fig. 3.3) is two orders of magnitude less than the radiogenic energy released. Despite the low magnitude of the tidal dissipation in this simulation, a number of mechanisms could increase the magnitude of the dissipation and these must be explored before the tidal heating mechanism for production of Ganymede's magnetic field can be rejected. All of the simulations described below assume a 10% sulfur mass fraction in the core; however, the conclusions apply to the full range of sulfur concentrations for which iron condenses at the top of the core.

3.4.1 Variation in the Silicate Rheology

Fundamentally, tidal dissipation in Ganymede’s silicate mantle is low because of the high effective viscosity of the silicates. The magnitude of tidal deformation is maximized when the Maxwell time of the material ($T_M = \eta_e/\mu$, where η_e is the effective viscosity and μ is the shear modulus) is close to the tidal forcing period. Using the rheological parameters for dislocation creep in Table 2.1, a typical convective stress of 0.01 MPa, and a typical silicate temperature of 1800 K, T_M is ~ 10 yrs. In contrast, the orbital period of Ganymede is ~ 7 days, thus minimal tidal dissipation occurs. Increasing the magnitude of tidal dissipation in the silicates therefore requires significantly lower silicate effective viscosities. For a typical convective scaling, the heat flux goes as $F_{conv} \propto 1/\eta_e^{1/3}$. However, for a Maxwell rheology the tidal dissipation goes as $F_{tidal} \propto 1/\eta_e$. Thus any increase in temperature (or decrease in viscosity) increases the tidal dissipation more than it increases the heat flux, providing the potential for thermal runaway to occur.

Several factors can contribute to decreasing the effective silicate viscosity. The grain size of the silicates is poorly constrained, with plausible values ranging from 100 μm to 10 cm (Karato, 1984). The choice of grain size can potentially have a profound effect on the model results. Not only do changes in the grain size affect the calculated viscosity (Eq. 2.14), but they can also change the dominant rheological flow mechanism: diffusion creep dominates if grains are small, dislocation creep dominates if grains are large. Such a change fundamentally alters the rate at which silicate cooling occurs. Additionally, we have already seen that the composition of Ganymede’s mantle strongly affects its thermal history. Olivine is the primary constituent of Earth’s mantle and its rheology has been widely studied. It is therefore a reasonable choice for modeling the rheology of Ganymede’s mantle. Furthermore, Ganymede’s high degree of differentiation (Anderson et al., 1996) is consistent with a dehydrated silicate composition (Kuskov and Kronrod, 2001; Sohl et al., 2002) suggesting dry rheologies are likely. Despite this, the uncertainty in the composition

and rheology of Ganymede’s silicates warrants an evaluation of whether use of an alternate rheology can increase tidal dissipation.

We performed a suite of simulations that varied the silicate grain size for both dry and wet olivine rheologies. These simulations use a core sulfur mass fraction of 10%. For the dry rheology, decreasing the grain size from 1 mm to 100 μm permits diffusion creep to dominate the flow, decreasing the effective viscosity and causing more rapid cooling to occur. The resulting thermal history is similar to that for a wet olivine rheology with a 1 mm grain size (Fig. 3.2). For grain sizes larger than or equal to 1 mm dislocation creep dominates the flow and silicate temperatures do not differ noticeably from the simulation described in section 3.4 (Fig. 3.4). For a wet rheology, dislocation creep dominates at grain sizes of 1 mm or greater and results in a thermal history essential identical to that shown in Fig. 3.2. Diffusion creep dominates at grain sizes of 100 μm , and results in even more rapid cooling of the silicate layer. However, while grain size and rheology affect the thermal history of the satellite, no combination of parameters permitted significantly increased tidal dissipation or triggered a thermal runaway in the silicate mantle. The thermal histories are therefore essentially identical to those described in Figs. 3.1 and Fig. 3.2. Our basic conclusion, that tidal dissipation in Ganymede’s silicate mantle does not enable magnetic field generation, is therefore robust to variations in grain size and assumed rheology.

3.4.2 Variations in Q_J

As described in Chapter 2, the tidal dissipation factor of Jupiter (Q_J) is a poorly constrained quantity. We must therefore consider the degree to which the above results depend on Q_J . We performed a series of simulations identical to the ones above but with lower values of Q_J . While using low values of Q_J that are constant over the history of the solar system is physically unrealistic, here we seek only to test the sensitivity of our model results to its assumed value.

Decreasing Q_J produces greater maximum tidal dissipation within Ganymede's silicate layer (Fig. 3.5). For $Q_J = 10^4$ the maximum tidal dissipation is 3.1×10^{11} W in the case of a dry rheology and 5.9×10^{11} W in the case of a wet rheology. The decrease in the magnitude of the maximum tidal dissipation with increasing Q_J is nonlinear, and differs for the wet and dry rheologies. Despite the relatively high values of tidal dissipation that can occur at low Q_J , tidal dissipation remains insufficient to produce a thermal runaway in the silicate mantle. Thus, the conclusion that resonance passage has not contributed to the production of the current-day magnetic field (section 3.4) is independent of the assumed value of Q_J . These results are again independent of the assumptions of grain size and composition of the silicates as described above (section 3.4.1).

3.4.3 The Influence of the Ice Shell

The structure of Ganymede's ice shell can strongly influence the magnitude of tidal dissipation in Ganymede's silicates and thus might play an essential role in driving Ganymede's magnetic field. Showman and Malhotra (1997) showed that, for values of $Q_3/Q_J \lesssim 10^{-3}$, the total power dissipated in the satellite saturates and is approximately independent of Q_3/Q_J (see their Fig. 7). However, the partitioning of the available tidal energy between the satellite's layers depends on each layer's physical parameters. Thus, if the ice is dissipative (i.e. it has a low viscosity) the majority of the tidal dissipation will occur in the ice. In contrast, if the ice is not dissipative (i.e. it has a high viscosity) the eccentricity is large and more tidal dissipation is forced into the silicate mantle. Here we address the question of whether the physical conditions of Ganymede's ice shell (i.e. grain size and total volume) might allow greater tidal dissipation to occur in Ganymede's silicates.

For the structure of the ice shell to influence the magnitude of tidal dissipation in the silicates, the range of Q_3/Q_J must be low enough that the total dissipation of tidal energy remains constant as we change the ice shell's physical parameters. Oth-

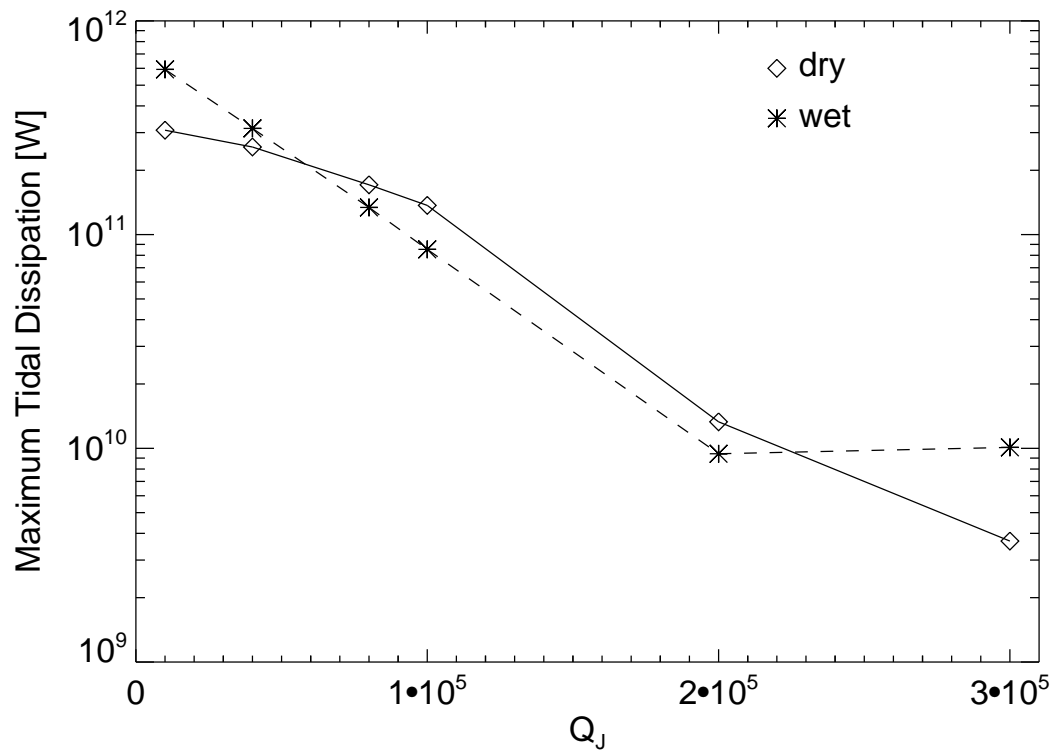


Figure 3.5: Maximum tidal dissipation in the silicate mantle as a function of the tidal dissipation factor of Jupiter for a dry (diamonds) and wet (asterisks) rheology. The silicate grain size is 1 mm. The maximum tidal dissipation varies nonlinearly with the tidal dissipation factor.

erwise, a change in ice shell parameters simply decreases the total tidal dissipation and the dissipation in the silicate layer will remain low. Figure 3.6a shows the total tidal dissipation during resonance passage ($\dot{E}_{sil} + \dot{E}_I$) as a function of the grain size of the ice shell. In these simulations $Q_J = 10^5$. Here, grain size acts as a proxy for Q_3 , where large grain sizes correspond to high Q_3 and small grain sizes to low Q_3 . Also shown is Ganymede’s average eccentricity (e_3) as a function of ice grain size. For grain sizes larger than ~ 1 mm the total power dissipated in the satellite is not constant but decreases by up to an order of magnitude at the largest grain sizes. The decrease in total tidal dissipation with increasing ice grain size fundamentally limits the magnitude of the tidal deformation that can be “forced” into the silicates.

Despite this limitation, Fig. 3.6b illustrates that both the absolute magnitude of the power dissipated in the silicates, and the magnitude relative to the total power dissipated in the satellite, increases as a function of ice grain size. In these simulations, only the ice grain size has been changed; the silicate grain size was held constant at 1 mm. At small ice grain sizes where ice is strongly dissipative, very little dissipation occurs in the silicate layer relative to the ice layer. However, as the ice grain size increases and the ice becomes less dissipative relatively more dissipation occurs in the silicates until, at very large grain sizes, essentially all of the tidal dissipation occurs in the silicates. Thus, in spite of the order of magnitude decrease in the total tidal dissipation, an order of magnitude more tidal dissipation occurs in the silicate layer when the ice has a large grain size (100 mm) than when the ice layer has a moderate grain size (1 mm, the nominal case).

The grain size of the ice is not the only parameter that affects the magnitude of tidal dissipation in the silicates. Extensive melting of the ice shell can force significantly more dissipation to occur in the silicate mantle. Figure 3.6c illustrates this effect. Large oceans result in less available ice in which tidal dissipation can occur. When nearly all the ice has melted the majority of the tidal dissipation *must* occur in the silicate mantle. We note that a cold, non-dissipative, ocean-free ice shell

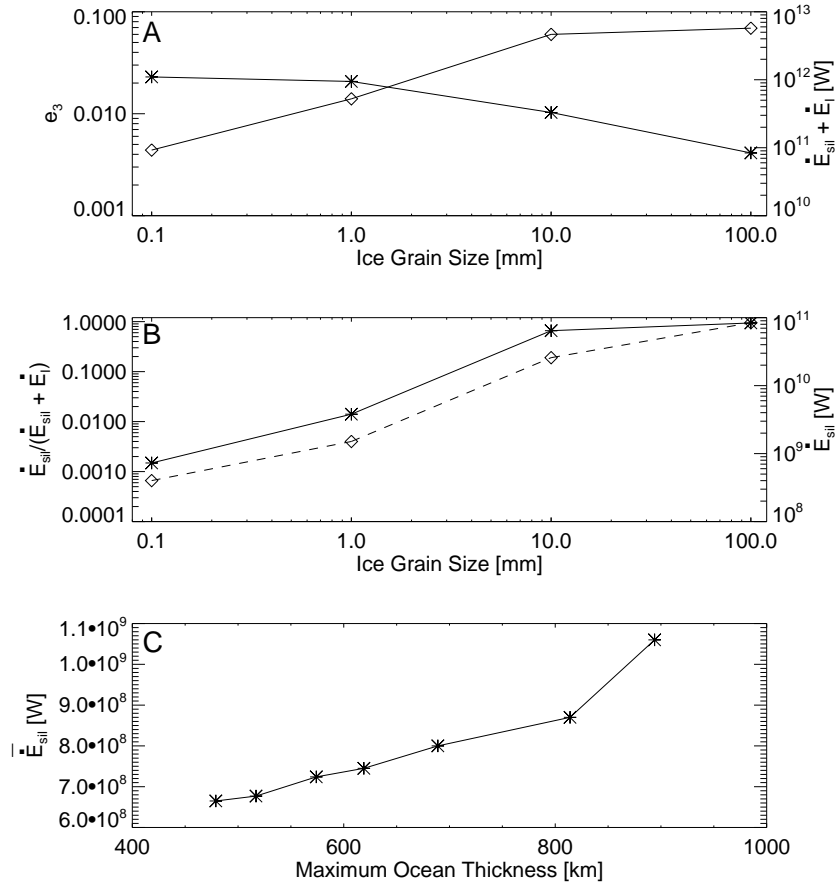


Figure 3.6: **A.** The average eccentricity of Ganymede (e_3) during resonance passage (diamonds) and the average total tidal dissipation in the satellite ($\dot{E}_{sil} + \dot{E}_I$ in W) during resonance passage (asterisks) as a function of ice grain size. Large ice grain sizes increase Q_3 , decreasing the total tidal dissipation and increasing the satellites eccentricity. **B.** The magnitude of the tidal dissipation in the silicates (\dot{E}_{sil} , solid line) and the magnitude relative to the tidal dissipation in the whole satellite ($\dot{E}_{sil} + \dot{E}_I$, dashed line) as a function of ice grain size. Despite the decrease in total tidal dissipation within the satellite (see A), the magnitude of tidal dissipation in the silicates increases as the ice becomes less dissipative. **C.** Average tidal dissipation (\dot{E}_{sil} in W) in the silicates during the period of resonance passage as a function of maximum ocean thickness. For an ocean thickness of ~ 900 km complete melting of the high pressure ice occurs. The ocean thickness was varied by modifying the thermal adiabat assumed for Ganymede's ocean. The ice grain size was 1 mm in each simulation.

would allow even greater dissipation in the silicates (Tobie et al., 2005b); however, such a cold ice layer cannot be maintained over a warm silicate mantle. The extent of the ice melting in these simulations was varied by modifying the parameters of the ocean adiabat.

Clearly, the ideal ice-shell structure for increasing tidal dissipation in the silicates requires an expansive ocean and a large grain size in the residual ice. To investigate whether the tidal dissipation produced in such a scenario can trigger a thermal runaway in the silicates we simulated Ganymede’s thermal history with a 10 cm ice grain size, an ocean adiabat that increases rapidly with depth, and a low Q_J of 4×10^4 . The steep ocean adiabat and the low Q_J value permit complete melting of Ganymede’s high pressure ice. Both dry and wet silicate rheologies were investigated. During resonance passage the magnitude of tidal dissipation in the silicates reached values as high as 3×10^{11} W (dry rheology) and 7×10^{11} W (wet rheology), but such dissipation again remained incapable of causing a thermal runaway. Thus, even the most favorable ice shell conditions cannot force enough tidal dissipation to occur in the silicates to allow a thermal runaway that can prevent the core from cooling during resonance passage.

3.4.4 Partial Melt

The temperature of Ganymede’s silicate mantle shown in Figs. 3.1-3.4 are in excess of the solidus temperature of olivine at the pressures typical of Ganymede’s silicate layer (~ 1650 K (Takahashi, 1990; Breuer and Spohn, 2006)). We therefore expect partial melting to occur. Partial melting has two primary effects. First, melting of the rocky material absorbs latent heat from the system, buffering temperature increases in a manner analogous to ocean formation in the ice shell (Fig. 3.4a). Second, the presence of even a few percent partial melt can have a profound effect on the rheology, decreasing the effective viscosity by an order of magnitude or more (Kohlstedt and Zimmerman, 1996; Jin et al., 1994). Because the rate of tidal

dissipation is strongly dependent on the viscosity of the material, the decrease in silicate viscosity associated with partial melting may allow increased dissipation in the silicates. If the magnitude of the dissipation is large enough, mantle temperatures may be maintained at the melting temperature throughout resonance passage. Rapid silicate and core cooling would then follow resonance escape.

To evaluate whether the inclusion of partial melt helps enable magnetic field generation we performed a suite of simulations that account for the effect of latent heating on the thermal balance of the silicates. In these simulations, if temperatures in the silicate mantle exceeds 1652 K (the solidus temperature at a pressure of 2 GPa) we modify the thermal balance (Eq. 2.2) to include the latent heat of melting as follows

$$\frac{4}{3}\pi(R_{sil}^3 - R_c^3)\rho_{sil}H + 4\pi R_c^2 F_c + \dot{E}_{sil} = 4\pi R_{sil}^2 F_{sil} + \left[M_{melt} \frac{df}{dT} L_{sil} + \frac{4}{3}\pi(R_{sil}^3 - R_c^3)\rho_{sil}c_{p,sil} \right] \frac{dT_{sil}}{dt}, \quad (3.10)$$

where M_{melt} is the mass of the melt region, df/dT is the increase in melt fraction per Kelvin, and L_{sil} is the latent heat of olivine. The mass of the melt region, M_{melt} , is determined by equating the olivine solidus curve ($T_{sol} = 1409. + 134.2P - 6.581P^2 + 0.1054P^3$, where P is the pressure in GPa (Takahashi, 1990; Breuer and Spohn, 2006)) to a mantle adiabat of the form $dT/dP = (\alpha_{sil}T)/(\rho_{sil}c_{p,sil})$ and solving for the depth at which the curves intersect, assuming hydrostatic equilibrium. The resulting melt region volume is then converted to a mass assuming a constant density mantle. The change in melt fraction with temperature, df/dT , is determined from the olivine solidus and liquidus curves assuming a simple linear relationship between melt fraction and temperature (Jaques and Green, 1980). In addition, we reduce the silicate viscosity calculated from Eq. 2.14 by a factor of 10 if partial melt is present.

Once the melt fraction exceeds 3%, we assume that melt is extracted from the mantle and erupted at the base of the ice shell. We make the simplifying assumption

at this point that the energy balance of the silicates is not dominated by changes in temperature (which is now held fixed) but by the production and removal of melt. In addition, the eruption of melt at the base of the ice shell alters the energy balance of the ice layer. A more complex thermal balance, such as that suggested by Moore (2001), is beyond the immediate scope of this feasibility study.

Figure 3.7 shows the temperature of the silicate mantle and metallic core, and the core cooling rate as a function of time for a simulation that includes partial melting. The simulation utilizes a wet silicate rheology with a grain size of 1 mm. Additionally, we use a low, constant Q_J of 4×10^4 to test the maximum plausible rate of tidal dissipation. We initialize the simulation with low silicate temperatures (1600 K) to avoid *a priori* assumptions regarding initial quantities of partial melt. Silicate temperatures initially rise rapidly due to radiogenic heating until reaching a temperature of 1652 K, at which point partial melting slows the increase in silicate temperatures. The melt fraction quickly reaches 3% and the silicate temperatures saturate, with melt production and removal dominating the thermal balance. After 1.4 Ga the melt fraction falls below 3% and the silicate mantle begins to cool. However, this cooling is still reduced by the latent heat of freezing of the silicate melt. The buffering of the silicate cooling briefly keeps silicate temperatures above the values expected if they were in quasiequilibrium with radiogenic heating. Thus, once all the melt has solidified, the silicates cool rapidly to come back into quasiequilibrium with radiogenic heat. During this brief cooling period silicate cooling rates can reach values as high as 200 K Ga^{-1} . This rapid cooling occurs *in spite* of the satellite being in the Laplace-like resonance. Thus, tidal heating again is unable to prevent core cooling.

The insufficient buffering of core cooling is further illustrated in Fig. 3.7b and 3.7c. The core cooling rate is initially quite high and core temperatures drop rapidly. This is due to the large difference between the initial core and mantle temperatures. After 0.7 Ga the core cooling rate drops below the requirement for thermal convec-

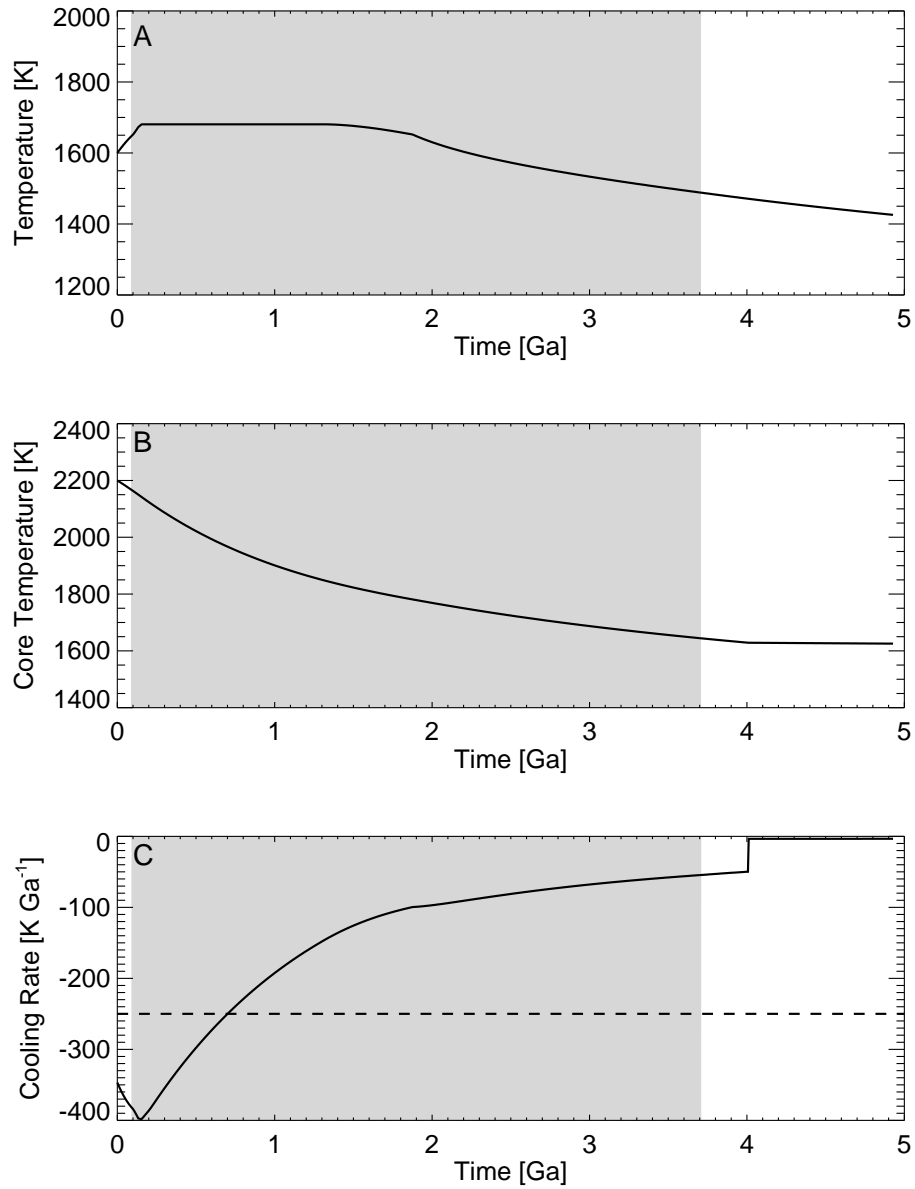


Figure 3.7: Temperatures in Ganymede’s silicate mantle (**A**) and core (**B**), and the core cooling rate (**C**) as a function of time for a simulation that includes partial melting in the silicate mantle. The simulation utilizes a wet rheology with a grain size of 1 mm. Initial silicate and core temperatures were 1600 K and 2200 K, respectively. $Q_J = 4 \times 10^4$ for the entire simulation. The shaded region indicates the period of Laplace-like resonance passage.

tion and never again attains such large values. At 4.1 Ga inner core growth begins and the core cooling rate approaches zero. Magnetic field production by chemical convection is possible during this period, but is subject to the same constraints described in section 3.3. Figure 3.7 clearly illustrates that, like the simulations described above, resonance passage is unable to modify the thermal history of the metallic core or silicate mantle when partial melt is included.

3.5 The Timing of Core Formation

All of the simulations described above assume that Ganymede differentiated early and that its silicate mantle and metallic core are initially hot. However, several authors have shown that metallic core formation in a large icy satellite can take an additional 1 to 2 Ga after initial differentiation of ice and rock (Grasset et al., 2000; Schubert et al., 2004). The simulations described above can therefore be considered an end member scenario in which complete differentiation occurs rapidly. In light of the stringent compositional requirements on chemical convection and the failure of tidal dissipation to delay or prolong thermal convection in the metallic core, late core formation may provide a mechanism by which magnetic field production is delayed until the present day. If the core is young, it may still be cooling rapidly enough for thermal convection to drive a magnetic dynamo.

As a preliminary test of the feasibility of dynamo generation by a young core we performed a series of simulations in which the radiogenic heating was initialized as if 1 or 2 Ga of decay had already occurred. Additionally, initial silicate mantle and metallic core temperatures were reduced to be consistent with the reduced radiogenic values. With these modifications to the initial conditions, the resulting model effectively simulated cooling of the metallic core beginning after 1 to 2 Ga of radiogenic heating has already occurred. For simplicity these simulations did not include the partial melting described in section 3.4.4.

As with the resonance passage models, these simulations failed to produce cooling

rates consistent with a present day thermally generated dynamo. For a simulation in which core formation occurs 1 Ga after ice-rock differentiation the maximum core cooling rate exceeds the requirement for thermal convection ($\sim 250 \text{ K Ga}^{-1}$) for the first 200 Ma. However, cooling rates quickly decline, reaching a value of only $\sim 50 \text{ K Ga}^{-1}$ at the present day, well short of the requirement for thermal convection. Maximum cooling rates are further reduced in the simulation in which core formation occurs after 2 Ga. In this simulation, cooling rates never exceed the basic requirement for thermal convection. The reduced cooling rates produced by these simulations can be attributed to the cooler initial silicate temperatures used, which lead to decreased silicate and core cooling rates relative to the simulations described above. Magnetic field generation by compositional convection is possible in these simulations but is again subject to the requirements described in section 3.3.

Our simplified modeling suggests late core formation cannot explain the existence of Ganymede's magnetic field. However, we have neglected the process of core formation itself which may substantially modify the thermal and physical conditions of both the metallic core and silicate mantle. If, for example, core formation produced a metallic core significantly hotter than the mantle above (c.f. Solomatov and Ke, 2007), sustained thermal convection and dynamo action may occur easily. Thus, detailed modeling of metallic core formation is required to fully assess the potential for magnetic field production in a late-formed core. Late core formation therefore remains a potential mechanism for enabling present day dynamo action.

3.6 Conclusions

We have shown that production of Ganymede's magnetic field by secular cooling and chemical convection requires that a very specific set of conditions be met: the mass fraction of sulfur in the core must be low (or alternatively very high), the core must have formed hot, and the silicate mantle must be able to cool rapidly (i.e. it

must have a viscosity consistent with wet olivine). If any of these criterion are not met, magnetic field production fails. These results contrast with those of previous workers who find that compositional convection can drive a core dynamo under a broad range of conditions (Hauck et al., 2006).

Because of the stringent conditions required for operation of a chemically driven dynamo, we investigated whether a period of tidal dissipation in Ganymede's past might enable production of the current magnetic field under a broader range of conditions. We have shown here, however, that passage through a Laplace-like resonance is insufficient to cause substantial tidal dissipation within Ganymede's silicate mantle. The cooling history of Ganymede's core is therefore unaffected by the satellite's orbital history and the presence of Ganymede's magnetic field cannot be attributed to resonance passage as suggested by previous authors (Stevenson, 1996; Showman et al., 1997). Modifying the rheology and grain size of the silicates, decreasing the value of Q_J , varying the structure of the ice shell, and allowing for partial melting all modify the thermal history of the satellite. However, no simulations were found that broaden the conditions under which magnetic field generation is predicted. The simulations described above examine passage through the Laplace-like resonance that most strongly pumps Ganymede's eccentricity ($\omega_1/\omega_2 = 2$); thus, other orbital histories that pass through weaker Laplace-like resonances ($\omega_1/\omega_2 = 3/2$ or $1/2$) are also unlikely to enable Ganymede's magnetic field.

Considering the difficulty of explaining Ganymede's magnetic field, is there another alternative? One possibility is that Ganymede differentiated late in its history. The discovery that Callisto may be only partially differentiated (Anderson et al., 1997b) has lead to the development of satellite formation models that allow for slow, cool satellite accretion that avoids early differentiation (e.g. Canup and Ward, 2002). While these models explain Callisto's partially differentiated state, they may also require that Ganymede formed partially differentiated (though see Mosqueira and Estrada (2003)). Ganymede's highly condensed current state suggests that differ-

entiation may have occurred later, perhaps during passage through one or more of the Laplace-like resonances described above. In such a scenario Ganymede's metallic core may have formed late in its history, and might therefore still be cooling convectively. The thermal modeling described above suggests that such thermal convection is only possible if the core formed hot relative to the silicates above it, and even then convection will only occur within the first 1 Ga of core formation. Such late core formation is marginally consistent with age of Ganymede's grooved terrain (thought to be 1 to 2 Ga (Zahnle et al., 2003)), which may have formed during the same differentiation event. Late core formation may therefore provide an alternative mechanism for production of Ganymede's magnetic field.

CHAPTER 4

THE FORMATION OF GANYMEDE'S GROOVED TERRAIN

The material in this chapter has been published in the journal Icarus: Bland, M. T. and A.P. Showman (2007). The formation of Ganymede's grooved terrain: Numerical modeling of extensional necking instabilities. Icarus, 189, 439-456.

4.1 Introduction

Covering nearly two-thirds of the satellite, Ganymede's grooved terrain is one of the most tectonically deformed surfaces in the solar system. First clearly resolved in Voyager images, the grooved terrain consists of series of roughly parallel, periodically spaced ridges and troughs (Fig. 4.1a) (Smith et al., 1979a,b). Photoclinometric profiles indicate that typical groove sets have a periodicity of 3 to 10 km and amplitudes of 300 to 400 m (Squyres, 1981). Rather than having steep scarps typical of fractures or faults, grooves are undulatory in nature with root-mean-square slopes near 6° and maximum slopes no larger than 20° (Squyres, 1981). Grooves tend to appear in large polygonal swaths 100s to 1000s of km long and 10 to 100 km wide. While grooves generally have consistent spacing and orientation within an individual groove swath, large regions of grooved terrain contain many such swaths, each crosscutting the others at a different orientation.

Digital terrain models of Uruk Sulcus confirm Voyager observations, indicating wavelengths of 2-6 km and amplitudes up to 500 m within the grooved terrain (Giese et al., 1998). However, high-resolution images from the Galileo spacecraft reveal that the grooved terrain is intensely tectonized at scales below the Voyager resolution limit (Fig. 4.1b) (Pappalardo et al., 1998). Fourier analysis of topography

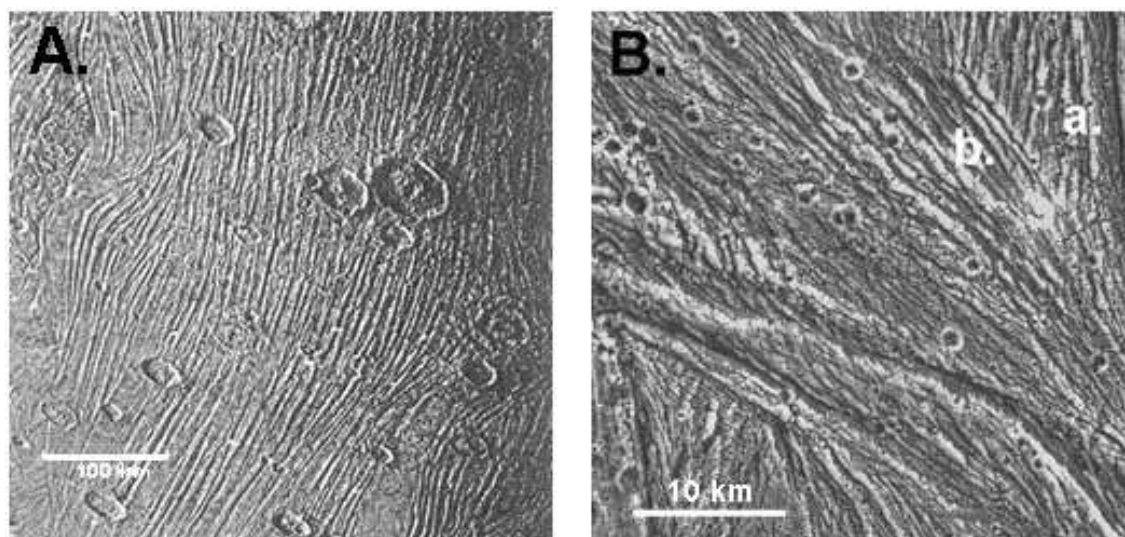


Figure 4.1: **A.** Voyager image of grooved terrain near the south pole of Ganymede. Grooves have a periodic spacing of ~ 10 km. Illumination is from the right. After Squyres (1982). **B.** High resolution Galileo image of grooves in the Uruk Sulcus region (PIA00276, Courtesy NASA/JPL-Caltech). Both Voyager-scale (~ 10 km wavelength) grooves and finer Galileo-scale (~ 1 km wavelength) grooves are visible. At high resolution individual groove swaths (labeled ‘a’ and ‘b’) are seen to cross-cut and partially disrupt one another implying that groove formation can tectonically resurface preexisting terrain. Note that this high-resolution deformation is at a finer scale than the deformation modeled here. Illumination is from the south (bottom). After Pappalardo et al. (2004).

in the Uruk Sulcus region indicates that short wavelength (~ 1 km) deformation is superimposed upon the regional-scale grooves seen in Voyager images (Patel et al., 1999). This small-scale deformation is lower in amplitude than the long-wavelength, Voyager-scale grooves, with heights of ~ 200 m (Pappalardo et al., 1998).

Based on the lack of identifiable contractional features on Ganymede’s surface, most authors accept that the grooved terrain formed by extensional processes during an epoch of global expansion (Squyres, 1982; Golombek, 1982; Pappalardo et al., 1998). As described in Chapter 2, the exact cause and magnitude of this expansion remains undetermined. Assuming the grooved terrain to be old, Squyres (1980) suggested that expansion resulted from internal phase changes during differentiation of

the satellite. Such volume expansion would increase Ganymede's surface area by 6-7% (Squyres, 1980). A reanalysis of cratering fluxes in the Jovian system, however, supports the idea that the grooved terrain formed within the last 2 Ga (Zahnle et al., 2003). While there is much uncertainty in this age constraint, it suggests that expansion could have occurred during a period of tidal heating, after differentiation had ceased, as the Galilean system evolved through a series of Laplace-like resonances (Showman and Malhotra, 1997). The combination of phase transitions and thermal expansion caused by tidal heating would increase Ganymede's surface area by up to 1-2% globally (Showman et al., 1997, Chapter 2). Alternatively, if Ganymede entered resonance in a partially differentiated state (like that of modern Callisto), tidal heating may have induced complete differentiation. The combination of tidal heating and differentiation can produce larger global strains than either mechanism alone. Observations of typical strains involved in the formation of specific groove types indicate that the global change in Ganymede's circumference was large: at least 1.4% but possibly as high as 5.9%, implying increases in surface area of 2.8% to 12.1% (Collins, 2006, 2007). These observations support the tidally induced differentiation mechanism for Ganymede's global expansion.

Despite relatively small values of global strain, significant extensional strain has occurred locally on Ganymede. Reconstruction of presumed tilt-block faulting in Ganymede's Uruk Sulcus region indicates that local strains exceeded 50% at the time of groove formation (Collins et al., 1998b). Furthermore, analysis of strained craters, mostly in dark terrain, shows that rift zones associated with these craters extended by as much as 180% (Pappalardo and Collins, 2005). The apparent conflicting evidence for relatively small values of global strain, but high values of local strain was addressed by Collins (2006) who found that, while the majority of low-relief groove terrain has experienced only a few percent strain, high-relief grooves typically experienced 25% to 50% strain. While these densely spaced, high-relief grooves tend to be thought of as "typical" grooved terrain, they actually represent only \sim 2-7%

of the length of a typical great circle transect of the surface. In contrast, more subdued, low-relief grooves and swaths of smooth bright terrain make up $\sim 45\%$ of a great-circle surface transect (Collins, 2006). Thus, values of localized strain between 25% and 100% in regions of high-relief grooves do not violate global strain estimates of order 10% because the majority of surface has undergone only 1%-3% strain. High strains are therefore likely to have been common in regions of high-density, high-relief grooves.

The exact mechanism by which grooves formed remains uncertain. Early work based on Voyager data proposed that the large-scale grooves were extensional fractures or horst-and-graben that were softened by viscous relaxation and mass wasting (Squyres, 1982; Golombek, 1982; Parmentier et al., 1982). While Galileo images indicate that at least some of the structures in the grooved terrain are consistent with horst-and-graben (Pappalardo et al., 1998), these models never adequately explained the strong periodicity of groove spacing within the bright terrain or the undulatory nature of many grooves. To account for these characteristics, Fink and Fletcher (1981) proposed that Ganymede's grooves resulted from the formation of periodic necking instabilities during unstable extension of the icy lithosphere.

The necking instability mechanism models Ganymede's lithosphere as a brittle surface layer underlain by a viscous half-space. When extended, any perturbation in the thickness of the brittle layer may amplify, deforming the lithosphere into a series of periodic pinches and swells (Fig. 4.2). This mechanism was employed by Fletcher and Hallet (1983) to explain the regular spacing of structures in the Basin and Range province of the western United States. Their semi-analytical, linearized, infinitesimal-strain model utilizes a perturbation analysis wherein a perturbing flow is added to uniform, horizontal extension. The velocity field of each Fourier component of the perturbing flow is calculated separately, allowing the amplitude growth of each component to be independently determined. In general, one Fourier component of the perturbation dominates the flow, growing significantly faster than

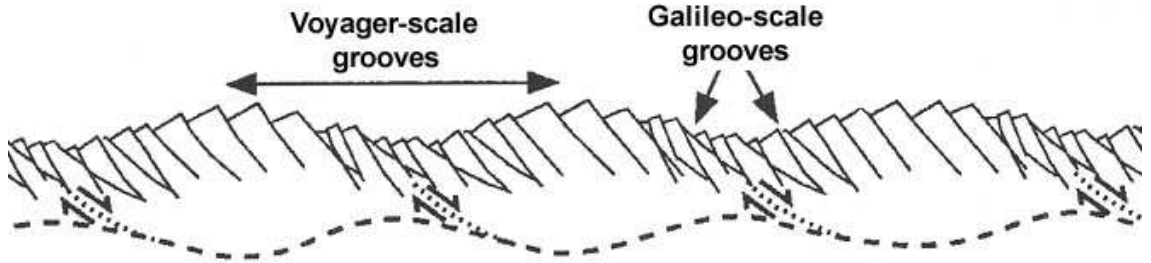


Figure 4.2: Cartoon of pinch-and-swell morphology caused by the formation of a periodic necking instability. Small-scale tilt-block normal faulting (Galileo-scale grooves) accommodates the formation of large-scale ridges and troughs (Voyager-scale grooves). Modified from Pappalardo et al. (1998).

the other components and producing strongly periodic topography. This dominant wavelength is generally three to four times the thickness of the deforming layer.

Assuming a constant growth rate (defined below) and background strain rate, the amplitude of each Fourier component of the initial perturbation changes exponentially with the form

$$\mathcal{A} = \mathcal{A}_o \exp[(q - 1)\dot{\epsilon}t], \quad (4.1)$$

where \mathcal{A} is the amplitude of the topography, \mathcal{A}_o is the amplitude of the initial perturbation, q is the exponential growth rate of the Fourier component in question, and $\dot{\epsilon}t$ is the strain. The growth rate q determines the degree to which instability growth occurs. If $q < 1$, no instability growth occurs and the perturbation decays with time. At $q = 1$, the growth rate of the perturbation exactly matches the rate of lithospheric thinning and topographic amplitudes remain constant. For $q > 1$ the initial perturbation amplifies. Fletcher and Hallet (1983) and Herrick and Stevenson (1990), assuming 10% strain and amplifications ($\mathcal{A}/\mathcal{A}_o$) of 10-100, suggested exponential growth rates (q) of ~ 40 are needed to produce instability growth consistent with large scale tectonic structures. Allowing for larger values of strain, Collins et al. (1998b) found that growth rates as low as 8-13 are capable of producing ridges

and troughs 250-500 m in amplitude.

Herrick and Stevenson (1990) applied the Fletcher and Hallet (1983) model to Ganymede and found that the satellite's high surface gravity and warm temperatures prevented instability growth large enough ($q > 40$) to allow the formation of grooved terrain. This model was later reexamined by Dombard and McKinnon (2001) who incorporated the grain-boundary-sliding (GBS) flow mechanism for ice and lower surface temperatures due to a dimmer young sun and a higher surface albedo at the time of groove formation and found that, in cases where thermal gradients exceeded 35 K km^{-1} (corresponding to a heat flow of $\sim 80 \text{ mW m}^{-2}$), exponential growth rates and dominant wavelengths of instabilities *are* consistent with ($q > 40$) grooved terrain.

Despite the success of Dombard and McKinnon (2001), the linear stability model suffers from several limitations. The analysis assumes infinitesimal strain and thus treats only the initiation of an instability. Thus, predicting the amplitude of grooves that result from instability growth requires an extrapolation from infinitesimal to finite strain. We expect, however, that nonlinear effects become important as strains become large. If, for example, instability growth creates lateral variations in the thickness of the lithosphere comparable to the lithospheric thickness itself, order unity lateral variations in the deviatoric tensile stress will exist. This causes the system to behave nonlinearly. Numerical models of finite-amplitude compressional folding support the prediction of nonlinear behavior at large strains. These models indicate that growth rates decrease at strains larger than $\sim 10\%$, in some cases approaching $q = 1$, suggesting a saturation limit to the amount of fold amplification that can occur under finite strain (Zuber and Parmentier, 1996). Furthermore, because the linear stability analysis treats the growth of each Fourier component of the perturbation separately, the Fourier components cannot interact with one another, an effect that may become important at large strains. Because of these limitations, the applicability of necking instabilities to groove formation remains

unresolved.

Nonlinear modeling of extensional necking instabilities can inform the debate about the mechanism for bright terrain formation (and the removal of older, pre-existing craters). Cryovolcanic (Parmentier et al., 1982; Allison and Clifford, 1987) and tectonic (Head et al., 1997) resurfacing mechanisms have been proposed, and both probably play important roles. Digital elevation models indicate that smooth, low-lying regions exist on Ganymede, suggesting infilling by a low-viscosity cryovolcanic material (Schenk et al., 2001). Liquid water can be pumped to the surface from depths of up to 10 km by topographically induced, subsurface pressure gradients (Showman et al., 2004). This self-limiting pumping mechanism fills low-standing regions with cryovolcanic material while explaining the observed lack of large-scale cryovolcanic flows across high-standing regions (Showman et al., 2004). However, some regions of Ganymede's terrain have been predominately resurfaced by tectonic, rather than cryovolcanic, processes (Head et al., 1997). Observations of truncated groove sets within the grooved terrain support this hypothesis. In these regions, young groove sets cross-cut and partially or completely destroyed structures in stratigraphically older groove sets (Fig. 4.1b) (Head et al., 1997). Furthermore, tectonically disrupted craters indicate that resurfacing should occur in cases where strains exceed 15% (Pappalardo and Collins, 2005). Despite these observations, it is not obvious that extensional tectonics can completely destroy preexisting structures. Elucidating how extensional instabilities respond to finite surface topography and large strains is therefore essential to understanding how Ganymede's grooved terrain was formed.

4.2 The Finite-Element Model

Using the two dimensional, finite-element model TEKTON (version 2.3) in plane strain (Melosh and Raefsky, 1980), we simulate the extension of an icy lithosphere to examine the growth of periodic necking instabilities over a range of strain rates

and temperature gradients. Our model incorporates the elastic, viscous, and plastic flow properties of ice. TEKTON solves the equations governing the equilibrium between internal stresses and external (applied) forces. These forces are related to the nodal displacement of each element by the Young's modulus, E , and Poisson ratio, ν . We model the elastic properties of ice using a Young's modulus of 10^{10} Pa and a Poisson ratio of 0.25. These values are appropriate for clean, unfractured water ice at terrestrial surface temperatures (Gammon et al., 1983). The sensitivity of our results to variations in the Young's modulus are described in section 4.14. The density of ice is assumed to be 980 kg m^{-3} .

In addition to elastic deformation, the model incorporates viscous flow. Although the standard version of TEKTON (2.3) does not include a composite flow law, we extended the model to utilize recent laboratory data for the power-law flow of ice (see Appendix B) to express the total viscous strain rate as (Goldsby and Kohlstedt, 2001; Durham et al., 1997; Kirby et al., 1987)

$$\dot{\epsilon}_{visco} = \dot{\epsilon}_A + \dot{\epsilon}_B + \dot{\epsilon}_C + \dot{\epsilon}_{diff} + \{1/\dot{\epsilon}_{GBS} + 1/\dot{\epsilon}_{BS}\}^{-1} \quad (4.2)$$

where subscripts A , B , C , $diff$, GBS , and BS refer to dislocation creep A, B, and C; diffusion creep; grain boundary sliding; and basal slip. Each of these mechanisms has a temperature and stress dependence of the form:

$$\dot{\epsilon} = \Lambda(1/d)^m \dot{\sigma}^n \exp\{-Q/RT\}, \quad (4.3)$$

where $\dot{\epsilon}$ and $\dot{\sigma}$ are the effective strain rate and deviatoric stress respectively, Λ is a mechanism-dependent constant, d is the grain size, m is the grain-size exponent, n is the power-law exponent, Q is the activation energy, R is the gas constant, and T is the absolute temperature. Diffusion creep is modeled following the approach of Barr and Pappalardo (2005) who cast volume diffusion in the form of Eq. 4.3 by defining an effective Λ based on the diffusion parameters of Goldsby and Kohlstedt (2001). Table 4.1 shows the relevant rheological parameters for each rheology. Because

TEKTON uses a different definition of equivalence than typical creep experiments, the constants Λ_{ex} given in Table 4.1 should be modified for use in Eq. 4.3 by multiplying by a factor such that $\Lambda = (3^{(n+1)/2}/2)\Lambda_{ex}$ (Ranalli, 1995, pg. 77). This factor was not included in these simulations; its effect is small, generally less than that introduced by uncertainties in the creep activation energies. Simulations including this correction factor show negligible differences from those without.

Under our simulation conditions, dislocation creep B and C and grain boundary sliding (GBS) dominate the viscous flow. GBS flow is rate limited by the basal slip (BS) flow mechanism such that the slower of the two mechanisms controls the flow (Eq. 4.2). In our simulations, GBS is the slower mechanism, so the presence of the BS flow regime has no impact on model results. Furthermore, Newtonian diffusion, which dominates viscous flow only in warm, low-stress regions, and dislocation creep regime A, which dominates viscous flow only in warm, high-stress regions, minimally affect the model results.

If grain-size-sensitive creep (such as GBS) dominates the viscous flow, the rheology depends heavily on the grain size of the ice. Linear models suggest that, under some conditions, the choice of grain size alone can determine whether instability growth is strong enough to be consistent with groove formation (Dombard and McKinnon, 2001). Unfortunately, we have only poor constraints on the grain sizes present in Ganymede's lithosphere; reasonable possibilities range from 100 μm to 10 cm (see Barr and McKinnon, 2007, for a discussion). Furthermore, grain size most likely is not constant with depth, as high temperatures can increase grain sizes, and high stresses can decrease them. For consistency with published linear models we have chosen a constant grain size of 1 mm for our simulations. We discuss the sensitivity of our results to the choice of grain size in section 4.4.

Plasticity is a continuum approach to modeling the brittle behavior of the lithosphere. Plastic rheologies assume that the surface is well fractured at a scale much smaller than the model resolution, and that the deformation resulting from the com-

Table 4.1: Rheological Parameters

Creep Regime	$\log \Lambda_{ex}$ ($\text{MPa}^{-n} \text{m}^m \text{s}^{-1}$)	m	n	Q (kJ mole^{-1})	Reference
Dislocation Creep					
Regime A	11.8	0	4.0	91	Kirby et al. (1987)
Regime B	5.1	0	4.0	61	Kirby et al. (1987)
Regime C	-3.8	0	6.0	39	Durham et al. (1997)
GBS	-2.4	1.4	1.8	49	Goldsby & Kohlstedt (2001)
BS	7.74	0	2.4	60	Goldsby & Kohlstedt (2001)
Volume Diffusion	-3.46	2	1.0	59.4	Goldsby & Kohlstedt (2001), Barr & Pappalardo (2005)

bined behavior of these fractures can be represented as an addition to the viscous strain rate. We incorporate plasticity into our model via the use of Drucker-Prager yielding in which the yield condition can be written as

$$\sigma_{yield} = \xi(C \cos \phi - \sigma_m \sin \phi), \quad (4.4)$$

where C is the cohesion, ϕ is the angle of internal friction, σ_m is the mean stress (negative in compression), and $\xi = 6/[\sqrt{3}(3 - \sin \phi)]$. If the square root of the second invariant of the deviatoric stress tensor within a given finite-element exceeds σ_{yield} , plastic flow initiates, and an additional term ($\dot{\epsilon}_{plastic}$) is added to Eq. 4.2. The elements in which plastic flow can occur are not determined *a priori*. Instead, the local stress state completely determines when and where the onset of plastic behavior occurs. This permits plastic flow, and thus higher strain rates, to localize in regions of high stress (i.e. in necked regions).

Using a cohesion (C) of 10 MPa and an angle of internal friction (ϕ) of 30° , the strength profile of the lithosphere is defined as

$$\sigma_{yield} = 12\text{MPa} - .69\sigma_m, \quad (4.5)$$

which conforms to “Byerlee’s rule” for a simple geologic stack. The strength profile given by equation 4.5 has an intercept value one order of magnitude higher than the laboratory-measured profile of Beeman et al. (1988), which has the form

$$\sigma_{yield} = 1.2\text{MPa} - 0.65\sigma_{zz}. \quad (4.6)$$

The use of a high cohesion value permits significant instability growth over a wide range of free parameters (e.g. temperature gradients, and strain rates) and therefore allows examination of how those parameters effect instability growth. An analysis of the dependence of our results on the choice of cohesion value is included below (section 4.4).

We assume a linear temperature gradient within Ganymede’s lithosphere. We explore temperature gradients ranging from 5 to 45 K km^{-1} , spanning the range of

geologically plausible heat flows on Ganymede during groove formation. Except at the surface, isotherms are initially horizontal. Following Dombard and McKinnon (2001), who argued that a weaker sun and higher surface albedo at the time of groove formation reduced surface temperatures on Ganymede relative to present conditions, we use a surface temperature of 70 K in all of our simulations. These temperatures likely represent the minimum plausible surface temperatures during groove formation (Dombard and McKinnon, 2001). Low surface temperatures are particularly favorable to instability growth (Dombard and McKinnon, 2001). The effect of surface temperature on instability growth rates is described in section 4.4. To insure numerical stability, we cut off the linear temperature increase with depth at 180 K; at depths greater than this point, the domain becomes isothermal. The exact value of the cut-off temperature used, within a range of 180-210 K, does not affect model results. Cut-off temperatures above 210 K can cause numerical instabilities to occur. The transition to an isothermal temperature profile is consistent with, but somewhat colder than, the thermal profile expected in a thick convecting ice layer; however, our model does not include convection. Nor does it include conduction, a process that can be important in some cases. The effects of including conduction are discussed in section 4.3.4.

We model the dynamics of extension over three orders of magnitude in background strain rate from 10^{-12} s^{-1} to 10^{-15} s^{-1} . Long computational times prevent the examination of even lower strain rates. We apply 31.5% extension to each simulation. As described above, such strains are consistent with strain measurements in regions of high-density, high-relief grooves. The combination of strain rates and total strains implies total extension timescales of 10^4 to 10^7 yrs. Because domains undergo finite extension at a constant velocity (described below), the background strain rates described above do not remain constant in time for a given simulation but decrease by $\sim 24\%$ as the domain elongates. For the sake of familiarity, we retain the strain rate terminology in the discussions below with the caveat that all strain

rates refer to the initial strain rate imposed on the domain.

We use a timestep of 0.1 yrs, 1 yr, and 10 yrs for simulations with times of 10^4 yrs, 10^5 yrs, and 10^6 yrs or greater, respectively. These timesteps fall below the shortest Maxwell times found in our models (~ 300 years). Decreasing the timestep produces minimal changes in nodal displacements, only $\sim 10\%$ of the dimensions of a single element, and thus has no bearing on the overall deformation produced by the model.

Our finite-element domains are generally 40-100 km long, 12-24 km deep, and utilize square elements 333 m or 167 m on a side. Our results are weakly dependent on the mesh resolution used: final deformation amplitudes vary by 6%-7% when resolution is increased by a factor of 2. However, these small variations do not affect our general conclusions. Domain lengths and resolutions permit a broad range of deformation wavelengths to develop. A small-amplitude (usually 10 m), sinusoidal topographic perturbation is imposed on the top surface of the domain to allow the instability to initiate. In general, we use domain lengths that are an integral number of half wavelengths of the initial perturbation. However, the initial perturbation is phase shifted to prevent symmetry planes from aligning with domain edges. This helps reduce numerical edge effects (described below). Domain depths insure that the effects due to the bottom boundary are negligible. Extension results from a horizontal fixed-displacement boundary condition on the left side of the domain and a horizontal constant velocity boundary condition on the right. Both the left and right sides of the domain use a vertical free-slip condition to allow extensional thinning to occur. The bottom of the domain utilizes a free slip condition in the horizontal direction and a fixed-displacement condition in the vertical.

We apply a constant gravitational acceleration of 1.4 m s^{-2} to the model, which we initialize by allowing stress to relax towards a purely hydrostatic state. In the upper 6 km of the domain, however, stresses never fully relax to hydrostatic due to the cold surface temperatures. While σ_{zz} (vertical normal stress) conforms to a

hydrostatic relationship, σ_{xx} and σ_{yy} (horizontal normal stress) are less compressive than hydrostatic. Thus the mean stress in this region is up to 40% lower than a purely hydrostatic case would predict. This, in turn, reduces the yield stress by up to 12%. However, upon extension, stresses in the upper region of the mesh quickly become tensional rather than hydrostatic (see below) suggesting that the effect of this initial deviation from a purely hydrostatic model is small.

4.3 Results

4.3.1 Form of the Instability

The deformation produced by extension of our model domain is consistent with the formation of a necking instability. Simulations produce a pinch-and-swell morphology in which deformation at the surface is inverted (of opposite sign) from the deformation at depth (Figs. 4.3 and 4.4). Plastic deformation is focused within the pinched regions, illustrating that increased yielding, and thus higher stress, occurs within the thinned portions of the lithosphere. Despite the focusing of plastic deformation within these regions, no obvious localization of plastic flow occurs along narrow fault-like planes.

Both the dominant wavelength and the total amplitude of the deformation depend heavily on the temperature gradient (Fig. 4.5a, c, and d) and strain rate (Fig. 4.5a and b) imposed on the simulation. Dominant instability wavelengths vary from 1.8 km (Fig. 4.5c) to 16.4 km (Fig. 4.5d) with maximum crest to trough amplitudes of approximately 75 m (Fig. 4.5a). Small edge effects are present in our simulations. These edge effects take the form of an increase or decrease in groove amplitude of up to 20% at the edges of the domain (Fig. 4.5). We detect no systematic variation in the degree to which groove amplitudes at the domain edges differed from the “average” groove amplitude in a simulation. Furthermore, the effects were not reduced by shifting the phase of the sinusoidal topography. For this reason, calculations

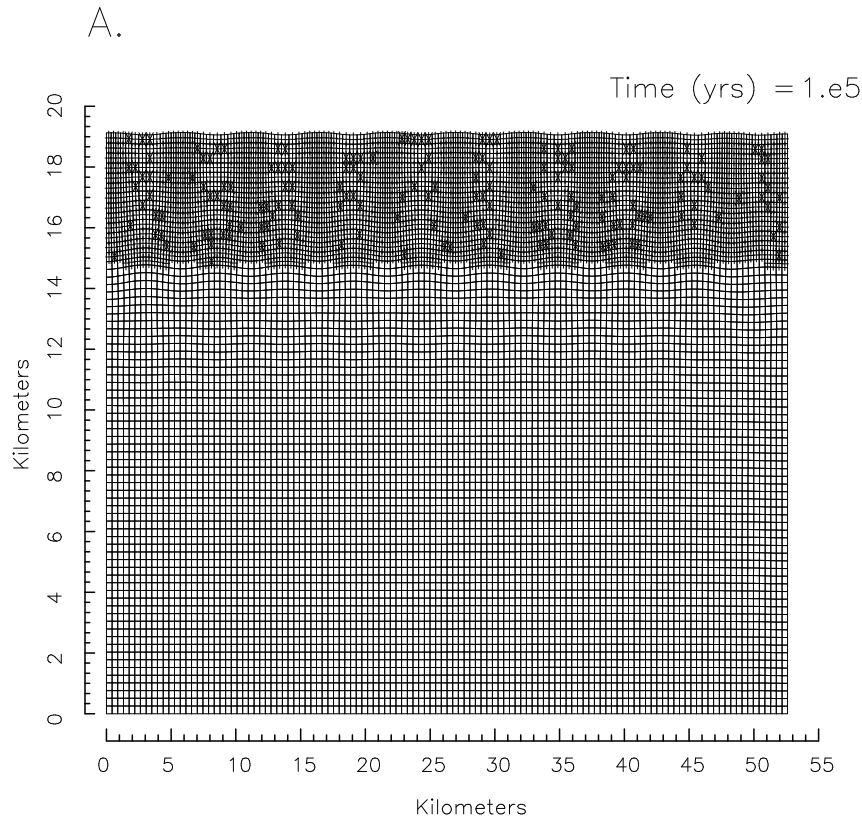


Figure 4.3: Deformed finite-element model after 31.5% extension illustrating the degree of deformation at the surface and at depth. The shaded layer indicates where plastic deformation has occurred at any point during the simulation, while black elements indicate where plastic flow has occurred in the most recent timestep. Vertical exaggeration is 2:1.

of total amplification reported in this manuscript disregard the topography at the edges of the domains.

Lateral variations of the stress field also match our expectations of a necking instability (Fig. 4.6a), with stresses deviating strongly from hydrostatic. Elements within the top 5 km of the lithosphere contain both compressional and tensile stresses. Compressive stresses result from gravitationally driven hydrostatic stress, and thus align vertically and increase with depth. Horizontally directed tensile stresses dominate the near-surface elements and focus within the pinched regions

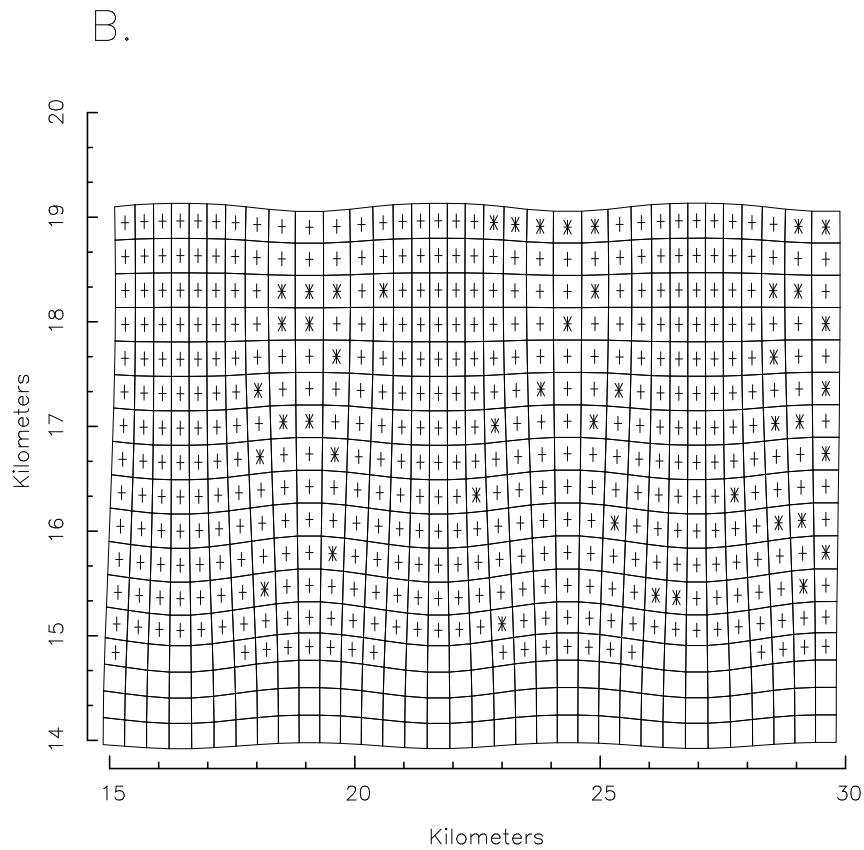


Figure 4.4: Enlargement of surface deformation showing material contours that were originally horizontal and vertical but are now deformed into pinches and swells. Asterisks indicate elements in which plastic flow has occurred in the most recent time-step. Plus signs indicate where plastic flow has occurred at any point during extension. The scattered distribution of plastic behavior reflects the fact that plastic failure relaxes local stresses back below the yield stress. These stresses require several timesteps (~ 3 or 4) to rebound far enough above the yield stress for plastic flow to occur again. Thus while the layer as a whole behaves plastically, only a fraction of the individual elements undergo plastic deformation in a given timestep. Vertical exaggeration is 2:1.

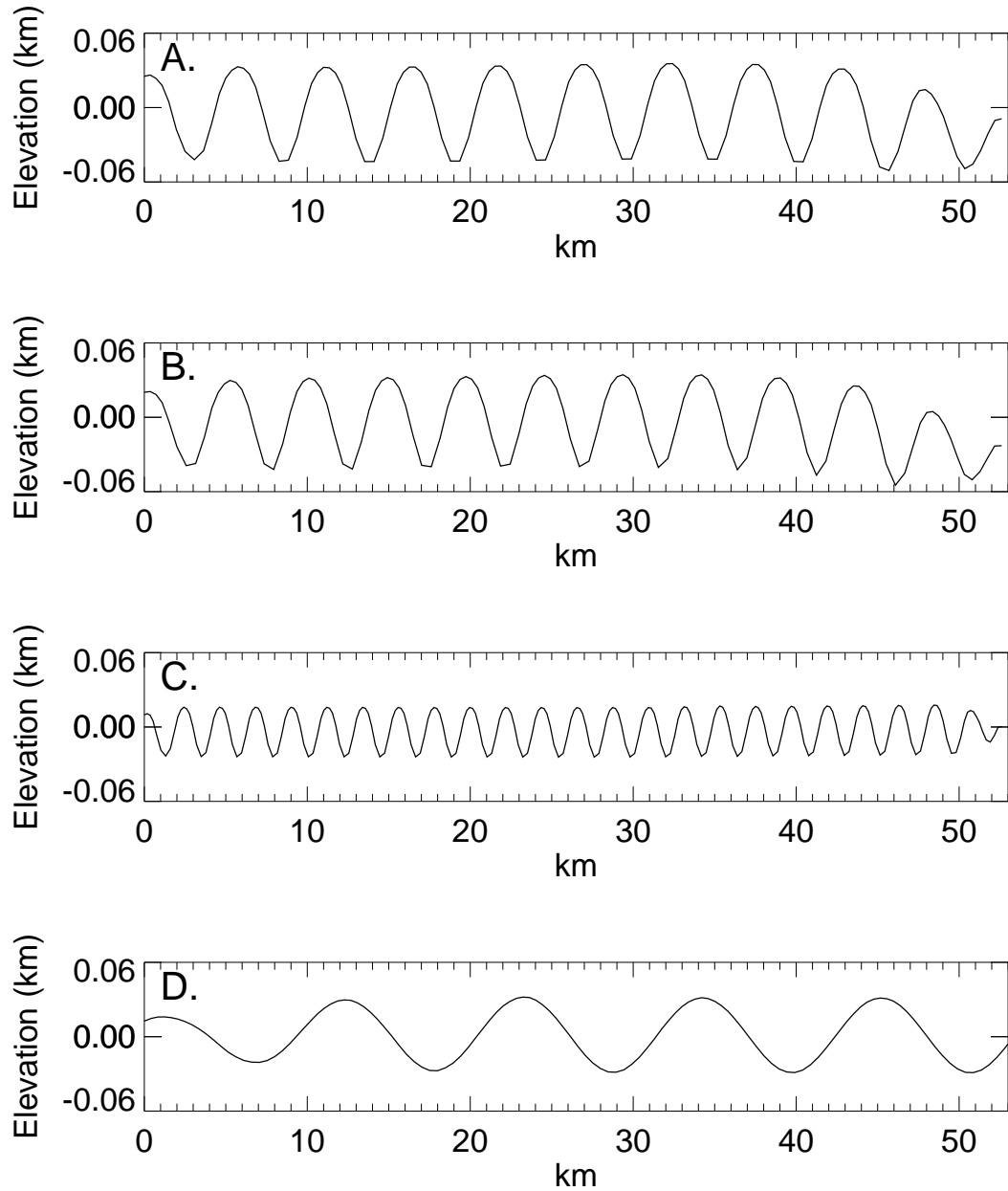


Figure 4.5: Typical topographic profiles produced by our simulations for a range of initial conditions: **A.** $dT/dz = 15 \text{ K km}^{-1}$ and $\dot{\epsilon} = 10^{-13} \text{ s}^{-1}$. **B.** $dT/dz = 15 \text{ K km}^{-1}$ and $\dot{\epsilon} = 10^{-14} \text{ s}^{-1}$. **C.** $dT/dz = 45 \text{ K km}^{-1}$ and $\dot{\epsilon} = 10^{-12} \text{ s}^{-1}$. **D.** $dT/dz = 5 \text{ K km}^{-1}$ and $\dot{\epsilon} = 10^{-15} \text{ s}^{-1}$. Each model was initialized with a single sinusoidal perturbation with an amplitude of 10 m and a wavelength corresponding to the dominant wavelength (see below). Domains were strained by 31.5%.

of the lithosphere, being 7-9% greater in groove troughs than in groove crests (Fig. 4.6b). This preferential concentration of tensile stress leads to the growth of the necking instability. Greater stress in the pinched regions promotes more frequent plastic deformation (i.e. more strain), which further decreases the thickness of the pinched region, localizing more tensile stress and reinforcing the positive feedback that drives the instability. At depths greater than ~ 5 km, hydrostatic stress dominates, and both principal stresses become compressional.

The magnitude of the local strain also varies across the domain (Fig. 4.7). In the near surface, maximum strains ($\varepsilon_I \sim 0.5$) occur within the topographic troughs and minimum strains ($\varepsilon_I \sim 0.05$) occur within topographic crests. These strains are primarily extensional. This distribution of strain agrees with the conception of lithospheric necking shown in Fig. 4.2. As in our simulations, high degrees of extension occur in Voyager-scale troughs and low degrees of extension occur in Voyager-scale crests (Pappalardo et al., 1998). At depth, the strain pattern in our simulations is reversed from that at the surface, with maximum strains occurring beneath topographic crests and minimum strains occurring below topographic troughs. This pattern indicates that the “pinch-and-swell” morphology produced by our necking instability is not vertically symmetric and may result from flow at depth accommodating necking at the surface.

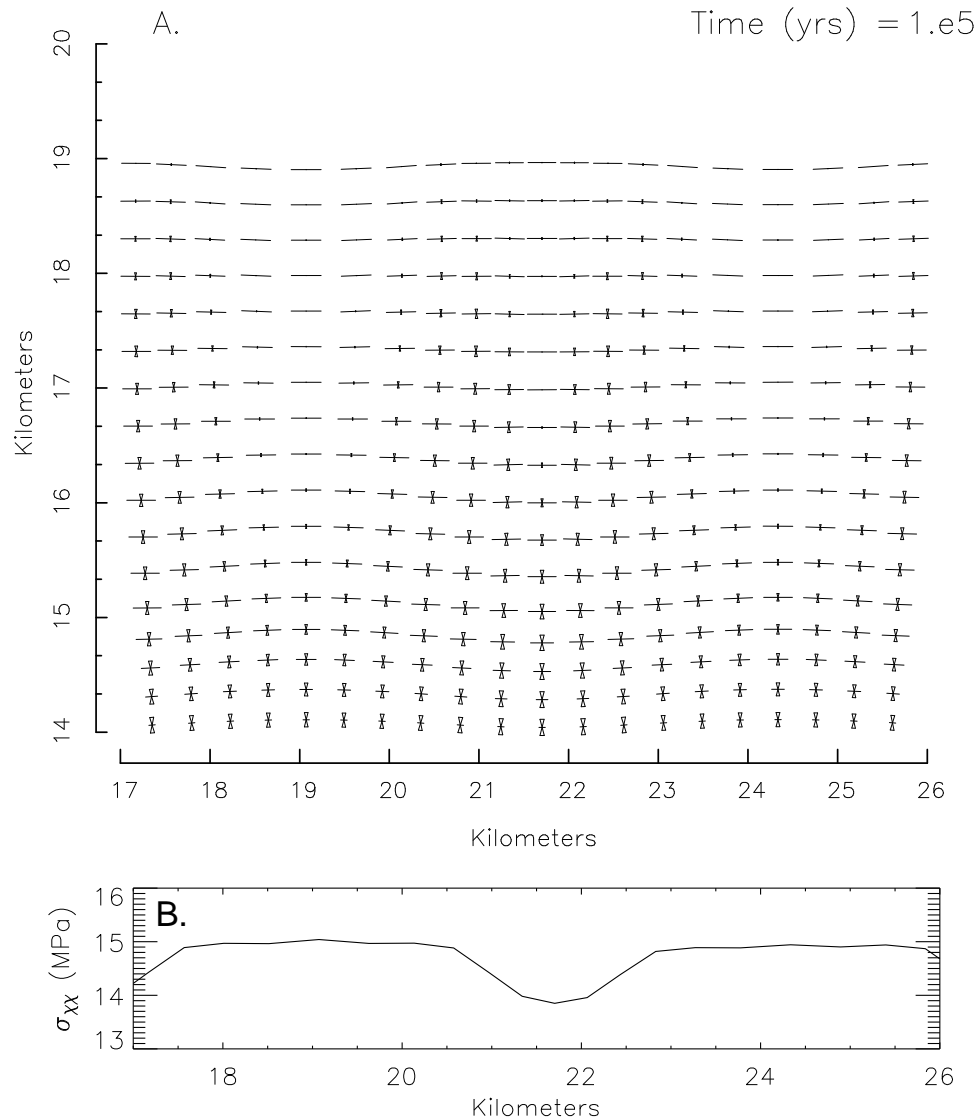


Figure 4.6: **A.** Orientation and relative magnitudes of principal stresses for a simulation with $dT/dz = 15 \text{ K km}^{-1}$ and $\dot{\epsilon} = 10^{-13} \text{ s}^{-1}$ extended by 31.5% (Fig. 4a). A two-part symbol designates the principal stress in each element, one part for each principal stress. Hour-glass shapes indicate compression, while lines indicate extension. The orientation of the symbol aligns with the orientation of the two principal stresses. **B.** Profile of horizontal stress (σ_{xx}) across the surface of the domain. The figures show only a small portion of the total domain.

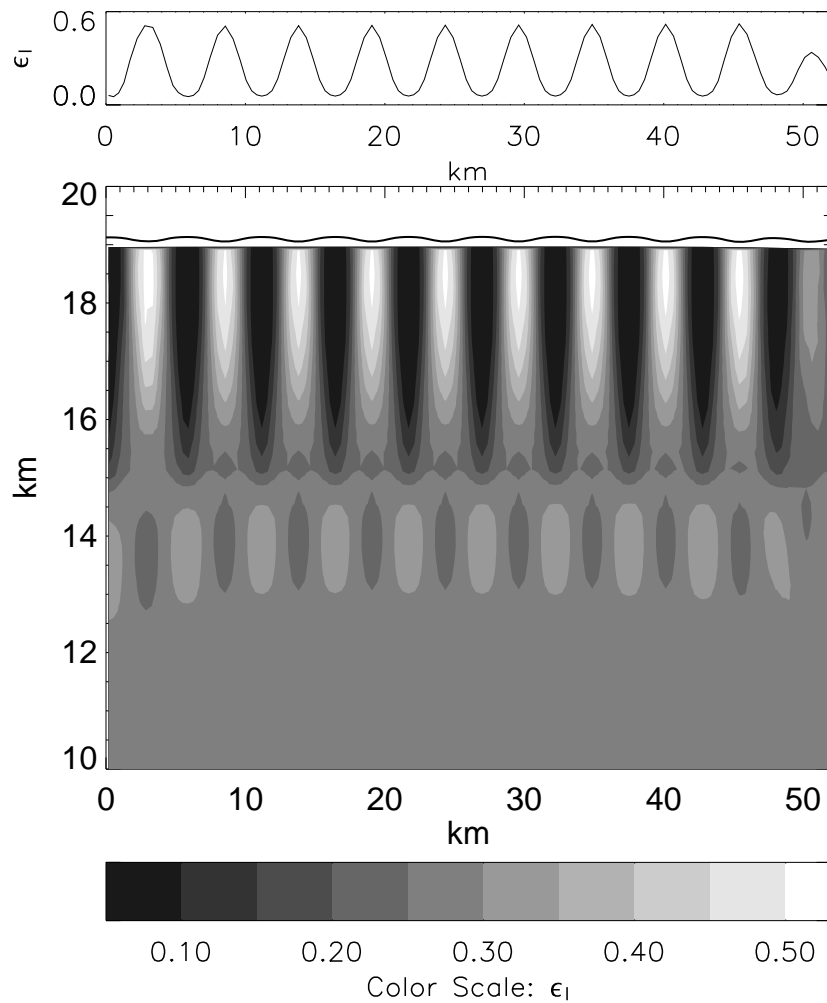


Figure 4.7: Grey-scale gives the square root of the second invariant of the total strain ($\varepsilon_I = \sqrt{\frac{1}{2}(\varepsilon_{xx}^2 + \varepsilon_{yy}^2) + \varepsilon_{xy}^2}$) within a domain extended by 31.5%, at a strain rate of 10^{-13} s^{-1} and a temperature gradient of 15 K km^{-1} (Fig. 4a). The surface deformation is plotted as a heavy black line in the grey-scale plot, and only the top half of the domain is shown. The surface trace of ε_I is shown above the grey-scale plot.

4.3.2 Infinitesimal Strain

We first examine the effect of infinitesimal strain on instability growth. To do this, we calculate exponential growth rates (q) of our simulated necking instabilities at small strains. We impose an initial perturbation consisting of a single sine wave of known amplitude and wavelength on a domain with a specific thermal gradient and strain rate. As extension occurs, we extract and Fourier transform topographic profiles of the surface to produce power spectra of the deformation. At small strains, the power spectra are strongly unimodal, with a peak at the imposed perturbation wavelength. These spectra provide a measure of the growth of the initial perturbation amplitude as a function of strain and allows calculation of exponential growth rates. The determination of exponential growth rates is only valid in the case where q is a constant, requiring strains to be small. We calculated growth rates after 3% extension, which is sufficient to allow accurate measurement but small enough to avoid the nonlinear behavior expected at large strains. Amplitude growth at these strains is in excellent agreement with Eq. 4.1. This method is consistent with linear models in both the use of small strains and the examination of the growth of each Fourier component of the initial perturbation individually.

Repetition of this procedure for a range of initial perturbation wavelengths permits measurement of the growth rate as a function of initial perturbation wavelength, $q(\lambda)$, for a particular thermal gradient and strain rate. We can then determine both the wavelength that amplifies the fastest (λ_d) and the maximum growth rate (q) for those particular conditions. Figure 4.8 is an example of a $q(\lambda)$ curve, and indicates that for an initial perturbation amplitude of 10 m, temperature gradient of 15 K km^{-1} and strain rate of 10^{-13} s^{-1} the dominant wavelength is 4.44 km and the maximum growth rate is 8.9. While the $q(\lambda)$ curve shown in Fig. 4.8 is typical of our simulations, the exact width of each curve varies as function of the temperature gradient. Low temperature gradients produce wide, broadly peaked $q(\lambda)$ curves in which a relatively large range of wavelengths have growth rates close to the maxi-

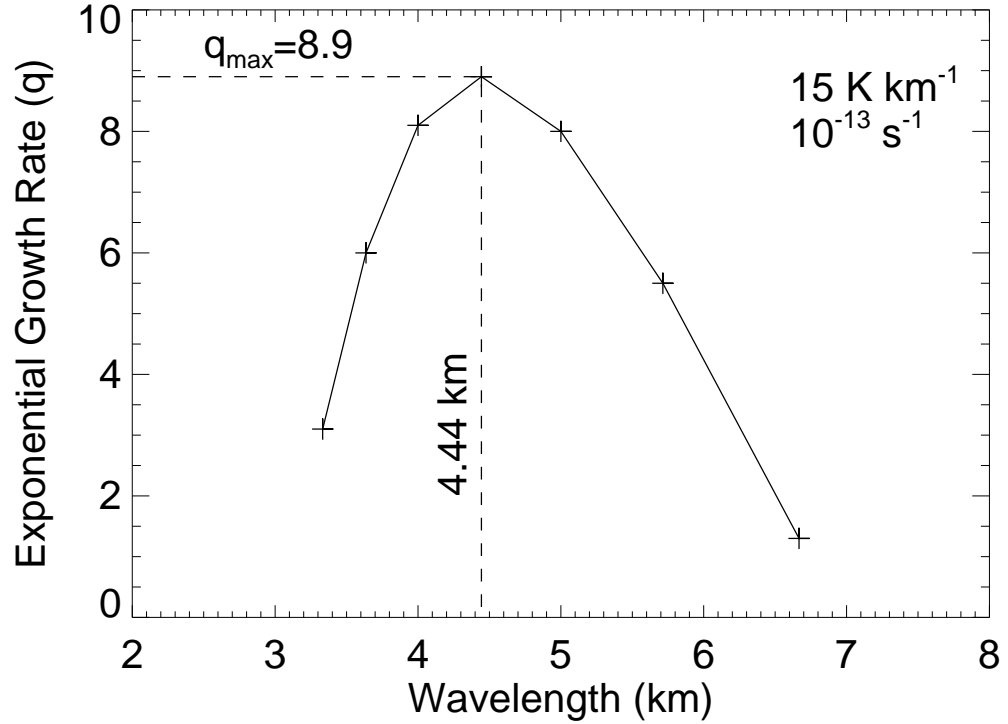


Figure 4.8: Exponential growth rate (q) as a function of the wavelength (λ) of the initial 10 m-amplitude perturbation imposed on the domain for a model with a temperature gradient of 15 K km^{-1} and strain rate of 10^{-13} s^{-1} . Dashed lines indicate values of the dominant wavelength (λ_d) and the maximum exponential growth rate (q) for this set of physical parameters.

mum. High temperature gradients produce narrow, sharply peaked $q(\lambda)$ curves in which deviations from the dominant wavelength as small as 25% produce little or no instability growth. This implies that, if the initial perturbation contains multiple topographic wavelengths, high temperature gradients better amplify a single dominant wavelength than low temperature gradients (see section 4.3.6).

The amplitude of the initial perturbation imposed on our simulations influences the magnitude of the growth rates calculated from these infinitesimal-strain simulations. Decreasing the perturbation amplitude to 1 m increases growth rates for high

temperature gradient simulations, but decreases growth rates for low temperature gradient simulations. At a temperature gradient of 45 K km^{-1} , q increases from 11.5 with a 10 m-amplitude perturbation to 12.7 with a 1 m-amplitude perturbation. In contrast, at a temperature gradient of 5 K km^{-1} , q decreases from 6.6 with a 10 m-amplitude-perturbation to 5.3 with a 1 m-amplitude-perturbation. Why growth rates depend on the amplitude of the initial perturbation remains unclear; however, this dependence suggests that all exponential growth rates calculated from our model have uncertainties of ~ 1.5 .

Using the methods described above, we calculated dominant wavelengths and maximum growth rates for the entire temperature-gradient and strain-rate parameter space, assuming an initial perturbation amplitude of 10 m (Fig. 4.9a). Dominant wavelengths decrease with increasing temperature gradient and decreasing strain rate, with λ_d ranging from 12.5 km at a temperature gradient of 5 K km^{-1} and strain rate of 10^{-12} s^{-1} to 1.4 km at a temperature gradient of 45 K km^{-1} and strain rate of 10^{-15} s^{-1} . Exponential growth rates, q , increase with increasing temperature gradient and are a maximum at moderate strain rates (10^{-13} s^{-1}). Values range from a maximum of 11.5 at a temperature gradient of 45 K km^{-1} and strain rate of 10^{-13} s^{-1} , to a minimum of 2.3 at a temperature gradient of 5 K km^{-1} and strain rate of 10^{-12} s^{-1} . The increase in exponential growth rates with increasing temperature gradient is qualitatively consistent with previous linearized, infinitesimal-strain models, which also show a preference for moderate to low strain rates (Herrick and Stevenson, 1990; Dombard and McKinnon, 2001).

Despite their qualitative similarities, however, our numerical results differ quantitatively from previous linear model results. At a given temperature gradient and strain rate, the numerical model produces dominant instability wavelengths a factor of two to three shorter than those calculated from the linear model. If H is the thickness of the layer in which plastic flow has occurred, then $\lambda_d/H \sim 1\text{-}1.5$ for the full range of temperature gradients used in our simulations, rather than 3 or 4 as

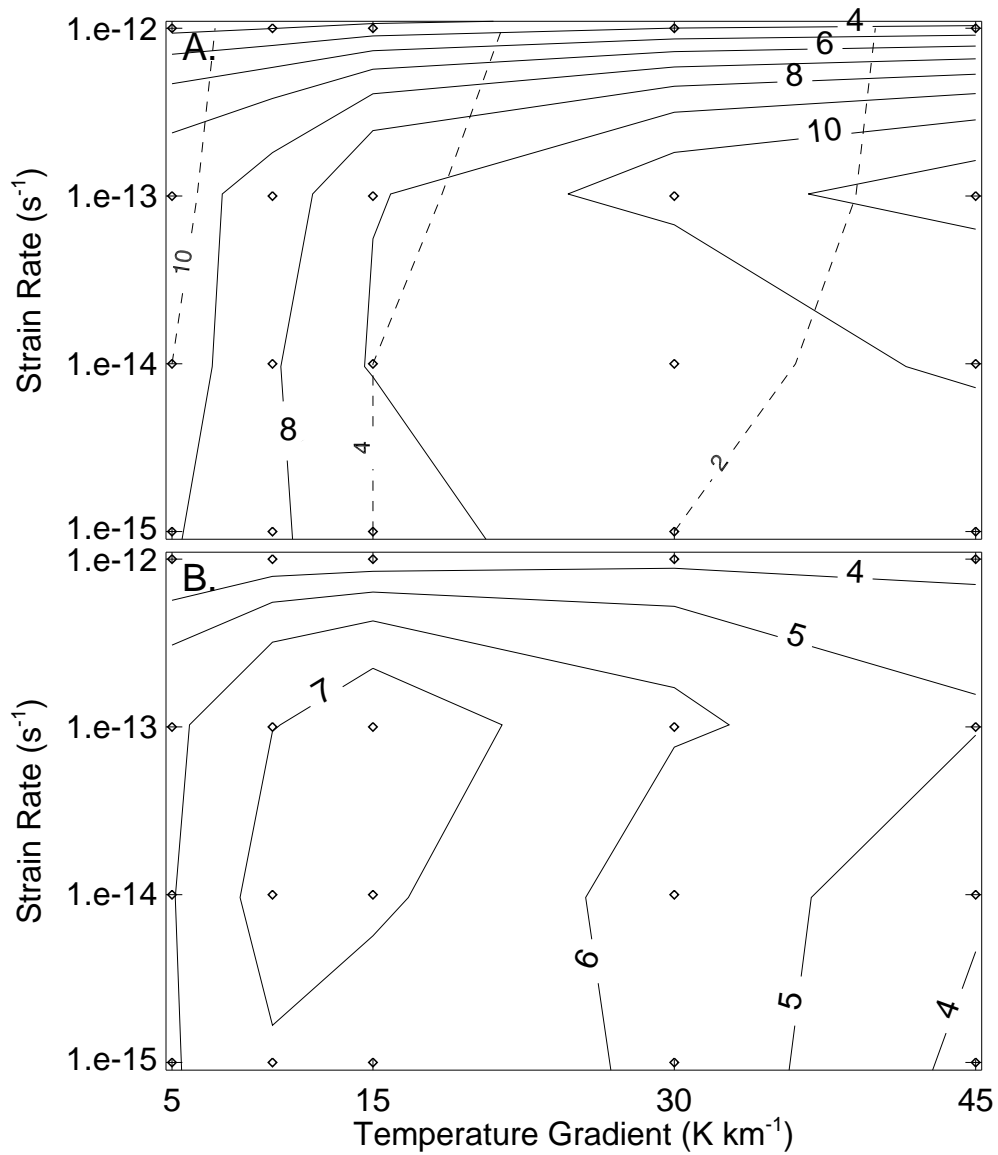


Figure 4.9: **A.** Contour plot of dominant wavelength λ_d in kilometers (dashed contours) and exponential growth rate q (solid contours) as a function of temperature gradient and strain rate at infinitesimal strain (3%). **B.** Contour plot of total amplification (ratio of the amplitude of the final deformation to the amplitude of the initial perturbation) at finite strain (31.5%). Dominant wavelengths show only modest changes at finite strains. Diamonds indicate parameter values of the simulations.

predicted by linear models (Fletcher and Hallet, 1983). Our smaller ratio is most likely caused by the increase in the strength of the lithosphere with depth, which results in an effectively thinner layer. This depth dependence was not included in the linearized models. Our numerical model also produces maximum exponential growth rates, q , an order of magnitude lower than growth rates calculated from linear models, which found that growth rates of 100 or more are possible at high thermal gradients (Dombard and McKinnon, 2001). The difference in magnitude between our numerical results and previous linearized, semi-analytical results is not consistent across the parameter space. The results of the two models are most similar in cases in which both the temperature gradients and strain rates are low (the lower left quarter of Fig. 4.9a), differing by as little as a factor of two. The difference increases with both increasing temperature gradient and increasing strain rate, with a difference in magnitude of up to a factor of fifteen both at high strain rates (10^{-12} s^{-1} , top of Fig. 4.9a), and at high temperature gradients and low strain rates (bottom right corner of Fig. 4.9a).

Our results, therefore, represent a significant departure from the results of previous linear models; however, we feel that this difference results from a more accurate representation of the rheological behavior of ice rather than from shortcomings of the numerical model. We emphasize that the numerical results described in this subsection occur at small strains, so nonlinear effects do not cause the discrepancy with the linear model results. Instead, differences in the implementation of the plastic rheology can probably account for the different model behavior. The linear model invokes plasticity by defining a near-surface layer in which the power-law exponent (n) of the rheology described by Eq. 4.3 is high ($\sim 10^6$). The relationship between stress (σ) and strain rate ($\dot{\epsilon}$) in Eq. 4.3 can be written in the generalized form $\dot{\epsilon} = \Gamma \sigma^n$. If we assume that the strain rate is related to the stress by a constant that depends on the yield strength with the form $\Gamma = D\sigma_{yield}^{-n}$, where D is a constant

with units of s^{-1} , the relationship between the stress and the strain rate becomes

$$\dot{\epsilon} = D(\sigma/\sigma_{yield})^n, \quad (4.7)$$

(Patterson, 1969). This model approximates plastic behavior for large values of n since if $\sigma > \sigma_{yield}$, the strain rate is nearly infinite, and if $\sigma < \sigma_{yield}$, the strain rate is negligible. This formulation is a tractable representation of pure plasticity and so is a reasonable choice for analytical models. However, Eq. 4.7 is not equivalent to true plasticity. The problem lies in the choice of the constant D that relates the stress ratio (σ/σ_{yield}) to the strain rate. Clearly, if $\sigma = \sigma_{yield}$, the strain rate depends sensitively on this parameter since, for this value, $\dot{\epsilon} = D$. However, the physical interpretation of D is unclear. In contrast, TEKTON provides a more realistic formulation of plastic behavior in which the magnitude of the plastic strain rate depends on the local stress field and a stress-relaxation timescale (Owen and Hinton, 1980). This formulation of plastic flow generates lower, but more physically meaningful growth rates than the formulation described above. Furthermore, we again note that the numerical model uses a depth-dependent yield stress while that in Dombard and McKinnon (2001) was depth-independent, and this difference may also cause some differences in the behavior of the two models.

Unlike our numerical model, the linear model also does not include elasticity. Because of this, all of the strain in the linear model partitions into plastic or viscous deformation. In the numerical model, however, strain partitions into elastic as well as viscous and plastic deformation. This reduces exponential growth rates in the numerical model because the plastic strain is the major contributor to necking instability growth in our simulations (Zuber and Parmentier, 1986). The importance of elasticity is illustrated by simulations in which the Young's modulus is two orders of magnitude higher than typical ice values; increasing the Young's modulus decreases the role of elasticity in the model since $\epsilon_{elastic} \propto (1/E)$, where $\epsilon_{elastic}$ is the elastic strain and E is the Young's modulus. As described in section 4.4, increasing the

Young’s modulus significantly increases the total amplification produced by extension. The inclusion of elasticity’s damping effects appears essential to understanding the growth of necking instabilities, thus exponential growth rates calculated from linear models without elasticity may be artificially high.

We emphasize that, while our growth rates are significantly smaller than previous calculations, they are still consistent with the requirement suggested by Collins et al. (1998b) that q must be greater than ~ 8 -13 to form Ganymede’s grooves. Thus simulations of necking instabilities at infinitesimal strain continue to support the concept that Ganymede’s grooves formed via extensional necking. As we describe below, however, nonlinear behavior at finite strains works to curtail the formation of grooves and presents a formidable challenge to groove formation via extensional necking.

4.3.3 Finite Strain

Although large temperature gradients ($dT/dz \geq 45 \text{ K km}^{-1}$) promote high *initial* growth rates, the formation of large amplitude grooves at finite strain actually occurs most easily at intermediate temperature gradients (~ 10 -15 K km^{-1}). Figure 4.10 shows the amplitude growth of the dominant wavelength of a necking instability for two different temperature gradients at large strains. These curves were constructed using the Fourier analysis method described above, and each plots the growth of the wavenumber that dominates the surface deformation of the extended domain. Here, the “wavenumber” we use is simply one over the number of wavelengths that fit into a domain (the “per-domain wavenumber”); note that a constant per-domain wavenumber corresponds to a wavenumber expressed as the inverse of the wavelength in kilometers (the “per-km wavenumber”) that decreases as the domain extends. In both simulations, amplitudes initially increase exponentially (as expected from Eq. 4.1), but exponential growth is not sustained outside the infinitesimal strain regime. Instead, growth rates decrease sharply at finite strain, approaching $q = 1$. These

results indicate that nonlinearities play a crucial role in instability growth at strains exceeding $\sim 10\%$. Linear extrapolation of initial growth rates, therefore, overpredicts actual groove heights. For example, at a temperature gradient of 45 K km^{-1} and strain rate of 10^{-13} s^{-1} the initial growth rate determined from our infinitesimal-strain models is 11.5. Using this initial growth rate to extrapolate to 31.5% strain predicts the formation of 270 m tall grooves. Instead, because growth rates decrease at large strains, these conditions produce grooves only 42 m tall, $\sim 15\%$ as tall as predicted by infinitesimal-strain models.

The fall-off in exponential growth rate occurs at lower groove amplitudes for higher temperature gradients (Fig. 4.10). In the 45 K km^{-1} temperature-gradient simulation, the growth rate of the dominant wavelength (1.67 km) begins to decrease after only 7% extension ($\mathcal{A} \sim 13 \text{ m}$), leading to a maximum amplitude of 42 m after 31.5% extension. For a similar simulation with a temperature gradient of 15 K km^{-1} the growth rate of the dominant wavelength (4.44 km) only begins to decrease after 20% extension ($\mathcal{A} \sim 40 \text{ m}$), leading to a maximum amplitude of 76 m after 31.5% extension. Thus, in the limit of large strains, the early fall-off in growth rate at high temperature gradients allows low-temperature-gradient simulations with low initial growth rates to produce more amplification than high-temperature-gradient simulations with high initial growth rates.

The fall-off in growth at high temperature gradients results in a shift in the ideal conditions for producing large-amplitude grooves to lower temperature gradients than predicted by linear models. Contours of total amplification ($\mathcal{A}/\mathcal{A}_o$) at large strain (31.5%), illustrate this fact (Fig. 4.9b). An extrapolation of the growth rates calculated at infinitesimal strain (Fig. 4.9a) predicts that the greatest amount of amplification should occur at temperature gradients of at least 45 K km^{-1} . However, the actual maximum amplification occurs at 15 K km^{-1} producing 7.6-fold amplification of the initial 10 m perturbation after 31.5% strain. Amplification depends only weakly on the strain rate with a slight preference for moderate strain rates near

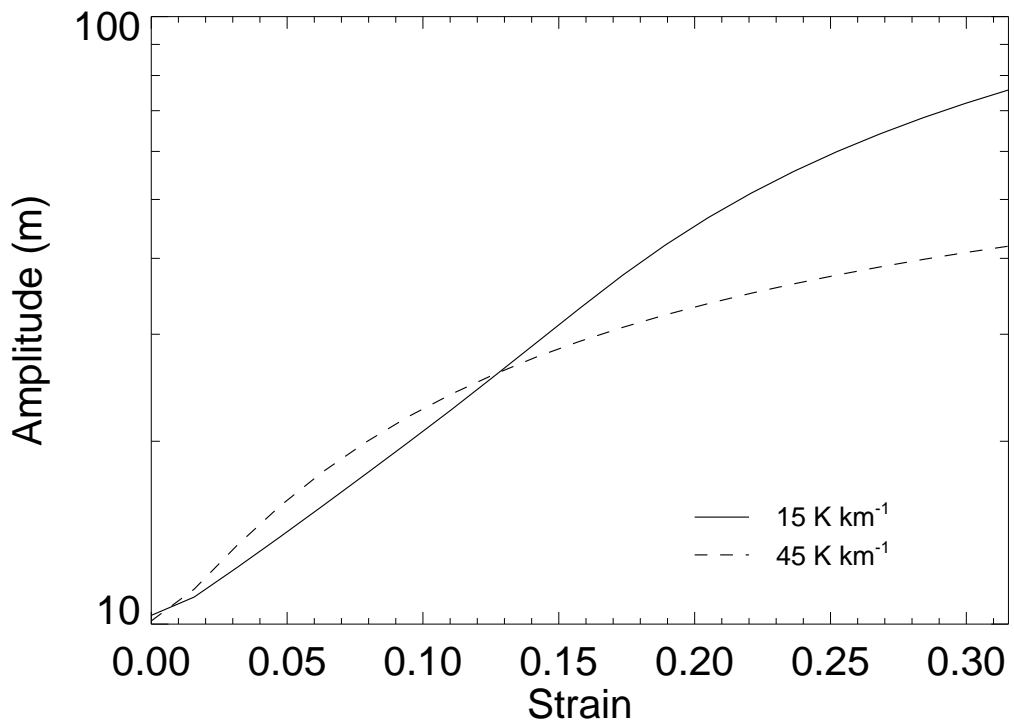


Figure 4.10: Amplitude of the per-domain wave number (see text) that dominates the final surface deformation as a function of strain for two models with different thermal gradients (15 K km^{-1} and 45 K km^{-1}), each with an initial 10 m-amplitude perturbation consisting of a single sinusoid of the corresponding expected dominant wavelength. In this figure, exponential growth would plot as a straight line. We note that plotting the amplitude of the per-km wave number yields qualitatively identical results. Because the amplitudes derived from the Fourier analysis (shown here) include edge effects (see text) while the amplitudes measured by direct measurement of deformation do not, amplitude values here vary slightly from those described elsewhere.

10^{-13} s^{-1} .

Because the conditions for maximum amplification depend on a balance between rapid growth at high thermal gradients and sustained growth at low thermal gradients, the exact values of temperature gradient and strain rate at which the maximum amplification occurs depends strongly on the total amount of strain imposed on the model. If strains are small, high thermal gradients are desired such that growth occurs rapidly during the brief period of extension. If large strains are imposed, low thermal gradients that produce sustained growth throughout the extension are preferable. Thus the physical conditions that produce a given groove amplitude are non-unique. One must therefore use caution when attempting to constrain the geophysical conditions that produced specific groove sets on Ganymede.

Two independent mechanisms appear to cause the fall-off in growth at large strains. First, amplitude growth becomes saturated because of the finite thickness of the deforming layer. Mass conservation suggests that the maximum crest-to-trough amplitude that can be formed by pinching an initially horizontal layer is on the order of the layer thickness itself. In reality, because instability growth can produce more deformation at depth than at the surface (in some cases by more than 50%), the maximum crest to trough amplitude of *surface* deformation will be some fraction of the layer thickness. The thickness of the deforming layer is primarily controlled by the temperature gradient of the lithosphere. Thus, growth fall-off due to amplitude saturation occurs at smaller strains (lower groove amplitudes) in high-thermal-gradient, thin-lithosphere simulations than in low-thermal-gradient, thick-lithosphere simulations.

Second, the increasing wavelength of the deformation as strains become large, and the finite width of the $q(\lambda)$ growth curve combine to limit amplitude growth. As extension begins, a necking instability forms with a particular dominant wavelength (the peak of $q(\lambda)$ curve). As strain continues, the wavelength of the topography will continually increase with the extending domain, moving off the peak of the

$q(\lambda)$ curve until, eventually, the surface deformation is substantially longer than the dominant wavelength and instability growth declines. Because the $q(\lambda)$ curve is broad for low temperature gradients and narrow for high temperature gradients (see section 4.3.2), the growth fall-off occurs earlier for high temperature gradient simulations than for low temperature gradient simulations. Furthermore, as extension occurs, thinning of the lithosphere increases the thermal gradient causing the dominant wavelength to shift towards shorter wavelengths and away from the extending wavelength of the growing topography. Thus, at finite strains, the wavelength of the surface deformation and the wavelength of dominant growth migrate away from each other.

There is evidence that both of these processes are occurring in our simulations. Amplitude saturation effects are seen when comparing simulations with an initial perturbation amplitude of 1 m to the 10 m perturbation simulations already described. In the 1-m-amplitude simulations, instability growth occurs exponentially through 17% strain for all temperature gradients. Only at higher strains do the highest-temperature-gradient (thinnest lithosphere) simulations begin to show a decrease in growth rate. In contrast, in the 10 m-amplitude simulations (Fig. 4.10), high temperature gradient simulations exhibit a fall-off in growth rate at strains as low as 7%. Thus we find that small initial perturbations can amplify extensively before reaching the saturation limit while large amplitude perturbations quickly saturate. However, even small amplitude initial perturbations show some decrease in growth at large strains. Growth fall-off at these small amplitudes is not likely due to amplitude saturation effects and must therefore be caused by the wavelength of deformation moving off the peak of the $q(\lambda)$ curve.

4.3.4 Effect of Heat Conduction

Our model does not include conduction (Sec. 4.2), but we *can* estimate how it would affect our results. Employing a simple model in which the timescale for heat

conduction, τ , across a layer of thickness H is given by $\tau = H^2/\kappa$, where κ is the thermal diffusivity (Turcotte and Schubert, 2002) we find that $\sim 3 \times 10^6$ years are required to conduct heat across a layer 10 km thick, a thickness consistent with the lithospheric thicknesses of our low-temperature-gradient simulations. This suggests that, at low temperature gradients, only the lowest-strain-rate runs are affected by heat conduction because extension occurs faster than heat can conduct out of the layer. Higher-temperature-gradient simulations have lithospheric thicknesses closer to 1 km. The timescale for conduction across such a layer is $\sim 3 \times 10^4$ years. Thus at high thermal gradients, heat conducts out of lithosphere faster than extension occurs at all but the very highest strain rates we examined.

Without conduction, extensional thinning effectively increases the thermal gradient in the lithosphere. The relative increase in thermal gradient is equal to the relative decrease in layer thickness, which is equal to the relative increase in domain length. Thus, in our simulations the temperature gradient increases by 31.5% over the course of extension. With conduction, simulations with high thermal gradients and low strain rates (i.e. when conduction occurs much faster than extension) would maintain their initial thermal gradient because any increases in temperature at a given depth (due to extensional thinning) would quickly decay back to the original thermal profile. Thus, after 31.5% extension, our low strain rate simulations have a higher temperature gradient than they should if conduction were included.

We can use these ideas to infer how conduction would affect our simulations. Amplification contours at high thermal gradients and low strain rates (lower right portion of Fig. 4.9b) would shift to lower temperature gradients. While our quantitative results (e.g. the thermal gradient at which maximum amplification occurs) may be slightly modified, our qualitative results would likely remain unchanged. Because growth rates in Fig. 4.9a are calculated after only 3% extension, these values would be unaffected by the inclusion of heat conduction.

4.3.5 Effect of the Initial Perturbation

The initial topographic perturbation influences instability growth. If the expected dominant wavelength produced by a particular thermal gradient and strain rate differs significantly from the wavelength of the imposed initial perturbation, complex wavelength interactions can occur. The most interesting type of deformation occurs when the imposed wavelength is somewhat longer (by a factor of ≥ 1.4) than the dominant wavelength. At these values, extension amplifies overtones of the imposed perturbation wavelength (generally half the imposed wavelength) rather than the dominant or imposed wavelengths themselves. Figure 4.11 shows a simulation in which we imposed an initial wavelength much longer than the expected dominant wavelength (Fig. 4.11a). Instead of simply failing to amplify the initial perturbation as expected from the linear model, extension amplifies an overtone wavelength half as long as the imposed perturbation, producing two wavelengths of deformation in the resulting topography (Fig. 4.11b). Figure 4.11c shows the amplitude growth for wavelengths of the imposed perturbation (initially 6.67 km - solid line), half the imposed perturbation (initially 3.33 km - dash-dot line), and the expected dominant wavelength (4.44 km - dashed line) as a function of strain. Both the imposed perturbation and the expected dominant wavelength show minimal growth with increasing strain, but half the imposed perturbation wavelength shows significant amplification at large strain, increasing from an amplitude of ~ 0 m to an average amplitude of ~ 15 m.

The amplitude of the initial perturbation strongly affects the results described above (Fig. 4.12). At small initial perturbation amplitudes (Fig. 4.12a), the imposed perturbation does not influence instability growth and the deformation wavelength equals the dominant wavelength. As the initial perturbation amplitude increases, however, its influence, along with that of its overtone, on the resulting topography increases (Fig. 4.12b, c, and d). These results suggest that the imposed perturbation must have an amplitude of at least 10 m before the imposed wave-

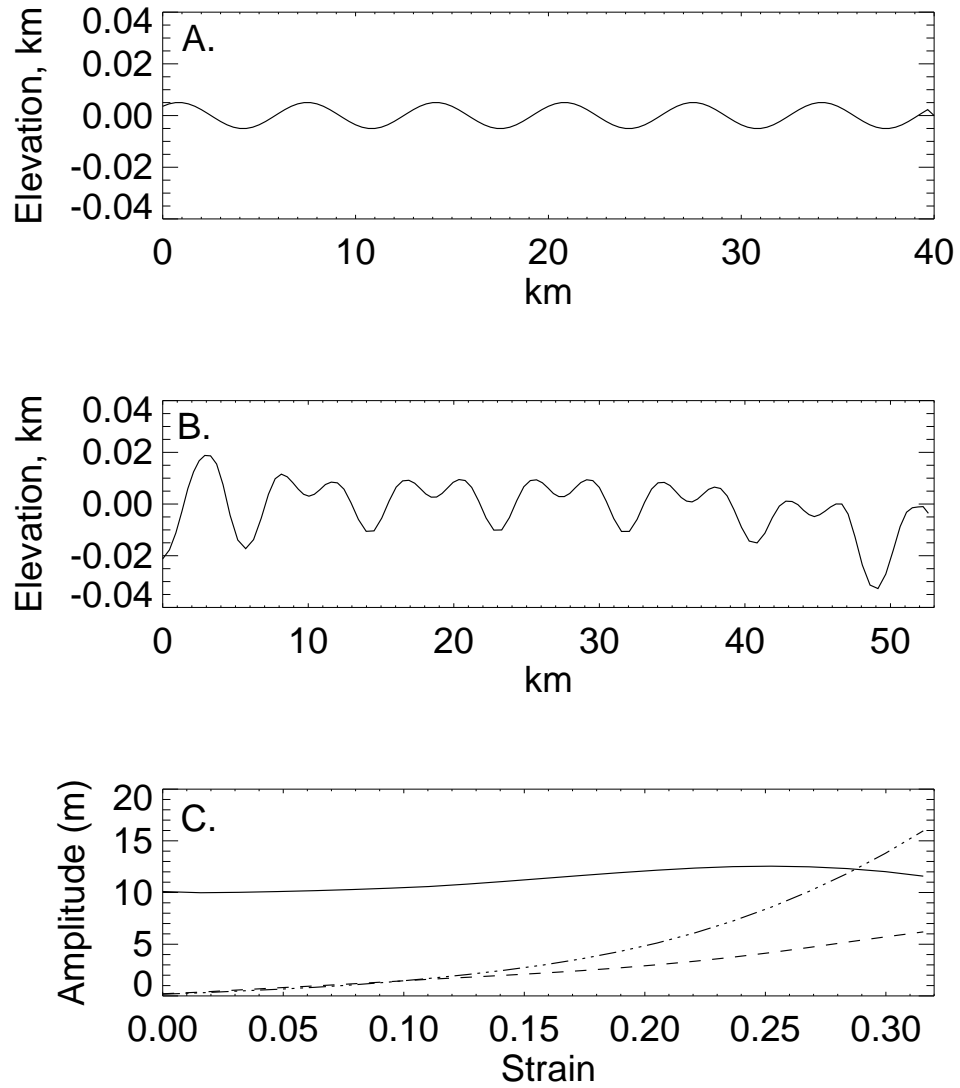


Figure 4.11: Illustration of the effect of initial perturbation on instability growth. **A.** Topographic profile of the initial perturbation of 6.67 km-wavelength imposed on a domain with physical conditions favoring growth of a 4.44 km-wavelength perturbation. **B.** Profile of final surface deformation after 31.5% extension. The final morphology is a superposition of the initial perturbation wavelength and an overtone of half the initial perturbation wavelength. **C.** Amplitude growth as a function of strain for the per-domain wavelengths of the initial perturbation (initially 6.67 km - solid line), the dominant wavelength (initially 4.44 km - dashed line), and half the initial perturbation wavelength (initially 3.33 km - dot dashed line).

length, rather than the expected dominant wavelength, controls the wavelength of the deformation.

These results indicate that instability growth on Ganymede depends not only on the conditions present during the most recent groove forming event, but also on the entire extensional history of the region. For example, if a small amount of extension occurs with a low lithospheric thermal gradient, moderate-amplitude, long-wavelength deformation occurs at the surface. If a later period of extension occurs with a higher thermal gradient, the pre-existence of long wavelength topography on the surface, rather than the physical conditions within the lithosphere, controls the wavelength of the deformation produced by the extension. Observations of Ganymede support such complex groove histories (Collins et al., 1998a). Inferences of the physical conditions that produced a given groove set must therefore carefully consider the entire strain history of the region.

4.3.6 Non-periodic Initial Perturbations

Numerical modeling of extensional necking instabilities allows a detailed investigation of how the presence of multiple wavelengths of topography affects instability growth. As previously noted, linear, infinitesimal-strain models are limited to examining the growth of each Fourier component of the initial perturbation independently. In reality, the pre-grooved surface of Ganymede contained a large number of topographic wavelengths simultaneously. The finite width of the $q(\lambda)$ curve shown in Fig. 4.8 indicates that, if present, a range of wavelengths, rather than a single dominant wavelength, will amplify as extension occurs. These simultaneously growing wavelengths may interact as topographic amplitudes become large. To investigate this interaction, we performed simulations in which the initial perturbation contained multiple wavelength components. These simulations provide insight into how extensional necking can contribute to the tectonic resurfacing of long-wavelength, preexisting terrain by modifying random initial topography into

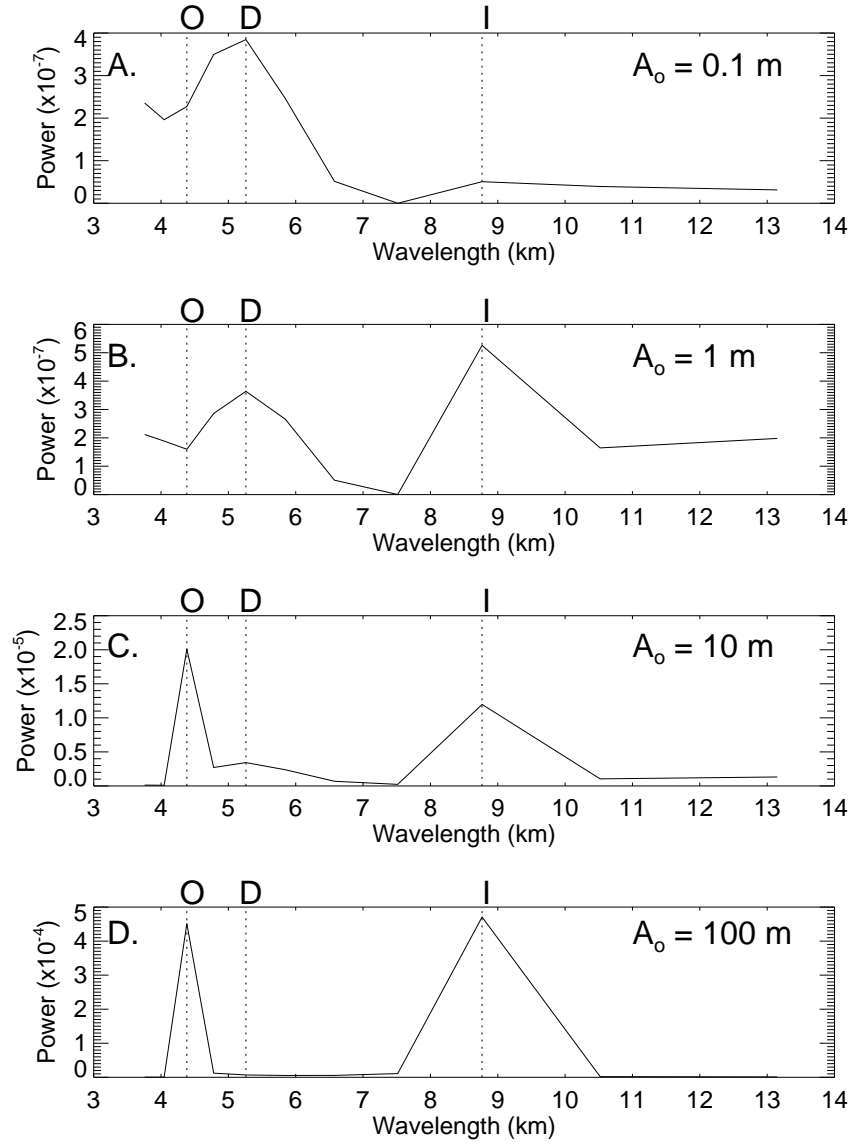


Figure 4.12: Illustration of the effect of initial perturbation amplitude (\mathcal{A}_o) on wavelength interactions. Power spectra of four simulations with temperature gradients of 15 K km^{-1} , strain rates of 10^{-13} s^{-1} , and total strains of 31.5% are shown in which the wavelength of the imposed perturbation (initially 6.67 km , which becomes 8.77 km after 31.5% extension) is significantly different than the dominant wavelength expected (5.26 km) for the conditions of the model. The simulations differ only in the amplitude of the initial perturbation. Initial perturbation amplitudes are **A.** 0.1 m , **B.** 1 m , **C.** 10 m , and **D.** 100 m . The dominant ('D'), imposed ('I'), and overtone ('O') wavelengths are indicated by dotted lines.

periodic ridges and troughs.

We created an initial perturbation containing 16 wavelengths ranging from 10 to 1.25 km, which were each given a random phase shift, added together and renormalized to have a maximum peak to trough amplitude of 15 m. Figure 4.13a and 4.13b show the resulting perturbation and a power spectrum of the topography. The Fourier approach to monitoring amplitude growth was again used, allowing the growth of each component of the deformation to be tracked separately.

Figure 4.13c and 4.13e show topographic profiles of the deformation caused by extending such a domain by 31.5%, at a strain rate of 10^{-13} s^{-1} , for temperature gradients of 15 K km^{-1} and 30 K km^{-1} respectively. Power spectra derived from these profiles are shown in Fig. 4.13d and Fig. 4.13f. Both the topographic profiles and their spectra indicate that growth of the necking instability has removed ($q \leq 1$) both the longest and shortest wavelength components of the initial perturbation while strongly amplifying a small range of wavelengths. Changing the temperature gradient within the model lithosphere results in significantly different surface deformation. The 15 K km^{-1} model produces a dominant wavelength of $\sim 5 \text{ km}$ and a maximum crest-to-trough amplitude of $\sim 60 \text{ m}$ suggesting amplification of the initial perturbation by a factor of 4-6. The 30 K km^{-1} model has a dominant wavelength of $\sim 3 \text{ km}$ and maximum crest to trough amplitudes of $\sim 45 \text{ m}$. The decrease in the amplitude of the deformation at higher temperature gradients matches our expectations from the finite strain modeling described above (section 4.3.3). Since the two models utilized the same initial perturbation, the differences in their final deformation results from differences in the physical conditions of the lithosphere. Furthermore, changing the phase shifts of the included wavelengths of topography has a negligible effect on the final form of the deformation. Thus, it is clear that only the wavelengths present in the topography, rather than its specific shape plays a significant role in instability growth.

Careful examination of the growth of the “removed” wavelengths indicates that

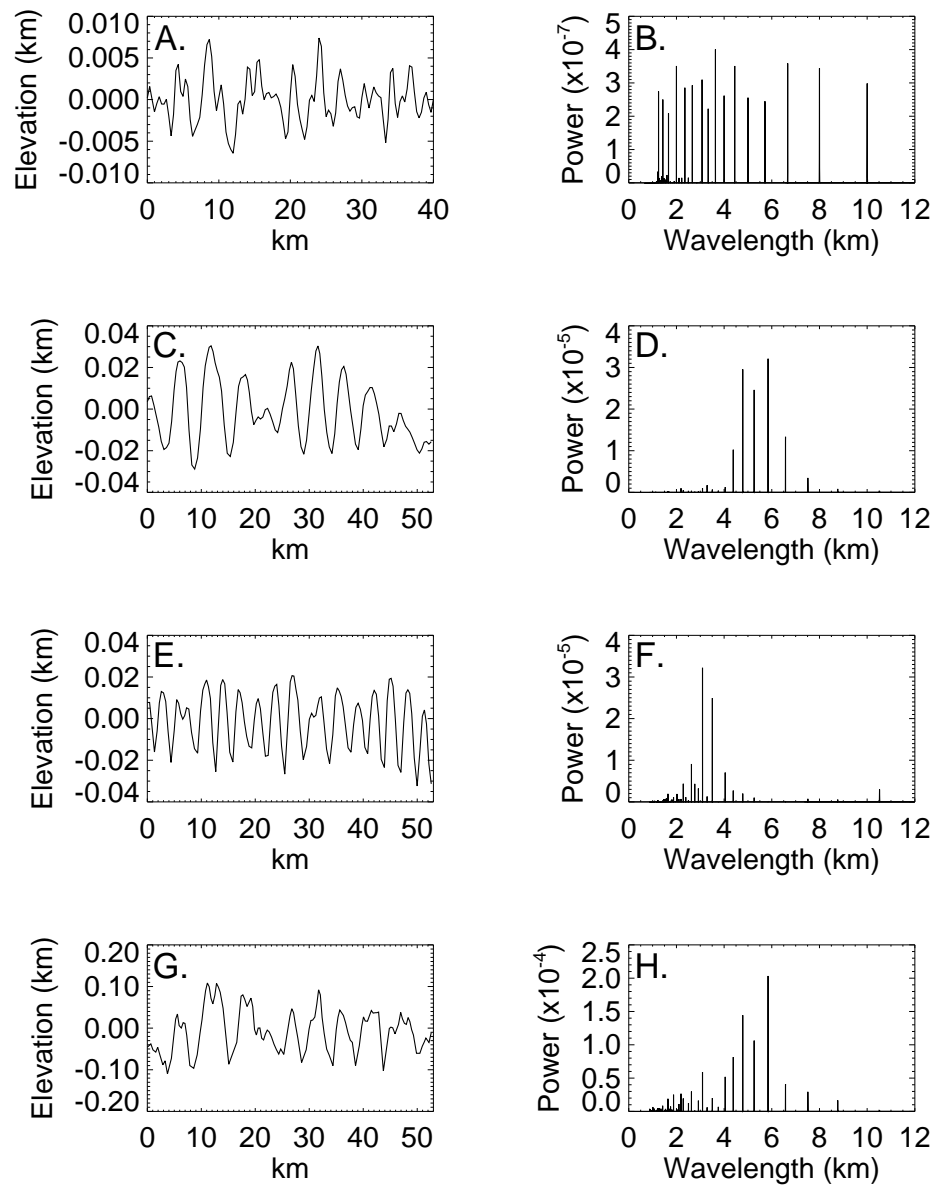


Figure 4.13: Demonstration of a necking instability's potential for modifying pre-existing terrain. The initial perturbation (A and B) is composed of 16 wavelengths between 1.25 and 10 km. Topographic profiles and power spectra of the final surface deformation after 31.5% extension are shown for a simulation with a temperature gradient of 15 K km^{-1} (C and D) and 30 K km^{-1} (E and F). The effect of initial perturbation amplitude is illustrated by a simulation with a 150 m amplitude perturbation and a temperature gradient of 15 K km^{-1} (G and H). In all cases the strain rate was 10^{-13} s^{-1} .

they have exponential growth rates ≤ 1 . Therefore, rather than the dominant wavelength simply outgrowing these wavelengths, extension of the surface actually damps them out. A correlation exists, however, between the width of the $q(\lambda)$ curve derived from infinitesimal-strain modeling (Fig. 4.8) and the range of wavelengths that show positive growth in the multiple-initial-wavelength simulations. As noted in section 4.3.2, the width of the growth curve depends on the thermal gradient of the lithosphere: high temperature gradients produce narrow, sharply peaked $q(\lambda)$ curves and low temperature gradients produce broadly peaked $q(\lambda)$ curves. We expect, therefore, that higher temperature gradients will more easily amplify a single wavelength of the deformation than lower temperature gradients. A comparison of the power spectra of the 15 K km^{-1} and the 30 K km^{-1} simulations shown in Fig. 4.13d and 4.13f illustrates this effect. In the 15 K km^{-1} model the power spectrum shows strong amplification of a range of wavelengths between 4.4 and 6.6 km. In contrast, the power spectrum of the 30 K km^{-1} model indicates that growth occurs only in the wavelength range between 3.1 and 3.5 km. Thus while the lower-temperature-gradient model produces greater-amplitude deformation, the higher-temperature-gradient model produces deformation with stronger periodicity. We might therefore expect that, on Ganymede, grooved terrain swaths with closely spaced grooves (short wavelengths) would contain a smaller range of wavelengths in their spectra (i.e. be more sinusoidal) than grooved terrain swaths with wide spacings (long wavelengths).

Current observational evidence is inconclusive on this point. Patel et al. (1999) performed a Fourier analysis to determine the dominant wavelengths present in three diverse swaths of grooves within bright terrain and one set of groove lanes within the dark terrain of Nicholson Regio. From this analysis no pattern emerges suggesting that groove swaths with shorter wavelengths (e.g. Uruk Sulcus with a longest dominant wavelength of 3.75 km) are more strongly periodic than groove swaths with longer wavelengths (e.g. Byblus Sulcus with a longest dominant wavelength of

10 km). However, the small number of groove swaths imaged at high enough resolution to accurately measure short topographic wavelengths, and the presentation of the Patel et al. (1999) wavelength data in binned histograms makes a conclusive analysis of variations in periodicity difficult.

Comparison of our numerical results to an analytical prediction of instability growth provides insight into the role of wavelength interactions in creating the surface deformation shown in Fig. 4.13. Equation 4.1 gives the final amplitude (\mathcal{A}_{max}) produced by instability growth at the dominant wavelength as $\mathcal{A}_{max} = \mathcal{A}_o \exp[(q_{max} - 1)\dot{\epsilon}t]$. Likewise, the amplitude of the deformation produced by the growth of a wavelength on the flank of the $q(\lambda)$ curve (Fig. 4.8) is given by $\mathcal{A}_{flank} = \mathcal{A}_o \exp[(q_{flank} - 1)\dot{\epsilon}t]$, where q_{flank} is the growth rate at that particular wavelength. The ratio of the amplitude of the deformation produced at the dominant wavelength to the amplitude of the deformation at a flanking wavelength is then:

$$\mathcal{A}_{max}/\mathcal{A}_{flank} = \exp[\Delta q \dot{\epsilon}t], \quad (4.8)$$

where Δq is the difference between the growth rates at the dominant (q_{max}) and flanking (q_{flank}) wavelength. This ratio provides an estimate of how well extension can amplify a single wavelength of deformation when the initial perturbation contains many wavelengths.

We can use the results of Fig. 4.8 to estimate the $\mathcal{A}_{max}/\mathcal{A}_{flank}$ predicted by our infinitesimal-strain models. For a temperature gradient of 15 K km^{-1} and strain rate of 10^{-13} s^{-1} the growth rate at the dominant wavelength is 8.9. At a wavelength of 3.63 km, on the flank of the $q(\lambda)$ curve, the growth rate is 6. Δq therefore equals 2.9 and, assuming 31.5% extension, $\mathcal{A}_{max}/\mathcal{A}_{flank}$ is 2.5. Thus, one might expect that the amplitude of the dominant wavelength in the multi-wavelength-perturbation model shown in Fig. 4.13c and 4.13d should be about twice the amplitude of the “off-peak” wavelengths. However, examination of the power spectrum shown in Fig. 4.13d indicates that the dominant wavelength (5 km) has an amplitude ~ 4 -7 times

greater (rather than ~ 2.5 times greater) than the flanking wavelength (3.63 km). This suggests that, at finite strains, a nonlinear interaction occurs between growing wavelengths in which faster growth of one particular wavelength inhibits the growth of all other wavelengths, producing more pronounced periodicity than is predicted by Eq. 4.8, where wavelengths do not interact.

To better understand how wavelengths interact as amplification occurs, we examine how the final form of the topography produced by extending a multi-wavelength perturbation depends on the amplitude of that initial perturbation. Decreasing the amplitude of the initial perturbation to 1.5 m (maximum peak to trough) in cases with $dT/dz = 15 \text{ K km}^{-1}$ and $\dot{\epsilon} = 10^{-13} \text{ s}^{-1}$ produced final topography very similar to Fig. 4.13c but with ten times smaller amplitude. The amplitude difference between the dominant and “off-peak” wavelengths is reduced relative to that of the 15 m-amplitude perturbation case, however, with the amplitude of the dominant wavelength ~ 3.5 - 4.5 times greater than the amplitude of the off-peak wavelengths. This result suggests that nonlinear effects play a more significant role in instability growth at higher amplitudes. Increasing the amplitude of the initial perturbation to 150 m (maximum peak to trough) more significantly affects instability growth (Fig 4.13g and 4.13h). While the resulting deformation is still periodic with a wavelength near 5 km, a significant short-wavelength component of the initial perturbation remains in the topography. The existence of residual topography is permitted by the smaller degree of amplification of the initial perturbation in the 150 m amplitude simulation; extension amplifies the perturbation by a factor of approximately 4-6 in the low amplitude models but by less than a factor of 2 in the 150 m amplitude model. Such small amplification apparently cannot sufficiently remove the short wavelength topography.

The growth of a single dominant wavelength from large-amplitude, random initial topography (as shown in 4.13c and 4.13e) is not an obvious result. One could imagine that, instead of producing periodic deformation, nonlinearities simply am-

plify whatever irregularities exist in the initial topography, leading to large-scale but irregular (non-periodic) deformation. In fact, numerical models of finite-amplitude compressional folding support this alternative conception of growth, finding that amplification of an initially random perturbation does *not* immediately lead to deformation that reflects the expected dominant wavelength (Mancktelow, 1999). Instead, these models show that, if initial perturbation amplitudes are large, the initial perturbation geometry exerts a strong influence on the final fold geometry, resulting in large-amplitude deformation that is only quasi-periodic (Mancktelow, 1999). Our results contrast with the results of Mancktelow (1999). Even in our large-amplitude initial perturbation simulations, long-wavelength initial topography is modified to reflect a single dominant wavelength. We speculate that these differences result from the rather substantial differences in the two model's rheologies and experimental setups.

The results described above provide significant support for the tectonic resurfacing hypothesis. Our modeling indicates that unstable extension can modify small-scale (~ 10 m or less), random, preexisting topography and replace it, through the action of necking, with moderate-amplitude periodic ridges and troughs. Large-amplitude topography (~ 100 m) is harder to modify due to decreased growth rates at large deformation amplitudes. However, even with random preexisting topography of 100 m, extension produces strongly periodic deformation with an amplitude of several hundred meters.

A number of important questions remain unaddressed by our model. The ability of extensional tectonic deformation alone to completely remove all evidence of the preexisting surface remains unclear. Our results suggest that remnants of large-amplitude, short-wavelength topography, such as crater rims, can remain after groove formation occurs (Fig. 4.13g), yet observations have not revealed any such "ghost" craters within the grooved terrain on Ganymede. Removal of such short-wavelength topography most likely requires significant faulting to break up

and obscure the original terrain. Such faulting is not included in this model. These results also provide little insight into the cause of the grooved terrain's high albedo. Suggestions that tectonic deformation alone can brighten groove terrain by exposing clean ice at the surface cannot be directly tested via this approach, but the relatively low strains present in groove crests (Fig. 4.7) suggests that, at least in those regions, surface brightening must occur by some mechanism other than tectonic deformation.

4.4 Sensitivity Analysis

The simulations described above treat only the temperature gradient, strain rate, and initial surface topography as free input parameters. However, factors such as the elastic properties of the lithosphere, the grain size of ice, the minimum yield strength of the lithosphere, and the surface temperature can also affect instability growth. We determined the sensitivity of our results to variations in these parameters by fixing the model's temperature gradient at 15 K km^{-1} , strain rate at 10^{-13} s^{-1} , and total strain at 31.5% and varying the parameters in question. This analysis provides a more complete understanding of how our results depend on model assumptions.

The elastic parameters of an icy lithosphere are poorly understood. Studies suggest that terrestrial lake and sea ice have average Young's Moduli of $9.3 \times 10^9 \text{ Pa}$ (Gammon et al., 1983). This value is insensitive ($\pm 1\%$) to sample age, impurity content, and crystal quality (Gammon et al., 1983). We used a nominal Young's modulus of 10^{10} Pa , in agreement with this value. A fractured lithosphere can experience larger strains at modest stress than an unfractured lithosphere, and this is sometimes modeled with an effective Young's modulus several orders of magnitude smaller than the actual value (Williams and Greeley, 1998). Figure 4.14a shows the effect of variations in Young's modulus on the total amount of amplification produced by the necking instability. The amplification is relatively insensitive to the exact value of the Young's modulus over the nominal range of 10^9 - 10^{10} Pa for intact ice, varying only by a factor of 0.1. At values of Young's modulus less than

10^9 Pa, however, amplification falls off sharply, suggesting that, if Ganymede's lithosphere behaves as a fractured elastic plate, the growth of necking instabilities may be inhibited. However, the applicability of a model with an artificially reduced Young's modulus to a fractured lithosphere remains questionable because the additional strain in a fractured plate is more properly modeled with a brittle (i.e. plastic) rheology than with an artificially compliant elastic system. Very large, if unrealistic, values of Young's modulus (10^{12} Pa) produce significantly more amplification than the nominal cases. This increase occurs because large values of Young's modulus permit the partitioning of more strain into plastic, rather than viscoelastic, deformation. Since necking due to plastic strain is significantly more efficient than necking due to viscous or elastic strain (e.g. Smith (1975); Fletcher and Hallet (1983); Zuber and Parmentier (1986)), instability amplification increases.

The grain size of the ice within Ganymede's lithosphere is also poorly constrained. Because grain-size-sensitive GBS flow dominates the viscous rheology of ice under the conditions considered in this model, the choice of grain size can strongly affect the rheological behavior of ice (Eq. 4.3). In zones of high shear, terrestrial sea ice has measured grain sizes of 1-7 mm (Budd and Jacka, 1989). However, the cold surfaces of the Galilean satellites may allow ice grains an order of magnitude smaller to form near the surface. To examine the effect of grain size on our results we compared simulations with grain sizes of 0.01 mm, 0.1 mm, 1 mm, and 10 mm (Fig. 4.14b). These grain sizes were held spatially and temporally constant throughout the simulation. Variations in grain size over the nominal range (0.1 - 10 mm) generally do not affect the amount of amplification produced by instability growth. Thus increasing the grain size by an order of magnitude does not appear to sufficiently inhibit the GBS mechanism to affect the viscous flow at depth. At very small grain sizes (0.01 mm) amplification is enhanced by a factor of 1.7, suggesting that, if small grain sizes exist in the lithosphere, unstable extension may be enhanced.

Both temperature and stress affect grain size, which can therefore vary spatially

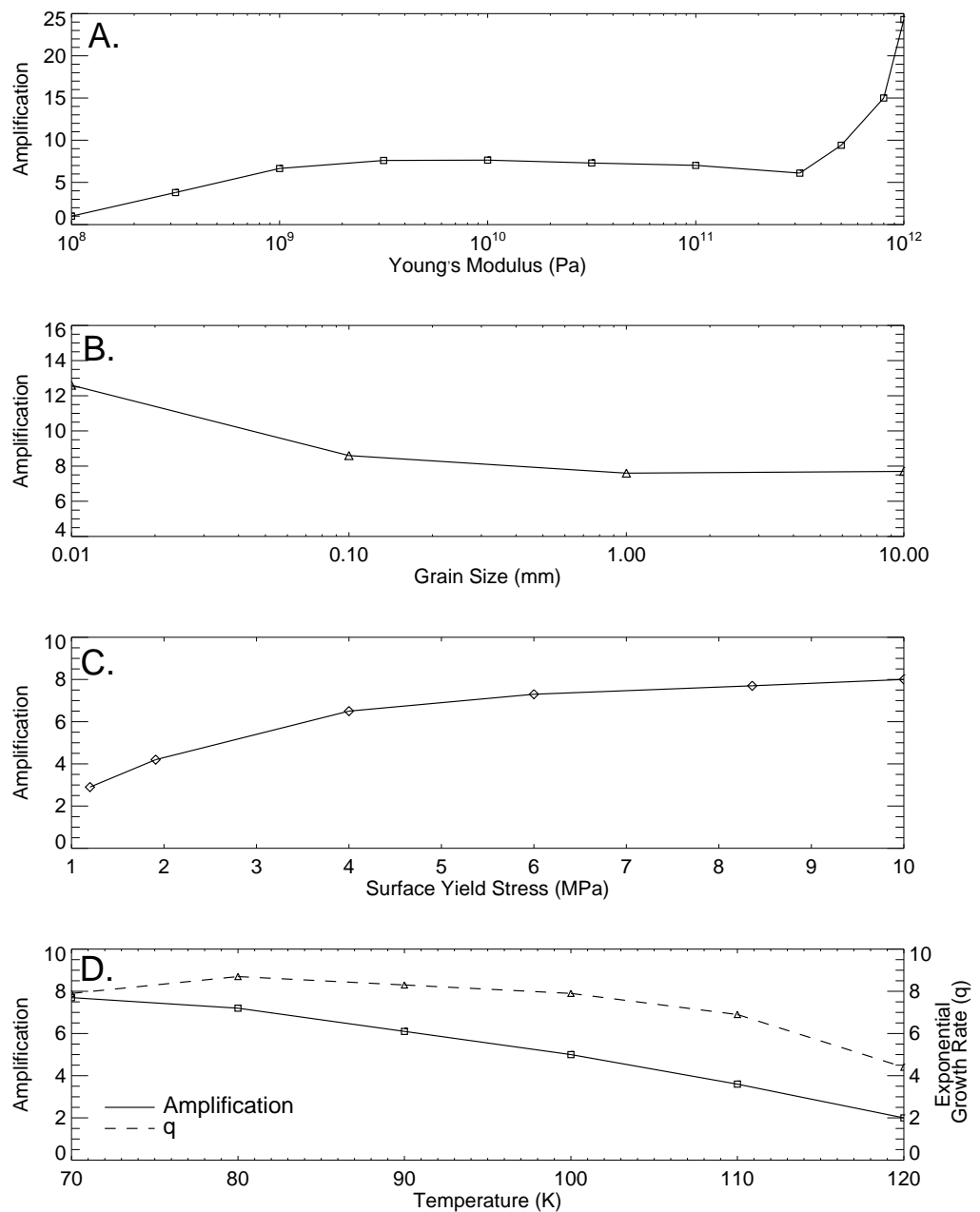


Figure 4.14: Amplification as a function of **A.** Young's modulus, **B.** grain size, and **C.** surface yield stress. Amplification (solid lines) and exponential growth rates calculated after 3.15% extension (dashed lines) as a function of surface temperature are also shown in **D.** See text for description of results.

and temporally within the lithosphere. Recent modeling of grain size variability in convective systems on icy satellites has illustrated that heterogenous distributions of grain size not only occur, but directly affect the convective flow (Barr and McKinnon, 2006; Tobie et al., 2006). High near-surface stresses in our simulations favor production of small grain sizes that can enhance strain rates and lead to strain weakening within these zones. This method of strain localization has been shown to be effective for olivine under certain terrestrial conditions (Braun et al., 1999). On the other hand, a reduction in instability growth can occur if high temperature gradients create large-grained ice at depth, reducing the strength contrast between the brittle surface layer and ductile substrate. A full examination of the effects of heterogenous grain size distributions exceeds the scope of this manuscript, but understanding its role in instability growth warrants further investigation.

The yielding behavior of ice also strongly affects instability growth. Previous modeling suggests that weak lithospheres (lower yield strength) produce smaller growth rates than strong lithospheres (higher yield strength) (Montési and Collins, 2005). The yield strength of our model lithosphere is given by Eq. 4.5. Its dependence on a dependent variable (σ_m) makes it difficult to define a minimum yield strength *a priori*. However, we *can* determine the effect that varying the cohesion (which strongly influences the minimum yield strength) has on our results.

Decreasing the cohesion from our nominal value of 10 MPa ($\sigma_{yield} \sim 8$ MPa at the surface) to 4.7 MPa ($\sigma_{yield} \sim 2$ MPa at the surface) decreases the total amount of amplification by 55% (Fig. 4.14c). Decreasing the cohesion to even lower values results in unphysical (negative) values of yield strength for typical model stresses. If, as measured by Beeman et al. (1988), the yield strength at the surface is 1.2 MPa, the formation of grooves via unstable extension clearly becomes difficult. These results indicate that, aside from the temperature gradient, strain rate, and total strain, the value of the near surface yield strength is the most important factor in influencing instability growth. Thus the formation of grooved terrain via unstable extensional

processes suggests that either the lithosphere behaves relatively strongly, or strain weakening and local heterogeneities can enhance the growth of necking instabilities.

The surface temperature (T_s) can also affect instability growth (Fig. 4.14d). While growth rates are insensitive to the surface temperature for T_s between 70 and 100 K, simulations with very high surface temperatures ($T_s = 120\text{K}$) have infinitesimal growth rates a factor of 2 smaller than low T_s simulations. Also, because increasing the surface temperature effectively decreases the thickness of the deforming layer, growth saturation (described above) occurs earlier in simulations with high surface temperatures than in simulations with low surface temperatures. Thus despite the insensitivity of initial growth rates to surface temperature, the total amount of amplification produced by extension decreases monotonically with increasing surface temperature. We again suggest that if surface temperatures were ~ 100 K or higher, the formation of the grooved terrain via extensional necking requires significant strain weakening or strain localization.

Finally, elucidating how gravitational relaxation, which is naturally included in our model, affected the development of large-scale grooves is essential to understanding the formation of the grooved terrain, a process that may have taken millions of years. Dombard and McKinnon (2006a) calculated relaxation timescales for impact craters on Ganymede and Callisto. Using a rheology consistent with our models (although with warmer surface temperatures), they found that, for a surface temperature of 120 K and heat flows of 10 mW m^{-2} , a 25 km crater will relax by $\sim 10\%$ in 10^7 yrs. In light of these results, we expect that gravitational relaxation can affect the development of ~ 10 -km-wavelength grooves under conditions of low strain rates (long formation timescales) and high heat flow. To test this, we imposed 100-m-amplitude, sinusoidal topography at the surface of a domain with a temperature gradient of 30 K km^{-1} . We separately examined wavelengths of 2 and 10 km, roughly corresponding to the minimum and maximum groove wavelengths produced by our models. The domains relaxed under gravity, without being extended, for a period of

10^7 years. We then measured the differences in the horizontal and vertical position of the surface nodes to determine the extent of the gravitational relaxation. We find that negligible relaxation of groove-like structures occurs after 10 million years; topography with wavelengths of 2 and 10 km changed in amplitude by only 1 m and 6 m respectively. We note that the application of tensile stress may increase the rate at which relaxation occurs. Despite this caveat, we conclude that gravitational relaxation plays an insignificant role in necking instability growth. These results are consistent with Dombard and McKinnon (2006a) who noted that when surface temperatures are low (80 K), viscous relaxation is inhibited.

4.5 Implications and Conclusion

Our simulations confirm that necking instabilities can occur under a broad range of conditions relevant to Ganymede. At infinitesimal strains, we find that maximum instability growth rates occur at high temperature gradients ($\geq 45 \text{ K km}^{-1}$) and moderate strain rates (10^{-13} s^{-1}). Dominant wavelengths range from 1.8-16.4 km (post extension), similar to the wavelengths of Ganymede's grooves. These results are qualitatively consistent with previous, linearized, infinitesimal-strain models (Dombard and McKinnon, 2001). We also find, however, that nonlinearities play a crucial role in instability growth at strains exceeding $\sim 10\text{-}20\%$. Instability growth rates decrease as strains become large, limiting the total amount of amplification that can result from unstable extension. Decline in growth primarily results from the finite thickness of the deforming lithosphere and the extension of the amplifying wavelength, and hence occurs at lower groove amplitudes for high-temperature-gradient, thin-lithosphere models, than for low-temperature-gradient, thick-lithosphere models. This result implies that linear extrapolation of initial growth rates overpredicts groove heights for large strains. Understanding groove formation at large strains therefore requires the use of finite-strain models.

The inclusion of large strains in the modeling of extensional necking instabilities

places new constraints on the formation of Ganymede's grooved terrain. Because instability growth does not continue exponentially at finite strains, the high thermal gradients ($\sim 35 \text{ K km}^{-1}$) required by linear infinitesimal-strain models to produce large amplitude grooves are unnecessary. Instead, thermal gradients as low as $10\text{-}20 \text{ K km}^{-1}$ are preferred as long as large strains are locally available. This suggests that the formation of grooved terrain required only modest heat fluxes of $\sim 20 \text{ mW m}^{-2}$, rather than the 75 mW m^{-2} predicted by linear models. Such a heat flux would almost certainly have been available on Ganymede as the value falls well below estimates of heat flux derived from the analysis of both furrow systems within Ganymede's dark terrain, and elastic thicknesses near rift zones (McKinnon and Parmentier, 1986; Nimmo et al., 2002).

In addition, we have shown that the formation of necking instabilities can modify preexisting terrains of up to 100-m topography, replacing them with moderate-amplitude, periodically spaced ridges and troughs. These structures are consistent with Ganymede's grooved terrain, although somewhat lower in amplitude. These models provide an important step in quantitatively examining the role of tectonic resurfacing in groove formation.

Our modeling also raises new difficulties for the necking instability model. The use of a more realistic viscoelastic-plastic rheology decreases the initial exponential growth rates by an order of magnitude compared to the results of linear models. These decreased growth rates combine with growth fall-off at large strains to limit the total amplitude of deformation produced by unstable extension. No more than 8-fold amplification of the initial perturbation occurred in any simulation after application of 31.5% strain. Thus, if Ganymede's pre-grooved terrain consisted of $\sim 10 \text{ m}$ amplitude topography, extension would produce grooves with amplitudes of $\sim 80 \text{ m}$, a factor of five smaller than is observed. If strains were typically less than 31.5%, the formation of Ganymede's grooved terrain via unstable extension becomes even more difficult. Furthermore, the inclusion of realistic near surface strength profiles, and

warmer surface temperatures may further curtail instability growth. We therefore emphasize that forming grooved terrain via unstable extension remains a difficult problem.

The challenges to groove formation may yet be overcome, however, by the inclusion of strain localization mechanisms not considered in the present model. The incorporation of strain or strain-rate softening (i.e. a reduction in the cohesion or effective viscosity of material at high strains or strain-rates respectively) into numerical models of terrestrial extension strongly affect the model results (Behn et al., 2002; Frederiksen and Braun, 2001; Poliakov and Buck, 1998; Lavier et al., 2000). Frederiksen and Braun (2001) demonstrated that strain softening in the Earth's mantle leads to significant strain localization for a range of assumptions about how softening occurs. Behn et al. (2002) further showed that including strain-rate softening in models of continental and oceanic rifting led to increases in local strain rates by two orders of magnitude, which in turn led to significantly more surface deformation than in models without strain softening. The inclusion of these processes in our model should have an analogous effect, significantly increasing groove amplification. Furthermore, the presence of discrete faults may also help localize strain. Montési and Collins (2005) found that long-distance fault interactions in an icy lithosphere could lead to structures similar to Ganymede's grooved terrain. Such fault interactions may help to focus strain within extensional necks, and lock-in the amplifying wavelength, preventing the fall-off in growth caused by the shifting wavelength of the perturbation at large strains. The inclusion of these processes appears to be essential to properly modeling groove formation.

The conditions that led to groove formation on Ganymede are not unique in the solar system. Evidence of extensional tectonics abounds on the icy satellites of both Saturn and Uranus. Our modeling of instability growth at finite strains suggests that the production of significant topography, via unstable extension, does not require high thermal gradients. Furthermore, the low surface temperatures and

reduced surface gravity of these small bodies permits higher instability growth rates than on Ganymede (Herrick and Stevenson, 1990). Unstable extension may have therefore played a significant role in modifying not only the surface of Ganymede but also the surfaces of icy satellites such as Enceladus and Miranda.

CHAPTER 5

UNSTABLE EXTENSION OF ENCELADUS' LITHOSPHERE

The material in the chapter has been published in the journal Icarus: Bland, M. T., R. A. Beyer, and A. P. Showman (2007). Unstable extension of Enceladus' lithosphere. Icarus, 192, 2007. Some material has been excised to avoid repetition with Chapter 4.

5.1 Background

Saturn's moon Enceladus is one of the great enigmas of the outer solar system. Its icy lithosphere bears witness to a long history of deformation, creating a surface that spans one of the broadest age ranges in the solar system: from nearly primordial (4.2 Ga) to perhaps less than one million years old (Plescia and Boyce, 1983; Porco et al., 2006). The variability in surface age is due to regional resurfacing caused by some combination of viscous relaxation of impact craters, cryovolcanism, and tectonic resurfacing (Passey, 1983; Squyres et al., 1983; Kargel and Pozio, 1996). Although it has an effective radius of only 251 km, the satellite is geologically active (Porco et al., 2006; Spencer et al., 2006). This activity is focused in the South Polar Terrain (SPT), which consists of young, tectonically disrupted terrain that is separated from the rest of Enceladus by a sinuous escarpment hundreds of meters high (Porco et al., 2006). The region is further marked by prominent, long, parallel fractures known as "tiger stripes" (Porco et al., 2006), high heat flow (Spencer et al., 2006) and a water ice plume (Hansen et al., 2006; Porco et al., 2006). The geologic activity in the SPT is likely driven by tidal heating resulting from resonant interactions in the Saturnian system (Yoder, 1979; Squyres et al., 1983; Lissauer et al., 1984; Ross and Schubert,

1989; Wisdom, 2004), though the specific mechanism remains unclear (Meyer and Wisdom, 2007, 2008).

There are several plausible mechanisms capable of creating Enceladus' SPT. One possibility is that the thermal activity and young surface age at the south pole is the result of a low-density diapir in Enceladus' ice or silicate mantle (Nimmo and Pappalardo, 2006). The rise of such a diapir can generate substantial extensional stress within the lithosphere (Janes and Melosh, 1988; Nimmo and Pappalardo, 2006), contributing to the tectonic resurfacing of the region and the creation of the tiger stripe fractures. An additional consequence of a low-density diapir is the reorientation of the satellite such that the density anomaly rotates towards the spin axis. This may explain why Enceladus' active region is centered on the pole (Nimmo and Pappalardo, 2006). Nimmo and Pappalardo (2006) showed that an ice diapir with a sufficient density contrast can cause up to 30° of poleward rotation if the elastic thickness exceeds 0.5 km. Collins and Goodman (2007) have also suggested that tectonic stress and global reorientation can be caused by localized melting within the ice mantle. This mechanism is not only consistent with the high heat flows observed in the SPT, but can also explain the anomalous shape of Enceladus (Collins and Goodman, 2007).

Somewhat older terrains (Sarandib and Diyar Planitia) with a similar geometry and scale to the SPT have also been observed in Enceladus' equatorial region (Helfenstein et al., 2006) (Fig. 5.1). These young terrains are set apart from the rest of Enceladus by large tectonic structures: Samarkand Sulcus to the west, Hamah Sulcus to the north, and Harran Sulcus to the east. While no tiger-stripe-like fractures are evident, extensive sets of parallel, north-south trending ridges and troughs occur within the planitiae themselves, and evidence for resurfacing and extensional tectonics abounds.

The ridges and troughs observed in the Sarandib-Diyar province can be formed by a variety of mechanisms (Pappalardo and Greeley, 1995). One such mechanism

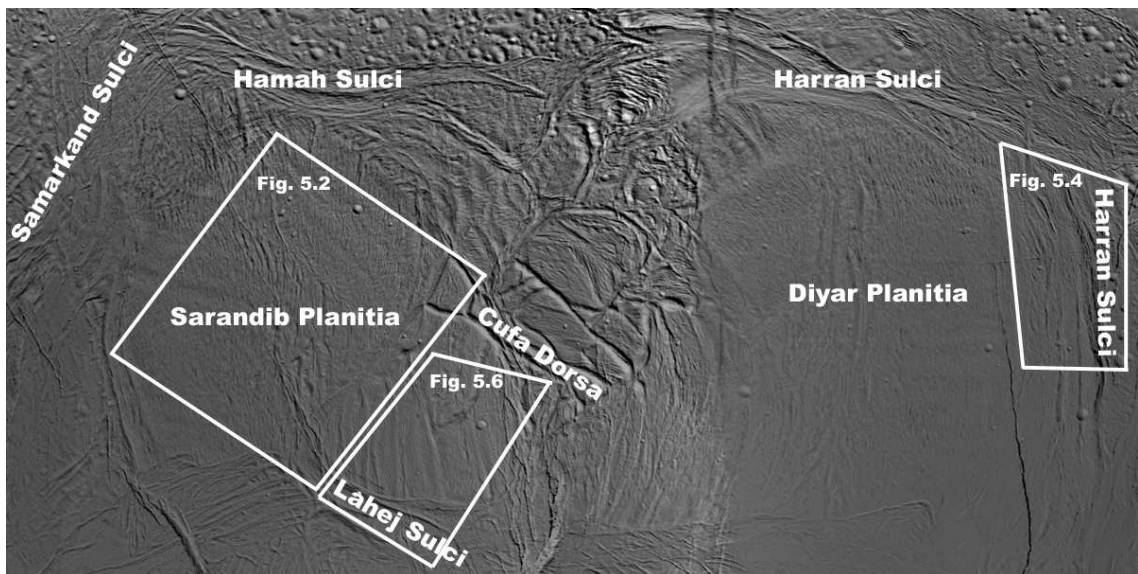


Figure 5.1: Cassini and Voyager image mosaic of Enceladus' equatorial region from longitude 225° to 330° W and latitude 20° S to 35° N. The region is marked by the young terrains of Sarandib and Diyar Planitia which are separated from Enceladus' older terrains by a near-continuous chain of Sulcis. The Planitia themselves contain extensive sets of ridges and troughs. White polygonal boxes indicate the approximate location of Figures 5.2, 5.4, and 5.6. Illumination angle varies across the image but is generally from the southwest. Image courtesy of NASA/JPL-Caltech.

is unstable extension (also known as extensional necking) of the lithosphere. This mechanism assumes that the lithosphere consists of a brittle surface layer underlain by a viscous substrate. When such a lithosphere extends it can become unstable, causing perturbations in the thickness of the brittle layer to amplify, deforming the surface into parallel, periodically spaced, undulating pinches and swells (Fletcher and Hallet, 1983). Because the ridges and troughs of Ganymede's grooved terrain (the archetypical example of ridge and trough terrain) are periodically spaced (Grimm and Squyres, 1985; Patel et al., 1999), and gently undulating (average slopes are $\sim 6^\circ$ (Squyres, 1981)), unstable extension has become the favored mechanism for their formation (e.g. Herrick and Stevenson, 1990; Pappalardo et al., 1998; Collins et al., 1998b; Dombard and McKinnon, 2001; Bland and Showman, 2007, Chapter 4). Furthermore, it has been suggested that unstable extension may be responsible for ridge and trough terrains throughout the icy satellites (Herrick and Stevenson, 1990).

As described in Chapter 4, semi-analytical, linearized, infinitesimal-strain models of unstable extension have found that, assuming a constant growth rate (defined below) and background strain rate, the amplitude of a topographic perturbation in an otherwise uniform flow changes exponentially with the form

$$\mathcal{A} = \mathcal{A}_o \exp[(q - 1)\dot{\epsilon}t], \quad (5.1)$$

where \mathcal{A} is the amplitude of the surface deformation, \mathcal{A}_o is the amplitude of the initial perturbation, q is the exponential growth rate, and $\dot{\epsilon}t$ is the strain (Fletcher and Hallet, 1983). The growth rate q determines the rate at which topographic amplitudes change under infinitesimal strain. For $q > 1$, the initial perturbation amplifies and extension occurs unstably. While multiple wavelengths may be present in the initial perturbation, the analysis assumes that each wavelength component amplifies independently from the rest, allowing the growth rate of each component to be calculated separately.

Production of large-scale topography, such as the ridges and troughs of the Sarandib-Diyar province, requires high exponential growth rates; adopting a topographic amplification ($\mathcal{A}/\mathcal{A}_o$) of 10-100 after 10% strain implies that growth rates must achieve ~ 40 (Fletcher and Hallet, 1983; Herrick and Stevenson, 1990). Herrick and Stevenson (1990) applied an analytical, infinitesimal-strain model of unstable extension to Enceladus and found that exponential growth rates were great enough (≥ 40) to produce ridges and troughs several hundred meters high under a broad range of strain rates and lithospheric thermal gradients. The highest growth rates ($q \sim 100$) occurred at high thermal gradients ($> 30 \text{ K km}^{-1}$) and moderate strain rates ($\sim 10^{-13} \text{ s}^{-1}$). Subsequent work has shown that the inclusion of grain-size-sensitive flow laws for ice, such as grain boundary sliding (GBS) (not included in Herrick and Stevenson (1990)), act to further increase instability growth rates (Dombar and McKinnon, 2001). Thus, based on these analyses, unstable extension could have produced much of Enceladus' periodic ridges and troughs.

The numerical modeling of unstable extension described in Chapter 4 has shown, however, that as extension progresses to finite strains ($> 5\%$), growth does not continue exponentially (as predicted by Eq. 5.1) but decreases rapidly, limiting the total amplitude of the deformation produced by extension (Bland and Showman, 2007, Chapter 4). Furthermore, the use of a more realistic plastic rheology and the inclusion of elastic behavior produces exponential growth rates an order of magnitude lower than those calculated by the linearized perturbation model described above (Bland and Showman, 2007, Chapter 4). These low growth rates further limit the total amount of amplification produced by extension. Because of these difficulties, the applicability of unstable extension to the formation of Enceladus' ridge and trough terrains must be reassessed.

A salient feature of unstable extension is that the morphology (wavelength and peak to trough amplitude) of the deformation produced depends sensitively on the thermal gradient of the lithosphere (Fletcher and Hallet, 1983). In general, a spe-

cific wavelength component amplifies significantly faster (has much larger q) than the other wavelengths, producing strongly periodic topography. High thermal gradients produce short-wavelength topography while low thermal gradients produce long-wavelength topography. Comparison between measurements of topographic wavelengths within ridge and trough terrains and models of extensional necking therefore permits estimation of the thermal conditions in the lithosphere during ridge and trough formation (Fink and Fletcher, 1981; Dombard and McKinnon, 2001).

In this chapter we first describe new measurements of ridge and trough topography within the Sarandib-Diyar province derived from photoclinometry profiles (Section 5.2). We then use a numerical, nonlinear, finite strain model to determine whether unstable extension is applicable to Enceladus (Section 5.3). We find that, under certain conditions, instability growth is strong enough to have produced the ridges and troughs of the Sarandib-Diyar province (Section 5.4). Comparison of the dominant wavelengths produced by the numerical model to our topographic profiles allows estimation of the thermal gradient and elastic thickness of the lithosphere during the extensional event (Section 5.5).

5.2 Photoclinometry

5.2.1 Method

In order to obtain an estimate of the topography of the ridge and trough terrain, we use a profiling photoclinometry technique based upon the point photoclinometry technique of Beyer et al. (2003). This technique provides a model slope for an individual pixel. By taking a profile of such pixels in the down-Sun direction, a topographic profile can be constructed.

The method uses a lunar-Lambert photometric function of the form (Beyer et al.,

2003)

$$I(\mu, \mu_0, \alpha) = B_0(\alpha) \left[\frac{2L(\alpha)\mu_0}{\mu + \mu_0} + (1 - L(\alpha))\mu_0 \right], \quad (5.2)$$

where $I(\mu, \mu_0, \alpha)$ is the reflectance function, μ is the cosine of the emission angle, μ_0 is the cosine of the incidence angle, α is the phase angle, $B_0(\alpha)$ is the intrinsic albedo, and $L(\alpha)$ is a function of the photometric properties of Enceladus' surface and is given by McEwen (1991). To calculate $L(\alpha)$ we use photometric properties derived from Voyager and ground based observations of Enceladus' surface (Verbiscer and Veverka, 1994): width parameter for the opposition effect (h) of 0.05 (Hapke, 1986), opposition surge amplitude (B_o) of 0.21, single-scattering albedo (w) of 0.998, macroscopic roughness parameter ($\bar{\theta}$) of 6° , and a Henyey-Greenstein asymmetry parameter (g) of -3.999 (Verbiscer and Veverka, 1994). While these parameters are uncertain, determination of model slope values is robust to small variations in the value of L (Beyer et al., 2003). The parameters listed above and the various phase angles of the profiles led to different values of L that were used for each image. They varied from 0.13 to 0.23.

When a profile of pixels is taken in the down-Sun direction, the average brightness of those pixels (I) is assumed to be the brightness of a flat surface. The brightness of each individual pixel (I^*) is then divided by the flat brightness. Because the incidence and emission angles of the flat surface are known from the spacecraft geometry, use of the ratio of I^*/I permits determination of the slope of an individual pixel (θ) relative to the flat surface. This study uses the same table-lookup mechanism quantized to the quarter degree in θ as described in Beyer et al. (2003). All Cassini ISS images (Porco et al., 2004, 2005b) were first processed with CISSCAL 3.3 (Porco et al., 2005a) and then imported into ISIS 2 (Gaddis et al., 1997; USGS, 2007) to obtain estimates of the photometric angles and image geometry.

The point photoclinometry method returns a slope for each pixel. To convert that slope into a change in elevation across that pixel, the width of the pixel in distance units as well as the down-Sun direction (equivalent to the profile direction)

must be known. We choose not to geometrically reproject the images that we used. While doing so would alleviate some sources of error, it would also introduce others. The pixels we measured did not represent a square area on the surface of Enceladus, but instead a rectangle (different resolution in the line and sample directions). Since we are only interested in the length of the profile segment, x , that runs through a given pixel in the down-Sun direction, we assume that the resolution of that pixel, r , is the resolution of the axis closest in direction (vertical or horizontal) to the strike of the profile direction. The profiles on the images in this study are mostly vertical, so the value of r was taken from the line resolution. We define ψ as the angle between the profile direction and pixel axis, where $0^\circ \leq \psi \leq 45^\circ$. We calculate the distance, x , across each pixel along the profile as

$$x = \frac{r}{\cos \psi}. \quad (5.3)$$

We make the simplifying assumption that ψ and r , hence x , do not change across the profile so Eq.5.3 is evaluated only once for each profile.

Once the distance across each pixel, x , is obtained from Eq.5.3, the elevation difference, Δz , can be determined across each pixel. If a given pixel has a angle, θ (derived from the Beyer et al. (2003) technique), then

$$\Delta z = x \tan \theta. \quad (5.4)$$

The distance and the elevation difference across each pixel can be put together to make a profile of elevation as a function of distance along that profile.

The creation of a topographic profile in this manner is a cumulative process. Unfortunately, the errors are cumulative as well. The error in the elevation across the first pixel depends on the error in the distance across that first pixel, x , and the error in the slope, θ , for that pixel. The error in the elevation after the second pixel is dependent on the errors in x and θ for the second pixel as well as those in the first, and so on. So in addition to the errors inherent in the point photogrammetry

technique (e.g. difficulties of albedo variation and slope azimuth (Beyer et al., 2003)), there is the added contribution of this cumulative error for the profiling photoclinometry technique. As a result, the absolute elevation difference between the beginning and end of a profile is not very reliable. However, relative elevation differences are reliable if they are separated by only a few tens of pixel distances.

An additional source of error comes from the fact that the photometric angles are going through significant changes from one end of the profile to another due to Enceladus' planetary curvature (the profiling photoclinometry technique assumes that the profile is on "flat" terrain). This causes the original profiles to have an artificial parabolic shape and contributes error to the amplitude of features in the topography, but does not affect wavelengths.

Finally, because any variation in pixel values is assumed to be due to variations in pixel slope alone, photoclinometry techniques can be strongly affected by shadows. True shadows in the image would cause the photoclinometry algorithm to report erroneously large negative slopes. The incidence angles for the profiles in this study are $35^\circ \pm 5^\circ$, which indicates that there would have to be a true slope steeper than $55^\circ \pm 5^\circ$ to cast such a shadow, and that slope would have to be at least 125 m tall to completely shadow one pixel in the highest-resolution image in this study (88 m/pixel). While landforms of this size are unlikely, they are not impossible. We carefully examined the model slopes produced by the algorithm for all profiles, and found no slopes greater than 45° . Although a true slope of $55^\circ \pm 5^\circ$ would cast a shadow, the model slope reported by the photoclinometry algorithm for such a shadowed pixel would be much greater. Therefore, we do not believe that our results are affected by the presence of shadows.

5.2.2 Topography

Photoclinometry profiles were obtained within Sarandib Planitia, Diyar Planitia, and the region between the two Planitiae, bounded to the north by Cufa Dorsa and

to the south by Láhej Sulcus (hence forth referred to as the Cufa-Láhej region) (Fig. 5.1). To determine whether the ridge and trough terrain is periodic, a Fourier analysis was performed on each profile. This analysis required that the parabolic shape of the profiles be removed. This was accomplished by fitting, and subsequently subtracting off a 3rd or 4th order polynomial from each profile, creating a “flattened” version of the topography. Because the topographic wavelengths of interest are much shorter than the long-wavelength artifact, and because subtraction of the polynomial fit has no effect on the wavelengths present within the terrain, the following results are independent of the details of the polynomial fit (e.g. order or y-intercept). With the long-wavelength artifact removed, the profile was Fourier transformed to search for periodicity. Because photoclinometry profiles were taken in the down-Sun direction rather than perpendicular to the ridges and troughs, the wavelengths determined from the Fourier analysis as well as topographic amplitudes required geometric correction. Furthermore, the Fourier method we used returns power values at constant interval wavenumbers (km^{-1}). The spectral resolution in kilometers is therefore not constant but decreases at long wavelengths. This has the affect of smearing out the long wavelength information contained in the spectra. The “flattened” profiles and their Fourier spectra are shown in Figs. 5.3, 5.5, and 5.7.

Three photoclinometry profiles were constructed within Sarandib Planitia (Figs. 5.2 and 5.3). Profile BB' indicates that the ridges and troughs of Sarandib have a strong periodicity with a wavelength of ~ 4 km. The dominant features in this profile have amplitudes of ~ 400 m, while the smaller ridges and troughs have amplitudes of 100-200 m. Profile CC' indicates that longer wavelength deformation (8 km to 10 km) also occurs within Sarandib. This gently undulating deformation (the average slope in profile CC' is 6°) is oriented roughly east to west, diagonal to the dominant northwest-southeast trend of the shorter-wavelength ridges and troughs in profile BB'. These features have amplitudes of ~ 200 m. Similar undulations can be seen just to the south of profiles AA' and BB'. Profile AA' shows no obvious moderate

wavelength (≥ 2 km) periodicity, though long wavelengths are clearly present in the spectrum. A weak peak at 1.5 km is observed, suggesting a fine scale tectonic fabric in the region. This fabric is also evident in the power spectra of profile BB' and CC' but tends to be washed out by the strong peaks at other wavelengths. We conclude that this tectonic fabric pervades the Sarandib Planitia region. Average (RMS) slopes in the Sarandib Planitia profiles are between 6° and 10° . Finally, we note that the low angles between the down-Sun direction and visually dominant northwest-southeast trending ridges and troughs makes accurate characterization of their true amplitudes and wavelengths difficult.

Despite their apparent diversity, the three profiles paint a coherent picture of complex extensional deformation within Sarandib Planitia. Profile BB', which shows strong periodicity, transects a swath of large-amplitude, periodically spaced ridges and troughs. These are the dominant tectonic features in the region. However, the amplitude of these features decreases to the west, until they are unobservable in profile AA'. This pattern suggests that the amount of strain (and thus amplitude of the topography produced) varied locally within the planitia during the extensional event. Long wavelength deformation (profile CC') trending diagonally to the dominant northwest-southeast ridges and troughs may be the result of overprinting, wherein deformation of one wavelength has formed on, but not completely destroyed, older deformation of a different wavelength.

Diyar Planitia bears a strong resemblance to Sarandib Planitia, with numerous parallel ridges and troughs oriented in the north-south direction (Fig. 5.4). Each of the three profiles constructed contains at least two deformation wavelengths (Fig. 5.5). The power spectrum of Profile AA' reveals a broad peak at 7.1 km and a smaller but significant peak at 4.3 km. This weaker peak appears to be associated with finer-scale ridges and troughs, similar in appearance to those of Sarandib Planitia, while the peak at 7.1 km appears related to the spacing of several large-amplitude graben-like features. Amplitudes within this profile are generally 300 to 400 m, the highest

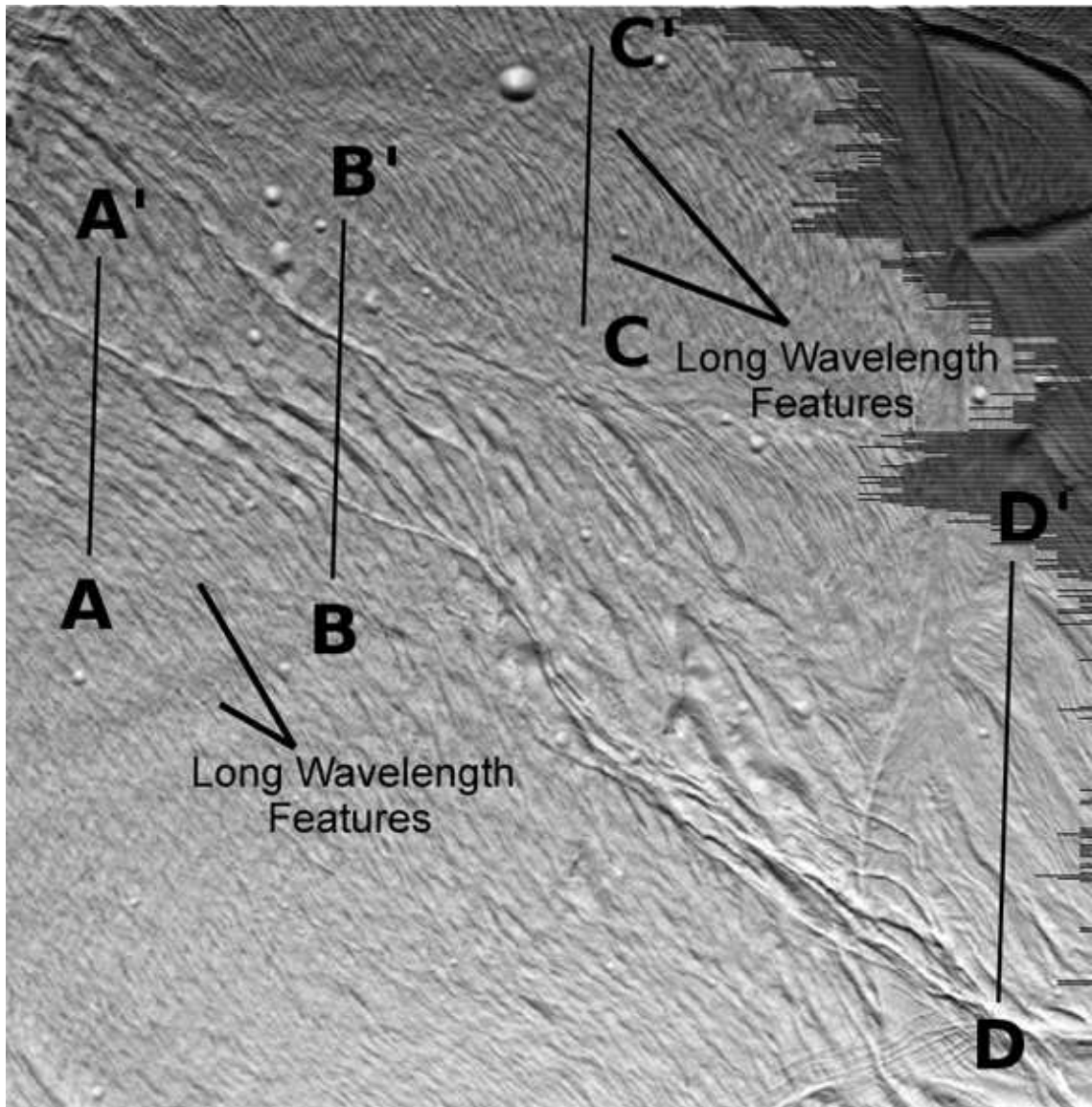


Figure 5.2: Portion of Cassini ISS image N1487300285_1 of Sarandib Planitia with positions of photoprofiles indicated (see Fig. 5.3). The topography and power spectrum of profile DD' is shown in Fig. 5.7. The long-wavelength features indicated in the image run approximately west-southwest to east-northeast near profiles AA' and BB' and approximately west-northwest to east-southeast near profile CC'. They show up as broad albedo features with a wavelength of ~ 10 km. Profiles AA', BB', CC', and DD' are 30.7 km, 37.0 km, 28.8 km, and 45.5 km long, respectively. Image resolution is approximately 200 m/pixel but varies across the image. North is up.

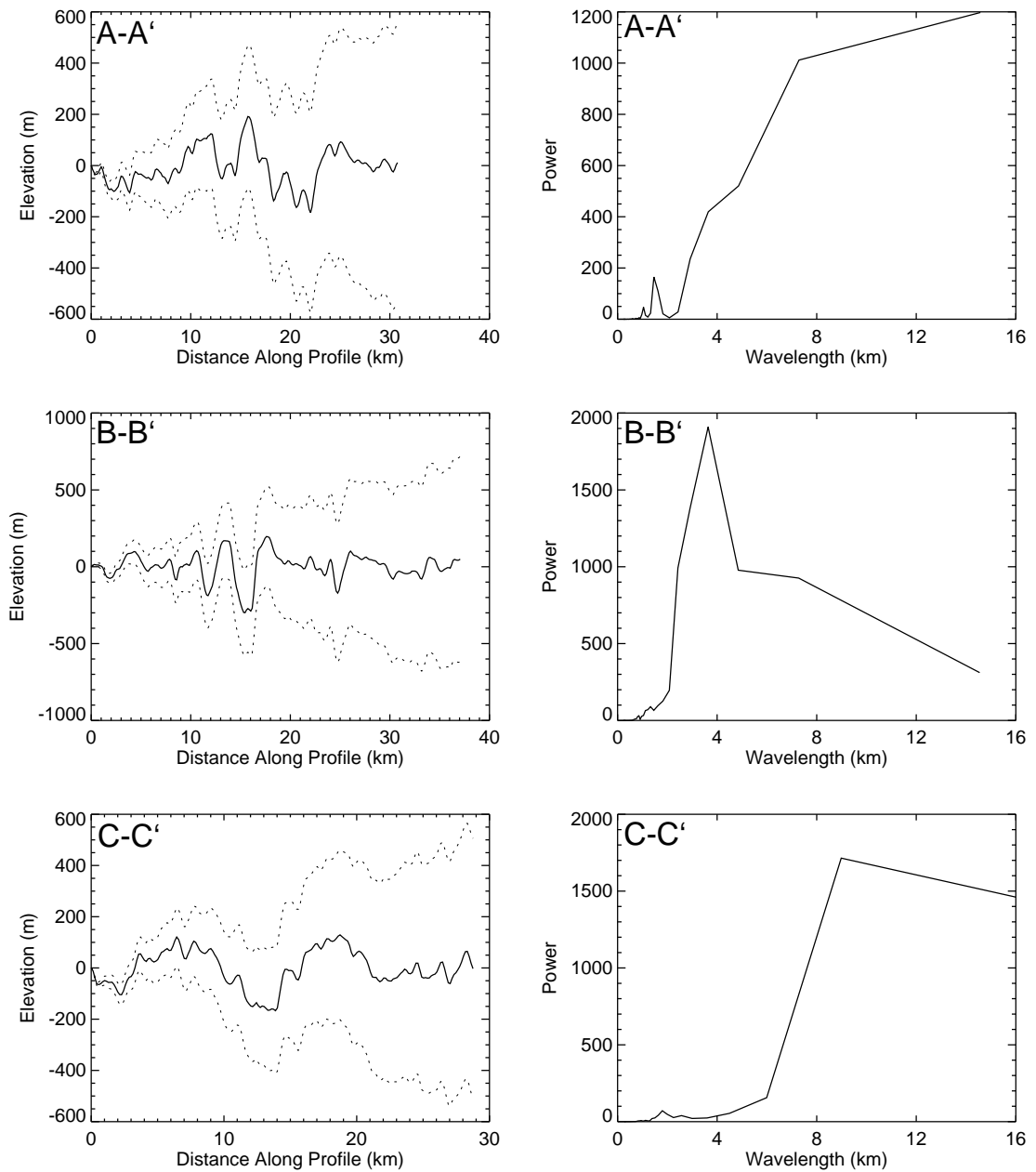


Figure 5.3: Photoclinometry and Fourier spectra of the profiles indicated in Fig. 5.2. In the profiles, solid lines indicate the measured topography and dotted lines indicate the $\pm 1^\circ$ error envelope. Spectra show geometrically corrected wavelengths.

of any ridged terrain we examined. The ridges and troughs of Profile BB', just north of profile AA', are strongly periodic with a wavelength of 2.7 km. A second, weaker peak at 5.4 km is also present. Topographic amplitudes in this region are 200 to 300 m. Profile BB' appears to transect fewer large-scale features and thus seems to provide a relatively uncomplicated profile of the ridge and trough topography of Diyar Planitia. Like profile AA', profile CC' in the northern reaches of Diyar Planitia contains a broad wavelength peak at 7 km and weaker but significant peak at 3.5 km. Again, the shorter wavelength peak appears related to ridge and trough terrain while the long wavelength peak results from the spacing of several-large amplitude features. Amplitudes within this profile approach 300 m. Finally we note that near the image resolution limit (~ 200 m), finer scale deformation occurs. This deformation appears in the power spectra as a very weak signal at short wavelengths, and is likely associated with small-scale faulting that accommodates the large-scale deformation. Average slopes in Diyar Planitia are 12° to 13° , somewhat higher than in Sarandib Planitia.

We conclude that Diyar Planitia contains periodically spaced ridges and trough with wavelengths between 2.7 and 4 km. The Fourier spectrum of each profile indicates a significant peak within this wavelength range. Superimposed on these ridges and trough are several large, long-wavelength features. Because these features have larger amplitudes than the shorter wavelength ridges and troughs, their spacing produces strong peaks in the power spectra. Finally, like Sarandib Planitia, short wavelength deformation may be accommodating the long-wavelength topography. While the geologic picture is complex, the appearance of multiple scales of deformation, including the coexistence of ridges-and-troughs and graben, is consistent with high-resolution images of grooved terrain on Ganymede (Pappalardo et al., 1998).

The Cufa-Láhej region also contains regularly spaced, parallel grooves trending northwest-southeast (Fig. 5.6). Topographic wavelengths within this region have peaks between 4 km and 9 km with amplitudes of ~ 100 m (Fig. 5.7). Comparison

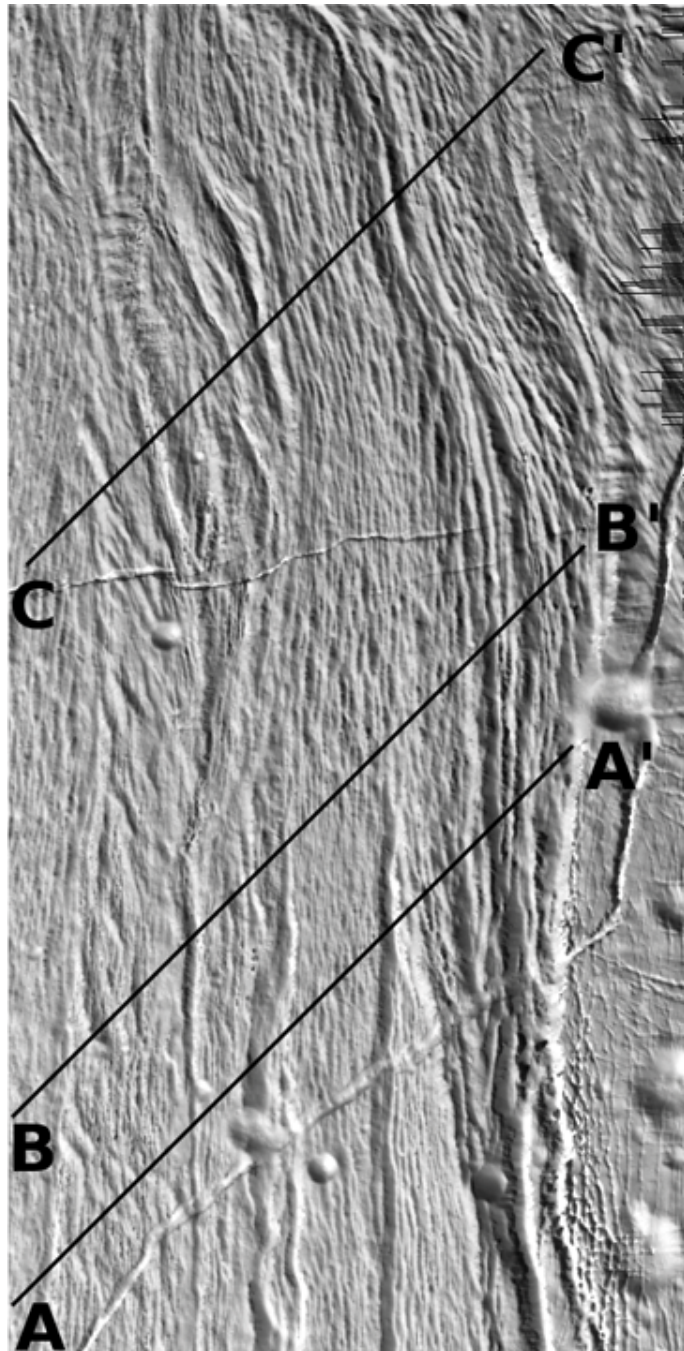


Figure 5.4: Portion of Cassini ISS image N1489049936_2 of Diyar Planitia indicating the positions of photoprofiles shown in Fig. 5.5. Profiles AA', BB', and CC' are 52.8 km, 53.9 km, and 48.7 km long respectively. Image resolution is approximately 200 m/pixel but varies across the image. North is up.

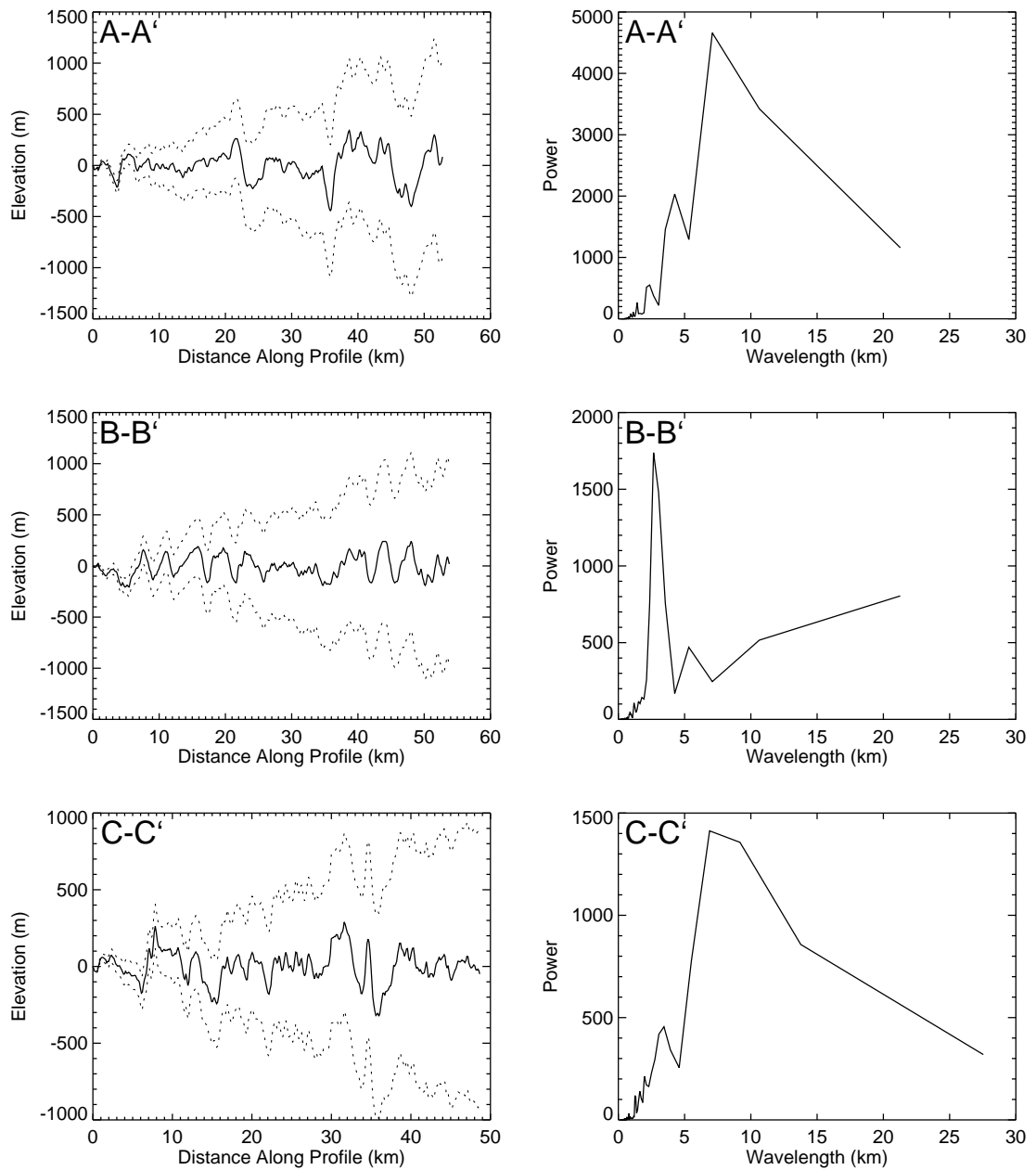


Figure 5.5: Photoclinometry and Fourier spectra of the profiles shown in Fig. 5.4. In the profiles, solid lines indicate the measured topography and dotted lines indicate the $\pm 1^\circ$ error envelope. Spectra show geometrically corrected wavelengths.

to the image (Fig. 5.6) suggests that the long-wavelength undulatory features (6-10 km) dominate the topography. These low amplitude features have average slopes between 5° and 7° and are reminiscent of the gently undulating east-west trending features in Sarandib Planitia (Fig. 5.2, Fig. 5.3 profile CC'). The power spectrum of profile BB' indicates that two wavelengths are present in the deformation, one at 4 km and one at 8.5 km, suggesting a complex history of extension. Several shorter wavelengths between 1 km and 2.5 km are also present in the region. These short-wavelength features are consistent with the tectonic fabric seen throughout Sarandib-Diyar province.

Several characterizations of the "typical" ridge and trough morphology found in the Sarandib-Diyar province may be made. Both Sarandib and Diyar Planitia contain northwest-southeast or north-south trending quasi-periodic ridges and troughs with wavelengths near 3 to 4 km. The Cufa-Láhej region contains longer wavelength deformation with dominant wavelengths of 4 to 9 km. Long-wavelength deformation is also present in both planitiae and suggests a complex history of tectonism in the region. Average slopes throughout the Sarandib-Diyar province are 5° to 13° with maximum slopes up to 45° . This indicates that, while there are exceptions, the ridges and troughs in the region are mostly low-slope features. Short-wavelength (generally 1 km to 2 km) deformation occurs throughout the entire Sarandib-Diyar Planitia and may be the result of small-scale fracturing that is accommodating the large-scale deformation (Pappalardo et al., 1998). These observations suggest that the ridges and troughs in the Sarandib-Diyar province consist of parallel, periodically spaced structures with low slopes and are therefore consistent with formation via unstable extension of the lithosphere.

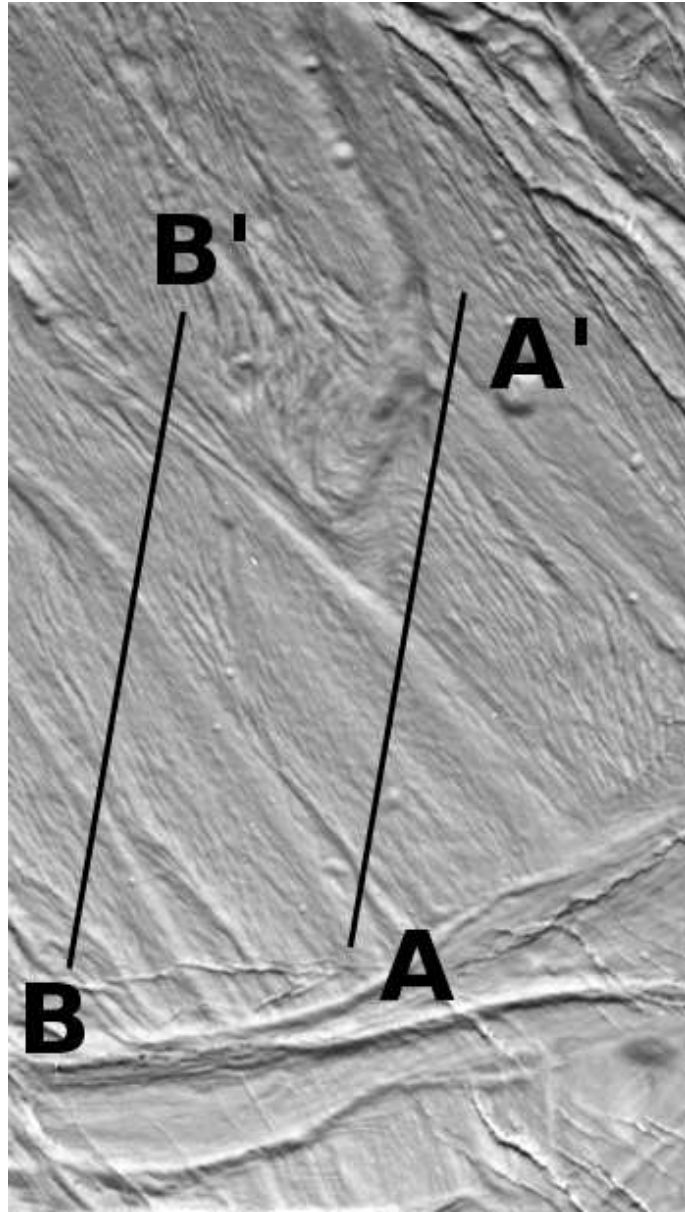


Figure 5.6: Portion of Cassini ISS image N1487300107.1 of the Cufa-Láhej region indicating positions of the photoclinoetry profiles shown in Fig. 5.7. Profiles AA', and BB' are 52.4 km, and 52.4 km long, respectively. Image resolution is approximately 200 m/pixel but varies across the image. North is up.

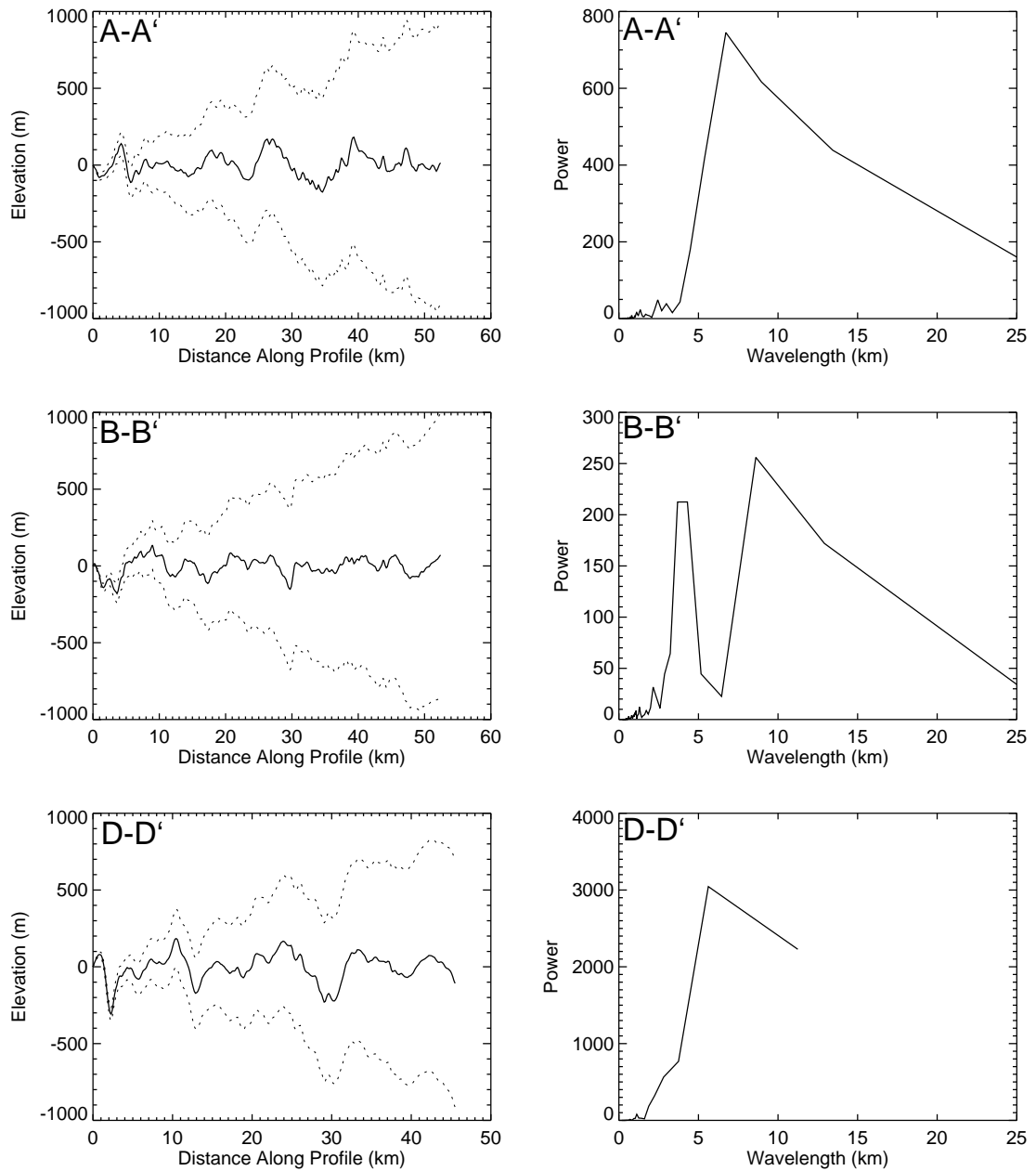


Figure 5.7: Photoclinometry and Fourier spectra of the profiles indicated in Fig. 5.6. In the profiles, solid lines indicate the measured topography and dotted lines indicate the $\pm 1^\circ$ error envelope. Spectra show geometrically corrected wavelengths. The location of profile DD', on the northwest edge of the Cufa-Láhej region, is shown in Fig. 5.2.

5.3 Numerical Modeling of Unstable Extension

In order to determine whether the ridges and troughs of the Sarandib-Diyar province are consistent with unstable extension, the necking instability mechanism must be reassessed under Enceladus-like conditions. Following the methods of Bland and Showman (2007, Chapter 4), we use the lagrangian, finite-element model TEKTON (version 2.3) in plane strain (Melosh and Raefsky, 1980) to examine the growth of instabilities during extension of an icy lithosphere as a function of strain rate and vertical temperature gradient. The model, which includes elastic, viscous, and plastic deformation, has been described in detail in Chapter 4. We again utilize the composite rheology described in Chapter 4 and Appendix B, which includes three dislocation creep flow mechanisms, grain boundary sliding (GBS), basal slip (BS), and Newtonian diffusion. All rheological data is given in Table 4.1 and we used a grain size of 1 mm in all simulations.

As in Chapter 4, a total extensional strain of 31.5% is applied to the model lithosphere over timescales ranging from 10^4 to 10^7 years. This implies strain rates spanning three orders of magnitude from 10^{-12} s^{-1} to 10^{-15} s^{-1} . The value of strain used is consistent with measurements of truncated craters in Enceladus' northern hemisphere, which suggest several tens of percent strain has occurred (Passey, 1983). Our model domains were 40 km to 200 km long, 12 km to 96 km deep, and have square elements 167 m to 1 km on a side. A small amplitude (generally 10 m peak to trough), sinusoidal perturbation is applied to the surface of the domain to allow instabilities to initiate.

We assume a linear thermal gradient within the lithosphere of Enceladus and investigate temperature gradients ranging from 2 K km^{-1} to 45 K km^{-1} . The surface temperature is assumed to be 70 K, consistent with a simple solar equilibrium temperature and, except at the surface, isotherms are initially horizontal. To insure numerical stability, we cut off the temperature increase with depth at 180 K. Neither

conduction nor convection are included in the model.

We apply a constant gravitational acceleration of 0.113 m s^{-2} to the model, which we initialize by letting the stress relax towards a purely hydrostatic state. Due to the cold surface temperatures, a true hydrostatic state is never reached in the upper portion of the domain; however, the effect of this initial deviation is small (Bland and Showman, 2007, Chapter 4). The low gravitational acceleration of Enceladus is favorable for instability growth as less work must be performed against gravity to displace material under lithospheric swells (Herrick and Stevenson, 1990). Furthermore, because of the low surface gravity, the increase in the plastic yield strength with depth is small. Typical Byerlee’s law strength profiles are shown in Fig. 5.8. We note, however, that the surface yield stress is an order of magnitude higher than laboratory yield stresses measured for ice (Beeman et al., 1988). Use of this high value of cohesion allows a simpler examination of how other parameters (i.e. strain rate and temperature gradient) affect unstable extension. Lowering the cohesion can have a strong effect on the amplitude of the simulated deformation; however, dominant wavelengths remain unchanged (Bland and Showman, 2007, Chapter 4).

We again monitor the growth of an instability by periodically extracting and Fourier transforming profiles of the surface to create spectra of the deformation. Additionally, because instability growth depends strongly on wavelength, we performed a range of simulations with different initial perturbation wavelengths for each combination of temperature gradient and strain rate. This allows determination of both the dominant wavelength and total peak to trough amplification ($\mathcal{A}/\mathcal{A}_o$) produced by extension (see Chapter 4). We also performed simulations in which the initial perturbation consisted of many (16) superposed wavelength components to assess unstable extension’s ability to produce strongly periodic topography from random initial topography. In these simulations each wavelength component was given a random phase shift, added together, and renormalized to have a maximum peak to trough amplitude of 15 m. The simulations were otherwise identical to those

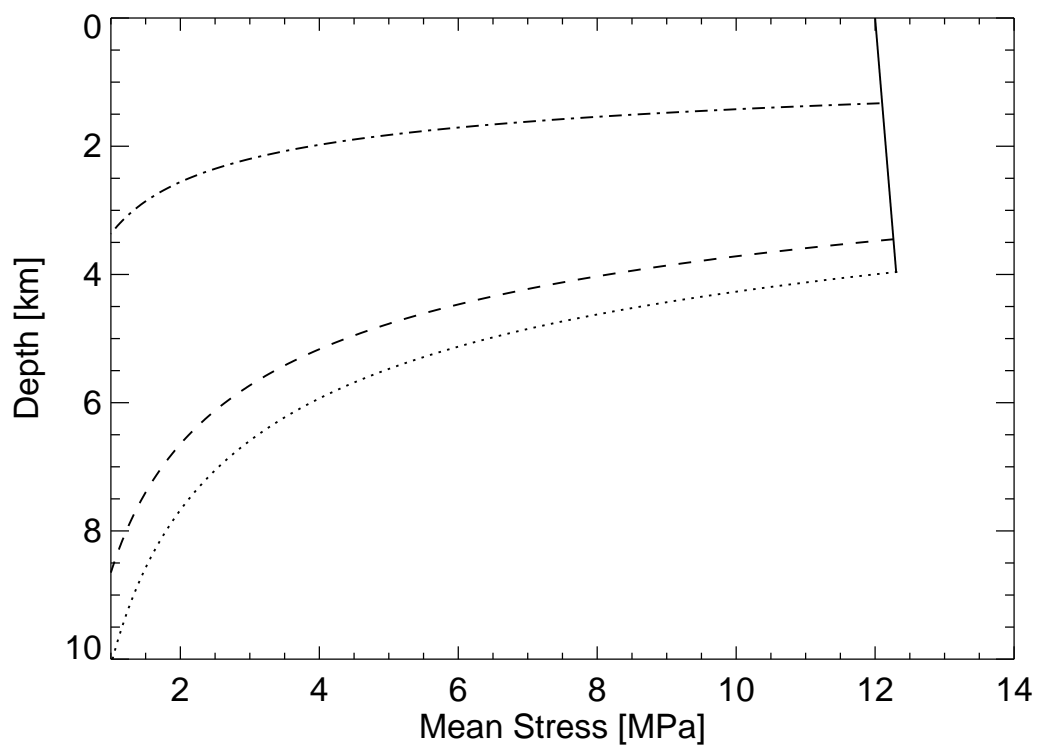


Figure 5.8: Model strength envelopes in Enceladus' initial lithosphere for three cases: $\dot{\epsilon} = 10^{-13} \text{ s}^{-1}$, $dT/dz = 15 \text{ K km}^{-1}$ (dotted); $\dot{\epsilon} = 10^{-14} \text{ s}^{-1}$, $dT/dz = 15 \text{ K km}^{-1}$ (dashed); $\dot{\epsilon} = 10^{-13} \text{ s}^{-1}$, $dT/dz = 45 \text{ K km}^{-1}$ (dot-dash). Because of Enceladus' low gravity, the frictional yield stress (solid line) has only a small increase with depth.

described above.

5.4 Modeling Results

Extension of the model domain described above produces moderate amplitude, periodically spaced pinches and swells (Fig. 5.9). Plastic deformation is limited to the upper portion of the domain where it concentrates within lithospheric pinches. Thus strain is highly focused in the pinched regions with little deformation occurring outside those zones. Tensional stress dominates the near-surface elements within the model, and like the strain, is especially concentrated within pinched regions. At depth, stresses become hydrostatic. These results are consistent with periodic necking occurring during unstable extension of the lithosphere.

The exact form of the surface deformation depends strongly on the thermal gradient and strain rate imposed on the simulation. Figure 5.10 shows typical profiles of the surface deformation after 31.5% extension for four simulations. In general, high thermal gradients produced low-amplitude, short-wavelength deformation (57 m amplitude, 2.2 km wavelength in Fig. 5.10a) and low thermal gradients produced large-amplitude, long-wavelength deformation (172 m amplitude, 18.8 km wavelength in Fig. 5.10c).

Figure 5.11 shows contours of the total amplification of the initial topography ($\mathcal{A}/\mathcal{A}_o$) and dominant wavelengths as a function of temperature gradient and strain rate after 31.5% strain. Because we have applied finite strain to the model, the strain rate is actually not constant throughout the simulation but decreases by $\sim 24\%$ as extension occurs. Furthermore, extensional thinning of the lithosphere causes an increase in the vertical thermal gradient during extension. Thus, the strain rates and temperature gradients shown in Fig. 5.11 indicate the initial values for each simulation. The maximum amplification (19.2) occurs at moderate strain rates (10^{-13} s^{-1}) and low thermal gradients (2 to 5 K km^{-1}). This amplification means that 10 m of initial topography was amplified to 192 m after 31.5% extension. Total

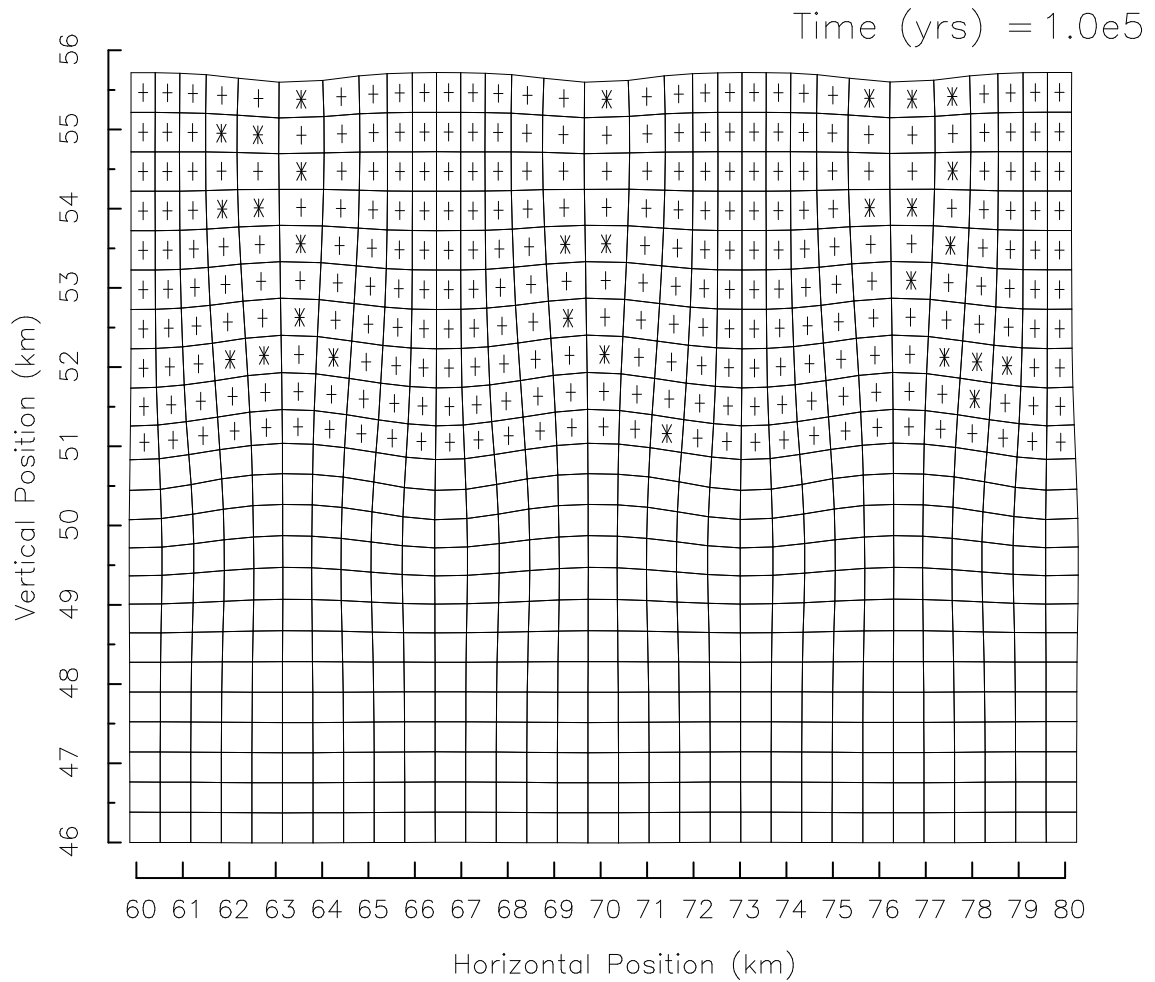


Figure 5.9: Portion of a typical output of the finite element model after 31.5% extension showing material contours that were originally horizontal and vertical. Asterisks indicate where plastic flow occurred in the most recent timestep. Plus signs indicate where plastic flow has occurred at some point during the simulation. The scattered distribution of plastic deformation occurring in the most recent timestep (asterisks) is due to plastic failure relaxing stresses back below the criterion for yielding. Several timesteps are required before stresses again exceed this criterion. Thus while the whole layer behaves plastically, only a fraction of the individual elements undergo plastic failure in a given timestep.

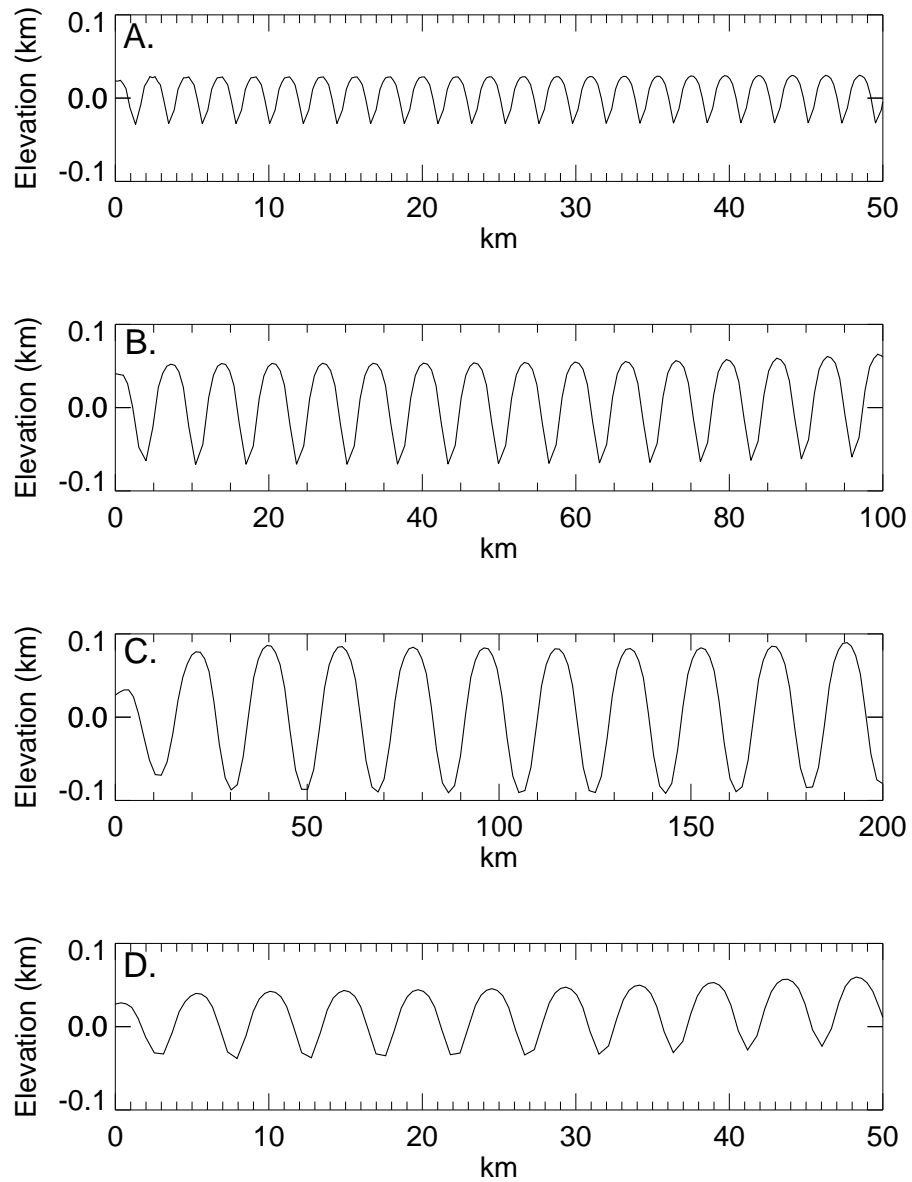


Figure 5.10: Typical profiles of the surface deformation produced after 31.5% strain. Each simulation was initialized with a 10 m sinusoidal perturbation with a wavelength equal to the dominant wavelength. The final surface deformation depends heavily on both the strain rate and the vertical thermal gradient imposed. **A.** $\dot{\epsilon} = 10^{-13} \text{ s}^{-1}$, $dT/dz = 45 \text{ K km}^{-1}$, **B.** $\dot{\epsilon} = 10^{-13} \text{ s}^{-1}$, $dT/dz = 15 \text{ K km}^{-1}$. **C.** $\dot{\epsilon} = 10^{-13} \text{ s}^{-1}$, $dT/dz = 5 \text{ K km}^{-1}$. **D.** $\dot{\epsilon} = 10^{-15} \text{ s}^{-1}$, $dT/dz = 15 \text{ K km}^{-1}$.

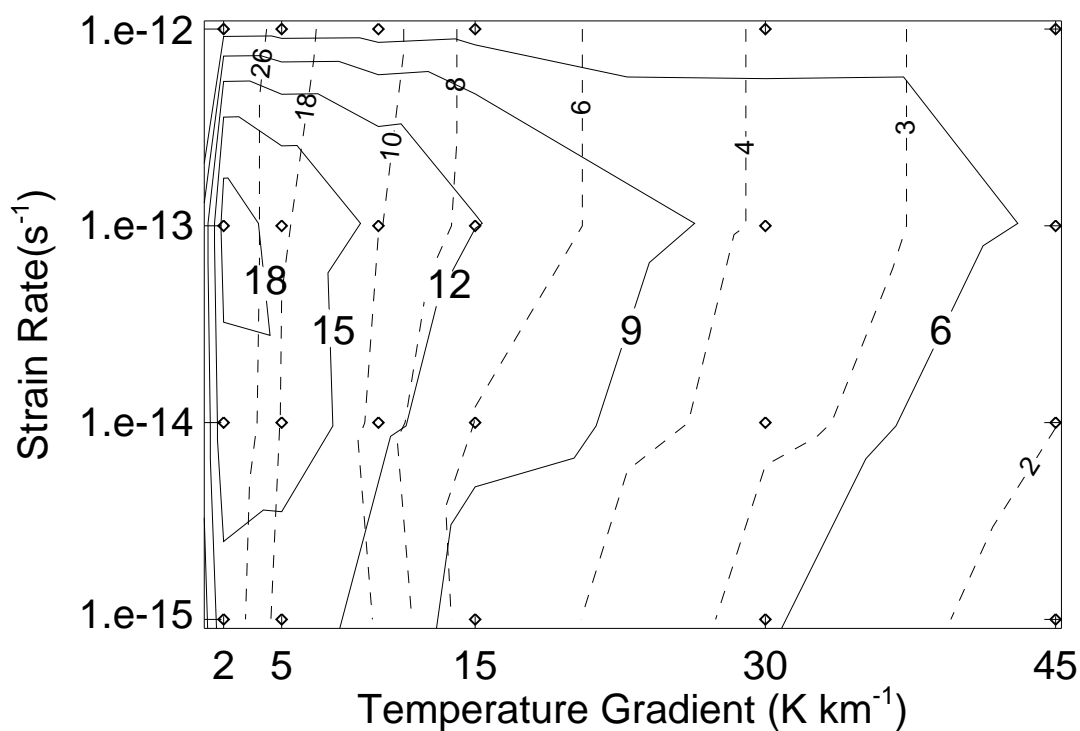


Figure 5.11: Contours of total amplification ($\mathcal{A}/\mathcal{A}_o$) (solid) and dominant wavelengths in km (dotted) after 31.5% strain as a function of strain rate and thermal gradient. Amplification is a maximum for moderate strain rates (10^{-13} s^{-1}) and low thermal gradients (2 K km^{-1}). Each simulation was initialized with a single 10-m amplitude, sinusoidal perturbation at the dominant wavelength. Diamonds indicate parameter values used for the simulations.

amplification falls off rapidly with increasing strain rate and more moderately with decreasing strain rate. This dependence on strain rate is consistent with the results of Herrick and Stevenson (1990) and Dombard and McKinnon (2001), and occurs because the strength contrast between the lithosphere and substrate is a peaked function of the strain rate and thus has a maximum at some value (Herrick and Stevenson, 1990).

Despite the large amplification occurring at low thermal gradients, amplification does approach zero as the thermal gradient approaches zero (as expected). Total

amplification also decreases with increasing temperature gradient, being a factor of three lower at 45 K km^{-1} than at 2 K km^{-1} . This decrease is not predicted by an extrapolation of exponential growth rates derived from analytical models and results from nonlinear processes at large strains (Bland and Showman, 2007, Chapter 4).

Minimum dominant wavelengths (1.6 km) occur at high thermal gradients (45 K km^{-1}) and low strain rates (10^{-15} s^{-1}). Wavelengths increase nonlinearly with decreasing thermal gradient with a maximum of 37.6 km at low thermal gradients (2 K km^{-1}) and high strain rates (10^{-12} s^{-1}). Dominant wavelengths depend only weakly on strain rate, with higher strain rates producing slightly longer wavelengths for a given thermal gradient.

Finite extension (31.5%) of a domain with multiple wavelength components in the initial perturbation (Fig. 5.12a) leads to the development of periodic structures in the final surface deformation (Fig. 5.12b). As in the simulations with a single sinusoidal perturbation, the amplitude and dominant wavelength of final surface deformation depends strongly on the imposed vertical thermal gradient: high thermal gradients produce short-wavelength deformation and low thermal gradients produce long-wavelength deformation. The final surface deformation does not depend on the exact form of the initial topography, only on the wavelengths present. Thus, changing the random phase shift given to each wavelength component in the initial condition changes the appearance of the initial topography but does not affect the final deformation.

The inclusion of multiple wavelengths of topography in the initial perturbation affects the resulting deformation in two ways. First, the total amplification decreases moderately. A simulation with a strain rate of 10^{-13} s^{-1} , thermal gradient of 15 K km^{-1} , and initial 10 m peak to trough perturbation consisting of a single sinusoid at the dominant wavelength produces an amplification of 12.1. In contrast, an identical simulation with multiple wavelengths in the initial perturbation (including the dominant wavelength) with a maximum peak to trough amplitude of

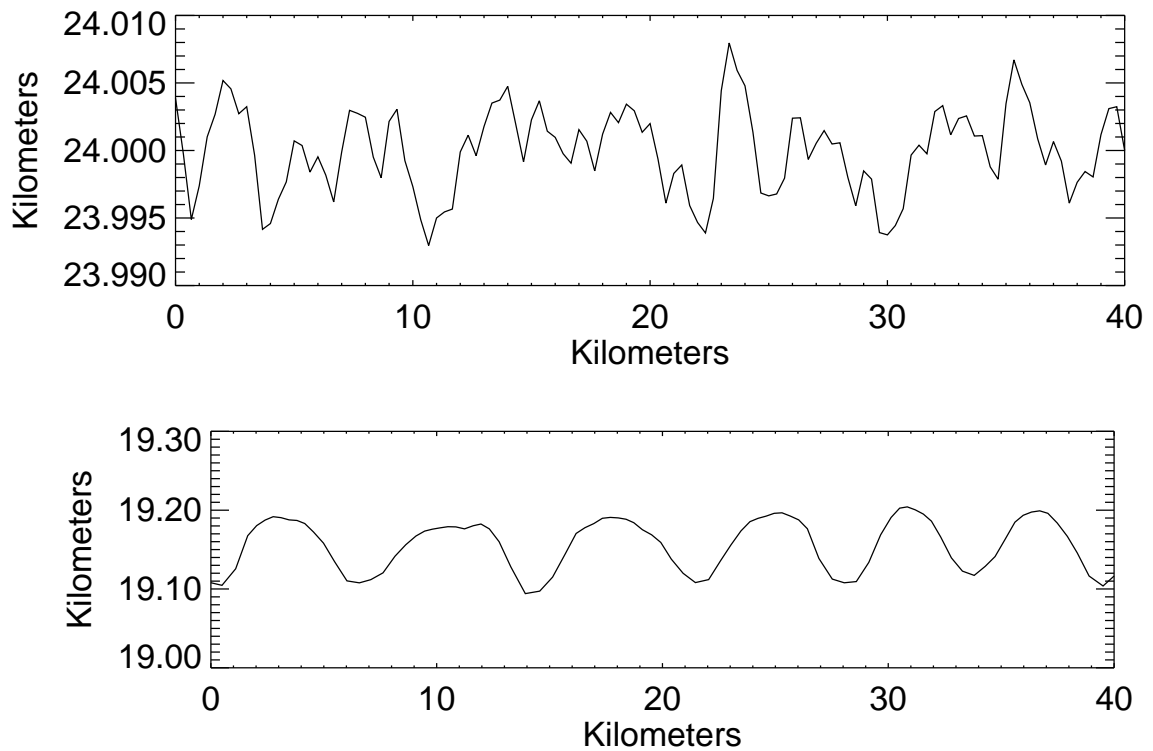


Figure 5.12: Surface profiles of **A** the initial perturbation and **B** the final deformation after 31.5% extension for a simulation with a strain rate of 10^{-13} s^{-1} and thermal gradient of 15 K km^{-1} . The initial perturbation is composed of 16 sinusoids of different wavelength, each given a random phase shift, added together, and renormalized to have a maximum peak to trough amplitude of 15 m. A single wavelength of the initial perturbation amplifies faster than all others, producing large amplitude, periodic pinches and swells in the final deformation. Note that in **B** only 40 km of the 52-km extended final domain are shown to allow direction comparison to **A**.

15 m produces an amplification of 10.2. This decrease in amplification is likely due to complex wavelength interactions as extension occurs. Second, short wavelength topography (~ 1 km) present in the initial perturbation is not easily removed by unstable extension, and in some cases can still be seen in the final surface deformation. We therefore do not expect unstable extension to completely disrupt features like crater rims. Instead, secondary faulting that accommodates necking (and is not included in this model) must be invoked to explain the complete tectonic resurfacing of vast regions of Enceladus.

The above results suggest that unstable extension can produce moderate amplitude deformation of the surface of Enceladus. Furthermore, instability growth is clearly capable of modifying low-amplitude, semi-random terrain into large-amplitude periodic ridges and troughs. Such modification may help to explain the existence of many young terrains on Enceladus. However, the greatest amplification produced by our simulations creates ridges and troughs a factor of two or three too low in amplitude to be consistent with our photoclinometric observations of Enceladus' ridges and troughs (Section 5.2.2). This is especially true for high thermal gradients that produce short-to-moderate wavelength deformation consistent with wavelengths in the Sarandib-Diyar province.

The low amplitude of the deformation produced by unstable extension determined here is consistent with previous results, which indicated that instability growth is a factor of five too low to be consistent with Ganymede's grooved terrain (Bland and Showman, 2007, Chapter 4). However, several mechanisms can increase the amplitude of deformation produced by extension. A moderate increase in the amplitude of the initial topography leads to higher-amplitude deformation in the extended domain; extension of a surface consisting of random, 30-m average amplitude topography results in ridges and troughs 1.5 times larger than a surface with 10-m initial topography. Furthermore, a surface temperature lower than the 70 K assumed here (perhaps due to a weaker young sun at the time of formation

(Showman et al., 1997; Dombard and McKinnon, 2001)) would also increase deformation amplitudes (Bland and Showman, 2007, Chapter 4). It is also possible that ice can undergo significant strain or strain-rate softening, which would lead to increased localization of strain within pinched regions and produce greater amplification of the initial topography (Bland and Showman, 2007, Chapter 4). Including such processes in simulations of terrestrial extension strongly affects model results (e.g. Buck et al. (2003); Behn et al. (2002); Frederiksen and Braun (2001); Lavier et al. (2000); Braun et al. (1999); Poliakov and Buck (1998)), in some cases leading to significant increases in localized strain. Thus, while we have not successfully recreated the full amplitude of Enceladus' ridges and troughs, it appears reasonable that unstable extension could have produced the deformation.

5.5 The Heat Flux and Elastic Thickness

The advantage of the unstable extension mechanism remains its ability to produce periodic deformation. The periodicity of the deformation depends strongly on the thermal conditions of the lithosphere. Comparison of photoclinometry and our numerical modeling therefore permits an estimation of the background heat flux present at the time the Sarandib-Diyar province was formed. As described in Section 5.2.2, dominant wavelengths in both Sarandib Planitia and Diyar Planitia are generally near 3 km to 4 km. These wavelengths correspond to a lithospheric thermal gradient of 20 to 40 K km⁻¹ (Fig. 5.11), depending on the strain rate assumed. The background heat flux at the time of extension can be estimated from

$$F = k \frac{dT}{dz}, \quad (5.5)$$

where F is the heat flux, dT/dz is the thermal gradient, and $k = (651 \text{ W m}^{-1})/T$ is the temperature-dependent thermal conductivity of ice (Petrenko and Whitworth, 1999, pg. 43). Integration of Eq.5.5 yields

$$F = \frac{651 \ln(T/T_o)}{z}, \quad (5.6)$$

where T_o and T are the surface temperature (70 K) and the maximum temperature allowed by our model (180 K) respectively. The depth z is the depth at which the maximum temperature is reached and depends on the imposed thermal gradient: $z = 5.5$ km for $dT/dz = 20$ K km⁻¹, $z = 2.75$ km for $dT/dz = 40$ K km⁻¹. These values suggest heat fluxes of 110 to 220 mW m⁻² in Sarandib and Diyar Planitia at the time of extension. The Cufa-Láhej region is dominated by longer wavelengths of 4 km to 10 km. These wavelengths correspond to thermal gradients of 10 to 20 K km⁻¹ and heat fluxes of 50 to 110 mW m⁻².

The inferred ancient heat fluxes in Sarandib and Diyar Planitia are broadly consistent with current heat fluxes measured in the south polar region. Cassini's Composite Infrared Spectrometer (CIRS) measured 3 to 7 GW of thermal emission in the region south of 65° S, corresponding to an average heat flux of 250 mW m⁻² (Spencer et al., 2006). However, caution must be used in making comparisons between the current SPT and the ancient Sarandib-Diyar province. Here we have determined background heat fluxes (averaged over the entire region) while the CIRS observations include significant contributions from highly localized, heterogeneous heat sources: temperature extremes as high as 157 K appear to correlate directly with the tiger stripes (Spencer et al., 2006). Such high temperatures may be the result of shear heating along the tiger stripe fractures (Nimmo et al., 2007). The background heat flux in the SPT may therefore be lower than 250 mW m⁻². Furthermore, it is not clear that necking is applicable to the SPT. While the SPT and the Sarandib-Diyar province share a similar extensional geometry, the fracture-like morphology of the tiger stripes is not predicted by models of unstable extension. The ~ 30 km spacing between the tiger stripes is much larger than that easily produced by necking at high heat flow, suggesting that necking is not the dominant factor in determining the spacing of the tiger stripes.

The high heat flux that we infer for the Sarandib-Diyar province at the time of its formation is unlikely to have existed globally. The total power produced

by tidal heating of Enceladus in its current orbital state is no more than ~ 4 GW, corresponding to a average global surface heat flux of 5 mW m^{-2} (Ross and Schubert, 1989). Thus, evidence of heat fluxes an order of magnitude higher than this value implies a regionally localized heating event, similar to that currently observed at Enceladus' south pole. We find, therefore, that the formation of Sarandib-Diyar province requires a source of both extensional stress and strongly localized heating. These conditions are both met by the existence of a now-inactive diapir within the ice or silicate mantle of Enceladus, as suggested by Helfenstein et al. (2006). Localized heating and melting of the ice mantle, as suggested by Collins and Goodman (2007) is also plausible; however, it is unclear whether the required extensional stress would be generated by this mechanism.

Knowledge of the local thermal gradient and rheological properties of ice allows us to determine elastic thickness (Nimmo et al., 2002) within the Sarandib-Diyar province at the time of their formation. The Maxwell time (τ_M) defines the timescale over which a material will behave elastically. Strains imposed over timescales much smaller than the Maxwell time are accommodated elastically while strains imposed over timescales much longer than the Maxwell time are accommodated viscously. The cross-over point between elastic and viscous behavior occurs when the Deborah number ($D_e = \tau_M \dot{\epsilon}$, where $\dot{\epsilon}$ is the strain rate) ~ 0.01 (Mancktelow, 1999). Combining the Maxwell time and the non-Newtonian, temperature-dependent viscosity of ice yields an expression for the temperature at the base of the elastic layer (i.e. the lithosphere) (Nimmo et al., 2002):

$$T_{base} = \frac{Q}{nR} \left[\ln \left(\frac{3D_e \Lambda^{\frac{1}{n}} \mu}{d^{\frac{m}{n}} \dot{\epsilon}^{\frac{1}{n}}} \right) \right]^{-1}, \quad (5.7)$$

where μ is the rigidity modulus ($= E/[2(1 + \nu)]$, where E is the Young's modulus and ν is the Poisson ratio), and the other parameters are defined in section 5.3. Since the surface temperature (T_s) and thermal gradient (dT/dz) are known, the elastic thickness, h_e , can be calculated as $h_e = [T_{base} - T_s]/[dT/dz]$.

In the near surface of our simulations, dislocation creep regime C dominates the viscous flow. Using parameters appropriate for this flow law (Table 1), a grain size of 1 mm, a Young's modulus of 10^{10} Pa, and Poisson ratio of 0.25, we calculate temperatures of 86 to 98 K (depending on the strain rate) at the base of the elastic layer. The thermal gradients described above (20 to 40 K km⁻¹) imply elastic thicknesses between 0.4 km and 1.4 km. These elastic thicknesses are consistent with the depth to which plastic deformation occurs within the numerical model. A diapir in the ice or silicate mantle has the potential to reorient the satellite if the elastic thickness is greater than 0.5 km (Nimmo and Pappalardo, 2006). Thus, except for the most extreme cases (very high strain rates and thermal gradients), our elastic thickness estimates are great enough to allow reorientation, if such a diapir existed.

5.6 Conclusions

We have shown that the ridges and troughs of Sarandib-Diyar province likely formed as a result of unstable extension of Enceladus' lithosphere. Unstable extension produces periodically spaced, undulating pinches and swells. Photoclinometry profiles within the region indicate that, while the deformation in the planitiae is complex, many of the ridges and troughs are, in fact, periodic, with wavelengths between 3 km and 4 km in Sarandib and Diyar Planitia, and 4 km to 9 km in the Cufa-Láhej region. These simple ridges and troughs are complicated by long wavelength deformation with a variety of morphologies. Shorter wavelengths (1 km to 2 km) are also present and are consistent with small-scale fracturing. Average topographic amplitudes in these regions are 100 m to 400 m.

Numerical modeling of unstable extension under Enceladus-like conditions indicates that amplifications of the initial topography between factors of 6 and 19 are possible after 31.5% extension. If initial topographic amplitudes were ~ 10 m, this implies maximum peak to trough topographic amplitudes of 60 m to 190 m after the extension. While these amplitudes are a factor of 2-3 lower than those

observed in the topographic profiles, a number of mechanisms can increase amplification rates. We therefore suggest that production of the ridges and troughs of the Sarandib-Diyar province by unstable extension is feasible. Furthermore, we have demonstrated that unstable extension can modify low-amplitude (tens of meters) semi-random topography into periodically spaced ridges and troughs, possibly contributing to the tectonic resurfacing of the region.

The modeling results described above are generally comparable to previous modeling results for unstable extension applied to the formation of Ganymede's grooved terrain (Bland and Showman, 2007, Chapter 4). However, differences do exist. The maximum amplification produced by unstable extension on Enceladus is 2.5 times greater than the maximum amplification calculated for Ganymede's grooves. Because of these larger amplifications and Enceladus' lower topographic amplitudes, unstable extension can more easily explain features on Enceladus than on Ganymede. Furthermore, for a given temperature gradient and strain rate, the dominant wavelengths on Enceladus are longer than on Ganymede. These differences are largely due to the difference in gravitational acceleration between the two satellites. Displacing material upward under Enceladus' lower gravity requires less work than under Ganymede's higher gravity. Initial growth rates are therefore higher on Enceladus than on Ganymede, and more total amplification occurs. Additionally, lower hydrostatic stress in Enceladus' lithosphere allows plastic deformation to occur at greater depths than on Ganymede. Because the thickness of the plastic layer controls the wavelength of the deformation, longer dominant wavelengths are produced.

Comparison of dominant wavelengths produced by our numerical models of Enceladus and topographic wavelengths determined from photogrammetry permit estimation of both the heat flux and elastic thickness of the lithosphere at the time resurfacing of the planitiae occurred. We suggest that formation of the ridges and troughs required heat fluxes of 110 to 220 mW m⁻². These fluxes require a source of intense tidal heating, which could have triggered extension via diapirism (Nimmo

and Pappalardo, 2006), internal phase changes, or other means. Our inferred heat fluxes imply elastic thicknesses of 0.4 km to 1.4 km, which are sufficient to allow reorientation of the satellite if the density of the heated region is sufficiently low. This supports the possibility that formation of the Sarandib and Diyar Planitiae, whether by ancient diapirs (Helfenstein et al., 2006) or other mechanisms, caused satellite reorientation. The global reorientation proposed by Nimmo and Pappalardo (2006) might then be but the latest in a series of reorientations that have occurred through Enceladus' history.

CHAPTER 6

CONCLUSIONS AND FUTURE DIRECTIONS

In this dissertation I have addressed four problems related to the evolution of icy satellites: the cause of Ganymede's resurfacing, the production of Ganymede's magnetic field, the formation of Ganymede's grooved terrain, and the formation of Enceladus' equatorial ridges and troughs. While significant work remains, the results described here provide an important step toward understanding the evolution of icy satellites. Below I highlight the advances I've made on each front and briefly describe possible directions for future work.

6.1 The Resurfacing of Ganymede

Ganymede's surface is marked by numerous tectonically and cryovolcanically resurfaced terrains (e.g. Smith et al., 1979a; Pappalardo et al., 1998). With an age of ~ 2 Ga, the formation of these terrains requires that resurfacing occurred during Ganymede's middle history. Malhotra (1991) and Showman and Malhotra (1997) showed that the Galilean satellites may have passed through one or more Laplace-like resonances before evolving into the current Laplace resonance. Some of these Laplace-like resonances can excite Ganymede's eccentricity, leading to tidal dissipation within its interior. The addition of tidal heating to Ganymede's energy budget mid-way through the satellite's history may have provided the driving mechanism for its resurfacing. The effects of resonance passage on Ganymede's thermal evolution were investigated by Showman et al. (1997), but advances in our understanding of stagnant-lid convection, tidal dissipation, and Ganymede's internal structure warrant a reevaluation of the tidal heating scenario.

Using a coupled orbital-thermal model, we simulated the thermal, and structural evolution of Ganymede's ice shell. I found that, in the absence of tidal dissipation, radiogenic heating alone is capable of creating a large internal ocean if the grain size of the ice shell is 1 mm or greater. For grain sizes of 1 cm or larger, the ocean will persist into the current epoch. However, the surface heat flux resulting from radiogenic heating alone is inconsistent with the moderate to high heat fluxes required for the formation of the grooved terrain. The inclusion of tidal dissipation during resonance passage significantly increases Ganymede's heat flux, consistent with groove formation. However, it also results in a thin, Europa-like ice shell. The presence of a thin ice shell on Ganymede may have enabled its tectonic and cryovolcanic resurfacing. However, the presence of a thin shell may be difficult to reconcile with the satellite's cratering record. Furthermore, the volume expansion that results from remelting a differentiated Ganymede is a factor of several smaller than the surface area expansion inferred to have occurred during groove formation. Thus an additional source of satellite expansion may be required.

Both the timing of Ganymede's resurfacing and the magnitude of strain observed on its surface can be explained if Ganymede accreted undifferentiated (Canup and Ward, 2002), and complete differentiation occurred later in the satellite's history. Such late-stage, secondary differentiation would allow large surface strains during Ganymede's mid-history. While promising, several aspects of this model require further examination, including the stability of an initially undifferentiated satellite against differentiation, the magnitude of the heat pulse required to trigger secondary differentiation, and the extent of the volume increase that can be produced by secondary differentiation.

6.2 Ganymede's Magnetic Field

Ganymede's magnetic field is a problem. Our simulations confirm previous arguments, which suggested that, if Ganymede has undergone secular cooling over

the age of the Solar System, its metallic core would currently be cooling conductively (e.g. Stevenson, 1996). Ganymede's magnetic field therefore cannot result from thermal convection within the core. Compositional convection is a plausible mechanism for generating fluid motion within the core; however, the melting behavior of the Fe-S system at pressures relevant to Ganymede (Fei et al., 1997) suggest that condensation of Fe may occur near the core-mantle boundary (CMB), rather than deep within the core (Kuang and Stevenson, 1996; McKinnon, 1996; Hauck et al., 2006). The latent heat released by Fe condensation at the CMB would be immediately removed to the mantle above, and thus unavailable to drive the core dynamo. Because the energetics of compositional convection in Ganymede's small core are dominated by latent heat release rather than gravitational energy release, the removal of the latent heat of Fe condensation compromises the ability of compositional convection to drive the core dynamo. A compositionally driven dynamo can only be assured if the sulfur content of Ganymede's core is very low or very high, in which case condensation occurs deep within the core.

Because of the difficulties associated with both thermal and compositional convection, Stevenson (1996) and Showman et al. (1997) suggested an alternate scenario in which tidal dissipation in Ganymede's silicate mantle enables the present-day field. In this scenario, tidal dissipation during passage through a Laplace-like resonance prevents the silicate mantle and metallic core from cooling. Upon exiting the resonance, tidal dissipation ends and the mantle and core quickly cool until reaching quasiequilibrium with radiogenic heating. Thermal (and plausibly compositional) convection occurs during this period of rapid cooling, driving the present-day magnetic field (Stevenson, 1996; Showman et al., 1997). Unfortunately, my modeling indicates that very little tidal dissipation would occur within Ganymede's silicate mantle during Laplace-like resonance passage. Even when pushing the model parameters, the magnitude of the tidal dissipation in the silicates is rarely more than the magnitude of early radiogenic heat production. In no cases was I able to buffer cool-

ing of the metallic core. To do so, the effective viscosity of the silicate mantle must be an order of magnitude lower than that suggested by my calculations. Explaining Ganymede's magnetic field by invoking passage through a Laplace-like resonance therefore becomes difficult, and we can effectively eliminate one hypothesis for the generation of the field.

Understanding the source of Ganymede's magnetic field will require a more complete understanding of Ganymede's geophysical history as a whole. The production of the magnetic field may be related to the formation of the metallic core itself. Thermal models of partially differentiated satellites suggest that metallic core formation may not occur until several billion years after initial separation of ice and rock (Grasset et al., 2000; Schubert et al., 2004). If Ganymede initially accreted undifferentiated (e.g. Canup and Ward, 2002), and fully differentiated later in its history, then Ganymede's metallic core may be quite young. If the metallic core formed hotter than the surrounding mantle (c.f. Ke and Solomatov, 2006), vigorous thermal convection would occur. Such convection would likely be sufficient to drive a core dynamo. However, this scenario depends strongly on the details of Ganymede's accretion, differentiation, and metallic core formation. Until these processes are better understood, the late core formation scenario for the generation of Ganymede's magnetic field will remain speculative.

6.3 Ganymede's Grooved Terrain

Ganymede's grooved terrain likely formed via unstable extension of the lithosphere (e.g. Pappalardo et al., 1998; Collins et al., 1998b; Dombard and McKinnon, 2001). The mechanism naturally explains the periodic spacing of the ridges and troughs, their undulatory nature, and the multiple scales of deformation observed. Instability growth rates derived from analytical, infinitesimal-strain models of necking are consistent with groove amplitudes (Dombard and McKinnon, 2001). However, these models require extrapolating growth rates from infinitesimal strain to

strains greater than 10%. Furthermore, the growth of periodic structures from complex initial surface deformation cannot easily be evaluated via analytical techniques. Thus, significant questions regarding groove formation on Ganymede remain.

To examine the development of periodic necking instabilities on icy satellites I used the finite element model TEKTON to simulate the finite extension of an icy lithosphere under a broad range of thermal gradients and strain rates. At small strains, instability growth rates are an order of magnitude lower than growth rates calculated from linearized, infinitesimal-strain models. At large strains, instability growth does not occur exponentially, as predicted by analytical models, but decreases at strains larger than 10%. Growth fall-off occurs at lower strains for high-thermal-gradient, thin-lithosphere simulations than for low-thermal-gradient, thick-lithosphere simulations. Thus, in the limit of large strains, moderate thermal gradients produce higher-amplitude surface deformation than high thermal gradients. These results contrast previous analytical models, which require high thermal gradients to produce large amplitude grooves.

The lower growth rates and the fall-off in growth at large strains severely limits the total amplitude of the deformation that results from unstable extension. Starting with a 10 m initial perturbation, the maximum groove amplitudes produced by our models were ~ 80 m, a factor of 5 to 10 lower than groove amplitudes observed on Ganymede's surface. The problem is exacerbated if a more realistic tensile yield strength for ice is used (instability growth rates go to zero as the surface yield strength goes to zero).

The inability to produce large amplitude deformation poses a challenge to the necking instability model. However, a number of mechanisms may allow greater amplitude deformation to occur. Strain or strain-rate weakening of ice may allow greater localization of deformation in "pinched" regions of the lithosphere, increasing deformation amplitudes. Such strain weakening is consistently used in models of terrestrial extension and can significantly increase deformation amplitudes (Buck

et al., 2003; Behn et al., 2002; Frederiksen and Braun, 2001; Poliakov and Buck, 1998; Lavier et al., 2000). In addition, the presence of discrete faults may help to localize strain and increase deformation amplitudes (Montési and Zuber, 2003; Montési and Collins, 2005). The inclusion of strain weakening and fault localization in models of groove formation is required before we can fully evaluate the relevance of unstable extension to the formation of the grooved terrain.

6.4 The Tectonic and Thermal Evolution of Enceladus

Enceladus is one of the few bodies in the Solar System on which vigorous geologic activity still occurs. Its young, heavily fractured south polar terrain exhibits high heat fluxes and an active cryovolcanic plume (Spencer et al., 2006; Hansen et al., 2006; Porco et al., 2006) that correlate with several long surface fractures (Spencer et al., 2006; Spitale and Porco, 2007). The activity in the south polar region is likely driven by tidal heating within the satellite, though the specific mechanism remains unclear (e.g. Meyer and Wisdom, 2007, 2008).

Beyond the south polar terrain, Enceladus' surface contains numerous regions that have been periodically resurfaced throughout its geologic history, including several broad planitiae in its equatorial region that contain sets of ridges and troughs. Spectral analysis of photoclinometrically derived topography indicates that these ridges and troughs have periodic spacings, low slopes, and moderate amplitudes. They therefore have a morphology similar to Ganymede's grooves, and may have formed via unstable extension of Enceladus' lithosphere. By applying our model of groove formation to Enceladus' ridge and trough terrains, I have constrained the lithospheric heat flux to have been greater than 110 mW m^{-2} at the time of their formation. These results provide context for the activity currently observed at Enceladus' south pole and imply that strong, localized heating and resurfacing have occurred periodically throughout the satellite's geologic history.

Much work remains to be done in understanding the evolution of Enceladus.

Most of the effort in the Cassini era has focused (understandably) on Enceladus' south polar terrain and active cryovolcanic plume. However, numerous features across the satellite also require explanation, including its sulci, its dorsa, and its relaxed craters. Only once we have examined all of its surface features will we fully elucidate Enceladus' tectonic and thermal evolution.

APPENDIX A

SYMBOLS AND PARAMETER VALUES FOR CHAPTERS 2 AND 3

Table A.1:
Symbols and Parameter Values

a_g	Ganymede's semi-major axis	1.07×10^9	m
a_1	constant for α_w	–	$\text{K}^{-1} \text{Pa}^{-1}$
a_2	constant for α_w	–	K^{-1}
\acute{a}_1	constant for α_w	–	$\text{K}^{-1} \text{Pa}^{-1}$
\acute{a}_2	constant for α_w	–	K^{-1}
b	length of burger vector	0.5	nm
\bar{B}	strength of magnetic field at CMB	–	nT
c	intermediate for Ra calculation	–	–
$c_{p,I}$	ice specific heat	1800	$\text{J kg}^{-1} \text{K}^{-1}$
$c_{p,w}$	water specific heat	4218	$\text{J kg}^{-1} \text{K}^{-1}$
$c_{p,sil}$	silicate specific heat	1149	$\text{J kg}^{-1} \text{K}^{-1}$
$c_{p,c}$	core specific heat	800	$\text{J kg}^{-1} \text{K}^{-1}$
\mathcal{C}	constant for k_i	651	W m^{-1}
C/MR^2	normalized rotational moment of inertia	–	–
d	grain size	–	m
e	satellite's eccentricity	–	–
E_G	gravitational energy of inner core formation	–	W
\dot{E}_I	ice tidal heating rate	–	W
\dot{E}_{sil}	silicate tidal heating rate	–	W
\dot{E}_{tot}	total energy supplied to ice shell	–	W
f	silicate melt fraction	–	–
f_t	tidal flattening	–	–
Δf	change in satellite flattening	–	–
F_{sil}	silicate heat flux	–	W m^{-2}
F_{ice}	ice heat flux	–	W m^{-2}

(Continued)

(Continued from Previous)

F_{core}	core heat flux	–	W m^{-2}
F_{cond}	conductive heat flux	–	W m^{-2}
$F_{cond,ad}$	maximum core conductive flux	–	W m^{-2}
F_{conv}	convective heat flux	–	W m^{-2}
F_{total}	total core flux	–	W m^{-2}
g	surface gravity	1.4	m s^{-2}
g_c	core/mantle boundary gravity	1.3	m s^{-2}
G	gravitational constant	6.672×10^{-11}	$\text{N m}^2 \text{kg}^{-2}$
h_{tide}	tidal heating per unit volume	–	W m^3
h_2	tidal Love number	–	–
H	radiogenic heating rate	–	W
H_μ	radial sensitivity to the shear modulus	–	$\text{m}^{-2} \text{s}^4$
k	thermal conductivity (general)	–	$\text{W m}^{-1} \text{K}^{-1}$
k_I	ice thermal conductivity	–	$\text{W m}^{-1} \text{K}^{-1}$
k_{sil}	silicate thermal conductivity	3.5	$\text{W m}^{-1} \text{K}^{-1}$
k_c	core thermal conductivity	32	$\text{W m}^{-1} \text{K}^{-1}$
k_2	degree 2 tidal love number	–	–
L	core convective length scale	–	m
L_w	latent heat of water	3.33×10^5	J kg^{-1}
L_{Fe}	latent heat of iron	3×10^5	J kg^{-1}
L_{sil}	latent heat of silicates	6×10^5	J kg^{-1}
\mathcal{L}	layer thickness	–	m
m_g	mass of Ganymede	1.48×10^{23}	kg
m_i	mass of i th ice layer melted	–	kg
m_I	mass of ice I layer melted	–	kg
m_{ic}	mass of inner core	–	kg s^{-1}
M_i	mass of the ice I shell	–	kg
M_J	mass of Jupiter	1.898×10^{27}	kg
M_{melt}	mass of silicate melt region	–	kg
M_w	mass of water	–	kg
n_1	Io mean motion	–	s^{-1}
n_2	Europa mean motion	–	s^{-1}
n_3	Ganymede mean motion	–	s^{-1}
Nu	Nusselt number	–	–
P	pressure at depth r	–	Pa

(Continued)

(Continued from Previous)

P_{cmb}	pressure at core/mantle boundary	7.0	GPa
P_t	pressure at the top of the ocean	–	Pa
P_{trans}	transition pressure for α_w	–	Pa
P_B	dynamo power requirement	–	W
q	dimensionless measure of tidal potential	–	–
Q_J	tidal dissipation factor of Jupiter	–	–
Q_1	tidal dissipation factor of Io	–	–
Q_3	tidal dissipation factor of Ganymede	–	–
r	radius within satellite	–	m
r_b	radius to the lower ocean interface	–	m
r_t	radius to the upper ocean interface	–	m
R	gas constant	8.314	$\text{kJ mol}^{-1} \text{K}^{-1}$
R_g	radius of Ganymede	2634	km
R_{sil}	radius of silicates	1720	km
R_c	radius of core	700	km
R_{inner}	radius of inner core	–	m
Ra	Rayleigh number	–	–
Ra_n	intermediate for Ra_{crit} calculation	–	–
Ra_{crit}	critical Rayleigh number	–	–
Re_m	magnetic Reynolds number	–	–
t	time	–	s
T	temperature (general)	–	K
T_I	ice temperature	–	K
T_c	core temperature	–	K
T_m	ice melting temperature	–	K
$T_{m,Fe}$	iron melting temperature	–	K
T_{sol}	olivine solidus temperature	–	K
T_{liq}	olivine liquidus temperature	–	K
T_o	FeS melting curve parameter	1880	K
T_{m1}	FeS melting curve parameter	1.36×10^{-11}	K Pa^{-1}
T_{m2}	FeS melting curve parameter	-6.2×10^{-23}	K Pa^{-2}
T_{cmb}	core/mantle boundary temperature	–	K
T_{oc}	ocean temperature at pressure P	–	K
T_s	surface temperature	100	K
T_{sil}	silicate temperature	–	K

(Continued)

(Continued from Previous)

T_{trans}	temp. at thermal expansivity transition	–	K
T_M	Maxwell time	–	s
ΔT	temperature change	–	K
ΔT_{rh}	temp. drop across convective sublayer	–	K
u	core convective flow velocity	–	m s^{-1}
ΔV	total satellite volume change	–	m^3
α	thermal expansivity (general)	–	K^{-1}
α_{ice}	ice thermal expansivity	1.6×10^{-4}	K^{-1}
α_{sil}	silicate thermal expansivity	3×10^{-5}	K^{-1}
α_c	core thermal expansivity	1×10^{-4}	K^{-1}
α_w	water thermal expansivity	1×10^{-4}	K^{-1}
δ_{BL}	boundary layer thickness	–	m
δ_{rh}	thickness of the convective sublayer	–	m
$\dot{\epsilon}$	strain rate	–	s^{-1}
ϵ	dynamo efficiency	0.05	–
η	magnetic diffusivity	2	$\text{m}^2 \text{s}^{-1}$
η_e	effective viscosity	–	Pa s
Θ	log rheologic viscosity contrast	–	–
θ	colatitude with respect to tidal axis	–	rad
κ	thermal diffusivity	–	$\text{m}^2 \text{s}^{-1}$
Λ	response coefficient	0.4	–
μ_I	ice shear modulus	3.52	GPa
μ_{sil}	silicate shear modulus	80	GPa
$\text{Im}\{\mu\}$	imaginary part of complex shear modulus	–	Pa
μ_o	magnetic permeability	$4\pi \times 10^{-7}$	N A^{-1}
ξ	non-dimensional size of inner core	–	–
ν	ice I poisson ratio	0.325	–
ρ	density (general)	–	Kg m^{-3}
ρ_I	average ice density	1200	Kg m^{-3}
ρ_w	water density	1000	Kg m^{-3}
ρ_{sil}	silicate density	3300	Kg m^{-3}
ρ_c	average core density	6500	Kg m^{-3}
ρ_{ic}	inner core density	7020	Kg m^{-3}
ρ_s	FeS density	5333	Kg m^{-3}
ς	non-dimensional slope of the FeS melting curve	2.09	–

(Continued)

(Continued from Previous)

$\sigma_{\theta\theta}$	meridional diurnal tidal stress	– Pa
$\sigma_{\phi\phi}$	azimuthal diurnal tidal stress	– Pa
σ_{NSR}	non-synchronous rotational stress	– Pa
τ	shear stress	– Pa
τ_m	timescale for ice melting	– s
v_i	local volume change of i th ice layer	– $\text{m}^3 \text{kg}^{-1}$
Φ	ohmic dissipation	– W
χ	mass fraction of light elements in core	– –
χ_o	initial mass fraction of light elements in core	– –
Ω	degrees of non-synchronous rotation	– rad
ω_1	Io-Europa conjunction drift rate	– s^{-1}
ω_2	Europa-Ganymede conjunction drift rate	– s^{-1}

APPENDIX B

INCLUSION OF MULTIPLE RHEOLOGIES IN TEKTON

B.1 Introduction

This appendix briefly describes how multiple flow laws were included in the TEKTON finite-element model. The source code containing these changes has been included in a TEKTON element library named ‘ice.f’, which is a modified version of the ‘plnplas.f’ library included with the standard TEKTON download. For context and clarity, some background material on the finite element method is included below; however, I make no attempt to outline the method in detail (see Bathe and Wilson, 1976, for a review).

B.2 The Inclusion of Viscous Deformation in TEKTON

If the solution to the finite element problem is time dependent, a viscoelastic (rather than a purely elastic) solution is required. TEKTON incorporates viscous deformation by calculating the pseudo-forces associated with viscous flow and adding them to the global force balance. TEKTON assumes a constitutive relationship for a power-law fluid with the form

$$\dot{\epsilon} = aJ_2^{(n-1)/2}\dot{\sigma} \quad (\text{B.1})$$

where $J_2 = 0.5(\dot{\sigma}_{xx}\dot{\sigma}_{xx} + \dot{\sigma}_{yy}\dot{\sigma}_{yy} + \dot{\sigma}_{zz}\dot{\sigma}_{zz}) + \dot{\sigma}_{xy}\dot{\sigma}_{xy}$ is the second invariant of the deviatoric stress, n is the rheological power-law exponent, $\dot{\sigma}$ is the deviatoric stress, and a is a rheological constant in units of $\text{MPa}^{-n} \text{s}^{-1}$. The parameter a can be used to relate Eq. B.1 to the more familiar constitutive relation given by

$$\dot{\epsilon} = A_0 d^{-m} \dot{\sigma}^n \exp\left\{\frac{-Q}{RT}\right\}, \quad (\text{B.2})$$

where A_o is an experimentally derived constant, d is the grain size, m is the grain size exponent, Q is the rheological activation energy, R is the gas constant, and T is the temperature. This yields

$$a = \frac{3^{(n-1)/2}}{2} A_o d^{-m} \exp \left\{ \frac{-Q}{RT} \right\}, \quad (\text{B.3})$$

where the prefactor $3^{(n-1)/2}/2$ is a term introduced to correct for the geometry of rheology experiments (see Ranalli, 1995, p.77). The power-law rheology defined above is entered into TEKTON via an effective viscosity with the form

$$\eta_f = (2a)^{-1/n}. \quad (\text{B.4})$$

With the appropriate rheology established and the deviatoric stresses known, TEKTON calculates the components of the strain rate for each element (β_i) as

$$\beta_i = \sigma \sigma_i \quad (\text{B.5})$$

where σ is given by

$$\sigma = \frac{1}{2\eta_f} \left(\frac{J_2^{1/2}}{\eta_f} \right)^{n-1}. \quad (\text{B.6})$$

The strain rate is then used to calculate the effective stress at each node as

$$\sigma_{\mathbf{v}} = \mathbf{D}\mathbf{e} \quad (\text{B.7})$$

where \mathbf{D} is the material matrix, which is constructed from the elastic material properties (Young's modulus and Poisson ratio) of each element, and \mathbf{e} is the component of the strain given by

$$\mathbf{e} = \Delta t \beta_{\mathbf{i}}, \quad (\text{B.8})$$

and Δt is the size of one time step. The local force vector is then constructed as

$$\mathbf{F}_{\text{loc}} = \mathbf{B}^T \sigma_{\mathbf{v}} \quad (\text{B.9})$$

where \mathbf{B} is the strain-displacement matrix, which is used to calculate the local stiffness matrix (\mathbf{k}) via $\mathbf{k} = \int \mathbf{B}^T \mathbf{D} \mathbf{B} d\Omega$ and is calculated by interpolating between

the local and natural coordinates using shape functions. The global force vector is updated by these viscous pseudo-forces before the rest of the solution is carried out.

We also require the Jacobian of the the strain-stress matrix β . The matrix is constructed from the derivatives of σ with respect to $J_2^{1/2}$ and with respect to the mean stress $\sigma_m = \frac{1}{3}(\sigma_{xx} + \sigma_{yy} + \sigma_{zz})$, which are given by

$$\frac{d\sigma}{dJ_2} = (n-1) \frac{1}{2\eta_f} \left(\frac{J_2^{1/2}}{\eta_f} \right)^{n-2} \quad (\text{B.10})$$

$$\frac{d\sigma}{d\sigma_m} = 0. \quad (\text{B.11})$$

The Jacobian of the strain-stress matrix is used to augment the material matrix for viscoelastic deformation.

B.3 The Inclusion of Multiple Flow Laws

The formulation described above is effective for modeling a rheology in which a single flow law dominates. However, the rheology of ice is complex, with multiple flow laws dominating under different temperature and stress regimes. Often, we don't know *a priori* which flow mechanisms will dominate. It is therefore useful to use a composite flow law in which the total viscous strain rate includes contributions from each possible flow mechanism. In Chapters 4 and 5 we utilized a flow law with the form (Goldsby and Kohlstedt, 2001)

$$\dot{\epsilon}_{visco} = \dot{\epsilon}_A + \dot{\epsilon}_B + \dot{\epsilon}_C + \dot{\epsilon}_{diff} + \{1/\dot{\epsilon}_{GBS} + 1/\dot{\epsilon}_{BS}\}^{-1}, \quad (\text{B.12})$$

where the subscripts A , B , C , $diff$, GBS , and BS refer to dislocation creep A, B, and C; diffusion creep; grain boundary sliding; and basal slip. Each of these mechanisms has a temperature and stress dependence of the form given in Eq. B.2. Note that in the case of the GBS and BS mechanisms it is the slower of the two mechanisms that dominates the flow.

A composite flow law was incorporated into TEKTON by modifying TEKTON's **formbt** subroutine such that Eq. B.5 has the form

$$\beta_i = [\sigma_A + \sigma_B + \sigma_C + \sigma_{diff} + \{1/\sigma_{GBS} + 1/\sigma_{BS}\}^{-1}] \dot{\sigma}, \quad (\text{B.13})$$

where each term in Eq. B.13 has the same form as Eq. B.6. The resulting expression is given by

$$\begin{aligned} \sigma = & \frac{1}{2\eta_{f,A}} \left(\frac{J_2^{1/2}}{\eta_{f,A}} \right)^{n_A-1} + \frac{1}{2\eta_{f,B}} \left(\frac{J_2^{1/2}}{\eta_{f,B}} \right)^{n_B-1} + \\ & \frac{1}{2\eta_{f,C}} \left(\frac{J_2^{1/2}}{\eta_{f,C}} \right)^{n_C-1} + \frac{1}{2\eta_{f,diff}} \left(\frac{J_2^{1/2}}{\eta_{f,diff}} \right)^{n_{diff}-1} + \\ & \left\{ \left[\frac{1}{2\eta_{f,GBS}} \left(\frac{J_2^{1/2}}{\eta_{f,GBS}} \right)^{n_{GBS}-1} \right]^{-1} + \left[\frac{1}{2\eta_{f,BS}} \left(\frac{J_2^{1/2}}{\eta_{f,BS}} \right)^{n_{BS}-1} \right]^{-1} \right\}^{-1}. \quad (\text{B.14}) \end{aligned}$$

The calculation of the strain rate and pseudo-forces then follows in the same manner as described above.

In addition to the calculation of the strain rate, a modification must be made to the calculation of the Jacobian of the stress-strain rate matrix in TEKTON subroutine **formjb**. This requires calculation of the derivative of σ with respect to

$J_2^{1/2}$. Using the chain rule, the derivative is given by

$$\begin{aligned}
\frac{d\sigma}{dJ_2} = & (n_A - 1) \frac{1}{2\eta_{f,A}} \left(\frac{J_2^{1/2}}{\eta_{f,A}} \right)^{n_A-2} + (n_B - 1) \frac{1}{2\eta_{f,B}} \left(\frac{J_2^{1/2}}{\eta_{f,B}} \right)^{n_B-2} + \\
& (n_C - 1) \frac{1}{2\eta_{f,C}} \left(\frac{J_2^{1/2}}{\eta_{f,C}} \right)^{n_C-2} + (n_{GBS} - 1) \frac{1}{2\eta_{f,diff}} \left(\frac{J_2^{1/2}}{\eta_{f,diff}} \right)^{n_{diff}-2} - \\
& \left\{ \left[\frac{1}{2\eta_{f,gs}} \left(\frac{J_2^{1/2}}{\eta_{f,gs}} \right)^{n_{GBS}-1} \right]^{-1} + \left[\frac{1}{2\eta_{f,BS}} \left(\frac{J_2^{1/2}}{\eta_{f,BS}} \right)^{n_{BS}-1} \right]^{-1} \right\}^{-2} \\
\times & \left\{ - \left(\frac{1}{2\eta_{f,gs}} \left(\frac{J_2^{1/2}}{\eta_{f,gs}} \right)^{n_{GBS}-1} \right)^{-2} (n_{GBS} - 1) \frac{1}{2\eta_{f,gs}} \left(\frac{J_2^{1/2}}{\eta_{f,gs}} \right)^{n_{GBS}-2} - \right. \\
& \left. \left(\frac{1}{2\eta_{f,BS}} \left(\frac{J_2^{1/2}}{\eta_{f,BS}} \right)^{n_{BS}-1} \right)^{-2} (n_{BS} - 1) \frac{1}{2\eta_{f,BS}} \left(\frac{J_2^{1/2}}{\eta_{f,BS}} \right)^{n_{BS}-2} \right\}. \quad (\text{B.15})
\end{aligned}$$

The Jacobian is then calculated analogously to the standard `plnpln.f` element library.

B.4 Additional Modifications to TEKTON Files

In addition to modifying the subroutines **formbt** and **formjb** as described above, adjustments were made to the standard TEKTON input file to permit additional rheological data to be input. In addition to the standard inputs of Young's Modulus, Poisson ratio, density, effective viscosity, and power law exponent, another ten parameters must be read from the input file (two for each of the five additional flow mechanisms considered). The input data is organized into six columns, followed by an additional four columns, all of which follow the standard material property inputs. The material id number must occur at the left of each row of material data. The definition of the effective viscosity occurs analogously to Eqs. B.3 and B.4 for each flow law. While the order in which flow mechanism are assigned is generally not important, care must be taken to insure that the data for the GBS and BS flow mechanisms are input in the final four columns. Additionally, an element ID

(idelem) number of 504 must be used to identify the correct element library with the input file. The input file is otherwise identical to an input file that would be used for plasticity (plnplas.f). Corresponding changes were made to the subroutine **intcon** in the element library to accommodate the additional material properties.

B.5 Testing and Validation

The modified element library was thoroughly tested and validated against TEKTON2.3-pln-plas. Initially, this was done by inputting one realistic rheology and assigning arbitrarily large effective viscosities for the other rheologies. These unrealistically large viscosities ensure that the one realistic rheology will dominate the strain rate calculation. The resulting finite element output was identical to the output from a “pln-plas.f” simulation with a single rheology identical to the realistic rheology used in the “ice.f” version. This method of validation was repeated for each flow regime.

For the final validation test, we performed a simulation that included all six flow mechanisms. We then plotted the horizontally averaged percent contribution to the total strain rate for each flow mechanism. The results are shown in Fig. B.1. For simplicity I have combined the effects of GBS and BS, but it is GBS that controls the deformation. In the near surface, dislocation creep regime C dominates the flow. Deeper in the mesh, GBS dominates. Between these two regions, a combination of dislocation creep C, B, and GBS contribute to the flow, suggesting a complex rheology in this temperature and stress regime.

These results can be compared to analytical calculations of which flow regime should dominate at a given temperature and stress. Figure B.2 shows the stress produced by each flow mechanism for a strain rate of 10^{-13} s^{-1} and conditions identical to those used in Fig. B.1. The flow mechanism that produced the lowest stress at a given depth is the mechanism that will dominate the viscous deformation. GBS and BS have again been combined as above. Dislocation creep regime C again dominates

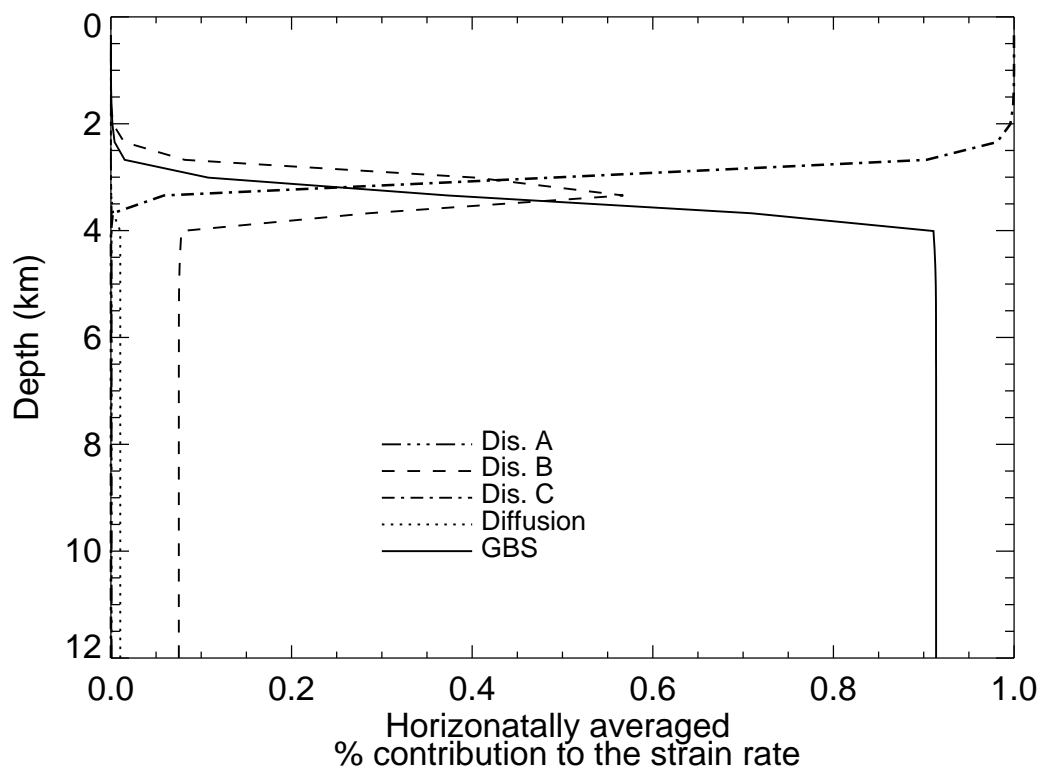


Figure B.1: The horizontally averaged percent contribution to the total strain rate for each ice flow mechanism considered in Chapters 4 and 5 as a function of depth. The thermal gradient in this test simulation was 30 K km^{-1} , the strain rate was 10^{-13} s^{-1} , and the ice grain size was 1 mm.

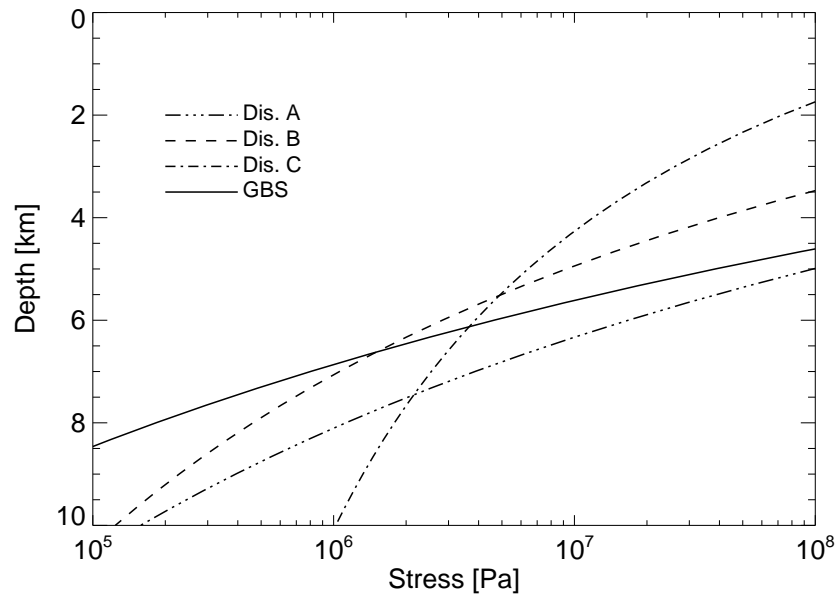


Figure B.2: Simple calculation of the stress as a function of depth for a thermal gradient of 30 K km^{-1} , grain size of 1 mm , and assuming a constant strain rate of 10^{-13} s^{-1} . Newtonian diffusion was neglected here but plays no role in the deformation. Comparison to Fig. B.1 suggests the multiple flow law rheology works as expected.

the near surface flow, with dislocation creep regime B becoming important in the middle of the mesh and GBS dominating the deformation at depth. The strong correspondence between Figs. B.1 and B.2 gives us confidence that our implementation of multiple flow laws into TEKTON is behaving properly.

REFERENCES

- Allison, M. L. and S. M. Clifford (1987). Ice-covered water volcanism on Ganymede. *J. Geophys. Res.*, **92**, pp. 7865–7876.
- Anderson, J. D., E. L. Lau, W. L. Sjogren, G. Schubert, and W. B. Moore (1996). Gravitational constraints on the internal structure of Ganymede. *Nature*, **384**, pp. 541–543.
- Anderson, J. D., E. L. Lau, W. L. Sjogren, G. Schubert, and W. B. Moore (1997a). Europa’s differentiated internal structure: Inferences from two Galileo encounters. *Science*, **276**, pp. 1236–1239.
- Anderson, J. D., E. L. Lau, W. L. Sjogren, G. Schubert, and W. B. Moore (1997b). Gravitational evidence for an undifferentiated Callisto. *Nature*, **387**, pp. 264–266.
- Anderson, J. D., G. Schubert, R. A. Jacobson, E. L. Lau, W. B. Moore, and J. L. Palguta (2004). Discovery of Mass Anomalies on Ganymede. *Science*, **305**, pp. 989–991.
- Anderson, J. D., G. Schubert, R. A. Jacobson, E. L. Lau, W. B. Moore, and W. L. Sjogren (1998). Europa’s Differentiated Internal Structure: Inferences from Four Galileo Encounters. *Science*, **281**, pp. 2019–2022.
- Barr, A. C. and W. B. McKinnon (2006). Convection in icy satellites with self-consistent grain size. In *Lunar Planet. Sci. Conf. XXXVII*, p. 2130. Abstract.
- Barr, A. C. and W. B. McKinnon (2007). Convection in ice I shells and mantles with self-consistent grain size. *J. Geophys. Res.*, **112**, p. 2012.
- Barr, A. C. and R. T. Pappalardo (2005). Onset of convection in the icy Galilean satellites: Influence of rheology. *J. Geophys. Res.*, **110**, p. E12005. Doi: 10.1029/2004JE002371.
- Bathe, K. J. and E. L. Wilson (eds.) (1976). *Numerical methods in finite element analysis*. Prentice Hall, Inc., New Jersey.
- Beeman, M., W. B. Durham, and S. H. Kirby (1988). Friction of ice. *J. Geophys. Res.*, **93**, pp. 7625–7633.
- Behn, M. D., J. Lin, and M. T. Zuber (2002). A continuum mechanics model for normal faulting using a strain-rate softening rheology: Implications for thermal and rheological controls on continental and oceanic rifting. *Earth Planet. Sci. Lett.*, **202**, pp. 725–740.

- Beyer, R. A., A. S. McEwen, and R. L. Kirk (2003). Meter-scale slopes of candidate MER landing sites from point photogrammetry. *J. Geophys. Res.*, **108**.
- Bland, M. T. and A. P. Showman (2007). The formation of Ganymede's grooved terrain: Numerical modeling of extensional necking instabilities. *Icarus*, **189**, pp. 439–456.
- Boehler, R. (1996). Fe-FeS eutectic temperatures to 620 kbar. *Phys. Earth Planet. Int.*, **96**, pp. 181–186.
- Braginsky, S. I. (1963). Structure of the F-layer and reasons for convection in Earth's core. *Dokl. Akad. Nauk SSSR*, **149**, pp. 8–10.
- Braun, J., J. Chéry, A. Poliakov, D. Mainprice, A. Vauchez, A. Tomassi, and M. Daignières (1999). A simple parameterization of strain localization in the ductile regime due to grain size reduction: A case study for olivine. *J. Geophys. Res.*, **104**, pp. 25167–25181.
- Breuer, D. and T. Spohn (2006). Viscosity of the Martian mantle and its initial temperature: Constraints from crust formation history and the evolution of the magnetic field. *Planet. Space Sci.*, **54**, pp. 153–169.
- Buck, W. R., L. L. Lavier, and A. Babeyko (2003). A numerical model of lithospheric extension producing fault-bounded basins and ranges. *Int. Geol. Rev.*, **18**.
- Budd, W. F. and T. H. Jacka (1989). A review of ice rheology for ice sheet modeling. *Cold Reg. Sci. Technol.*, **16**, pp. 107–144.
- Buffett, B. A. (2002). Estimates of heat flow in the deep mantle based on the power requirements for the geodynamo. *Geophys. Res. Lett.*, **29**, p. 7.
- Buffett, B. A., H. E. Huppert, J. R. Lister, and A. W. Woods (1996). On the thermal evolution of the Earth's core. *J. Geophys. Res.*, **101**, pp. 7989–8006.
- Canup, R. M. and W. R. Ward (2002). Formation of the Galilean satellites: conditions of accretion. *Astron. J.*, **124**, pp. 3404–3423.
- Christensen, U. R. and J. Aubert (2006). Scaling properties of convection-driven dynamos in rotating spherical shells and application to planetary magnetic fields. *Geophys. J. Int.*, **166**, pp. 97–114.
- Chyba, C. F. and C. B. Phillips (2002). Europa as an Abode of Life. *Orig. Life Evol. Biosph.*, **32**, pp. 47–67.
- Collins, G. C. (2006). Global expansion of Ganymede derived from strain measurements in grooved terrain. In *Lunar Planet. Sci. Conf. XXXVII*, p. 2007. Abstract.

- Collins, G. C. (2007). Bright terrain tectonics and the evolution of Ganymede. In *Workshop on Ices, Oceans, and Fire: Satellites of the Outer Solar System*, p. 6041. Abstract.
- Collins, G. C. and J. C. Goodman (2007). Enceladus' south polar sea. *Icarus*, **189**, pp. 72–82.
- Collins, G. C., J. W. Head, and R. T. Pappalardo (1998a). Formation of Ganymede grooved terrain by sequential extensional episodes: Implications of Galileo observations for regional stratigraphy. *Icarus*, **135**, pp. 345–359.
- Collins, G. C., J. W. Head, and R. T. Pappalardo (1998b). The role of extensional instability in creating Ganymede grooved terrain: Insights from Galileo high-resolution stereo imaging. *Geophys. Res. Lett.*, **25**, pp. 233–236.
- Consolmagno, G. J. and J. S. Lewis (1976). Structural and thermal models of icy Galilean Satellites. In Gehrels, T. A. (ed.) *Jupiter*, pp. 1035–1051. University of Arizona Press.
- Consolmagno, G. J. and J. S. Lewis (1977). Preliminary thermal history models of icy satellites. In Burns, J. A. (ed.) *Planetary Satellites*, pp. 492–500. University of Arizona Press.
- Consolmagno, G. J. and J. S. Lewis (1978). The evolution of icy satellite interiors and surfaces. *Icarus*, **34**, pp. 280–293.
- Crary, F. J. and F. Bagenal (1998). Remanent ferromagnetism and the interior structure of Ganymede. *J. Geophys. Res.*, **103**, pp. 25757–25773.
- Crawford, G. D. and D. J. Stevenson (1988). Gas-driven water volcanism and the resurfacing of Europa. *Icarus*, **73**, pp. 66–79.
- Dombard, A. J. and W. B. McKinnon (2001). Formation of grooved terrain on Ganymede: Extensional instability mediated by cold, superplastic creep. *Icarus*, **154**, pp. 321–336.
- Dombard, A. J. and W. B. McKinnon (2006a). Elastoviscoplastic relaxation of impact crater topography with application to Ganymede and Callisto. *J. Geophys. Res.*, **111**, p. E01001.
- Dombard, A. J. and W. B. McKinnon (2006b). Folding of Europa's icy lithosphere: an analysis of viscous-plastic buckling and subsequent topographic relaxation. *J. Struct. Geo.*, **28**, pp. 2259–2269.
- Dorsey, N. E. (1940). *Properties of ordinary water-substance*. Reinhold Publishing Corporation, New York.

- Drake, S. (1978). *Galileo at work, his scientific biography*. University of Chicago Press, Chicago.
- Durham, W. B., S. H. Kirby, and L. A. Stern (1992). Effects of dispersed particulates on the rheology of water ice at planetary conditions. *J. Geophys. Res.*, **97**, pp. 20883–20897.
- Durham, W. B., S. H. Kirby, and L. A. Stern (1997). Creep of water ices at planetary conditions: A compilation. *J. Geophys. Res.*, **102**, pp. 16293–16302.
- Ellsworth, K. and G. Schubert (1983). Saturn's icy satellites - Thermal and structural models. *Icarus*, **54**, pp. 490–510.
- Fei, Y., C. M. Bertka, and L. W. Finger (1997). High-pressure iron-sulfur compound, Fe₃S₂, and melting relations in the Fe-FeS system. *Science*, **275**, pp. 1621–1623.
- Figueredo, P. H. and R. Greeley (2000). Geologic mapping of the northern leading hemisphere of Europa from Galileo solid-state imaging data. *J. Geophys. Res.*, **105**, pp. 22629–22646. doi:10.1029/1999JE001107.
- Figueredo, P. H. and R. Greeley (2004). Resurfacing history of Europa from pole-to-pole geologic mapping. *Icarus*, **167**, pp. 287–312.
- Fink, J. H. and R. C. Fletcher (1981). Variations in thickness of Ganymede's lithosphere determined by spacings of lineations. *Lunar Planet. Sci. 12. Abstract 277*.
- Fink, U., N. H. Dekkers, and H. P. Larson (1973). Infrared Spectra of the Galilean Satellites of Jupiter. *Astrophys. J.*, **179**, pp. L155–L159.
- Fischer, H. J. and T. Spohn (1990). Thermal-orbital histories of viscoelastic models of Io (JI). *Icarus*, **83**, pp. 39–65.
- Fletcher, N. H. (1970). *The chemical physics of ice*. Cambridge University Press, Cambridge.
- Fletcher, R. C. and B. Hallet (1983). Unstable extension of the lithosphere: A mechanical model for basin-and-range structure. *J. Geophys. Res.*, **88**, pp. 7457–7466.
- Frederiksen, S. and J. Braun (2001). Numerical modeling of strain localisation during extension of the continental lithosphere. *Earth Planet. Sci. Lett.*, **188**, pp. 241–251.
- Freeman, J. (2006). Non-Newtonian stagnant lid convection and the thermal evolution of Ganymede and Callisto. *Planet. Space Sci.*, **54**, pp. 2–14.

- Friedson, A. J. and D. J. Stevenson (1983). Viscosity of rock-ice mixtures and applications to the evolution of icy satellites. *Icarus*, **56**, pp. 1–14.
- Gaddis, L., J. Anderson, K. Becker, T. Becker, D. Cook, K. Edwards, E. Eliason, T. Hare, H. Kieffer, E. M. Lee, J. Mathews, L. Soderblom, T. Sucharski, J. Torson, A. McEwen, and M. Robinson (1997). An Overview of the Integrated Software for Imaging Spectrometers (ISIS). In *Lunar Planet. Sci. Conf. XXVIII*, p. 387. Abstract.
- Galilei, G. (1989). *Sidereus Nuncius. Translated by A. Van Helden*. University of Chicago Press, Chicago.
- Gammon, P. H., H. Klefte, and M. J. Clouter (1983). Elastic constants of ice samples by brillouin spectroscopy. *J. Phys. Chem.*, **87**, pp. 4025–4029.
- Geissler, P. E., R. Greenberg, G. Hoppa, P. Helfenstein, A. McEwen, R. Pappalardo, R. Tufts, M. Ockert-Bell, R. Sullivan, R. Greeley, M. J. S. Belton, T. Denk, B. E. Clark, J. Burns, and J. Veverka (1998). Evidence for non-synchronous rotation of Europa. *Nature*, **391**, pp. 368–370.
- Giese, B., J. Oberst, T. Roatsch, G. Neukum, J. W. Head, and R. T. Pappalardo (1998). The local topography of Uruk Sulcus and Galileo Regio obtained from stereo images. *Icarus*, **135**, pp. 303–316.
- Goldreich, P. and S. Soter (1966). Q in the solar system. *Icarus*, **5**, pp. 375–389.
- Goldsby, D. L. and D. L. Kohlstedt (2001). Superplastic deformation of ice: Experimental observations. *J. Geophys. Res.*, **106**, pp. 11017–11030.
- Golombek, M. P. (1982). Constraints on the expansion of Ganymede and the thickness of the lithosphere. *J. Geophys. Res.*, **87A**, pp. 77–83.
- Grasset, O., C. Sotin, and F. Deschamps (2000). On the internal structure and dynamics of Titan. *Planet. Space. Sci.*, **48**, pp. 617–636.
- Greeley, R., C. F. Chyba, J. W. Head, T. B. McCord, W. B. McKinnon, R. T. Pappalardo, and P. H. Figueredo (2004). Geology of Europa. In Bagnell, F., T. Dowling, and W. B. McKinnon (eds.) *Jupiter. The Planet, Satellites and Magnetosphere*, pp. 330–362. Cambridge University Press.
- Greeley, R., G. C. Collins, N. A. Spaun, R. J. Sullivan, J. M. Moore, D. A. Senske, B. R. Tufts, T. V. Johnson, M. J. S. Belton, and K. L. Tanaka (2000). Geologic mapping of Europa. *J. Geophys. Res.*, **105**, pp. 22559–22578.

- Greeley, R., R. Sullivan, J. Klemaszewski, K. Homan, J. W. Head, R. T. Pappalardo, J. Veverka, B. E. Clark, T. V. Johnson, K. P. Klaasen, M. Belton, J. Moore, E. Asphaug, M. H. Carr, G. Neukum, T. Denk, C. R. Chapman, C. B. Pilcher, P. E. Geissler, R. Greenberg, and R. Tufts (1998). Europa: Initial Galileo Geological Observations. *Icarus*, **135**, pp. 4–24.
- Greenberg, R. (1987). Galilean satellites: Evolutionary paths in deep resonance. *Icarus*, **70**, pp. 334–347.
- Greenberg, R., P. Geissler, G. Hoppa, B. R. Tufts, D. D. Durda, R. Pappalardo, J. W. Head, R. Greeley, R. Sullivan, and M. H. Carr (1998). Tectonic Processes on Europa: Tidal Stresses, Mechanical Response, and Visible Features. *Icarus*, **135**, pp. 64–78.
- Greenberg, R., P. Geissler, B. R. Tufts, and G. V. Hoppa (2000). Habitability of Europa's crust: The role of tidal-tectonic processes. *J. Geophys. Res.*, **105**, pp. 17551–17562.
- Greenberg, R. and S. J. Weidenschilling (1984). How fast do Galilean satellites spin? *Icarus*, **58**, pp. 186–196.
- Grimm, R. E. and S. W. Squyres (1985). Spectral analysis of groove spacing on Ganymede. *J. Geophys. Res.*, **90**, p. 2013.
- Gubbins, D. (1977). Energetics of the Earth's core. *J. Geophys.*, **43**, pp. 453–464.
- Gubbins, D., D. Alfè, G. Masters, G. D. Price, and M. Gillan (2004). Gross thermodynamics of two-component core convection. *Geophys. J. Int.*, **157**, pp. 1407–1414.
- Gurnett, D. A., W. S. Kurth, A. Roux, S. J. Bolton, and C. F. Kennel (1996). Evidence for a magnetosphere at Ganymede from plasma wave observations by the Galileo spacecraft. *Nature*, **384**, pp. 535–537.
- Hansen, C. J., L. Esposito, A. I. F. Stewart, J. Colwell, A. Hendrix, W. Pryor, D. Shemansky, and R. West (2006). Enceladus' water vapor plume. *Science*, **311**, pp. 1422–1425.
- Hapke, B. (1986). Bidirectional reflectance spectroscopy. IV - The extinction coefficient and the opposition effect. *Icarus*, **67**, pp. 264–280.
- Hauck, S. A., J. M. Aurnou, and A. J. Dombard (2006). Sulfur's impact on core evolution and magnetic field generation on Ganymede. *J. Geophys. Res.*, **111**, p. E09008.

- Head, J. W., R. T. Pappalardo, G. Collins, and R. Greeley (1997). Tectonic resurfacing on Ganymede and its role in the formation of grooved terrain. In *Lunar Planet. Sci. Conf. XXVIII*, pp. 535–536. Abstract.
- Helfenstein, P. and E. M. Parmentier (1985). Patterns of fracture and tidal stresses due to nonsynchronous rotation: Implications for fracturing on Europa. *Icarus*, **61**, pp. 175–184.
- Helfenstein, P., P. C. Thomas, J. Veverka, C. Porco, B. Giese, R. Wagner, T. Roatsch, T. Denk, G. Neukum, and E. Turtle (2006). Surface geology and tectonism on Enceladus. In *Eos Trans. AGU, Fall Meet. Suppl.*, pp. P22B–02. Abstract.
- Herrick, D. L. and D. J. Stevenson (1990). Extensional and compressional instabilities in icy satellite lithospheres. *Icarus*, **85**, pp. 191–204.
- Hobbs, P. V. (1974). *Ice physics*. Clarendon Press, Oxford.
- Hoppa, G. V., B. R. Tufts, R. Greenberg, and P. E. Geissler (1999). Formation of cycloidal features on Europa. *Science*, **285**, pp. 1899–1902.
- Hurford, T. A., P. Helfenstein, G. V. Hoppa, R. Greenberg, and B. G. Bills (2007). Eruptions arising from tidally controlled periodic openings of rifts on Enceladus. *Nature*, **447**, pp. 292–294.
- Hussman, H. and T. Spohn (2004). Thermal-orbital evolution of Io and Europa. *Icarus*, **171**, pp. 391–410.
- Hussmann, H., F. Sohl, and T. Spohn (2006). Subsurface oceans and deep interiors of medium-sized outer planet satellites and large trans-neptunian objects. *Icarus*, **185**, pp. 258–273.
- Hussmann, H., T. Spohn, and K. Wiczerkowski (2002). Thermal Equilibrium States of Europa's Ice Shell: Implications for Internal Ocean Thickness and Surface Heat Flow. *Icarus*, **156**, pp. 143–151.
- Ioannou, P. j. and R. S. Lindzen (1993). Gravitational tides in the outer planets. II. Interior calculations and estimatoin of the tidal dissipation factor. *Astrophys. J.*, **406**, pp. 266–278.
- Jacobson, R. A., P. G. Antreasian, J. J. Bordi, K. E. Criddle, R. Ionasescu, J. B. Jones, R. A. Mackenzie, M. C. Meek, D. Parcher, F. J. Pelletier, W. M. Owen, Jr., D. C. Roth, I. M. Roundhill, and J. R. Stauch (2006). The Gravity Field of the Saturnian System from Satellite Observations and Spacecraft Tracking Data. *Astron. J.*, **132**, pp. 2520–2526.

- Janes, D. M. and H. J. Melosh (1988). Sinkers tectonics: an approach to the surface of Miranda. *J. Geophys. Res.*, **93**, pp. 3127–3143.
- Jaques, A. L. and D. H. Green (1980). Anhydrous melting of peridotite at 0-15 Kb pressure and the genesis of tholeiitic basalt. *Contrib. Mineral. Petrol.*, **73**, pp. 287–310.
- Jin, Z., H. W. Green, and Y. Zhou (1994). Melt topology in partially molten mantle peridotite during ductile deformation. *Nature*, **372**, pp. 164–167.
- Karato, S. (1984). Grain-size distribution and rheology of the upper mantle. *Tectonophysics*, **104**, pp. 155–176.
- Karato, S. and P. Wu (1993). Rheology of the upper mantle. *Science*, **260**, pp. 771–778.
- Kargel, J. S. and S. Pozio (1996). The volcanic and tectonic history of Enceladus. *Icarus*, **119**, pp. 385–404.
- Ke, Y. and V. S. Solomatov (2006). Early transient superplumes and the origin of the Martian crustal dichotomy. *J. Geophys. Res.*, **111**, p. 10001.
- Khurana, K. K., M. G. Kivelson, D. J. Stevenson, G. Schubert, C. T. Russell, R. J. Walker, and C. Polanskey (1998). Induced magnetic fields as evidence for subsurface oceans in Europa and Callisto. *Nature*, **395**, pp. 777–780.
- Kirby, S. H., W. B. Durham, M. L. Beeman, H. C. Heard, and M. A. Daley (1987). Inelastic properties of ice I_h at low temperatures and high pressures. *J. Physique*, **48**, pp. 227–232.
- Kirk, R. L. and D. J. Stevenson (1987). Thermal evolution of a differentiated Ganymede and implications for surface features. *Icarus*, **69**, pp. 91–134.
- Kivelson, M. G., K. K. Khurana, F. V. Coroniti, S. Joy, C. T. Russell, R. J. Walker, J. Warnecke, L. Bennett, and C. Polanskey (1997). The magnetic field and magnetosphere of Ganymede. *Geophys. Res. Lett.*, **24**, pp. 2155–2158.
- Kivelson, M. G., K. K. Khurana, C. T. Russell, S. P. Joy, M. Volwerk, R. J. Walker, C. Zimmer, and J. A. Linker (2001). Magnetized or unmagnetized: Ambiguity persists following Galileo's encounters with Io in 1999 and 2000. *J. Geophys. Res.*, **106**, pp. 26121–26136.
- Kivelson, M. G., K. K. Khurana, C. T. Russell, M. Volwerk, R. J. Walker, and C. Zimmer (2000). Galileo Magnetometer Measurements: A Stronger Case for a Subsurface Ocean at Europa. *Science*, **289**, pp. 1340–1343.

- Kivelson, M. G., K. K. Khurana, C. T. Russell, R. J. Walker, J. Warnecke, F. V. Coroniti, C. Polanskey, D. J. Southwood, and G. Schubert (1996). Discovery of Ganymede's magnetic field by the Galileo spacecraft. *Nature*, **384**, pp. 537–541.
- Kivelson, M. G., K. K. Khurana, D. J. Stevenson, L. Bennett, S. Joy, C. T. Russell, R. J. Walker, C. Zimmer, and C. Polanskey (1999). Europa and Callisto: Induced or intrinsic fields in a periodically varying plasma environment. *J. Geophys. Res.*, **104**, pp. 4609–4626.
- Kivelson, M. G., K. K. Khurana, and M. Volwerk (2002). The permanent and inductive magnetic moments of Ganymede. *Icarus*, **157**, pp. 507–522.
- Kivelson, M. G., J. Warnecke, L. Bennett, S. Joy, K. K. Khurana, J. A. Linker, C. T. Russell, R. J. Walker, and C. Polanskey (1998). Ganymede's magnetosphere: Magnetometer overview. *J. Geophys. Res.*, **103**, pp. 19963–19972.
- Kohlstedt, D. L. and M. E. Zimmerman (1996). Rheology of Partially Molten Mantle Rocks. *Annu. Rev. Earth Planet. Sci.*, **24**, pp. 41–62.
- Kuang, Z. and D. J. Stevenson (1996). Magnetic field generation in the Galilean satellites. In *Eos Trans. AGU, Fall Meet. Suppl.*, p. F437. Abstract.
- Kuiper, G. P. (1952). Planetary atmospheres and their origins. In Kuiper, G. P. (ed.) *Atmospheres of the Earth and planets*, pp. 306–405. University of Chicago Press.
- Kuiper, G. P. (1957). Infrared observations of planets and satellites. In *Astron. J.*, p. 245. Abstract.
- Kuskov, O. L. and V. A. Kronrod (2001). Core Sizes and Internal Structure of Earth's and Jupiter's Satellites. *Icarus*, **151**, pp. 204–227. doi:10.1006/icar.2001.6611.
- Lavier, L. L., W. R. Buck, and A. N. B. Poliakov (2000). Factors controlling normal fault offset in an ideal brittle layer. *J. Geophys. Res.*, **105**, pp. 23431–23442.
- Leith, A. C. and W. B. McKinnon (1996). Is There Evidence for Polar Wander on Europa? *Icarus*, **120**, pp. 387–398.
- Lewis, J. S. (1971). Satellites of the Outer Planets: Their Physical and Chemical Nature. *Icarus*, **15**, pp. 174–185.
- Lissauer, J. J., S. J. Peale, and J. N. Cuzzi (1984). Ring torque on Janus and the melting of Enceladus. *Icarus*, **58**, pp. 159–168.

- Lister, J. R. and B. A. Buffett (1995). The strength and efficiency of thermal and compositional convection in the geodynamo. *Phys. Earth Planet. Int.*, **91**, pp. 17–30.
- Loper, D. E. (1975). Torque balance for precessionally driven dynamos. *Phys. Earth Planet. Int.*, **11**, pp. 43–60.
- Loper, D. E. (1978a). Some thermal consequences of a gravitationally powered dynamo. *J. Geophys. Res.*, **83**, pp. 5961–5970.
- Loper, D. E. (1978b). The gravitationally powered dynamo. *Geophys. J. R. Astro. Soc.*, **54**, pp. 389–404.
- Lopes, R. M. C., K. L. Mitchell, E. R. Stofan, J. I. Lunine, R. Lorenz, F. Paganelli, R. L. Kirk, C. A. Wood, S. D. Wall, L. E. Robshaw, A. D. Fortes, C. D. Neish, J. Radebaugh, E. Reffet, S. J. Ostro, C. Elachi, M. D. Allison, Y. Anderson, R. Boehmer, G. Boubin, P. Callahan, P. Encrenaz, E. Flamini, G. Francescetti, Y. Gim, G. Hamilton, S. Hensley, M. A. Janssen, W. T. K. Johnson, K. Kelleher, D. O. Muhleman, G. Ori, R. Orosei, G. Picardi, F. Posa, L. E. Roth, R. Seu, S. Shaffer, L. A. Soderblom, B. Stiles, S. Vetrella, R. D. West, L. Wye, and H. A. Zebker (2007). Cryovolcanic features on Titan’s surface as revealed by the Cassini Titan Radar Mapper. *Icarus*, **186**, pp. 395–412.
- Lorenz, R. D., B. W. Stiles, R. L. Kirk, M. D. Allison, P. Persi del Marmo, L. Iess, J. I. Lunine, S. J. Ostro, and S. Hensley (2008). Titan’s Rotation Reveals an Internal Ocean and Changing Zonal Winds. *Science*, **319**, pp. 1649–1651.
- Malhotra, R. (1991). Tidal origin of the Laplace resonance and the resurfacing of Ganymede. *Icarus*, **94**, pp. 399–412.
- Malkus, W. V. R. (1963). Precessional torques as the cause of geomagnetism. *J. Geophys. Res.*, **68**, pp. 2871–2886.
- Mancktelow, N. S. (1999). Finite-element modelling of single-layer folding in elasto-viscous materials: The effect of initial perturbation geometry. *J. Struct. Geo.*, **21**, pp. 161–177.
- Manga, M. and C. Y. Wang (2007). Pressurized oceans and the eruption of liquid water on Europa and Enceladus. *Geophys. Res. Lett.*, **34**, p. L07202.
- McEwen, A. S. (1986). Tidal reorientation and the fracturing of Jupiter’s moon Europa. *Nature*, **321**, pp. 49–51.
- McEwen, A. S. (1991). Photometric functions for photoclinometry and other applications. *Icarus*, **92**, pp. 298–311.

- McKinnon, W. B. (1981). Tectonic deformation of Galileo Regio and limits to the planetary expansion of Ganymede. In *Lunar Planet. Sci. Conf. XII*, pp. 1585–1597. Abstract.
- McKinnon, W. B. (1996). Core evolution in the icy satellites, and the prospects for dynamo-generated magnetic fields. In *Bull. Am. Astron. Soc.*, p. 1076. Abstract.
- McKinnon, W. B. (1998). Geodynamics of Icy Satellites. In Schmitt, B., C. De Bergh, and M. Festou (eds.) *Solar System Ices*, pp. 525–550. Kluwer Academic Publishers.
- McKinnon, W. B. (1999). Convective instability in Europa’s floating ice shell. *Geo. Res. Lett.*, **26**, pp. 951–954.
- McKinnon, W. B. and E. M. Parmentier (1986). Ganymede and Callisto. In Burns, J. A. and M. S. Matthews (eds.) *Satellites*, pp. 718–763. University of Arizona Press.
- Melosh, H. J. (1977). Global tectonics of a despun planet. *Icarus*, **31**, pp. 221–243.
- Melosh, H. J. (1980). Tectonic patterns on a tidally distorted planet. *Icarus*, **43**, pp. 334–337.
- Melosh, H. J. and A. Raefsky (1980). The dynamical origin of subduction zone topography. *Geophys. J. R. Astr. Soc.*, **60**, pp. 333–354.
- Meyer, J. and J. Wisdom (2007). Tidal heating in Enceladus. *Icarus*, **188**, pp. 535–539.
- Meyer, J. and J. Wisdom (2008). Tidal evolution of Mimas, Enceladus, and Dione. *Icarus*, **193**, pp. 213–223.
- Montési, L. G. J. and G. C. Collins (2005). On the mechanical origin of two-wavelength tectonics on Ganymede. In *Lunar Planet. Sci. XXXVI*, p. 2093. Abstract.
- Montési, L. G. J. and M. T. Zuber (2003). Spacing of faults at the scale of the lithosphere and localization of instability: 1. Theory. *J. Geophys. Res.*, **108**, p. 2110.
- Moore, W. B. (2001). The Thermal State of Io. *Icarus*, **154**, pp. 548–550.
- Moore, W. B. (2006). Thermal equilibrium in Europa’s ice shell. *Icarus*, **180**, pp. 141–146.
- Morrison, D. (1982). Introduction to the satellites of Jupiter. In Morrison, D. (ed.) *Satellites of Jupiter*, pp. 3–43. University of Arizona Press.

- Mosqueira, I. and P. R. Estrada (2003). Formation of the regular satellites of giant planets in an extended gaseous nebula I: subnebula model and accretion of satellites. *Icarus*, **163**, pp. 198–231.
- Mueller, S. and W. B. McKinnon (1988). Three-layered models of Ganymede and Callisto: Compositions, structures, and aspects of evolution. *Icarus*, **76**, pp. 437–464.
- Multhaup, K. and T. Spohn (2007). Stagnant lid convection in the mid-sized icy satellites of Saturn. *Icarus*, **186**, pp. 420–435.
- Nimmo, F. (2004). Dynamics of rifting and modes of extension on icy satellites. *J. Geophys. Res.*, **109**, p. E01003. doi:10.
- Nimmo, F. and E. Gaidos (2002). Strike-slip motion and double ridge formation on Europa. *J. Geophys. Res.*, **107**, p. 5021.
- Nimmo, F. and R. T. Pappalardo (2004). Furrow flexure and ancient heat flux on Ganymede. *Geophys. Res. Lett.*, **31**, p. 19701.
- Nimmo, F. and R. T. Pappalardo (2006). Diapir-induced reorientation of Saturn’s moon Enceladus. *Nature*, **441**, pp. 614–616.
- Nimmo, F., R. T. Pappalardo, and B. Giese (2002). Effective elastic thickness and heat flux estimates on Ganymede. *Geophys. Res. Lett.*, **29**, p. 62.
- Nimmo, F., J. R. Spencer, R. T. Pappalardo, and M. E. Mullen (2007). Shear heating as the origin of the plumes and heat flux on Enceladus. *Nature*, **447**, pp. 289–291.
- Ogilvie, G. I. and D. N. C. Lin (2004). Tidal Dissipation in Rotating Giant Planets. *Astrophys. J.*, **610**, pp. 477–509.
- Ojakangas, G. W. and D. J. Stevenson (1986). Episodic volcanism of tidally heated satellites with application to Io. *Icarus*, **66**, pp. 341–358.
- Ojakangas, G. W. and D. J. Stevenson (1989). Thermal state of an ice shell on Europa. *Icarus*, **81**, pp. 220–241.
- Olson, P. and U. R. Christensen (2006). Dipole moment scaling for convection-driven planetary dynamos. *Earth Planet. Sci. Lett.*, **250**, pp. 561–571.
- Owen, D. R. J. and E. Hinton (1980). *Finite elements in plasticity: Theory and practice*. Pineridge Press Limited, Swansea, UK.
- Palguta, J., J. D. Anderson, G. Schubert, and W. B. Moore (2006). Mass anomalies on Ganymede. *Icarus*, **180**, pp. 428–441.

- Pappalardo, R. T., M. J. S. Belton, H. H. Breneman, M. H. Carr, C. R. Chapman, G. C. Collins, T. Denk, S. Fagents, P. E. Geissler, B. Giese, R. Greeley, R. Greenberg, J. W. Head, P. Helfenstein, G. Hoppa, S. D. Kadel, K. P. Klaasen, J. E. Klemaszewski, K. Magee, A. S. McEwen, J. M. Moore, W. B. Moore, G. Neukum, C. B. Phillips, L. M. Prockter, G. Schubert, D. A. Senske, R. J. Sullivan, B. R. Tufts, E. P. Turtle, R. Wagner, and K. K. Williams (1999). Does Europa have a subsurface ocean? Evaluation of the geological evidence. *J. Geophys. Res.*, **104**, pp. 24015–24056.
- Pappalardo, R. T. and G. C. Collins (2005). Strained craters on Ganymede. *J. Struct. Geo.*, **27**, pp. 827–838.
- Pappalardo, R. T., G. C. Collins, J. W. Head, P. Helfenstein, T. B. McCord, J. M. Moore, L. M. Prockter, P. M. Schenk, and J. R. Spencer (2004). Geology of Ganymede. In Bagnell, F. and M. W. B. Dowling, T. (eds.) *Jupiter. The Planet, Satellites and Magnetosphere*. Cambridge University Press.
- Pappalardo, R. T. and R. Greeley (1995). A review of the origins of subparallel ridges and troughs: Generalized morphological predictions from terrestrial models. *J. Geophys. Res.*, **100**, pp. 18985–19007.
- Pappalardo, R. T., J. W. Head, G. C. Collins, R. L. Kirk, G. Neukum, J. Oberst, B. Giese, R. Greeley, C. R. Chapman, P. Helfenstein, J. M. Moore, A. McEwen, B. R. Tufts, D. A. Senske, H. H. Breneman, and K. Klaasen (1998). Grooved terrain on Ganymede: First results from Galileo high-resolution imaging. *Icarus*, **135**, pp. 276–302.
- Parmentier, E. M. and J. W. Head (1979). Internal processes affecting surfaces of low-density satellites: Ganymede and Callisto. *J. Geophys. Res.*, **84**, pp. 6263–6276.
- Parmentier, E. M., S. W. Squyres, J. W. Head, and M. L. Allison (1982). The tectonics of Ganymede. *Nature*, **295**, pp. 290–293.
- Passey, Q. R. (1983). Viscosity of the lithosphere of Enceladus. *Icarus*, **53**, pp. 105–120.
- Passey, Q. R. and E. M. Shoemaker (1982). Craters and basins on Ganymede and Callisto: morphological indicators of crustal evolution. In Morrison, D. (ed.) *Satellites of Jupiter*, pp. 379–434. University of Arizona Press.
- Patel, J. G., R. T. Pappalardo, J. W. Head, G. C. Collins, H. Hiesinger, and J. Sun (1999). Topographic wavelengths of Ganymede groove lanes from Fourier analysis of Galileo images. *J. Geophys. Res.*, **104**, pp. 24057–24074.

- Patterson, W. S. B. (1969). *The Physics of Glaciers*. Pergamon Press, New York.
- Peale, S. J. (1999). Origin and evolution of the natural satellites. *Annu. Rev. Astron. Astrophys.*, **37**, pp. 533–602.
- Peale, S. J. and P. Cassen (1978). Contribution of tidal dissipation to lunar thermal history. *Icarus*, **36**, pp. 245–269.
- Peale, S. J., P. Cassen, and R. T. Reynolds (1979). Melting of Io by tidal dissipation. *Science*, **203**, pp. 892–894.
- Peale, S. J., P. Cassen, and R. T. Reynolds (1980). Tidal dissipation, orbital evolution, and the nature of Saturn’s inner satellites. *Icarus*, **43**, pp. 65–72.
- Peale, S. J. and M. H. Lee (2002). A primordial origin of the Laplace relation among the Galilean satellites. *Science*, **298**, pp. 593–597.
- Petrenko, V. F. and R. W. Whitworth (1999). *Physics of Ice*. Oxford University Press, Oxford.
- Pilcher, C. B., S. R. Ridgway, and T. B. McCord (1972). Galilean satellites: Identification of water frost. *Science*, **178**, pp. 1087–1089.
- Plescia, J. B. and J. M. Boyce (1983). Crater numbers and geological histories of Iapetus, Enceladus, Tethys and Hyperion. *Nature*, **301**, pp. 666–670.
- Poliakov, A. N. B. and W. R. Buck (1998). Mechanics of stretching elastic-plastic-viscous layers: Applications to slow-spreading mid-ocean ridges. In Buck, W. R., P. T. Delaney, J. A. Karson, and Y. Lagabriele (eds.) *Faulting and magmatism at mid-ocean ridges*, pp. 305–323. American Geophysical Union.
- Porco, C., S. L. Adams, J. M. Diehl, B. D. Knowles, L. J. Pieri, and J. J. Riley (2005a). *Cassini Orbiter Calibration ISSNA/ISSWA 2 EDR Version 1.0*. CO-CAL-ISSNA/ISSWA-2-EDR-V1.0, COISS-0011. NASA Planetary Data System.
- Porco, C., S. L. Adams, J. M. Diehl, B. D. Knowles, L. J. Pieri, and J. J. Riley (2005b). *Cassini Orbiter Saturn ISSNA/ISSWA 2 EDR Version 1.0*. CO-S-ISSNA/ISSWA-2-EDR-V1.0. NASA Planetary Data System.
- Porco, C. C., P. Helfenstein, P. C. Thomas, A. P. Ingersoll, J. Wisdom, R. West, G. Neukum, T. Denk, R. Wagner, T. Roatsch, S. Kieffer, E. Turtle, A. McEwen, T. V. Johnson, J. Rathbun, J. Veverka, D. Wilson, J. Perry, J. Spitale, A. Brahic, J. A. Burns, A. D. DelGenio, L. Dones, C. D. Murray, and S. Squyres (2006). Cassini Observes the Active South Pole of Enceladus. *Science*, **311**, pp. 1393–1401.

- Porco, C. C., R. A. West, S. Squyres, A. McEwen, P. Thomas, C. D. Murray, A. Delgenio, A. P. Ingersoll, T. V. Johnson, G. Neukum, J. Veverka, L. Dones, A. Brahic, J. A. Burns, V. Haemmerle, B. Knowles, D. Dawson, T. Roatsch, K. Beurle, and W. Owen (2004). Cassini Imaging Science: Instrument characteristics and anticipated scientific investigations at Saturn. *Space Sci. Rev.*, **115**, pp. 363–497.
- Ranalli, G. (1995). *Rheology of the Earth*. Chapman and Hall, London.
- Reese, C. C., V. S. Solomatov, and J. R. Baumgardner (2005). Scaling laws for time-dependent stagnant lid convection in a spherical shell. *Phys. Earth Planet. Int.*, **149**, pp. 361–370.
- Reynolds, R. T. and P. M. Cassen (1979). On the internal structure of the major satellites of the outer planets. *Geophys. Res. Lett.*, **6**, pp. 121–124.
- Rochester, M. G., J. A. Jacobs, D. E. Smylie, and K. R. Chong (1975). Can precession power the geodynamo? *Geophys. J. R. Astro. Soc.*, **43**, pp. 661–678.
- Ross, M. N. and G. Schubert (1989). Viscoelastic models of tidal heating in Enceladus. *Icarus*, **78**, pp. 90–101.
- Sarson, G. R., C. A. Jones, K. Zhang, and G. Schubert (1997). Magnetoconvection dynamos and the magnetic fields of Io and Ganymede. *Science*, **276**, pp. 1106–1108.
- Schenk, P. M. (2002). Thickness constraints on the icy shells of the galilean satellites from a comparison of crater shapes. *Nature*, **417**, pp. 419–421.
- Schenk, P. M., C. R. Chapman, K. Zahnle, and J. M. Moore (2004). Ages and interiors: The cratering record of the Galilean satellites. In Bagnell, F., T. Dowling, and W. B. McKinnon (eds.) *Jupiter. The Planet, Satellites and Magnetosphere*, pp. 427–456. Cambridge University Press.
- Schenk, P. M. and W. B. McKinnon (1989). Fault offsets and lateral crustal movement on Europa: Evidence for a mobile ice shell. *Icarus*, **79**, pp. 75–100.
- Schenk, P. M., W. B. McKinnon, D. Gwynn, and J. M. Moore (2001). Flooding of Ganymede’s bright terrains by low-viscosity water-ice lavas. *Nature*, **410**, pp. 57–60.
- Schubert, G., J. D. Anderson, T. Spohn, and W. B. McKinnon (2004). Interior composition, structure and dynamics of the Galilean satellites. In Bagnell, F., T. Dowling, and W. B. McKinnon (eds.) *Jupiter. The Planet, Satellites and Magnetosphere*, pp. 281–306. Cambridge University Press.

- Schubert, G., J. D. Anderson, B. J. Travis, and J. Palguta (2007). Enceladus: Present internal structure and differentiation by early and long-term radiogenic heating. *Icarus*, **188**, pp. 345–355.
- Schubert, G., M. N. Ross, D. J. Stevenson, and T. Spohn (1988). Mercury's thermal history and the generation of its magnetic field. In Vilas, F., C. R. Chapman, and M. S. Matthews (eds.) *Mercury*, pp. 429–460. University of Arizona Press.
- Schubert, G., D. G. Stevenson, and K. Ellsworth (1981). Internal structure of the Galilean satellites. *Icarus*, **47**, pp. 46–59.
- Schubert, G., K. Zhang, M. G. Kivelson, and J. D. Anderson (1996). The magnetic field and internal structure of Ganymede. *Nature*, **384**, pp. 544–545.
- Showman, A. P. and R. Malhotra (1997). Tidal evolution into the Laplace resonance and the resurfacing of Ganymede. *Icarus*, **127**, pp. 93–111.
- Showman, A. P., I. Mosqueira, and J. W. Head (2004). On the resurfacing of Ganymede by liquid-water volcanism. *Icarus*, **172**, pp. 625–640.
- Showman, A. P., D. J. Stevenson, and R. Malhotra (1997). Coupled orbital and thermal evolution of Ganymede. *Icarus*, **129**, pp. 367–383.
- Smith, B. A., L. A. Soderblom, R. Beebe, J. Boyce, G. Briggs, M. Carr, S. A. Collins, A. F. Cook, G. E. Danielson, M. E. Davies, G. E. Hunt, A. Ingersoll, T. V. Johnson, H. Masursky, J. McCauley, D. Morrison, T. Owen, C. Sagan, E. M. Shoemaker, R. Strom, V. E. Suomi, and J. Veverka (1979a). The Galilean satellites and Jupiter: Voyager 2 imaging science results. *Science*, **206**, pp. 927–950.
- Smith, B. A., L. A. Soderblom, T. V. Johnson, A. P. Ingersoll, S. A. Collins, E. M. Shoemaker, G. E. Hunt, H. Masursky, M. H. Carr, M. E. Davies, A. F. Cook, J. M. Boyce, G. E. Danielson, T. Owen, C. Sagan, R. F. Beebe, J. Veverka, R. G. Strom, J. F. McCauley, D. Morrison, G. A. Briggs, and V. E. Suomi (1979b). The Jupiter system through the eyes of Voyager 1. *Science*, **204**, pp. 951–972.
- Smith, R. B. (1975). Unified theory of the onset of folding, boudinage, and mullion structure. *Geol. Soc. Amer. Bull.*, **86**, pp. 1601–1609.
- Smith-Konter, B. R. and R. T. Pappalardo (2007). Tidally Driven Stress Accumulation and Fault Displacements of Enceladus's Tiger Stripes. In *Eos Trans. AGU, Fall Meet. Suppl.*, pp. P11F–06. Abstract.
- Sohl, F., T. Spohn, D. Breuer, and K. Nagel (2002). Implications from Galileo Observations on the Interior Structure and Chemistry of the Galilean Satellites. *Icarus*, **157**, pp. 104–119.

- Solomatov, V. S. (1995). Scaling of temperature- and stress-dependent viscosity convection. *Phys. Fluids*, **7**, pp. 266–274.
- Solomatov, V. S. and A. C. Barr (2006). Onset of convection in fluids with strongly temperature-dependent, power-law viscosity. *Phys. Earth Planet. Int.*, **155**, pp. 140–145.
- Solomatov, V. S. and A. C. Barr (2007). Onset of convection in fluids with strongly temperature-dependent, power-law viscosity 2. Dependence on the initial perturbation. *Phys. Earth Planet. Int.*, **165**, pp. 1–13.
- Solomatov, V. S. and Y. Ke (2007). Coupled core-mantle thermal convection after a giant impact. In *Eos Trans. AGU, Fall Meet. Suppl.*, pp. U21D–01. Abstract.
- Solomatov, V. S. and L. N. Moresi (2000). Scaling of time-dependent stagnant lid convection: Application to small-scale convection on Earth and other terrestrial planets. *J. Geophys. Res.*, **105**, pp. 21795–21817.
- Sotin, C., R. Jaumann, B. J. Buratti, R. H. Brown, R. N. Clark, L. A. Soderblom, K. H. Baines, G. Bellucci, J.-P. Bibring, F. Capaccioni, P. Cerroni, M. Combes, A. Coradini, D. P. Cruikshank, P. Drossart, V. Formisano, Y. Langevin, D. L. Matson, T. B. McCord, R. M. Nelson, P. D. Nicholson, B. Sicardy, S. Lemouelic, S. Rodriguez, K. Stephan, and C. K. Scholz (2005). Release of volatiles from a possible cryovolcano from near-infrared imaging of Titan. *Nature*, **435**, pp. 786–789.
- Spencer, J. R., J. C. Pearl, M. Segura, F. M. Flasar, A. Mamoutkine, P. Romani, B. J. Buratti, A. R. Hendrix, L. J. Spilker, and R. M. C. Lopes (2006). Cassini encounters Enceladus: Background and the discovery of a south polar hot spot. *Science*, **311**, pp. 1401–1405.
- Spitale, J. N. and C. C. Porco (2007). Association of the jets of Enceladus with the warmest regions on its south-polar fractures. *Nature*, **449**, pp. 695–697.
- Spohn, T. and G. Schubert (2003). Oceans in the icy Galilean satellites of Jupiter? *Icarus*, **161**, pp. 456–467.
- Squyres, S. W. (1980). Volume changes in Ganymede and Callisto and the origin of grooved terrain. *Geophys. Res. Lett.*, **7**, pp. 593–596.
- Squyres, S. W. (1981). The topography of Ganymede's grooved terrain. *Icarus*, **46**, pp. 156–168.
- Squyres, S. W. (1982). The evolution of tectonic features on Ganymede. *Icarus*, **52**, pp. 545–559.

- Squyres, S. W. and S. K. Croft (1986). The tectonics of icy satellites. In Burns, J. A. and M. S. Matthews (eds.) *Satellites*, pp. 293–341. University of Arizona Press.
- Squyres, S. W., R. T. Reynolds, P. M. Cassen, and S. J. Peale (1983). The evolution of Enceladus. *Icarus*, **53**, pp. 319–331.
- Stevenson, D. J. (1983). Anomalous bulk viscosity of two-phase fluids and implications for planetary interiors. *J. Geophys. Res.*, **88**, pp. 2456–2474.
- Stevenson, D. J. (1996). When Galileo met Ganymede. *Nature*, **384**, pp. 511–512.
- Stevenson, D. J. (2003). Planetary magnetic fields. *Earth Planet. Sci. Lett.*, **208**, pp. 1–11.
- Stevenson, D. J., T. Spohn, and G. Schubert (1983). Magnetism and thermal evolution of the terrestrial planets. *Icarus*, **54**, pp. 466–489.
- Sverdrup, H. U., M. W. Johnson, and R. H. Fleming (1946). *The Oceans: Their Physics, Chemistry, and General Biology*. Prentice-Hall, Inc., New York.
- Takahashi, E. (1990). Speculations on the Archean mantle: Missing link between komatiite and depleted garnet peridotite. *J. Geophys. Res.*, **95**, pp. 15941–15954.
- Tittemore, W. C. (1990). Chaotic motion of Europa and Ganymede and the Ganymede-Callisto dichotomy. *Science*, **250**, pp. 263–267.
- Tobie, G., G. Choblet, and C. Sotin (2003). Tidally heated convection: Constraints on Europa’s ice shell thickness. *J. Geophys. Res.*, **108**, p. 5124.
- Tobie, G., P. Duval, and C. Sotin (2006). Grain size controlling processes within Europa’s ice shell. In *Lunar Planet. Sci. XXXVII*, p. 2125. Abstract.
- Tobie, G., O. Grasset, J. I. Lunine, A. Mocquet, and C. Sotin (2005a). Titan’s internal structure inferred from a coupled thermal-orbital model. *Icarus*, **175**, pp. 496–502.
- Tobie, G., A. Mocquet, and C. Sotin (2005b). Tidal dissipation within large icy satellites: Applications to Europa and Titan. *Icarus*, **177**, pp. 534–549.
- Turcotte, D. L. and G. Schubert (2002). *Geodynamics*. Cambridge University Press, Cambridge.
- USGS (2007). Integrated Software for Imagers and Spectrometers (ISIS). US Geological Survey, Flagstaff, AZ.

- Usselman, T. M. (1975). Experimental approach to the state of the core; Part I, The liquidus relations of the Fe-rich portion of the Fe-Ni-S system. *Am. J. Sci.*, **275**, pp. 278–290.
- Vanyo, J., P. Wilde, P. Cardin, and P. Olson (1995). Experiments on precessing flows in the Earth's liquid core. *Geophys. J. Int.*, **121**, pp. 136–142.
- Veeder, G. J., D. L. Matson, T. V. Johnson, D. L. Blaney, and J. D. Goguen (1994). Io's heat flow from infrared radiometry: 1983-1993. *J. Geophys. Res.*, **99**, pp. 17095–17162.
- Verbiscer, A. J. and J. Veverka (1994). A photometric study of Enceladus. *Icarus*, **110**, pp. 155–164.
- Verhoogen, J. (1961). Heat balance of the Earth's core. *Geophys. J.*, **4**, pp. 276–281.
- Wienbruch, U. and T. Spohn (1995). A self sustained magnetic field on Io? *Planet. Space Sci.*, **9**, pp. 1045–1057.
- Williams, D. J., B. H. Mauk, R. W. McEntire, E. C. Roelof, T. P. Armstrong, B. Wilken, J. G. Roederer, S. M. Krimigis, T. A. Fritz, L. J. Lanzerotti, and N. Murphy (1997). Energetic partial signatures at Ganymede: Implications for Ganymede's magnetic field. *Geo. Res. Lett.*, **24**, pp. 2163–2166.
- Williams, K. K. and R. Greeley (1998). Estimates of ice thickness in the Conamara Chaos region of Europa. *Geophys. Res. Lett.*, **25**, pp. 4273–4276.
- Wisdom, J. (2004). Spin-orbit secondary resonance dynamics of Enceladus. *Astron. J.*, **128**, pp. 484–491.
- Yoder, C. F. (1979). How tidal heating on Io drives the galilean orbital resonance locks. *Nature*, **279**, pp. 767–770.
- Yoder, C. F. and S. J. Peale (1981). The tides of Io. *Icarus*, **47**, pp. 1–35.
- Zahnle, K., P. Schenk, H. F. Levison, and L. Dones (2003). Cratering rates in the outer solar system. *Icarus*, **163**, pp. 263–289.
- Zahnle, K., P. Schenk, S. Sobieszczyk, L. Dones, and H. F. Levison (2001). Differential Cratering of Synchronously Rotating Satellites by Ecliptic Comets. *Icarus*, **153**, pp. 111–129.
- Zimmer, C., K. K. Khurana, and M. G. Kivelson (2000). Subsurface Oceans on Europa and Callisto: Constraints from Galileo Magnetometer Observations. *Icarus*, **147**, pp. 329–347.

- Zuber, M. T. and E. M. Parmentier (1984). Lithospheric stresses due to radiogenic heating of an ice-silicate planetary body: Implications for Ganymede's tectonic evolution. *J. Geophys. Res.*, **89**, pp. 429–437.
- Zuber, M. T. and E. M. Parmentier (1986). Lithospheric necking: A dynamic model for rift morphology. *Earth Planet. Sci. Lett.*, **77**, pp. 373–383.
- Zuber, M. T. and E. M. Parmentier (1996). Finite amplitude folding of a continuously viscosity-stratified lithosphere. *J. Geophys. Res.*, **101**, pp. 5489–5498.
- Zuber, M. T., E. M. Parmentier, and R. C. Fletcher (1986). Extension of continental lithosphere - A model for two scales of basin and range deformation. *J. Geophys. Res.*, **91**, pp. 4826–4838.